Dissertation

submitted to the

Combined Faculties for the Natural Sciences and for Mathematics

of the Ruperto-Carola University of Heidelberg, Germany

for the degree of

Doctor of Natural Sciences

presented by

Diplom-Physicist Thilo Kranz
born in Frankfurt/Main

Oral examination: May 15, 2002

Dark matter in spiral galaxies

Referees: **Prof. Dr. Hans-Walter Rix**
Priv. Doz. Dr. Rainer Spurzem

Zusammenfassung

Die vorliegende Dissertation umfasst eine gründliche dynamische Analyse von fünf leuchtkräftigen Spiralgalaxien späten Hubbletyps, NGC 3810, NGC 3893, NGC 4254, NGC 5676 und NGC 6643, mit dem Ziel, das Verhältnis von sichtbarer und dunkler Materie im Zentralbereich der Galaxien quantitativ zu bestimmen. Die Analyse der Galaxien basiert auf dem Vergleich von beobachteter Morphologie und Gaskinematik mit hydrodynamischen Simulationen des interstellaren Mediums. Modellrechnungen wurden herangezogen, um gasdynamische Prozesse in realistischen, zweidimensionalen Gravitationspotentialen vorherzusagen. Die Gravitationspotentiale bestehen aus unterschiedlich skalierten Kombinationen von Scheiben– und Halopotential. Das Gravitationspotential der Scheibe wurde auf der Grundlage von farbkorrigierter Nahinfrarot-Photometrie berechnet, der dunkle Halo wurde als isotherme Sphäre mit einem "Core" modelliert.
Die zumeist gute Übereinstimmung von simulierter und gemessener Gasdynamik erlaubte den Schluss, dass die massereichsten Galaxien auch sehr massereiche stellare Scheiben besitzen, die die Gasdynamik im Zentralbereich weitgehend dominieren. In weniger massereichen Galaxien mit maximalen Rotationsgeschwindigkeiten von $< 200\,\mathrm{km\,s^{-1}}$ entfällt bereits etwa die Hälfte der Gesamtmasse auf den Halo. Als typischer Wert für das stellare Masse zu Leuchtkraft Verhältnis ergibt sich $\mathrm{M/L}_K \approx 0.6$ im K-Band.
Ferner ermöglichen die gasdynamischen Simulationen, unabhängig von einer speziellen Dichtewellentheorie, die Kreisgeschwindigkeit des Spiralmusters zuverlässig zu bestimmen. Der damit im Zusammenhang stehende Korotationsradius liegt im Falle der untersuchten Galaxien in einem engen radialen Bereich bei drei exponentiellen Skalenlängen der Scheibe. Die Korotationsresonanz liegt außerhalb der "starken" stellaren Spiralstruktur. Aufgrund der Erfahrungen, die im Rahmen dieses Projekts gesammelt wurden, erscheint das Konzept einer Farbkorrektur, um lokalen Unterschieden in der Sternpopulation Rechnung zu tragen, eine empfehlenswerte Maßnahme, sobald eine Studie von der stellaren Massenverteilung einer Galaxie abhängt.

Abstract

This thesis presents a detailed dynamic analysis of five high surface brightness, late type spiral galaxies NGC 3810, NGC 3893, NGC 4254, NGC 5676 and NGC 6643, which were studied with the aim to quantify the luminous-to-dark matter ratio inside their optical radii. In order to meet this goal, the galaxies' morphology and gas kinematics have been observed and compared to hydrodynamic gas simulations which were performed to predict the gas dynamics arising in response to realistic two dimensional gravitational potentials, combined from stellar disk and dark halo contributions. The gravitational potential of the stellar disk was derived from color-corrected NIR photometry and for the dark halo, the mass density distribution of an axisymmetric isothermal sphere with a core was chosen.
The rather good agreement between the simulated and observed gas kinematics permitted to conclude that the most massive galaxies tend to possess also very massive stellar disks, dominating the gas dynamics within the optical radius. In less massive galaxies with a maximal rotation velocity of $< 200\,\mathrm{km\,s^{-1}}$, the mass of the dark halo already equals the stellar mass. The maximal disk stellar mass-to-light ratio in the K-band was found to lie at about $\mathrm{M/L}_K \approx 0.6$.
Furthermore, the gas dynamic simulations provide a powerful tool to accurately determine the spiral pattern speed for galaxies, independent of a specific density wave theory. It was found that the location of the corotation resonance falls into a narrow range of around three exponential disk scale lengths for all galaxies from the sample. The corotation resonance encloses the strong part of the stellar spiral in all cases. Based on the experience gained from this project, the use of a color-correction to account for local stellar population differences is strongly encouraged when properties of galactic disks are studied which rely on their stellar mass distributions.


WE'VE GOT TO CONTEND WITH VORTEXES AND LIGHT SPEEDS! ANYTHING COULD GO WRONG! OF COURSE WE NEED TO WEAR GOGGLES!
© Watterson

Contents

CHAPTER I
Introduction to dark matter

During the last decades, evidence has constantly grown stronger that the mass fraction of the baryonic matter might have only a minor contribution to the total mass that is found in the universe. In fact it is argued today that up to 95 % of the mass in the universe eludes the eyes of the observers. Considering this large overabundance of dark matter, we still know very little about its nature and its distribution on large and small scales.

For the last few years the Cold Dark Matter (CDM) model has been used fairly successfully in explaining the large scale structure formation in the universe. However, on the scale of galaxies, the theoretical predictions of dark halo shapes disagree with observational evidence. Several alternatives have been proposed to fix the shortcomings of the CDM scenario, but there is no widely agreed on solution available yet. In spite of the dispute about the nature of the dark matter, there is plenty of evidence that can be considered as good proof of its presence. This introduction provides some overview on the current understanding of dark matter related issues. It is not intended to serve as an exhaustive review, but rather to highlight the fundamental ideas on which present research of dark matter is based.

1.1. Evidence for dark matter in the universe

1.1.1. Galaxy clusters

The first finding indicating evidence for a considerable amount of dark matter in the universe is credited to F. Zwicky (1937) who estimated the virial mass of the Coma cluster of galaxies from the peculiar motions of the cluster's members and compared it to the visible mass estimate. This method is still valid today, but bears large uncertainties from small number statistics, unvirialized systems, and kinematically unrelated interloper galaxies. Modern analyses (Carlberg et al. 1996) determined cluster mass-to-light ratios (M/L, always in solar units) to $\sim 300\ M_\odot/L_\odot$.

Another method of estimating the mass in galaxy clusters is by their X-ray luminosity. Most of the intra-cluster gas is diffuse, ionized and very hot, especially in dense and massive clusters. In fact, the temperature of the gas correlates with the velocity dispersion of the cluster's member galaxies and allows for an alternative probe of the gravitational potential of clusters (see Sarazin 1988 for a review). Assuming the gas in a hydrostatic equilibrium

– which might be a good approximation in some cases – the potential and thus the total gravitating mass of the cluster might be derived from the radial brightness profile. This has been done for several galaxy clusters; e.g., the Virgo cluster (Schindler et al. 1999), the Fornax cluster (Jones et al. 1997), and several Abell clusters (David et al. 1995; Cirimele et al. 1997). These studies conclude that the cluster systems are widely dominated by dark matter with typical values of M/L = 100 – 150, reaching as high as M/L $\approx$ 500 (Schindler et al. 1999).

1.1.2. Lensing

Gravitational lensing provides a fairly unbiased method of gauging the gravitating mass in the universe. It gives us the chance to probe the present galaxy and cluster mass profiles independent of the dynamic state of the systems. A very indicative example is strong lensing in galaxy clusters. There are several known examples, where giant lensed arcs in clusters are observed and may be used to trace the cluster's gravitational potential; e.g., Abell 2218 (Kneib et al. 1995; Cannon et al. 1999), CL 0024+1654 (Shapiro et al. 2000). In most cases the mass estimates derived from X-ray luminosities and gravitational lensing tend to disagree slightly. The lensing studies generally find cuspy matter distributions, coinciding often with the central cD galaxy of the lensing system. The inferred matter profiles of these clusters agree fairly well with the assumptions of CDM and demonstrate clearly the need for large amounts of dark matter within galaxy cluster systems.

In recent years weak lensing has turned out to provide a powerful tool to probe the dark matter distribution on large scales. The idea of weak lensing is that the underlying mass distribution exerts a weak cosmic structural shear on the galaxies in the line of sight. From this shear a two dimensional map of the total mass can be reconstructed (see Mellier 1999 for a review). This method profits from modern, more sophisticated numerical techniques as well as from new generation wide field imaging instruments. There have been weak lensing studies of galaxy clusters and superclusters (e.g., Squires et al. 1996; Gray et al. 2001) and of blank fields (e.g., Bacon et al. 2000; Wilson et al. 2001). Besides high values for M/L in the cluster regions, weak lensing results show that M/L in the intercluster space might also be high. Since for some studies the density of early type galaxies seems to coincide fairly well with the highest concentrations in the mass maps from weak lensing, it is argued that M/L for early-type galaxies may be universal. If this is the case the early-type M/L_B lies in the range of 150 to 300 $M_\odot/L_\odot$ and a range for Ω_m of 0.2 to 0.3 is favored.

1.1.3. Halos of galaxies

Additional evidence for the need of dark matter comes from the analysis of galactic rotation curves. Rotation curves of spiral galaxies have been explored for over forty years, beginning with the pioneering works of V. Rubin and W. Roberts. The fact that the rotation curves stay flat out to great radii argues for a large amount of dark matter in an unseen halo that surrounds the visible part of the galaxy. It turns out that the dynamical mass of the galaxy is largely dominated by the non-baryonic dark matter in the halo. The inferred total M/L is typically in the range of 10 to 50 $M_\odot/L_\odot$, depending on the class of the galactic system. While huge high surface brightness spirals supposedly sit in the centers of massive halos, low surface brightness and dwarf galaxies are especially

dominated by dark matter on all scales. Elliptical galaxies, considered to account for most of the visible mass in the universe today, reside most probably also in giant dark matter halos (Griffiths et al. 1996; Rix et al. 1997, Loewenstein & White 1999). However, since stars in elliptical systems do not exhibit well ordered kinematics like that found in disks, testing for a dark matter halo requires different techniques. Results were achieved by the kinematics of gravitationally bound objects (e.g., globular clusters, planetary nebulae), the velocity dispersion from spectral analysis, and lensing. Thus, also for ellipticals the total M/L is rather large and in the range of 20 to 100.

The dark matter distribution in the central parts of galaxies is an issue with no widely agreed on solution. It is this part of the dark matter problem, which I address in this thesis. The challenges of separating out the different mass contributions and the implications for disk kinematics issues will be the focus of the following chapters.

1.1.4. Cosmological implications and the baryon fraction

The average density of baryonic and non-baryonic matter in the universe ρ_m is typically referred to in terms of the density parameter, Ω_m, which is defined as the ratio of the present ρ_m to the critical density $\rho_c = 3H_0^2/8\pi G$, where H_0 is the Hubble constant and G is the gravitational constant. Additionally, a cosmological constant Λ can be formally identified with the vacuum mass density ρ_v to account for "dark energy" in the universe that contributes to the final mass budget. A corresponding density parameter $\Omega_\Lambda = \rho_v/\rho_c$ can be defined. The total average mass-energy density in the universe Ω is the sum: $\Omega = \Omega_m + \Omega_\Lambda$.

In recent years there has been progress in constraining the possible range for Ω. Especially the very recent BOOMERANG and MAXIMA balloon experiments allow to probe the fine structure of the cosmic microwave background (CMB) to determine various cosmological parameters from the CMB anisotropies. These studies yield strong evidence for a flat universe with $\Omega \approx 1$ (de Bernardis et al. 2000; Stompor et al. 2001). These findings are in good agreement with the results from the Supernova Cosmology Project (Perlmutter et al. 1999). There is strong evidence for an accelerating universe and hence $\Omega_\Lambda > 0$. For an $\Omega = 1$ universe these results, including estimates from galaxy cluster analyses, yield a best fit of $\Omega_m \approx 0.3$ and $\Omega_\Lambda \approx 0.7$ to the data. Ω_m was defined to include both normal matter and dark matter, $\Omega_m = \Omega_B + \Omega_{DM}$. From M/L estimates it is already clear that Ω_{DM} comprises a large fraction of the total mass density. Another constraint for the baryonic mass fraction ρ_B comes from studies of primordial nucleosynthesis. The relative abundances of the light elements, especially deuterium, which was produced shortly after the Big Bang, can be used to confine the total baryonic mass content in the universe. In a recent review article, Tytler et al. (2000) conclude from a variety measurements of the deuterium to hydrogen abundance ratio that the derived value for $\Omega_B h^2 = 0.019 \pm 0.0024$, which with a Hubble constant of $75\,\mathrm{km\,s^{-1}\,kpc^{-1}}$ yields $\Omega_B \approx 0.036$. This value is in very good agreement with other estimates for Ω_B from Lyman-α forest absorption within the intergalactic medium and from galaxy clusters by means of their X-ray luminosity or the Sunyaev-Zel'dovich effect (see Tytler et al. 2000 and references therein).

In order to account for $\Omega_m \approx 0.3$ dark matter must be 5 to 10 times more abundant in the universe than the kind of matter that we know and that is made up mostly from baryons. Furthermore, perhaps less than half of the baryonic material is visible to the eye in the form of stars, gas and dust.

1.2. The nature of dark matter

We now know fairly well the amount of dark matter in the universe and how it is distributed on large scales. However, the nature and the physics of this elusive mass component remains very much unknown. As it has become evident, the missing amount of matter in the present universe cannot be explained by a single, hitherto undetected matter component. The matter budget is a multi-piece puzzle that is just being sorted out now.

1.2.1. Baryonic dark matter

Primordial nucleosynthesis can be used to convincingly predict the baryon fraction in the universe. A comparison of these predictions with presently observed baryons in the luminous components of galaxies and in the intergalactic medium shows that the observed baryons account for only about half of the existing baryons (Cen & Ostriker 1999). Interestingly, results from Lyman-α forest absorption studies find that the baryon budget seems to agree with nucleosynthesis expectations at $z \sim 3$ (Fukugita, Hogan & Peebles 1998). Apparently, a considerable fraction of the baryons must have eluded the processes of structure and star formation and remains hidden to the observers.

The stellar contribution of the baryonic matter ranges only at $\sim 10\,\%$ (Valageas, Silk, & Schaeffer 2001). Most of the present baryons are stored in the form of gas, mainly in galaxies and galaxy groups. The amount of baryons in these various gas components – fully ionized gas, diffuse, warm intergalactic medium, nearby Lyman-α absorption clouds, or cold diffuse of clumpy H_2 gas – is very difficult to assess. About 75 % of the baryonic matter is very likely to be composed of gas and stars, leaving about 25 % of the baryonic mass unaccounted.

The majority of these missing dark baryons can presumably be found in the halos of galaxies. These dark matter candidates are collectively called 'MAssive Compact Halo Objects' (MACHOs). There are extensive monitoring projects of stars in the Magellanic Clouds to look for microlensing events caused by the passage of a MACHO close to the line-of-sight (MACHO (Alcock et al. 2000), EROS (Lasserre et al. 2000), OGLE (Udalski et al. 1992)). These surveys showed that the Milky Way halo cannot be made entirely of MACHOs; at most, MACHOs contribute $\sim 20\,\%$ to the halo mass (Alcock & The MACHO-collaboration 2000; Lasserre & The EROS-collaboration 2000). However, if the MACHOs are as numerous as this upper limit allows, they could eventually make up for most of the missing dark baryonic component. If so, there would be twice as much mass in MACHOs than there is in stars.

On the other hand, the microlensing surveys constrain the average mass of halo objects to a range of $0.1 - 1\ M_\odot$. Building up the halo from such low-mass objects requires relatively high MACHO numbers. However, for an abundant mass component it is difficult to come up with a suitable formation process. The only dark objects known that have masses in the required range are old white dwarfs. Asteroid sized rocks are too small to cause the mircolensing events by their low gravity, while brown dwarfs and K-dwarfs seem to comprise only $\sim 1\,\%$ of the galactic halo mass. Despite the detection of white dwarfs in the HDF and proper motion surveys (Ibata et al. 1999, 2000), metal enrichment and infrared background considerations lead to the conclusion that white dwarfs cannot be sufficiently abundant to contribute significantly to the baryonic dark matter compo-

nent (Fields, Freese, & Graff 2000). Thus, there is no consistent explanation for what a MACHO is and how the microlensing events can be satisfyingly explained. Alternative explanations are also being explored, like a LMC thick disk or halo star clumps. In such a case the cosmological relevance would be less.

There are more exotic dark matter types of baryonic origin being discussed, such as primordial black holes, which might be able to explain microlensing events. Primordial black holes might date back from radiation dominated stages of the universe and originate from the gravitational collapse of horizon-size energy density fluctuations (Jedamzik 2001). Yet, these objects have not been observationally confirmed and there is not much known about their quantity or their mass function.

1.2.2. Non-baryonic dark matter

Although the baryonic dark matter seems to be close to completely sampled, there is still a huge amount of missing mass to match the $\Omega_m \approx 0.3$ requirement. This component is referred to as non-baryonic dark matter. Likely, there is not only a single particle type that accounts for all the missing mass, but rather a variety of particles of varying significance (Sellwood 2000).

In the early 1980's neutrinos emerged as very attractive dark matter candidates. They are the only dark matter candidates known to exist. Although being massless in the standard model for particle physics, there has been recent evidence that neutrinos actually carry mass, which relies on the observational fact of neutrino oscillations. New Superkamiokande measurements allowed to estimate the $\mu-\tau$ neutrino mass-square difference to a few meV^2, attributing only tiny masses to the neutrinos themselves (see Caldwell 1999, and references therein). The small masses of neutrinos make it highly unlikely for neutrinos to represent the bulk of non-baryonic dark matter. Furthermore neutrinos belong to the hot dark matter type, being still relativistic when decoupling from the radiation field in the early universe. A universe dominated by a hot dark matter scenario does not agree with current galaxy evolution theories. These findings lead to the fall of the neutrino as the top dark matter candidate (for a review, see Primack & Gross 2001).

According to current theories most of the dark matter particles are rather massive and, as the universe became matter-dominant, they would have cooled to non-relativistic temperatures: this is cold dark matter (CDM). Particle physicists have assembled a vast zoo of possible CDM candidates, where most of them can be characterized as "Weakly Interacting Massive Particles" (WIMPs). Besides the initial requirement that WIMPs are massive and the postulation that they are susceptible to weak interactions they might also carry color charges. The stringent requirement is that they don't carry electrical charge. The strength with which the WIMPs interact with ordinary matter might span a wide range. The most physically motivated candidates for non-baryonic WIMP dark matter include neutralinos and axions (Kamionkowski 1998).

The neutralino is perhaps the best candidate for a WIMP. It is a neutral Majorana particle[1] and it is the lightest stable particle in the theory of supersymmetry (SUSY). It couples to ordinary matter with a weak-interaction strength, which might be in the sensitivity range of present-day high energy particle detectors (for a review, see Jungman 1996). Since it is

[1] A Majorana particle is equal to its own anti-particle.

stable, the neutralino itself is not supposed to interact via strong interactions or it would bind in nuclei and become observable in exotic heavy isotopes.

Another very good candidate for non-baryonic dark matter is the axion and its fermionic partner, the axino. They were introduced by particle physicists to solve the strong CP-violation problem in quantum chromo-dynamics (Peccei & Quinn 1977). In contrast to other CDM particles, the axion is relatively light, but symmetry breaking occurs at high energy scales; Hence early in the universe, existing axions could have cooled to become non-relativistic CDM.

There are several more highly exotic particles that might account for non-baryonic material, but the two kinds mentioned above, the neutralino and the axion, have the best chance for experimental verification. In fact, there have already been measurements of annual modulations in particle fluxes claimed as possible WIMP signatures in particle physics experiments (Bernabei & The DAMA Collaboration 1999), but the findings are very controversial and are still waiting verification of falsification by other experiments probing the same energy range. Eventually there are high hopes of finding SUSY particles with the Large Hadron Collider at CERN which is currently being constructed.

Until non-baryonic dark matter can be confirmed by particle experiments, it is worthwile to look at the spatial distribution of dark matter in the universe. A quite successful cosmological evolution model uses the ΛCDM scenario, which assumes cold dark matter and a non-zero cosmological constant. These models successfully recover cosmic large scale structure (e.g., Pearce et al. 2001), while high resolution simulations find strong subclustering and central dark matter cusps in galaxies (Fukushige & Makino 1997; Moore et al. 1999a). Since in observed galaxies evidence for these density cusps is very poor and there is no evidence for strong dark matter subclustering, modifications to WIMP properties are applied to solve for these shortcomings. Tests were made for self-interacting (Yoshida et al. 2000; Meneghetti et al. 2001) or fluid-like particles (Peebles 2000). Also warm dark matter has been proposed (Avila-Reese et al. 2001). However, all these modifications do not improve the situation satisfyingly; more questions arise and more options need to be checked. Of immediate need certainly is to constrain the dark matter distribution in galaxies more precisely before firm constraints can be issued regarding the nature and the interaction cross-sections of non-baryonic dark matter particles. Eventually, this thesis might contribute here a small piece to the solution of the grand puzzle.

1.2.3. MOND – A universe without dark matter

Although modern cosmology tends to adopt the idea of dark matter to account for discrepancies in the mass balance of the universe there is also a well elaborated approach explaining these discrepancies by a slightly modified gravitational acceleration. This concept called "MOdified Newton Dynamics" (MOND) was introduced by M. Milgrom (1983). MOND can be interpreted as either a modification of gravity through a change to the Poisson equation, or as a modification of inertia through a breaking of the equivalence of inertial and gravitational mass. MOND is implemented as a non-relativistic modification to the standard Newtonian gravitational acceleration field $\mathbf{g}_N$. The relation between the $\mathbf{g}$ in MOND and $\mathbf{g}_N$ is given by: $\mathbf{g}\mu(|\mathrm{g}|/a_0) = \mathbf{g}_N$, where a_0 is a new physical parameter with units of acceleration, and $\mu(x)$ is some function that asymptotically converges to $\mu(x) = x$

when $x \ll 1$ and $\mu(x) = 1$ when $x \gg 1$ ($x = \mathrm{g}/a_0$). For very low accelerations MOND predicts $\mathrm{g} = \sqrt{\mathrm{g}_N a_0}$. Apparently a_0 – which is of order $10^{-10}\,\mathrm{m\,s^{-2}}$ – scales with cH_0 to within a factor of 5 or 6. This ad hoc assumption has two immediate consequences for the dynamics in galaxies: (1.) The rotation curve for any galaxy becomes asymptotically flat and (2.) the asymptotic rotation velocity v_∞ depends only on the galaxy's total mass M as $v_\infty^4 = MGa_0$.

The implications of MOND are rather extensive. It solves not only the problems it was designed to solve, i.e., the explanation of galactic rotation curves without dark matter, but can be applied to a variety of problems. MOND seems to explain the dynamics of high and low surface brightness galaxies with reasonable values for M/L. Moreover, MOND satisfies the Tully-Fisher relation for spirals (McGaugh & de Blok 1998) and the fundamental plane for ellipticals (Sanders 2001). MOND also reproduces the actual velocity dispersions in all kinds of galaxy groups and clusters (Milgrom 1998). Furthermore the theory can also be used to explain the recently observed angular power spectrum of the CMB from the BOOMERANG and MAXIMA experiments (McGaugh 2000).

Still, despite all its successes, there are conceptual difficulties with MOND theory. The idea of modifying such an universal law as gravity is not straightforward and has many severe consequences. In a recent article Scott et al. (2001) review conceptual, empirical and cosmological difficulties with MOND. The main criticisms are: (*i*) Explicit violation of the equivalence principle resulting from the fact that in MOND inertial mass and gravitational mass are not the same. Derived from this (*ii*) momentum is not conserved and Newton's third law is violated. In fact, any multi component mass assembly faces difficulties in its dynamic description since (*iii*) gravity is no longer linear anymore and MOND does not allow for superpositions of gravitational fields. Evidently, since what applies to accelerations should also be valid for decelerations MOND suggests that (*iv*) all bodies are bound to each other, since gravitational forces decelerate any particle never less than a_0. The fundamental constant a_0 with the dimensions of acceleration that MOND introduces violates most of what fundamental physics relies on. It (*v*) violates Lorentz invariance because coordinate invariance, one of the fundaments of relativity, is not preserved. Also any concept of modelling forces by exchange particles fails. With the loss of coordinate invariance even the (*vi*) Cosmological Principle seems to not apply any more.

With these fundamental problems MOND has not won vast support within the astronomical community. Acceptance for MOND might improve if either a stronger theoretical framework is devised in which MOND is embedded or the concept of CDM comes into severe conflict with observations.

CHAPTER II
Luminous and Dark Matter in Spiral Galaxies: A New Test

In almost all galaxy formation scenarios non-baryonic dark matter plays an important role. Today's numerical simulations of cosmological structure evolution reproduce fairly well the observed distribution of galaxy properties in the universe (e.g., Kauffmann et al. 1999) and attempts to model the formation of single galaxies have been made as well (Steinmetz & Müller 1995). In these simulations the baryonic matter cools and settles in the centers of dark halos where it forms stars. The distribution of stars and gas in a galaxy depends strongly on the local star formation and merging history. At the same time that the stars are forming the halos evolve and merge as well.

2.1. Maximal disks or not?

The final relative distribution of luminous and dark matter in the centers of the resulting galaxies is under debate because the mass distribution of the dark matter component is difficult to assess directly. Measuring luminous and dark matter mass profiles separately requires innovative strategies because the halo is poorly constrained and equally good fits to measured rotation curves can be achieved for a wide range of visible mass components (e.g., Broeils & Courteau 1997). In order to define a unique solution to this so called "disk-halo degeneracy", the "maximal disk" solution was introduced. It assumes the highest possible mass-to-light ratio (M/L) for the stellar disk (van Albada et al. 1985; van Albada & Sancisi 1986). A practical definition is given by Sackett (1997) who attributes the term "maximal" to a stellar disk if it accounts for 85% ± 10% of the total rotational support of the galaxy at $R = 2.2\ R_{exp}$. This approach has proven to be very successful in matching observed H I and Hα rotation curves (van Albada et al. 1985; Kent 1986; Broeils & Courteau 1997; Salucci & Persic 1999, Palunas & Williams 2000) and also satisfies some dynamical constraints, such as the criteria of forming $m = 2$ spirals (Athanassoula, Bosma & Papaioannou 1987) as well as observational constraints on the structure of the Milky Way (Sackett 1997). However, modern numerical N-body simulations find significant central dark matter density cusps (Fukushige & Makino 1997; Moore et al. 1999a). Even if the prediction of these strong density cusps may not be entirely correct, the simulations find that the dark matter is of comparable importance in the inner parts of galaxies (Blumenthal et al. 1986; Moore 1994; Navarro, Frenk & White 1996, 1997) and it thus has a

considerable influence on the kinematics. In this case a stellar disk of a galaxy would turn out to be "sub-maximal".

It is important to determine the relative proportion of dark and luminous matter in galaxies for a better understanding of the importance of the baryonic mass in the universe. This proportion also bears information on the dynamics and structure of the dark matter itself. Spiral galaxies are well suited to study dark matter distributions because their distinctly ordered kinematics provide an excellent tracer of the gravitational potential in the disk plane. Since bars in galaxies are very prominent features with distinct dynamic characteristics, they are especially well suited to evaluate the amount of luminous matter. Sophisticated studies of barred galaxies indicate that their stellar disks alone dominate the kinematics of the inner regions – the stellar contribution is maximal (Debattista & Sellwood 1998, 2000; Weiner et al. 2001a). However, studies of our own Milky Way, found also to be a barred spiral, still do not give a clear answer as to whether the disk is maximal (Sackett 1997; Englmaier & Gerhard 1999) or not (Kujiken 1995; Dehnen & Binney 1998).

Bottema's analysis of the stellar velocity dispersion in various galactic disks led to the conclusion that disks cannot comprise most of the mass inside the radial range of a few exponential scale lengths (Bottema 1997). Aside from the dynamical analysis of single systems, other attempts to tackle this problem have been undertaken. Maller et al. (2000) used the geometry of gravitational lens systems to probe the potential of a lensing galaxy. They concluded that a maximum disk solution is highly unlikely. Courteau & Rix (1999) applied statistical methods to learn about the mass distribution in galaxies. In their analysis they found no dependence of the maximum rotation velocity on a galaxy's disk size. The conflicting findings of different studies leave the question of the relative proportion of dark and luminous matter in galaxies still open.

2.2. The concept

In this thesis the fact is exploited, that the stellar mass in disk galaxies is often organized in spiral arms, thus in kinematically cold non-axisymmetric structures. In the canonical CDM cosmology the dark matter is collisionless and dominated by random motions. Although the introduction of weakly self-interacting dark matter was proposed to avoid current shortcomings of the CDM model (Spergel & Steinhardt 2000) it seems to raise other, comparably severe problems (Yoshida et al. 2000; Ostriker 2000; Miralda-Escude 2002). Hence it seems reasonable to assume that CDM is not substantially self-interacting, but dynamically hot and therefore not susceptible to non-axisymmetric spiral or other small scale structure.

In light of this, the key to measuring the baryonic and dark matter mass fractions is to make use of the non-axisymmetric structure that can be observed in the stellar light distribution. Using deviations from axisymmetry of stellar disks, several efforts have already been made to constrain the dark matter content of non-barred spiral galaxies (e.g., Visser 1980; Quillen 1999, and references therein). Some of the most significant conclusions came from studies of massive bars, which are the strongest non-axisymmetric structures in disk galaxies. Spiral arms comprise a less prominent, but still significant mass concentration. Already very early theoretical calculations of gas shocking in the gravitational potential of a spiral galaxy (e.g., Roberts 1969) came to the conclusion that "velocity wiggles" with

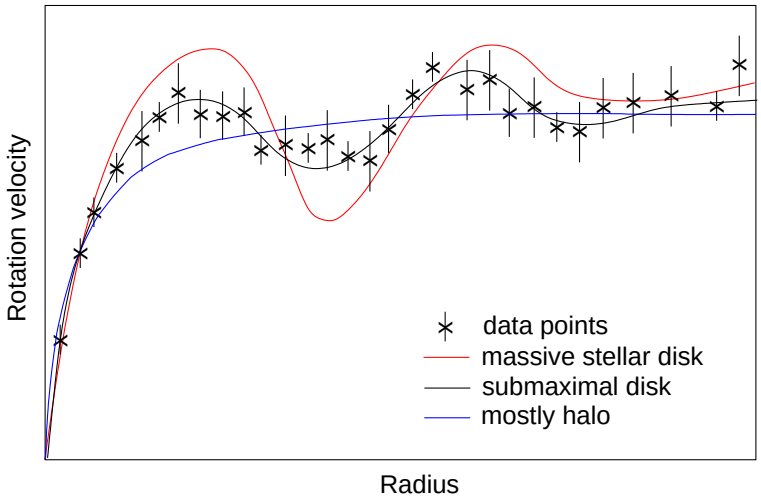

Figure 2.1 Idea of the project. The measured gas velocity field (fictional data points) should be matched by a modelled gas velocity field from hydrodynamical simulation (continuous lines). The mass fraction of the non-axisymmetric stellar mass contribution determines the amplitude of the "velocity wiggles" in the simulations and is adjusted to match the observations. In the depicted scenario a submaximal disk (black line) yields the best fit to the data.

an amplitude of 10 to 30 km s^{-1} could be expected while crossing massive spiral arms. For ionized gas, measurements of the velocity to this precision can be achieved with common longslit spectrographs. The imprint of the spiral pattern in the velocity field of observed galaxies is indeed not very strong, as apparent in the 2D velocity fields of M 100 (Canzian & Allen 1997), of low surface brightness galaxies (Quillen & Pickering 1997) or of a sample of spiral galaxies (Sakamoto et al. 1999). There are only a few spiral galaxies without bars that show stronger wiggles in the velocity field that are associated with the arms, e.g., M 81 (Visser 1980; Adler & Westpfahl 1996) and M 51 (Aalto et al. 1999).

In order to still achieve the goal of measuring mass-to-light ratios it is needed to compare the expectedly weak features in the measured velocity field to detailed kinematic models. The use of new high resolution K-band photometry to map the stellar component and the application of a modern hydro-code to simulate galactic gas flows establishes a sound basis for the models to show enough details and enable the measurement of mass-to-light ratios. If the arms are a negligible mass concentration relative to the dark matter distribution in the galaxy, these wiggles should appear only very barely in the velocity field. The main aim of this project is to find out what fraction of the rotation speed comes from a mass component with spiral arms. In order to do this the strength of the wiggles in a galaxy's observed velocity field have to be compared to a model of the gas velocity field arising in a potential whose disk-halo fraction is known. As input for the gas dynamical simulations, it is necessary to derive the stellar potential of the galaxy from color-corrected K-band photometry, while the dark matter component is modelled as an isothermal sphere with a core. Simulations are performed for a variety of potential combinations and values for the pattern speed of the spiral structure. The results from these simulations are then compared to the observed kinematics.

2.3. The spiral structure of galaxies

For the present analysis the key element is the non-axisymmetric spiral structure observed in the stellar and gaseous components of many disk galaxies and the way it is depicted in their velocity fields. Understanding the basics of spiral morphology is essential in order to apply the appropriate modelling process. In this Section I briefly review the relevant concepts. For a thorough introduction in the field see Athanassoula (1984).

The spiral structure is closely related with the global dynamics of disk galaxies. Due to the differential rotation in the disk, a once established spiral would wind up into a very tight curl within a few dynamical time scales. Thus, the observed spirals cannot comprise of an aligned, fixed population of stars, but rather involve all stars maintaining a "kinematic density wave" in the disk. The spiral arms appear in domains, where the stars are packed more densely and move slower on their orbits. The density wave also induces shocks in the interstellar medium, causing star formation along the spiral arms. Under these circumstances, the newly formed stars make the spiral arms to appear bluer than the inter-arm regions. However, grand design spirals are not the product of a self propagating star formation wave as suggested by Gerola & Seiden (1978). This becomes apparent from NIR imaging, mainly tracing the old stellar populations, where the spiral arms are still clearly visible.

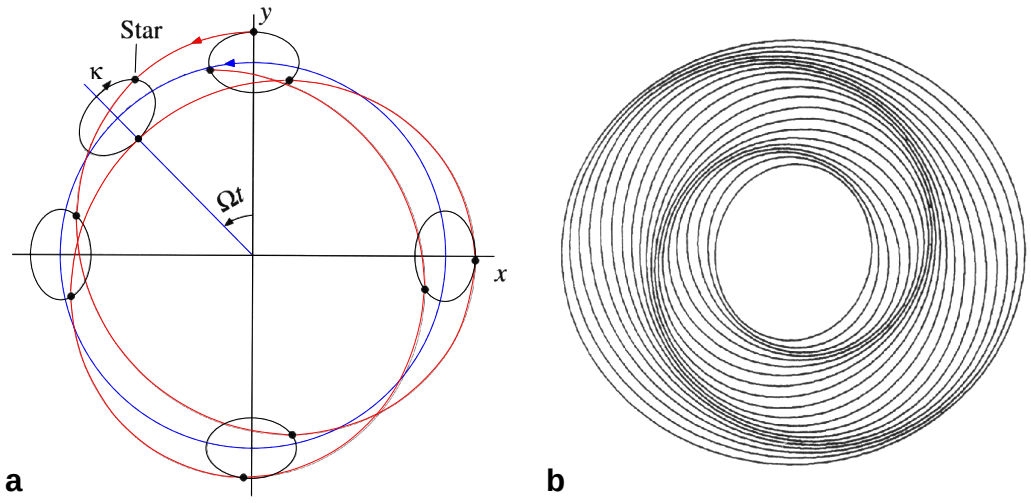

Figure 2.2 The principles of spiral structure. **a)** In an inertial reference frame (x,y) a star's orbital motion can be imagined as being a combination of a retrograde orbit about an epicycle with frequency κ and the prograde orbital motion (blue line). In this reference frame the star's path forms a non-closing rosette pattern (red curve). **b)** Nested oval orbits with a relative phase shift, as seen in a non-inertial reference frame rotating the global angular pattern speed Ω_p, can result in a grand design spiral density wave. Adapted from Carroll & Ostlie (1996)

The principles of a spiral density wave were developed by B. Lindblad and J. Oort in the mid of last century, namely the epicycle theory. In an inertial reference frame a star's orbital motion can be described by its circular motion of frequency Ω around the galactic

center, superposed with an oscillation of frequency κ around the guiding center. In this "epicyclic approximation", stellar orbits generally follow a non-closing rosette trajectory in the galactic disk (see Figure 2.2a).

However, for a variety of applications it is useful to introduce some non-inertial reference frame, rotating with an orbital frequency $\Omega_{\rm p}$. The advantage of this reference frame is, that $\Omega_{\rm p}$ can be chosen such that the orbit of the star is closed. For nearly circular orbits the requirement for a closed orbit is fulfilled, when $(\Omega - \Omega_{\rm p})/\kappa$ is rational:

$$\Omega_{\rm p}(R) = \Omega(R) - \frac{n}{m}\kappa(R). \quad n \text{ and } m \text{ are integers.} \tag{2.1}$$

While for most values for n and m $\Omega - \frac{n\kappa}{m}$ varies rapidly with radius, for $n = 1$ and $m = 2$ it is relatively constant across much of the galaxy. In this scenario, the orbits of the stars as seen from the rotating reference frame are ellipses. If these orbits are nested and aligned in a collective manner across the disk, different wave patterns can be created (see Figure 2.2b). As viewed from an inertial frame the pattern retains its morphology, but rotates with the angular frequency $\Omega_{\rm p}$. Thus, $\Omega_{\rm p}$ is called the pattern speed.

In the 1960s Lin and Shu (1964, 1966) developed the more elaborate quasi-stationary, linear density wave theory (for a review, see Bertin & Lin 1996). In this approach the spiral density wave is described as a the most unstable oscillation mode of the galactic disk. The amplitude of the spiral pattern evolves by interactions of these modes with the dissipative character of the interstellar medium. The stellar spiral pattern extends in the radial range between the inner Lindblad resonance (ILR) and the corotation if they are stationary. If they are growing they can extend even out to the outer Lindblad resonance (OLR) (e.g., Lin et al. 1969; Toomre 1981; Bertin et al. 1989a,b). The ILR and OLR are resonances between the epicyclic precession frequencies $\Omega \pm \kappa/2$ and the pattern speed $\Omega_{\rm p}$.

Due to the stability of the spiral structure resonances play a crucial role also for the morphological appearance of the galaxy. For example at the corotation radius, where the pattern speed $\Omega_{\rm p}$ is equal to the orbital frequency Ω, the response of the gas is not periodic since the gas rotates along with the spiral perturbations and thus the non-axisymmetric forcing vanishes. In light of this, it is expected that at the corotation radius star formation cannot get excited by the density wave and should not be observed in a quiescent galaxy. The location of this resonance should become visible as a ring of largely reduced star formation (Shu et al. 1973).

However, in real galaxies the situation seems to be more complicated. In normal spiral galaxies with relatively open spirals, orbits belonging to the main orbital families deviate significantly from circular orbits, with the consequence that non-linear effects become important. The importance of non-linear effects in realistic models of spiral galaxies was studied by Contopoulos & Grosbøl (1986, 1988) and Patsis et al. (1991). It was found that at least for late type spiral galaxies, non-linear effects cause the response density to grow out of phase with the underlying potential already inside corotation and consequently the strong part of the spiral terminates at the 4/1 resonance, that is located roughly half way to corotation. If, however, the potential perturbation is weak, non-linear effects play a minor role. It is very difficult to settle these issues on an observational basis, since the locations of the resonances are generally not very well known for real galaxies.

Besides retaining the morphological shape of the spiral pattern, the question must be assessed on how the spiral maintains the amplitude of the density wave. Like any other wave travelling through a medium, also the spiral density wave needs to get regenerated continuously, or at least at certain times, to prevent it from dispersing and fading away. One internal mechanism has been proposed for galaxies that is referred to as swing amplification (Toomre 1981). If the pattern speed Ω_p is high enough that no ILR is present, density waves can travel through the center of the disk, changing from a trailing to a leading spiral. Due to the differential rotation in the disk, the leading wave, propagating outwards towards corotation gets converted into a trailing wave. During this process the wave can get amplified by a factor 10 or more. If the swing amplification is not embedded into a feedback cycle, the mechanism would not provide a quasi-stationary spiral pattern.

Another internal mechanism to drive a spiral pattern is a central bar or oval asymmetry. Indeed, it has been found that already in simple models central bars can induce strong spiral features in the disk (Sanders & Huntley 1976). Important for the bar driving mechanism is a dissipative interstellar medium. Modern analyses find that the induced spiral structure depends on the rotation speed of the bar. Spirals associated with the outer Lindblad resonance, i.e. for fast bars, are tightly wound, while those associated with the inner Lindblad resonances for slow bars are relatively open (Yuan & Kuo 1997).

Finally, tidal interaction due to a companion galaxy's flyby may enhance the spiral density wave (Toomre 1974). During the flyby angular momentum is exchanged between the companion and the wave. As observed in the prominent examples of M 51 and M 81, the spiral pattern, driven by external tidal interaction, might result in very regular grand design structure. The tidal forcing depends strongly on the orbital parameters of the flyby. It matters, for example, if the companion orbits prograde or retrograde (Athanassoula 1978). Furthermore, the companion must pass fairly fast and close to have a noticeable effect on the spiral's disk morphology (Howard et al. 1993). To assure a tidally driven quasi-stationary spiral pattern, the companion must orbit very closely around the galaxy. However, this scenario would also only work for a limited time because on a closeby, periodic orbit the companion is predestined to merge with the spiral galaxy.

There are even more scenarios that have been proposed to cause or maintain spiral structure. Nevertheless, the spiral structure of a real galaxy in the universe is the product of several, simultaneously acting physical mechanisms. For selected objects one particular process might play a dominant role. These galaxies may then be considered as test cases for that specific theory. For the present project, the primarily important criterion is a strong spiral pattern. Its origin or driving process is a different issue.

CHAPTER III
The Observed Stellar Mass Distribution and Gas Velocity Fields

Based on: "K-band Photometry and Hα Kinematics for Spiral Galaxies"
Kranz & Rix, to be submitted to A&A (2002)

Many aspects of galactic research are closely related to the study of the galaxies' stellar mass distributions and kinematics. The appearance of galaxies is rather dependent on the observed wavelength, and for different scientific purposes different spectral ranges are preferred to yield the desired information. To estimate the stellar mass content in galaxies, near infrared (NIR) wavebands are best suited since in the NIR dust absorption and population effects have the least effect on the surface brightness (e.g., Rix & Rieke 1993, Frogel et al. 1996). With the development of new infrared detector arrays that became operational mainly in the 90's, objects can now be observed in the NIR with a resolution that compares to the one of CCD's in visible wavelengths.

3.1. The galaxy sample

The need for obtaining a new data sample came from the specific requirements for this project. Since for the sample photometric as well as kinematic data are needed, there were some constraints which applied to the selection of candidates. First of all, the galaxies should be closeby and large enough to allow a fairly detailed sampling of their mass distribution. This requirement was met by considering only galaxies with an apparent diameter of $> 2'$. To reasonably resolve a their morphologies and to avoid extensive self absorption by gas and dust in the disk, for obtaining the photometry data galaxies with low inclinations with respect to the line-of-sight (LOS) would be preferred. However, the LOS component of the circular motion increases with inclination i, thus galaxies with low inclinations would be preferred. Due to the fact that the projection of the galaxy scales with $\cos(i)$ and the LOS fraction of the velocity scales with $\sin(i)$, galaxies in the inclination range between $\approx 30°$ and $\approx 60°$ yield the most favorable conditions and were included in the sample.

In light of modelling the global gas dynamics in the galaxies, strong bars should be avoided because of their distinctly different dynamics from the rest of the disk. Still, strong spiral

Table 3.1 Sample of galaxies observed in this project. For all galaxies NIR photometry is available. Kinematic data is available for a subsample of 8 galaxies.

Galaxy	α (2000) [hh mm ss.ss]	δ (2000) [dd mm ss.s]	Morph. type	B_{tot} [mag]	velocity $km\,s^{-1}$	kin. data
NGC 2336	07 27 03.76	+80 10 39.6	SBc	13.46	+2200	
NGC 2339	07 08 20.66	+18 46 47.8	SBc	12.3	+2252	✓
NGC 2964	09 42 54.22	+31 50 48.5	Sb/Sc	12.0	+1328	✓
NGC 2985	09 50 22.20	+72 16 44.4	Sb	11.1	+1299	
NGC 3583	11 14 11.11	+48 19 04.6	SBb	11.6	+2098	
NGC 3810	11 40 58.88	+11 28 17.3	Sc	11.4	+958	✓
NGC 3893	11 48 38.43	+48 42 34.7	Sc	11.23	+972	✓
NGC 3953	11 53 49.08	+52 19 36.5	SBb	10.8	+1055	
NGC 4254	12 18 49.52	+14 25 00.4	Sc	10.2	+2453	✓
NGC 4321	12 22 54.95	+15 49 19.5	Sc	10.6	+1586	
NGC 4535	12 34 20.39	+08 11 51.3	SBc	11.1	+1962	
NGC 4653	12 43 50.89	–00 33 41.6	Sc	13.7	+2628	
NGC 5248	13 37 32.16	+08 53 05.9	Sbc	11.4	+1189	
NGC 5364	13 56 12.06	+05 00 52.8	Sc	13.2	+1267	✓
NGC 5371	13 55 39.97	+40 27 42.8	SBb	11.5	+2575	
NGC 5676	14 32 47.18	+49 27 28.6	Sc	11.7	+2114	✓
NGC 5985	15 39 36.77	+59 19 51.8	Sb	12.0	+2467	
NGC 6118	16 21 48.60	–02 17 02.8	Sc	13.2	+1574	
NGC 6643	18 19 46.58	+74 34 07.9	Sc	11.8	+1489	✓

Note: The data for the compilation of this Table are taken from the SIMBAD database, operated at CDS, Strasbourg, France

features are needed as the basis for the analysis. Thus, the sample was chosen to consist mainly of closeby, non-barred high luminosity galaxies with spiral arms that also appear strong in the NIR regime. Since all data were acquired at the Calar Alto observatory the last requirement is the visibility from southern Spain.

3.2. The data

First of all the NIR photometry was taken to determine, whether a galaxy was suited for this project, i.e. if its morphology shows strong and well defined spiral arms also in the NIR. The requirement for the kinematic measurements was to trace the gas velocity perturbations caused by the spiral arms, ideally across the whole disk. The two classical methods for obtaining 2D gas velocity fields are H I or CO radio observations and Fabry-Perot interferometry. Alternatively, longslit spectra taken at different position angles can be used to map the disk.

Single dish H I or CO observations are not suited for this project because they suffer from relatively bad angular resolution and poor sensitivity to faint emission between spiral arms

and the outer part of the disk. Sakamoto et al. (1999) recently published CO observations of a sample of spiral galaxies. In the velocity maps the signature of the spiral arms is in the majority of cases not or only barely visible. This most likely results from blurring the already weak velocity perturbations bybeam smearing. 2D Fabry-Perot velocity fields provide the required angular resolution but usually give only a very patchy representation of the disk: Mainly the H II regions show up in the map (e.g., Weiner et al. 2001b). Because the coverage that can be achieved by taking eight longslit spectra across a galaxy's disk is reasonably high it was decided to collect the kinematic information by using a longslit spectrograph. Furthermore, this method yields good angular resolution and high sensitivity to faint Hα-emission.

All observations were done with the 3.5 m telescope of the Calar Alto observatory in southern Spain. The Omega Prime camera with the K'-filter was used to acquire the NIR photometry and the TWIN longslit spectrograph was used to obtain the gas kinematics from the Hα emission line.

3.2.1. NIR photometry observations

The Omega Prime infrared camera (Bizenberger et al. 1998) is located at the prime focus of the 3.5 m telescope. The detector is a 1024 $\times$ 1024 pixel HgCdTe (1–2.5 µm) array made by Rockwell. The image scale is $0\farcs3961$ per pixel, resulting in a field-of-view of $6\farcm76 \times 6\farcm76$. With this relatively large field-of-view, almost all galaxies fitted well on the detector, superseding the need for mosaicking.

The NIR photometric observations were carried out in 5 nights during two observing runs: 25. – 26. May 1999 and 16. – 18. March 2000. The weather conditions during the first run were only moderate, thus only a small part of the collected data was actually used later on. The March 2000 run had good conditions, although the seeing was not optimal ($\sim 1\farcs4$ in K'). The final sample consisted of 19 galaxies with good photometry that could be used to chose the candidates for the kinematic measurements. The sample is displayed in Figure 3.1.

At the first run the "Double Correlated Read" (dcr) readout mode was used for the array. The array is read immediately after the initial reset and again just before the final reset at the end of the integration. While one readout takes about 0.8 s for Omega-Prime, it has an enormous fraction of the telescope time, if one considers that a single integration time takes 2 to 3 s, and two readouts are needed per frame. For the second run a new readout mode was available, the "Full MPIA Mode" (rrr-fmpia). The new Full MPIA mode is "line oriented". It reads out single lines while the whole array is integrating, leaving virtually no overhead time for the readout. This reduces the telescope time needed to effectively integrate 20 minutes on target by about 15 minutes to lie in the order of $\sim$ 80 minutes, including sky background observations and telescope slewing. The use of the "Full MPIA Mode" is highly encouraged!

Since the objects fill the complete array, a separate closeby background position was observed alternately with the galaxy to allow for sky background correction. The observing sequence was chosen to look like: G G – B B – G G – B B – ... (G = galaxy, B = background position), taking two exposures of 30 s at each position. Any of these exposures is a stack of either 15 2-second exposures or 10 3-second exposures, depending on the atmospheric

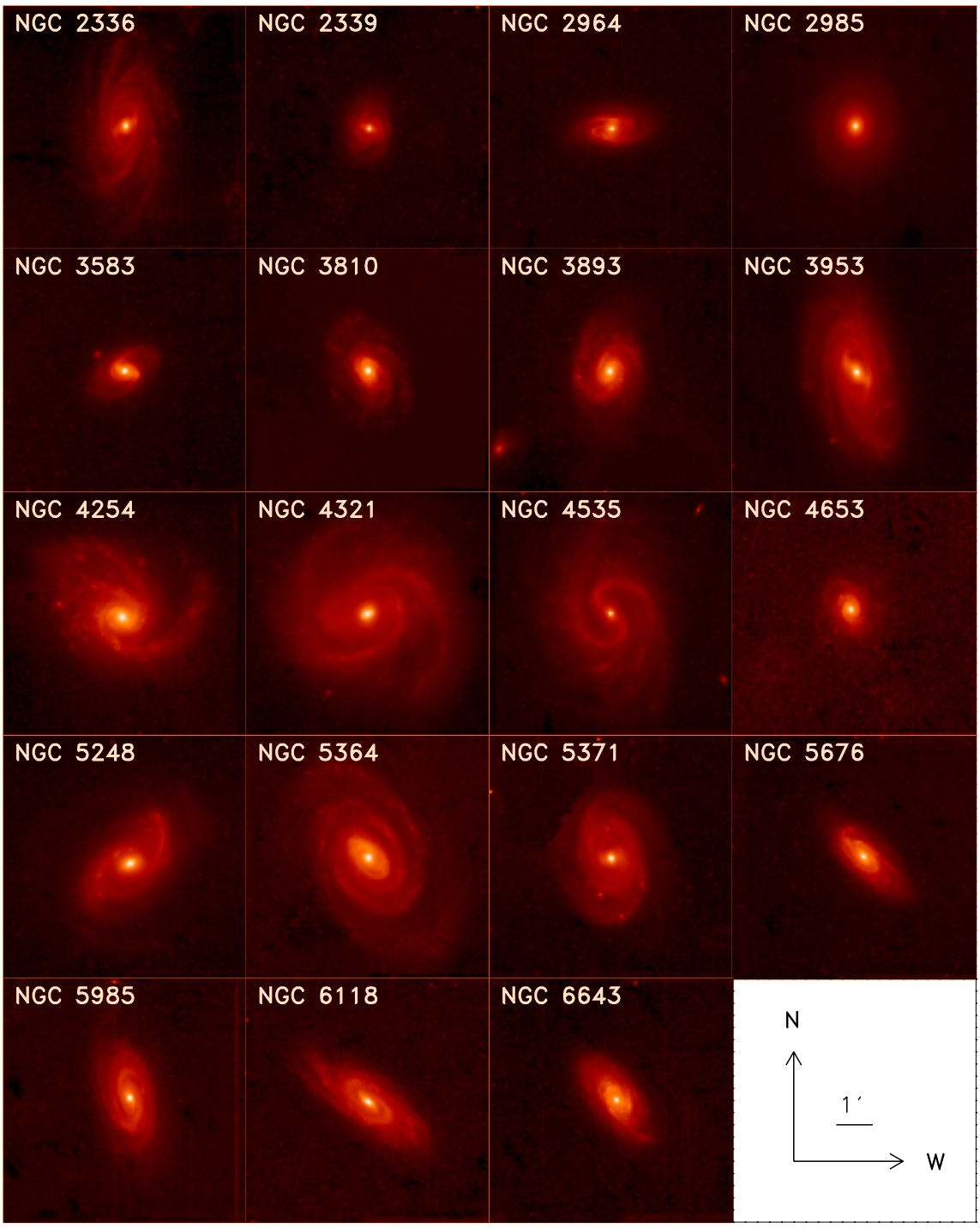

Figure 3.1 K'-band (2.2 µm) images of all observed galaxies. For the images the entire field of view of the Omega Prime camera (6.′76 × 6.′76) is displayed. Bright foreground stars are masked out in all frames.

Table 3.2 Observing log for the NIR photometry.

Galaxy	exposure [s]	seeing [″ FWHM]	date [mm/yy]
NGC 2336	1260	1.14 ± 0.02	Mar 2000
NGC 2339	1200	1.05 ± 0.02	Mar 2000
NGC 2964	1260	1.18 ± 0.04	Mar 2000
NGC 2985	1260	1.13 ± 0.02	Mar 2000
NGC 3583	1260	1.24 ± 0.04	Mar 2000
NGC 3810	1200	1.11 ± 0.02	Mar 2000
NGC 3893	1320	1.16 ± 0.03	Mar 2000
NGC 3953	1800	1.15 ± 0.03	Mar 2000
NGC 4254	1350	1.74 ± 0.05	May '99, Mar '00
NGC 4321	1260	1.96 ± 0.04	Mar 2000
NGC 4535	1440	1.24 ± 0.03	Mar 2000
NGC 4653	1500	1.42 ± 0.04	Mar 2000
NGC 5248	1260	1.28 ± 0.04	Mar 2000
NGC 5364	2130	1.63 ± 0.05	Mar 2000
NGC 5371	1500	1.71 ± 0.03	Mar 2000
NGC 5676	2340	1.47 ± 0.03	May '99, Mar '00
NGC 5985	1260	1.56 ± 0.03	Mar 2000
NGC 6118	1440	1.39 ± 0.04	Mar 2000
NGC 6643	1860	1.44 ± 0.01	May '99, Mar '00

conditions. To perform two exposures of 30 s each instead of one with one minute exposure time was motivated to allow flexibility during short time weather changes. To account for stars at the background position, some dithering was introduced to enable a later removal of the stars. For calibration purposes, several standard stars from the Persson et al. (1998) sample were observed during the night. The final sample of the 19 galaxies with good K'-band photometry is given in Table 3.2.

3.2.2. Hα spectroscopy observations

The gas kinematics were measured from the Hα emission line. The data were taken during three observing runs with a total of about 10 nights at the 3.5 m telescope: 7. – 10. June 1999 (4 nights), 5. – 8. May 2000 (4 × 0.8 nights) and 2. – 7. December 2000 (6 × 0.5 nights). One more observing run was granted in February/March 2001, but no data could be attained due to bad weather. Finally, kinematic data for eight galaxies was collected, while for three of them the data set could not be completed.

The TWIN is a two channel longslit spectrograph, located at the cassegrain focus of the 3.5 m telescope. The data for this project were taken in the red channel, centered at the wavelength around the Hα line. The slit of the TWIN was set to measure $4' \times 1\farcs5$ on the sky. With the setup used, the TWIN achieved a spectral resolution of 0.54 Å per detector pixel, which translates to 24.8 km s^{-1} LOS-velocity resolution per pixel. The

Table 3.3 Observing log for the Hα spectroscopy.

Galaxy	NGC 2339						taken Dec 2000	
Slit position	13.°1	33.°4	57.°5	85.°0	112.°6	136.°6	157.°0	175.°0
Integration time	1200s	1200s	1200s	1200s	1200s	1200s	1200s	1200s
Galaxy	NGC 2964						taken Dec 2000	
Slit position	5.°0	43.°0	67.°0	82.°3	95.°0	107.°4	123.°0	147.°0
Integration time	1200s	1200s	1200s	1200s	1200s	1200s	1200s	1200s
Galaxy	NGC 3810						taken May 2000	
Slit position	15.°0	30.°5	49.°0	73.°2	105.°0	136.°8	161.°2	179.°5
Integration time	1200s	1200s	1200s	1200s	1500s	1200s	1200s	$\approx$ 400s
Galaxy	NGC 3893						taken Dec 2000	
Slit position	4.°4	25.°5	49.°0	75.°0	101.°0	125.°0	145.°8	165.°0
Integration time	1200s	1200s	1200s	1200s	1200s	1200s	1200s	1200s
Galaxy	NGC 4254						taken Jun 1999	
Slit position	0.°0	22.°5	45.°0	67.°5	90.°0	112.°5	135.°0	157.°5
Integration time	1800s	1800s	930s	900s	900s	1200s	1200s	900s
Galaxy	NGC 5364						taken May 2000	
Slit position	14.°2	30.°0	45.°8	64.°3	88.°8			
Integration time	1200s	1200s	900s	1800s	2300s			
Galaxy	NGC 5676						taken Jun 1999	
Slit position	0.°0	22.°5	45.°0	67.°5	90.°0	112.°5	135.°0	157.°5
Integration time	–	2400s	900s	1200s	1200s	1200s	1200s	1000s
Galaxy	NGC 6643						taken Jun 1999	
Slit position	0.°0	22.°5	45.°0	67.°5	90.°0	112.°5	135.°0	157.°5
Integration time	–	1000s	1200s	1200s	1200s	1000s	1000s	1000s

spatial resolution of the CCD was reduced by a factor of two to increase the spectrograph's sensitivity to faint emission. It sampled the rotation curves of the galaxies with a resolution of 1.″12, which is in accordance with the average seeing conditions. For each galaxy eight slit positions were planned to be taken across the disk to sample the 2D velocity field reasonably well. The angular separation of the different slit positions was chosen to 22.°5 for the June 1999 observations. For later runs the sampling was chosen to provide an equidistant spacing in the deprojected reference frame of the galaxy. For that purpose an assumption for the major axis position angle and the inclination of the galaxy was made. The orientation of the slit positions and their individual exposure times are listed in Table 3.3 and is displayed in Figure 3.2 together with the reduced rotation curves along all taken slit positions. After each exposure a comparison exposure of a He-Ar arclamp was taken to constantly monitor the wavelength solution of the spectrograph.

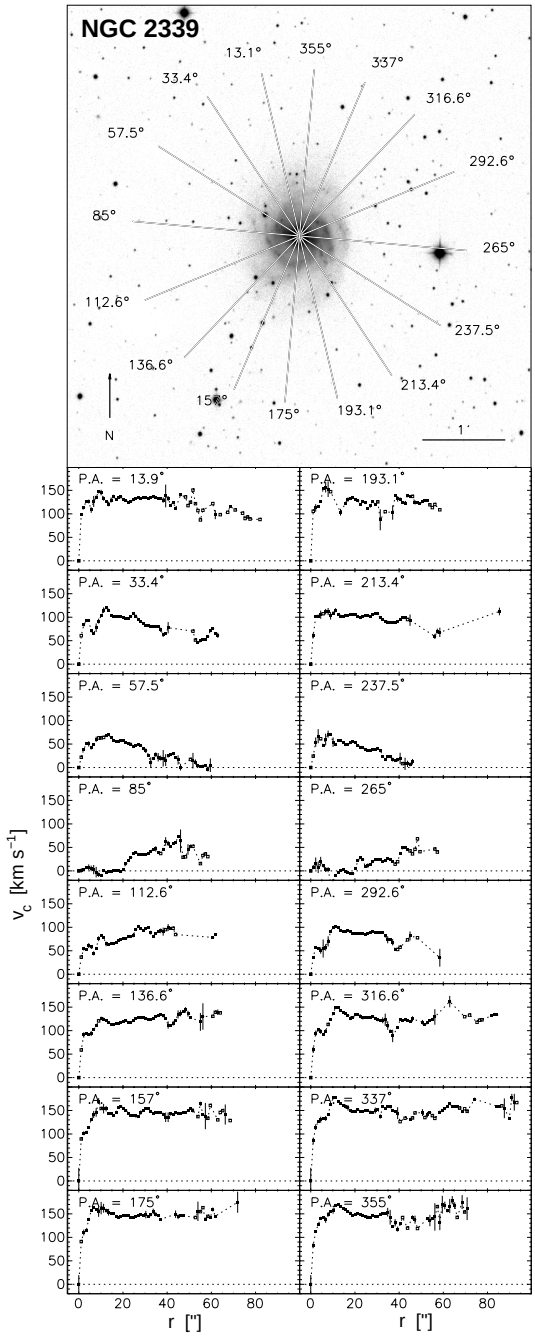

Figure 3.2 NGC 2339

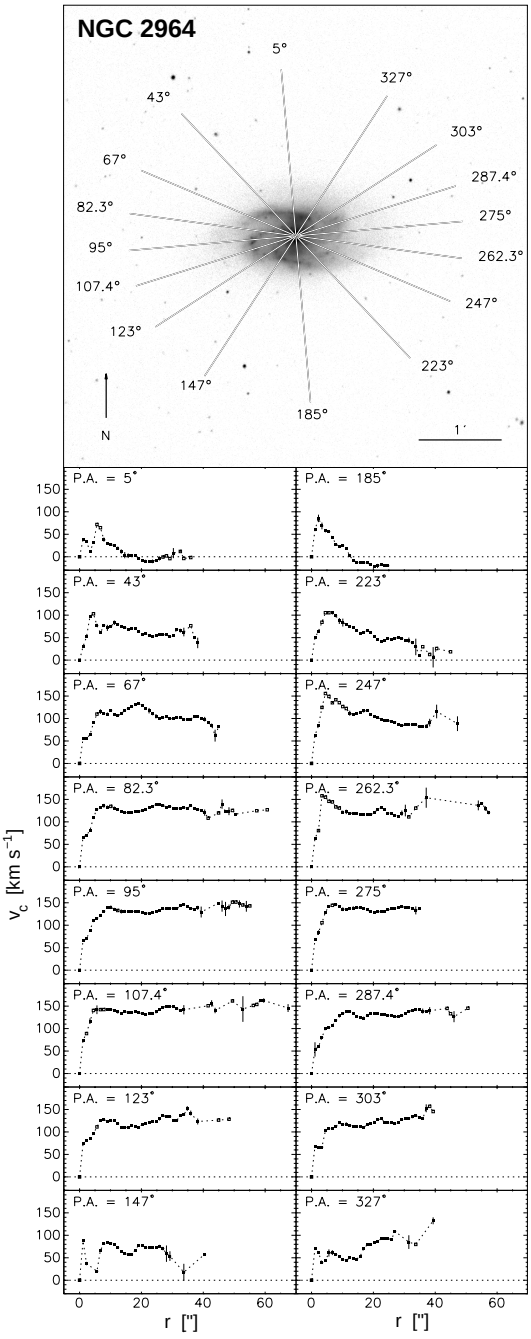

Figure 3.2 continued. NGC 2964

Data for the subsample of galaxies with kinematic observations. The upper frame shows the K'-band image. The overlay shows the orientations of the spectrograph. In order to measure the 2D velocity field, ideally 8 longslit spectra were taken across the galaxies' disks (angles labelled in bold font) all crossing the nucleus. The measured rotation curves along the 16 slit positions are shown in the lower part of the Figure. Non-filled data points indicate errors larger than 30 km s^{-1}.

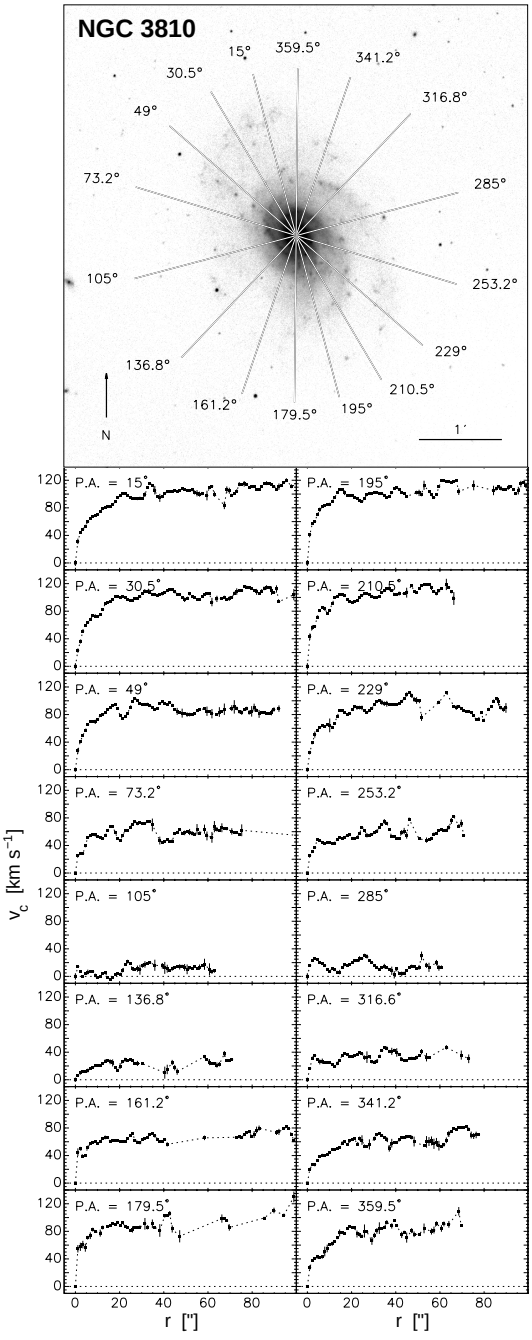

Figure 3.2 continued. NGC 3810

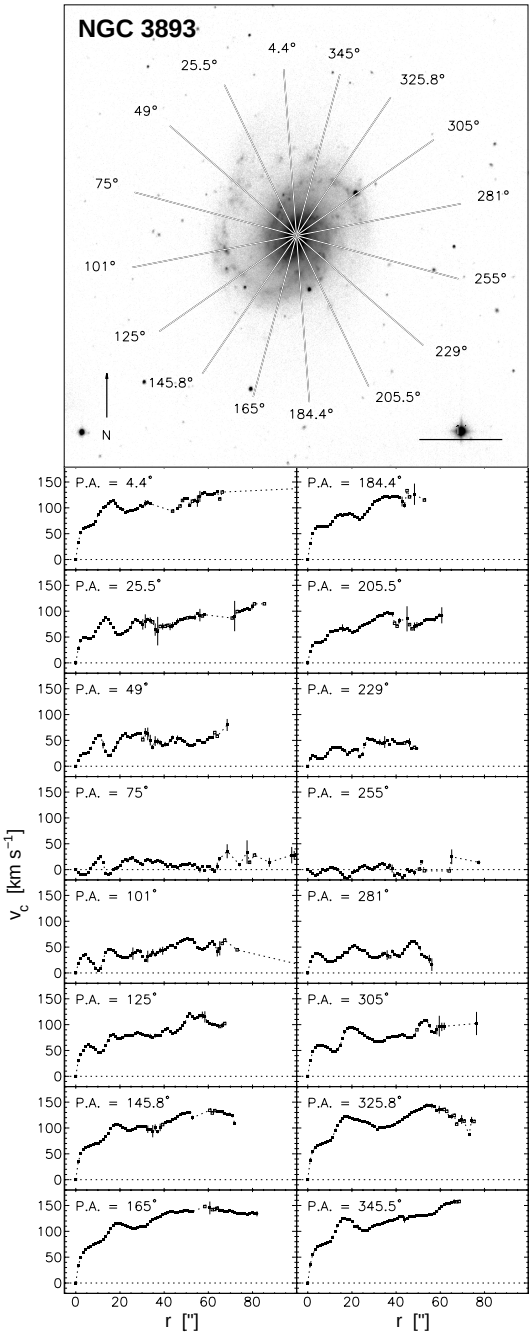

Figure 3.2 continued. NGC 3893

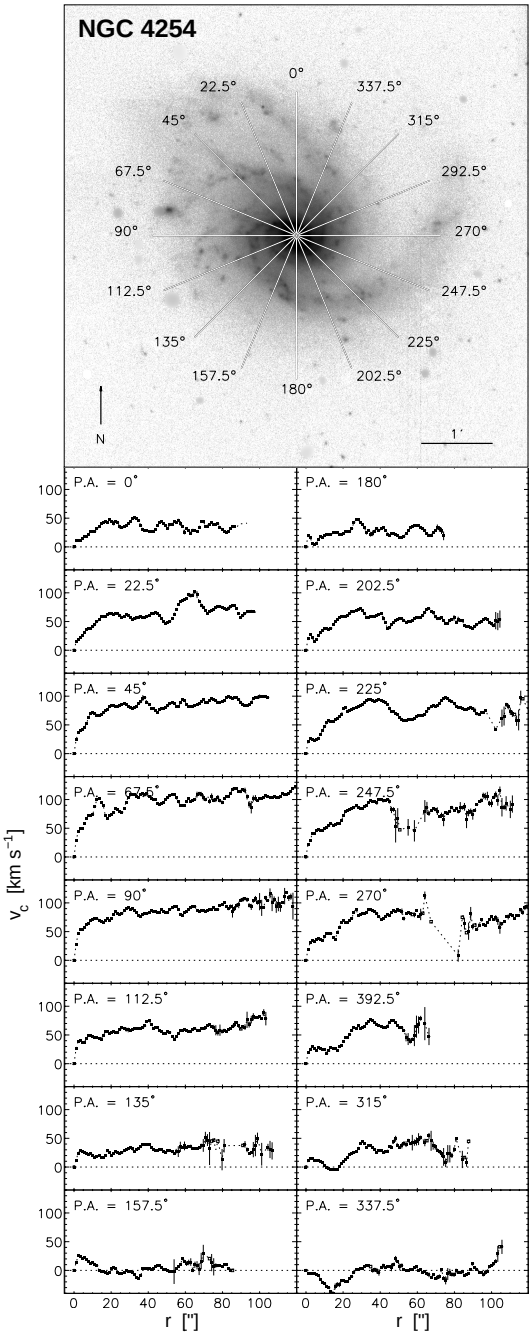

Figure 3.2 continued. NGC 4254

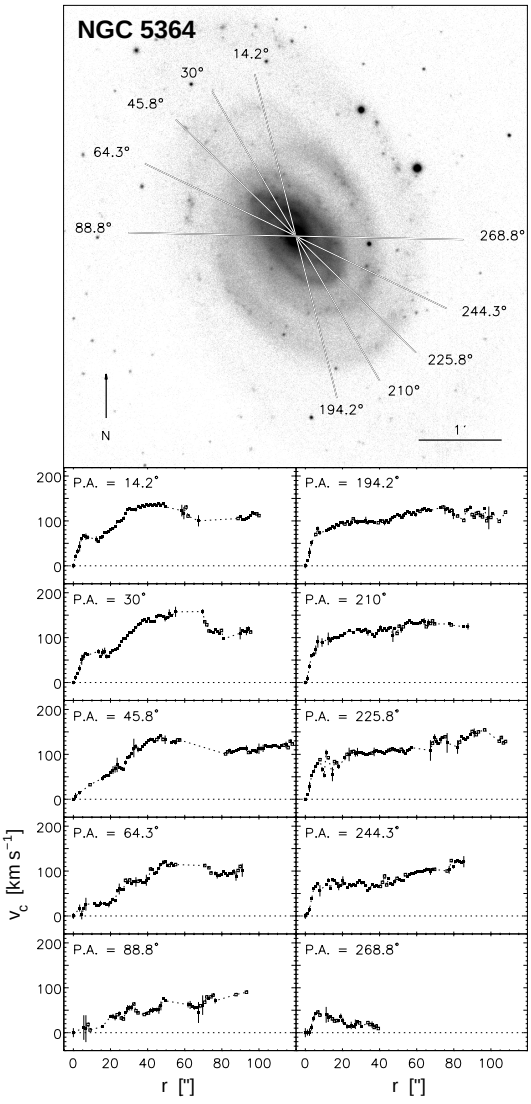

Figure 3.2 continued. NGC 5364, only 5 spectra could be taken.

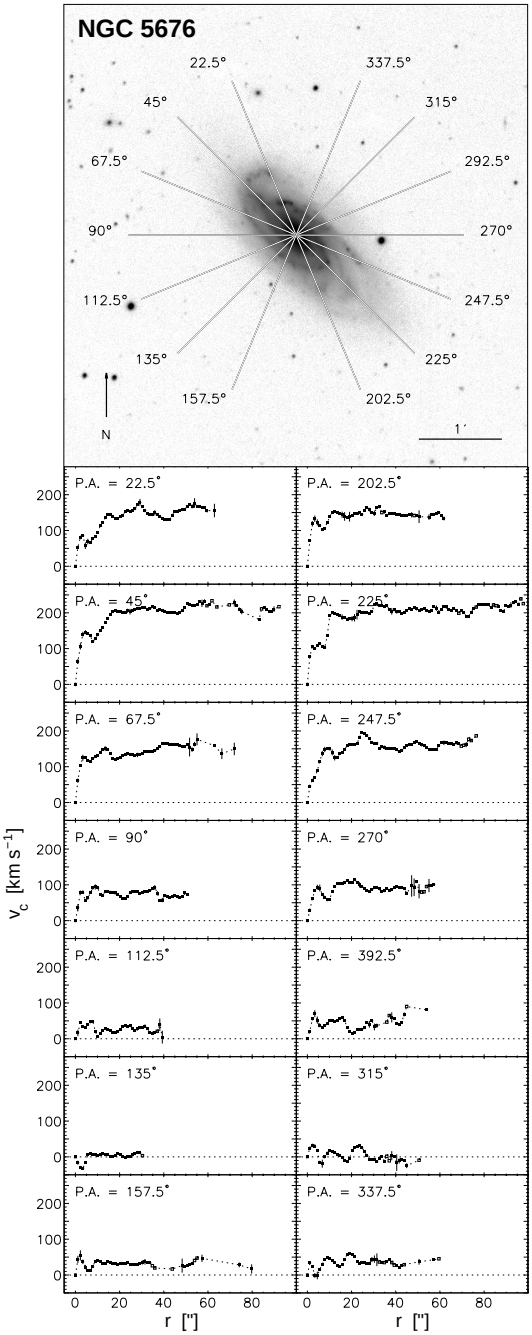

Figure 3.2 continued. NGC 5676, only 7 spectra could be taken.

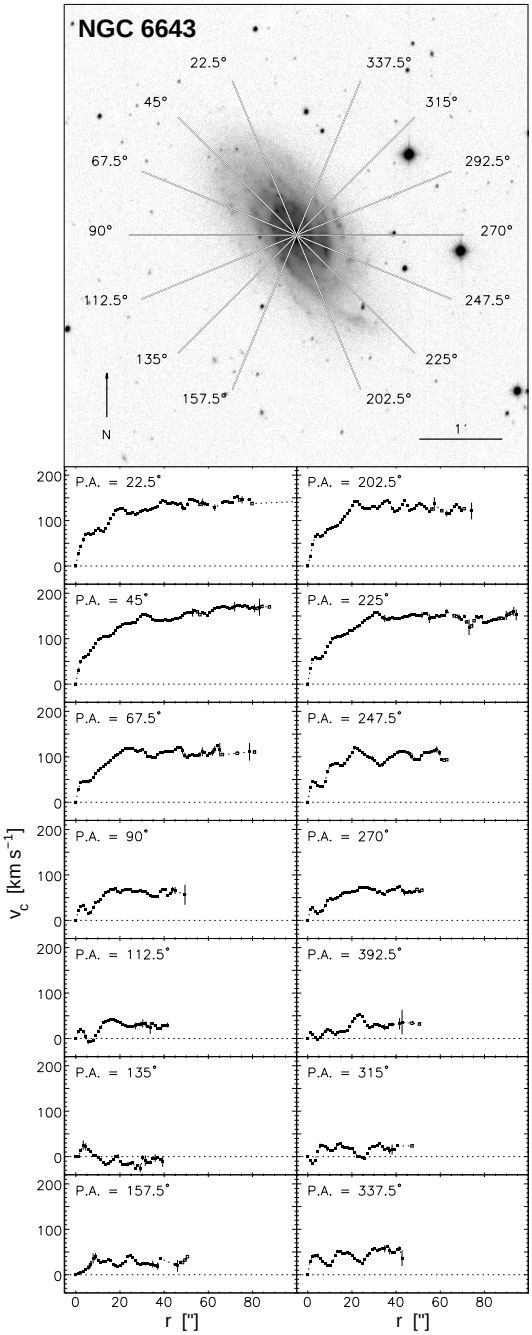

Figure 3.2 continued. NGC 6643, only 7 spectra could be taken.

3.3. Data reduction

3.3.1. NIR photometry

For NIR detector arrays most of the calibration procedures, such as correcting for pixel to pixel gain variations or dark current subtraction, are very similar to those of optical CCD's. However, one basic difference is the sky brightness, which is outshining almost any astronomical object. During the Omega Prime runs, the sky brightness was in the range of 3500 counts per second per detector pixel, which translates to $\approx$ 12 mag $\square''^{-1}$. These conditions allowed only exposure times of 2 or 3 s, in order to not let the galaxy's nucleus reach the range where the chip shows deviations from linearity, which happens at $\approx$ 25 000 counts. Furthermore, the sky brightness is highly variable and needs constant monitoring. In the end, the observing runs yielded as many sky background frames as science frames.

The actual measured detector voltage, or counts, contains several additional contributions besides the source flux. The main components that contribute to the measured voltage $V(x,y)_\mathrm{m}$ at each pixel for a measurement on target are:

$$V(x,y)_\mathrm{m} = [G(x,y) \cdot (F(x,y)_\mathrm{g} + F_\mathrm{s}) + I_\mathrm{d}]\, t \tag{3.1}$$

where $G(x,y)$ is each pixel's photometric gain (e^-/photon), $F(x,y)_\mathrm{g}$ is the extended source flux that should be isolated and F_s is the sky flux (photons/s), I_d is the dark current (e^-/s) and t is the integration time. In principle F_s and I_d also exhibit pixel to pixel variations, but at first order both are approximately constant across the chip. The main components that contribute to the measured voltage $V(x,y)_\mathrm{s}$ at each pixel for a sky background measurement are as above:

$$V(x,y)_\mathrm{s} = [G(x,y) \cdot (F_\mathrm{s}) + I_\mathrm{d}]\, t \tag{3.2}$$

The difference of the frame on target and the sky background frame eliminates all undesired effects except the pixel to pixel gain variation:

$$V(x,y)_\mathrm{m} - V(x,y)_\mathrm{s} = G(x,y) F_\mathrm{g} t \tag{3.3}$$

The sky frames can also be used to correct for the chip's gain variations, since they exhibit only negligible flux variations across the field of view. Their use as "flatfield frames" is further motivated by their relatively high flux and the fact that numerous sky frames were taken. The sky frames are, however, not entirely free of sources. There are still stars in the field of view. The final flatfield frame used for data reduction was derived by calculating a median of a large set of scaled sky frames, to eliminate features from the background fields. Furthermore the dark current has to be subtracted from the sky flatfield frame. If $N = F_\mathrm{s} t$ is assumed to be a constant that normalizes the flatfield frame, from equation (3.2) it is found:

$$G(x,y) = (V(x,y)_\mathrm{s} - I_\mathrm{d} t)/N. \tag{3.4}$$

This procedure yields the source object's flux per unit time. To relate this quantity to astrophysical magnitudes, measurements of objects with known flux have to be evaluated.

For calibration purposes, several standard stars were observed repeatedly during the observations. The standard star measurements revealed only a very small variation of the zero point throughout the nights: in the three nights when most of the data were taken, the zero point variation was less than 0.095 mag, and even smaller in one single night (< 0.05 mag). Figure 3.3 displays the standard star measurements for the night of March 17^{th}, 2000.

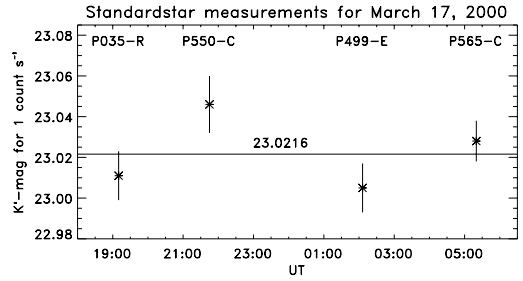

Figure 3.3 Standardstar measurements in the night of March 17^{th}, 2000. The four different stars (P035-R, P550-C, P499-E, P565-C) from the Persson et al. (1998) NIR standard star sample were observed during the night. The error bars refer to 1σ errors.

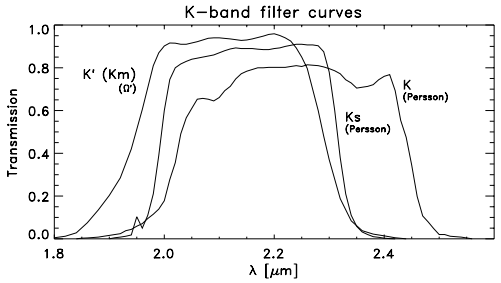

Figure 3.4 Transmission curves of the K-band filters used for the observations (K' with Omega Prime) and the Persson et al. (1998) filters, for which the standard star fluxes are given.

A systematic error was introduced by the fact that the fluxes for the standard stars were only given for the K and Ks filters (Persson et al. 1998), whereas for the measurements the K' filter was used, whose filter curve differs slightly from both other filters (see Figure 3.4. However, the filter curves of the K' and Ks filter are very similar: about 93 % of the integrated area of the Ks filtercurve is inside that of the K' filter curve. Since the flux through the different K and Ks filters for the used subset of the Persson sample is compatible with being equal within their measured error bars and varies by maximally 0.02 mag, the expected difference between the Ks and K' filter would be even less. Thus, the Persson Ks-fluxes were used to calibrate the standard stars for the Omega Prime observations.

The data reduction was done using the ESO-`MIDAS` software package and self developed IDL routines. `MIDAS` was used for sky subtraction, flatfielding and for coaligning the dithered frames. For the sky subtraction sky frames were used that were interpolations of the sky frames taken before and after the object frame. The normalized flatfield frame was divided into the object frames. From all object frames a median image was computed to correct for strongly deviating pixels in the frames. Deviating pixels within single frames were then replaced by median values. The final image was derived from a mean of all preprocessed frames. The fine tuning of finding the zero-point of the sky background was done by looking at the radial light profiles of the disks. The sky background level was adjusted to not cause strong bends in the light profile while fading into the sky. Possible physical disk truncation effects were considered and an attempt was made to avoid them from being removed by adjusting the sky level. Finally, the images were cleaned from bright foreground stars. The magnitudes listed in Table 3.4 are given for the flux inside the 22 K'-mag $\square''^{-1}$ isophote.

3.3.2. Hα kinematics

To extract the individual rotation curves from the raw data, the `IRAF` data reduction package, and again IDL routines were used. The `IRAF` package was used following the instructions given in Massey (1997) and Massey et al. (1992). The longslit spectra were reduced to a level that was required for extracting the rotation curves. Less priority was attributed to illumination corrections or flux calibration. The latter was not at all performed. To subtract the dark current from the frames and to flatfield the images with domeflat exposures the `IRAF`-tasks ***zerocombine*** and ***flatcombine*** were used in combination with the ***ccdproc*** task. The correction for distortions along the spatial axis of the longslit was a very important step to assure correct velocity measurements at all radii in the rotation curves. This correction procedure also included the wavelength solution for the spectra. The following tasks from the ***noao/twodspec/longslit*** package were used:

identify was used to identify the lines of the He-Ar lamp comparison spectrum along one dispersion line.

reidentify was then applied to re-identify these features at other (≈ 20) dispersion lines along the spatial axis.

fitcoords then performs a fit of a two-dimensional function to the identified grid points all over the frame.

transform finally applies the geometrical correction to the original frame, correcting for the distortions along the spatial axis and giving the log of the wavelength as a linear function along the dispersion axis.

Residual distortions can be mapped from night sky lines and get accounted for when determining the line centers.

The further data reduction was done using self developed IDL routines. In a first step the cosmic rays were removed from the relevant parts of the spectra by replacing the spikes with adjacent pixel values. This process was kept interactive to assure the quality of the correction. After removal of (all but one) night sky lines and the galaxy's continuum emission, the rotation curves could be measured. The line-of-sight (LOS) velocity component of the ionized gas was determined as a function of radius from the galactic center from Doppler shifts of the Hα-line and the brighter N II-line at 6584 Å (the right emission line in Figure 3.5). The central values for the LOS velocity of the emission lines were determined by fitting a single Gaussian profile to the observed line profile. The single Gaussian appeared to be a good enough description of the real line profiles to determine the line centers to sub-pixel resolution. The final rotation curve was calculated from the 3:1 weighted coaddition of the two fits (see Figure 3.5). The weights were derived from the relative line strengths. The comparison of the two fits yielded the uncertainty of the line center position, which was taken as $\sigma = \sqrt{0.75(\mathrm{H}\alpha - \mathrm{mean})^2 + 0.25(\mathrm{NII} - \mathrm{mean})^2}$. Residual slit distortions along the spatial axis were corrected by fitting a low order polynomial to spatial distribution the night sky line center and subtracting the deviations of the polynomial from its mean from the rotation curve.

The final step was to find the zero-point of the spectra, defining the dynamic center of the disk. As it was apparent from the spectra, the dynamic center didn't always coincide with

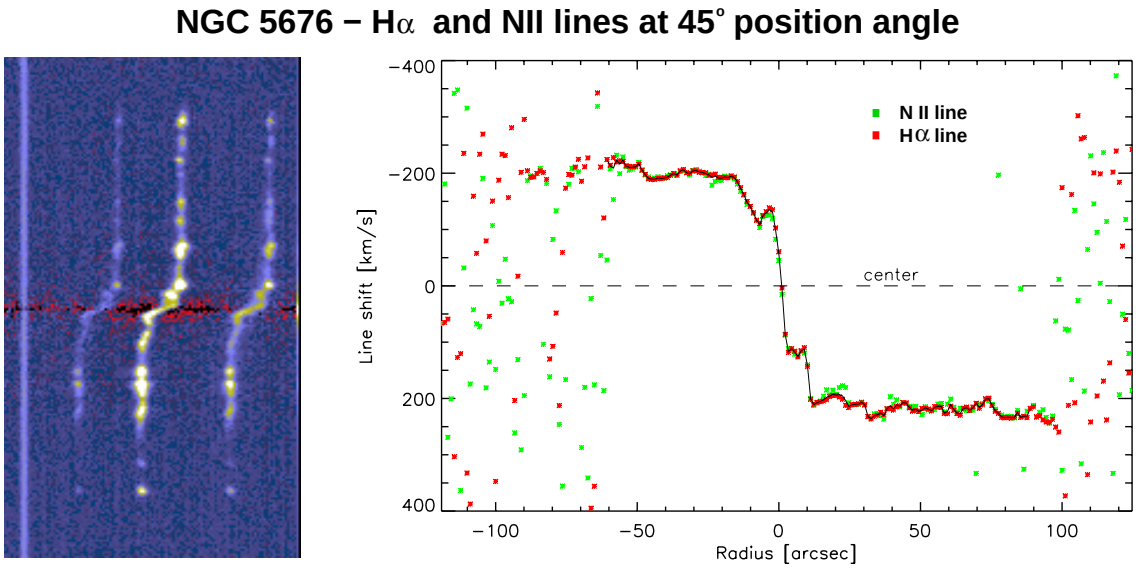

Figure 3.5 Data example for NGC 5676. Shown is the spectrum from slit position 45°, which is very close to the major axis position angle. At left the fully reduced TWIN spectrum is shown for the wavelength region of the Hα-line and the two N II-lines for a width of 68 Å. One night sky line (left in the image) had not been removed to check for residual distortions along the spatial axis. At right, the derived line shifts are plotted. The green data points refer to the line shifts determined from the N II-line (the right one in the image at left), while the red data points refer to the Hα-line. The line shift has been translated into line-of-sight velocities. The continuous black line is the weighted average rotation curve

the light center of the continuum emission. In these cases the zero-point was determined such that the asymptotic rotation curves reached about the same velocity on both sides of the galaxy. Systematic errors arising from all these procedures were accounted for by adding an overall systematic error to all rotation curves when comparing with the results from the simulations.

The line shifts were translated into LOS rotation velocities making use of

$$\mathrm{d}v = c\frac{\mathrm{d}\lambda}{\lambda} = c\,\mathrm{d}\ln\lambda = c\,2.3026\,\mathrm{d}\log\lambda \tag{3.5}$$

where $\mathrm{d}\log\lambda$ is the line shift in the wavelength calibrated spectrum. The per pixel resolution is 3.596×10^{-5} for the TWIN spectrograph, corresponding to $24.8\,\mathrm{km\,s^{-1}}$.

3.4. Derived quantities

For this discussion, the focus will be on the NIR properties of the galactic disks. A first step to analyze the light distribution is to find the inclination and position angles of the galaxies and to perform the deprojection of the disks. In cases where there is only NIR photometry available, the inclinations and position angles were estimated by approximating an ellipse to the faintest isophotes of the galaxy. The precision with which the values can be determined from this method depends on the inclination of the particular galaxy.

Best results were obtained for $i \approx 60°$. An average uncertainty of $\sim 3°$ must be attributed to all values. The inclinations and position angles of these galaxies, for which observed gas kinematics is available, could be determined quite reliably from the spectra. They were derived from a global χ^2-fit of an axisymmetric rotation curve model to the 16 observed rotation curves. The model was based on a combination of stellar and dark halo rotation curves which were scaled to an average rotation curve from the six slit positions closest to the major axis (as shown in Figure 3.7). The uncertainty range for the kinematic fitting method is less than 1°. However, for NGC 4254 it has been found during the modelling procedure that it might matter whether an axisymmetric rotation curve model is used for the fit or a 2D velocity field from a hydrodynamical gas simulation. In most cases those different methods lead to very similar results. Only for NGC 4321 literature values had to be adopted since this galaxy's size on the sky is larger than the field-of-view of the Omega Prime camera. A reliable estimate from the data was not possible. The derived parameters for the sample galaxies are compiled in Table 3.4.

Table 3.4 Derived parameters from the NIR photometry.

Galaxy	P.A. [°]	incl [°]	Method (see Note)	$K'_{\rm tot}$ < 22 mag $\Box''^{-1}$ [mag]	central surface brightness bulge [mag $\Box''^{-1}$]	disk [mag $\Box''^{-1}$]
NGC 2336	0.0	59.0	E	7.83	14.93	18.12
NGC 2339	175.0	41.4	K	8.53	12.78	16.68
NGC 2964	95.0	56.0	K	8.44	13.95	16.98
NGC 2985	175.0	41.4	E	7.51	13.24	15.89
NGC 3583	123.0	53.1	E	8.51	13.95	16.56
NGC 3810	22.0	46.0	K	8.02	14.46	16.21
NGC 3893	166.0	42.0	K	7.94	14.80	16.74
NGC 3953	10.0	60.8	E	7.37	14.58	17.70
NGC 4254	67.5	41.2	K	6.85	14.83	16.78
NGC 4321	32.0	30.0	L	6.60	14.15	17.59
NGC 4535	0.0	44.0	E	7.31	13.87	17.98
NGC 4653	26.0	32.2	E	9.86	17.02	18.19
NGC 5248	135.0	54.5	E	7.32	14.37	17.22
NGC 5364	30.0	46.6	K	7.62	16.26	18.32
NGC 5371	7.0	38.2	E	7.66	16.54	17.44
NGC 5676	46.5	63.2	K	8.03	14.97	16.79
NGC 5985	13.0	60.9	E	8.13	15.77	17.89
NGC 6118	55.0	67.8	E	8.32	16.97	18.58
NGC 6643	39.0	57.5	K	8.18	15.64	17.19

Note: The abbreviations for the method of determining the galaxy's position angles and inclinations stand for the following: E = from ellipse fitting; K = from gas kinetic measurements; L = from the literature.

Having determined the projection angles of the galaxies, the IDL routine '`GAL_FLAT`' from the astrolib was used to deproject the galaxy images to face-on (the deprojection process will be described in more detail in Section 4.1.3). These deprojected frames were then

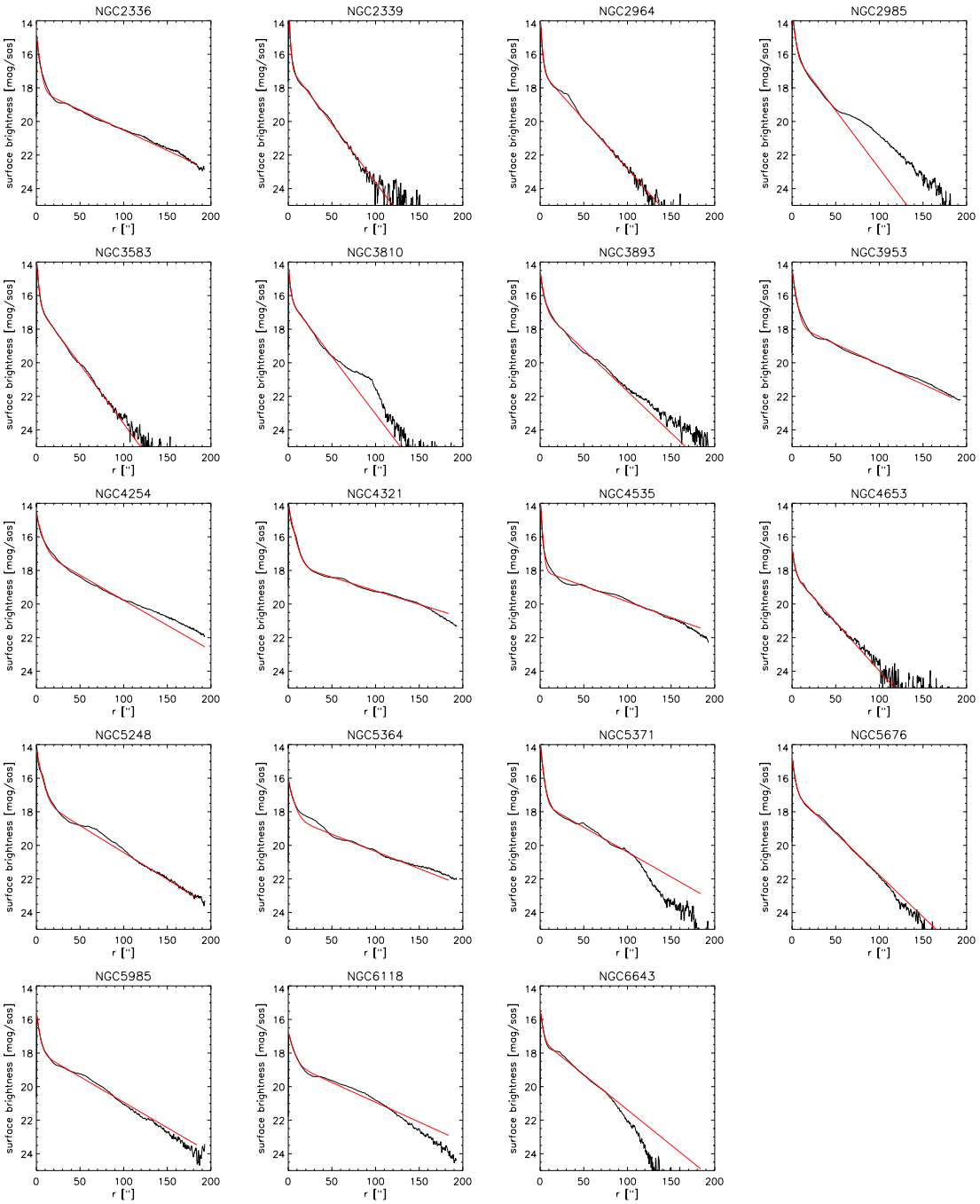

Figure 3.6 Radial light profiles in K' for all galaxies from the sample. For most galaxies the K-band light is well approximated by a double exponential profile, given by the red line.

used to find the averaged radial K-band light profile and the disk scale lengths. Since the sample consisted of late type spirals with small bulges, for most of the galaxies a double exponential bulge/disk model provides a very good fit to the radial K-band light profile as shown in Figure 3.6. The parameters that were derived from the photometry are given in

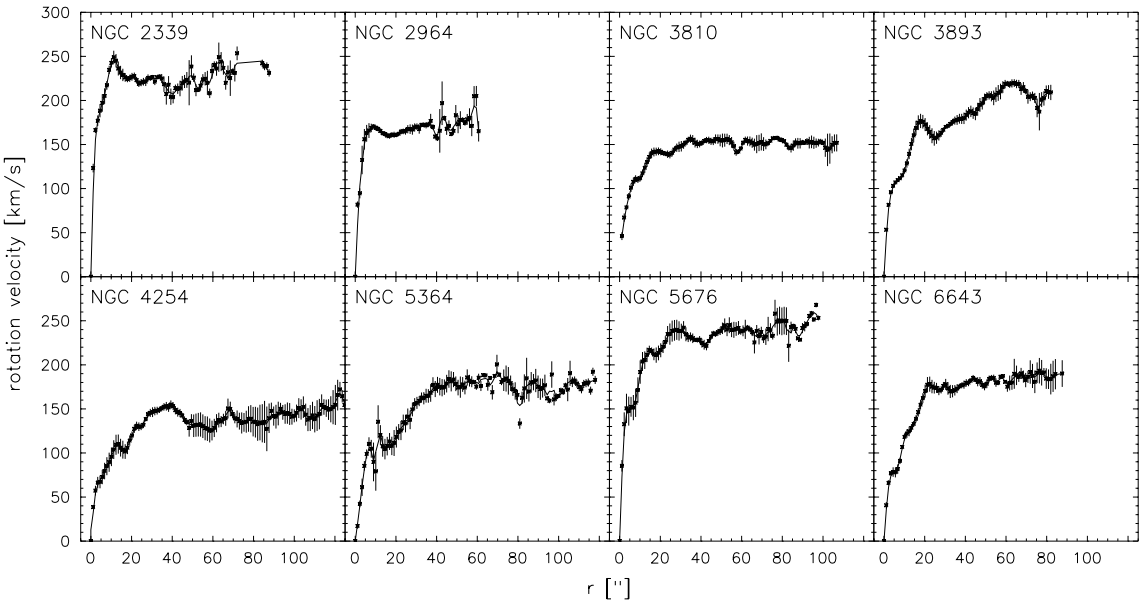

Figure 3.7 Averaged rotation curves of the sample galaxies. Each Hα rotation curve shown above is an average of rotation curves from six spectrograph slit positions that were oriented closest to the major axis position angle. The rotation curves are inclination-corrected and render intrinsic velocities.

Table 3.4. It shows that the sample comprises mainly of high surface brightness galaxies which have a central disk surface brightness of ≈ 17 mag $\Box''^{-2}$ in K'.

Figure 3.7 shows the rotation curves that were derived from the Hα-longslit spectra. The presented rotation curves are averages of spectra taken at those six slit position angles that were taken closest to the major axis position angle. The rotation curves are presented to show intrinsic velocities, i.e. projection effects were taken into account and were corrected according to the parameters given in Table 3.4.

3.4.1. Remarks to individual galaxies

For the galaxies for which both photometric and kinematic data are available, a few remarks about their morphology and environment are given. More detailed information will be provided in Chapter 5 and Chapter 6, where the modelling of individual objects is being discussed.

NGC 2339 exhibits a small, very bright nucleus in a weak complex bar. In the K-band there are faint arms, revealing an inner 3-arm morphology. It is a bright IRAS source.

NGC 2964 is a starburst galaxy that exhibits strong star formation activity across the whole disk and the nucleus. It does not exhibit a clear grand design spiral structure, although there is a prominent arm-structure in the disk. NGC 2964 is a non-interacting pair with NGC 2968 at $5'.8$ projected distance.

NGC 3810 is a Sc galaxy in the Leo group. In the central parts ($< 45''$) NGC 3810 looks like a grand design spiral but further out the arms become more flocculent. There

are no closeby galaxies interacting with NGC 3810. The radial profile of the outer disk deviates considerably from exponential and beyond $100''$ the disk appears to be truncated.

NGC 3893 is a grand design Sc galaxy in the Ursa Major Cluster of Galaxies. In the outer parts the symmetry of the spiral is disturbed by interaction with its companion NGC 3896 located $3'.9$ to the south-east. There is enhanced star formation activity in the interacting arm as compared to the arm at the opposite side.

NGC 4254 is a bright Sc galaxy, located in the Virgo galaxy cluster. It exhibits a lopsided three-arm morphology, that is seen much stronger in the optical than in the NIR. The south-western arm is more pronounced than the others. There is vigorous star forming going on along the spiral arms. Although there is no major galaxy in the immediate vicinity, it has been found that NGC 4254 interacts with the gaseous medium of the cluster (Phookun et al. 1993). It appears to have a weak bar at a position angle of $\sim 45°$.

NGC 5364 is an extremely regular galaxy whose spiral arms can be clearly traced for more than 400°. They emerge from an inner ring that is completely closed. Inside this ring there is a nuclear spiral winding in the same sense. It has been argued (Braine et al. 1993) that this galaxy might be disturbed because the spiral arms wind "too much" and there are several galaxies very nearby.

NGC 5676 is a starburst galaxy with a fairly regular grand design structure. There are many bright, knotty star forming regions and filamentary arms overimposed. It has several sudden changes in the spiral's pitch angle.

NGC 6643 is – like NGC 5676 – a starburst galaxy with a fairly regular grand design structure. It exhibits a considerable lopsided morphology with a third arm and filamentary arms at the outer regions. There is no evidence for interaction.

CHAPTER IV
The modelling

The modelling involves several discrete steps before conclusions can be drawn. First, the potential of the galaxy has to be modelled and assembled from luminous and dark matter components. This includes the derivation of the stellar gravitational potential from the K-band images and, for each pre-defined disk mass fraction, a dark matter halo profile to match the observed rotation curve. The second step involves the hydrodynamic gas simulations within the combined stellar and dark matter potential. The final third step comprises the comparison of the simulated and observed gas properties, which then lead to the conclusions.

4.1. Deriving the potential from NIR observations

4.1.1. K-band Light as Tracer of the Stellar Mass

The stellar potential of a galaxy must be derived directly from its stellar mass density. To this end, it is important to understand how well the NIR surface brightness traces the stellar mass density. Stellar population and galaxy evolution modelling suggests that the overall M/L might vary by about a factor of 2, caused by the broad range of possible underlying star formation histories (see, e.g., Gavazzi, Pierini, & Boselli 1996; Cole et al. 2000; Bell & de Jong 2001). Also within a single system M/L is not entirely constant. There are two major concerns which complicate the direct translation of K-band light to mass: both dust extinction and spatial population differences could introduce local K-band mass-to-light ratio variations.

Observing at $\sim 2\,\mu$m reduces the effect of the dust extinction significantly. Since most galaxies are seen from a nearly face-on perspective, the optical depths are expected to be low, ~ 0.5 in the K-band, leading to local flux attenuations of $< 10\%$ (Rix & Rieke 1993, Rix 1995).

Population effects most likely introduce the dominant uncertainty, although also here the NIR provides a much more homogeneous estimate than optical imaging. Significant global M/L-variations may arise mainly from red supergiants; they emit most of their light in the near infrared and are fairly numerous and thus could considerably affect the total light distribution in K-band images. Supergiants evolve very rapidly and therefore are primarily found close to the spiral arms where they were born. This would tend to increase the arm-interarm contrast, leading to stronger inferred spiral perturbations in the stellar potential.

Recent studies have revealed however, that the stellar M/L correlates tightly with galaxy colors (Giraud 1998; Bell & de Jong 2001). This correlation can be used to correct for differences in the stellar M/L arising from population effects.

4.1.2. Color correction

From spiral galaxy evolution models, and assuming a universal IMF, Bell & de Jong (2001) find that stellar mass-to-light ratios correlate tightly with galaxy colors. Their models of radially resolved stellar population colors were constructed using the stellar population synthesis models of Bruzual & Charlot (2002, in preparation), and adopting a scaled Salpeter IMF (Salpeter 1955). The original Salpeter IMF was modified by globally scaling down its stellar M/L by a factor of 0.7 (see Fukugita, Hogan, & Peebles 1998) forcing it to agree with observational maximum disk M/L constraints. This global reduction in stellar M/L is essentially the same as adopting an IMF with fewer low-mass stars, as the low-mass stars contribute only to the mass, but not to the luminosity or color, of the stellar population (Bell & de Jong 2001). Derived from these models, Bell & de Jong provide color dependent correction factors, which can be used to adjust the K-band images to constant M/L.

In light of this, it is useful to stress again that the absolute M/L of a particular galaxy strongly depends on its underlying star formation history that is very difficult to assess. However, the M/L–color correlation allows the correction for relative differences in the stellar M/L, providing a mass map with some unknown value for the global M/L.

4.1.2.1. Performing the color correction

The color correction was done using the relations provided by Bell & de Jong (2001). For $(V-K)$ and $(B-K)$ colors they are:

$$\log_{10}(\mathrm{M/L}) = (-1.078 + 0.314\,(V-K)) \tag{4.1}$$

$$\log_{10}(\mathrm{M/L}) = (-0.930 + 0.206\,(B-K)) \tag{4.2}$$

The correction is done on a pixel by pixel basis for coaligned NIR and optical images. To remove the effect of noise in the images, they were convolved to a resolution of $\approx 5''$. At each point, $\mathrm{M/L}(x,y)$ was calculated according to the above equations. In a second step the M/L-map was normalized by the M/L from the global color of the galaxy, $\langle \mathrm{M/L} \rangle$, and multiplied with the K-band image.

$$\mathrm{F}(x,y)_{\mathrm{corr}} = \mathrm{F}(x,y)_K \, \frac{\mathrm{M/L}(x,y)}{\langle \mathrm{M/L} \rangle}. \tag{4.3}$$

All dust reddening effects (self absorption and galactic reddening) were ignored because the dust extinction vector nearly coincides with the color-M/L correlation of the population effects (see Figure 1d in Bell & de Jong 2001). Moreover, the typical internal extinction caused by the presence of dust at the levels expected in most galaxies is very low and on the order of 0.05 mag in the K-band (Silva et al. 1998). Still, as it has been pointed out by Bell & de Jong (2001), for optically thick dust lanes the visible light can get totally absorbed and the correction fails, if used on a pixel by pixel basis. For the

intended purposes a global mass map of the galaxies is mainly of interest. Furthermore, the moderate resolution V- and B-band images – that were even convolved to a $\approx 5''$ resolution for the correction – do not permit the discernment of thin dust lanes from regions of low surface brightness reliably. On the other hand, none of the sample galaxies exhibits prominent dust absorption features, hence one can be confident that the errors introduced from optically thick dust lanes are minor and might be ignored in a first order correction.

The optical V- and B-band images needed for the color correction were taken from the literature and from the dataset of Ph. Héraudeau (Héraudeau & Simien 1996). Table 4.1 provides a list of the optical data that was used.

Table 4.1 Sample of optical data for the color correction of the simulation sample.

Galaxy	band	brightness [mag]	resolution [$''$ FWHM]	reference
NGC 3810	B	11.30	4.4	Frei et al. 1996
NGC 3893	B	11.20	1.5	Tully et al. 1996
NGC 4254	g^*	9.86 (V)	2.4	Frei et al. 1996
NGC 5364	B	11.25	4.5	Frei et al. 1996
NGC 5676	V	11.20	2.3	Héraudeau & Simien 1996
NGC 6643	B	11.77	3.3	Héraudeau & Simien 1996

* Note: The g-filter (Thuan & Gunn 1976) has a passband that is very similar to the Johnson V-filter. Thus, the color correction given for $V-K$ can be applied to $g-K$ colors, without introducing substantial systematic errors.

The correction was performed for the galaxies for which kinematic data is available. Unfortunately for the galaxies NGC 2339 and NGC 2964 there is no useful optical image available from the literature.

4.1.2.2. Results from the color correction

The color correction was performed to obtain a better stellar mass map of a galaxy than the K-band image provides. For the sample of the 6 galaxies for which the color correction was performed the two main effects of the color correction on the galaxy and rotation curve modelling are: the change in disk scale length and the change of the non-axisymmetric force components.

The disk scale length gets shorter for all sample galaxies due to the fact that galaxy disks tend to get bluer with increasing radius (e.g., Gadotti & dos Anjos 2001). A comparison of the different scale lengths is provided in Table 4.2. The scale lengths were derived from inclination corrected images and were determined from azimuthally averaged density profiles. The disk slope was taken from a simultaneous fit of two exponentials. The effects of the color correction are displayed for NGC 5676 in Figure 4.1.

As is apparent from Table 4.2, the effect of the color correction on the disk scale length is on the order of 10 %. A shorter disk scale length is equivalent to a steeper decrease of the stellar mass with radius. The rotation curve that results from this mass distribution has a slightly shifted radius of its maximum velocity and a faster decline for large radii.

Table 4.2 Disk scale lengths for color corrected galaxies.

Galaxy	Distance	disk scale length						$\Delta R_{\rm exp}$
		optical		K'-band		color corr.		$K' \rightarrow$ c. c.
	[Mpc]	[″]	[kpc]	[″]	[kpc]	[″]	[kpc]	[%]
NGC 3810	13.5	29.2	1.91	16.3	1.07	13.9	0.91	14.7
NGC 3893	17	24.0	1.98	21.9	1.80	21.1	1.74	3.5
NGC 4254	20	43.1	4.18	36.5	3.54	31.5	3.06	13.6
NGC 5364	25	63.0	7.64	53.1	6.43	49.9	6.06	5.7
NGC 5676	33	27.7	4.43	22.4	3.59	19.5	3.12	12.9
NGC 6643	23	31.4	3.50	24.4	2.72	22.3	2.48	8.6

This fact plays a role for disk-halo decompositions for which an axisymmetric disk and halo model generally provides the basis on which to derive the rotation curves. The effect of how the color correction influences the shape of the rotation curve is shown in Figure 4.2.

Although the rotation curve does not dramatically change its shape, the correction has consequences for disk-halo decompositions. Many studies try to constrain the properties of dark halo profiles by fitting halo models on top of the stellar mass rotation curve estimates to match the galaxies' rotation curves (e.g., Verheijen 1997; Palunas & Williams 2000). The conclusions of these studies sometimes depend extremely on the accurate rotation curve shapes, i.e. the underlying mass distributions.

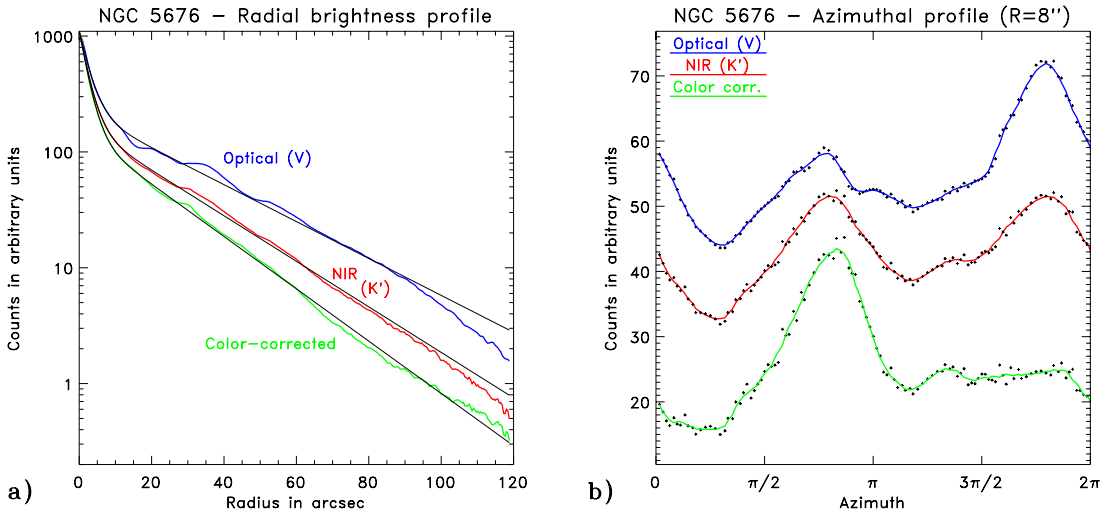

Figure 4.1 The effects of the color correction, displayed for the example of NGC 5676. **a)** shows the V-band, K-band and color corrected radial brightness profiles. Due to the outward blueing of the disk, the color corrected profile becomes steeper than both other profiles. **b)** shows how the color correction affects the local light profile. Displayed is an azimuthal cut (radius = 8″, azimuth 0 is north) through the optical, NIR and color corrected images. The two-arm profile of the galaxy is clearly visible. Features get enhanced if they are redder, or attenuated if they are bluer.

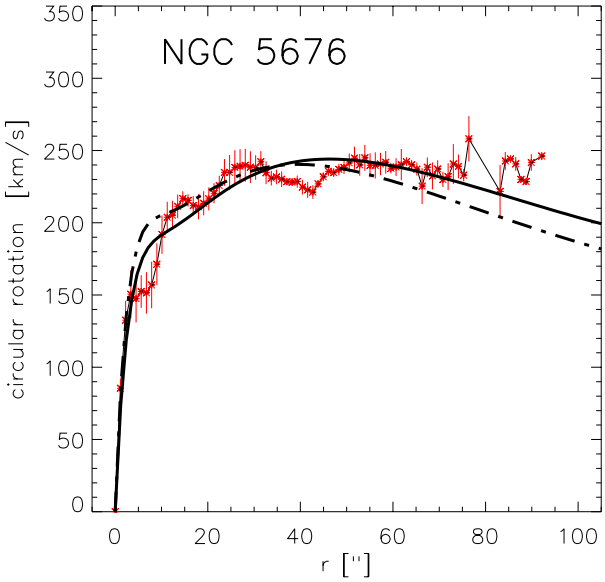

Figure 4.2 Maximal disk-only fits to the Hα rotation curve (red data points). The solid line represents the axisymmetric rotation curve taken from the K-band mass model while the dash-dotted line is the resulting rotation curve from a mass model taken from the color-corrected K-band image.

Here the color correction may help to improve the significance of the findings and might be considered. It is also expected that the color correction has an effect on the magnitude of the forces that act inside the disk. In particular the change in the radial mass distribution and the fact that the spiral arms themselves tend to be bluer, modifies the force components. In light of hydrodynamical gas modelling, where perturbations from non-axisymmetric features are studied, it is of immediate interest to quantify the change that the color correction introduces.

In this study, the force field in a galaxy gets calculated by first deriving the galaxy's gravitational potential from its surface mass distribution (as described in more detail in § 4.1.5) and by performing a numerical differentiation of the 2D potential to yield the forces. To investigate the effect of the color correction, the forces on each point in the image array were then separated into radial (F_R) and tangential (F_ϕ) components and a non-axisymmetric force fraction was defined by $F_{\rm nax} = F_\phi / F_R$. When calculating the force-field from K-band images it is found that $F_{\rm nax}$ for the sample galaxies is on the order of a few percent: The median value of $F_{\rm nax}$ for the 2D force field ranges from 2.3 % for NGC 3893 to 4.6 % for NGC 5364. Interestingly, the color correction leaves this quantity essentially unchanged. However, the change in forces on local scales is not at all constant. If $F_{\rm nax}$ is compared to $F_{\rm nax}^{\rm corr}$ and a parameter $\Delta F_{\rm nax}$ is defined by $\Delta F_{\rm nax} = |F_{\rm nax} - F_{\rm nax}^{\rm corr}|/|F_{\rm nax}|$, the median of $\Delta F_{\rm nax}$ turns out to be ~ 30 %. That means on a local scale, the color correction modifies the forces by non-negligible amounts.

4.1.3. Deprojection

Before the two dimensional gravitational potential can be calculated from the color corrected K-band image, the image needs to be deprojected to correct for the inclination with which the galaxy appears on the sky. To deproject the K-band images to face on, the IDL routine `GAL_FLAT` was applied. `GAL_FLAT` comes with the non-standard astrolib IDL package and, with the use of standard IDL routines, performs polynomial warping of the images. The deprojection of the image is realized by a geometrical transformation by bilinear interpolation between the pixels of the original image.

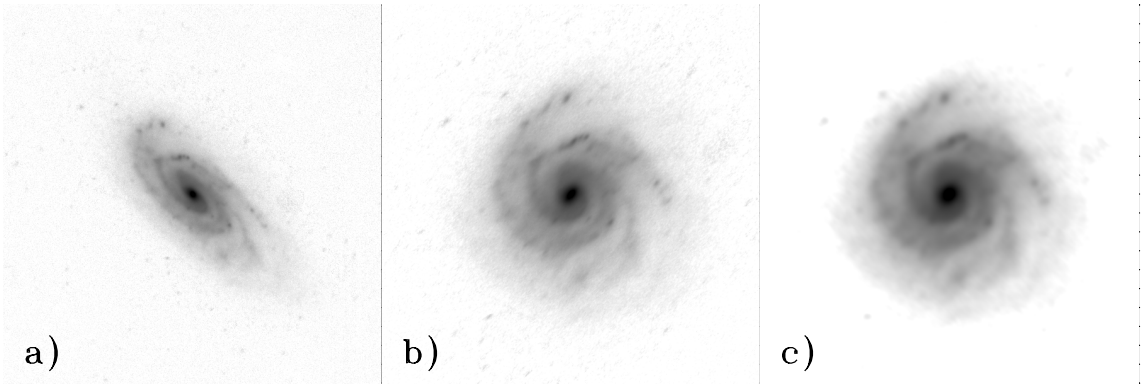

Figure 4.3 Deprojection and convolution shown for the example of NGC 5676. **a)** shows the color corrected image of the galaxy. **b)** displays the same galaxy after deprojection with a PA = 45.°8 and $i = 64°$. In panel **c)** the image was convolved with a transposed distortion function of a star in the image. Although the resolution becomes worse, point sources appear round.

Since the deprojection is in principle just a stretch of all the features in the image, for high galaxy inclinations round objects, like the nucleus of the galaxy, get exceedingly elongated. If not corrected, those asymmetric structures propagate into the potential and could introduce unwanted effects in the simulations. To correct for these distortions, the images of galaxies with inclinations of $\sim 60°$ were convolved with a transposed image of the distorted point spread function. This treatment decreases the resolution of the image, but leaves the global mass distribution virtually unchanged. The deprojection and deconvolution processes are displayed in Figure 4.3 for the exapmle of NGC 5676.

4.1.4. Cleaning the image

Some galaxies from the sample reveal quite a lot of star forming regions that are distinctly visible even in the K-band data. These regions are dominated by an overabundance of young, infrared luminous stars that exhibit a low stellar M/L. To reduce the influence of these star forming H II-regions and OB-associations, the image was filtered by means of an azimuthal Fourier decomposition. For this purpose the disk of the galaxy was modelled in Fourier space applying only the lowest, usually 8, Fourier terms. The low Fourier terms render well the overall structure of the disk, while local deviating peaks cannot be modelled. A difference map of the real galaxy and the Fourier model comprises all small scale features in the disk, such as H II-regions. After defining a certain threshold, below which the diffence map contains only noise, this clipped map can be subtracted from the

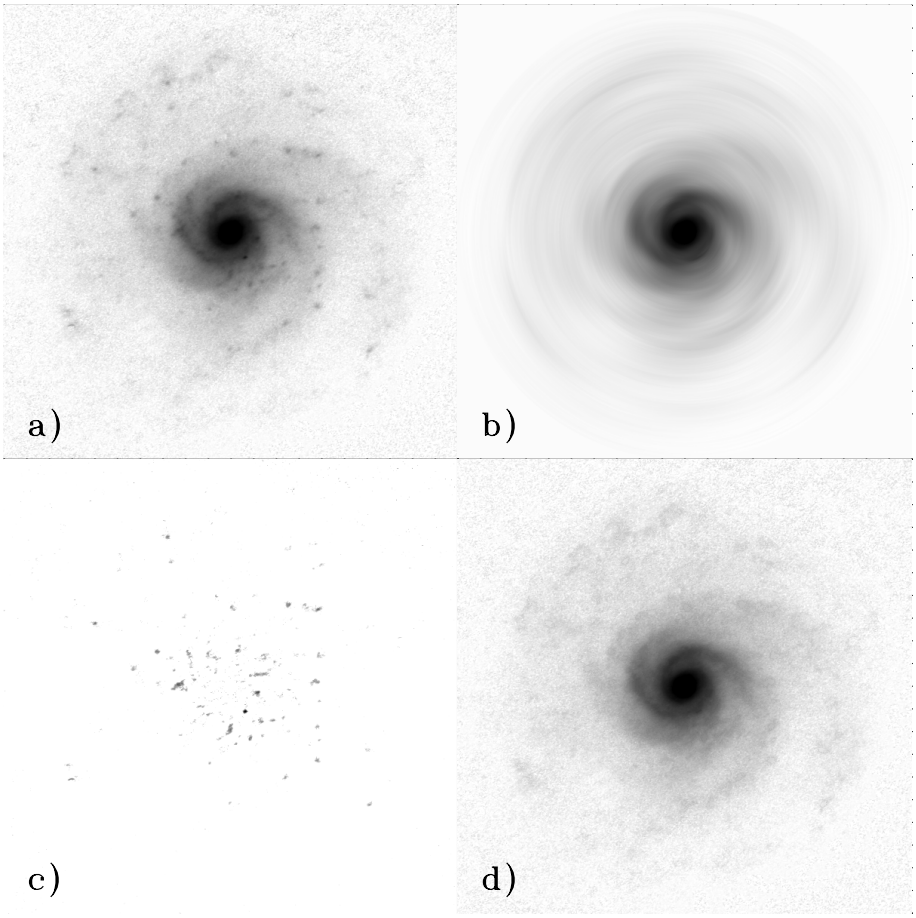

Figure 4.4 Fourier cleaning of the images shown for the example of NGC 3810. **a)** shows the color corrected, deprojected image of the galaxy. **b)** displays the Fourier model of the same galaxy applying the lowest 6 Fourier terms. In panel **c)** the clipped difference image between a) and b) is shown which is subtracted from a), yielding **d)**, the final image.

original image, cleaning it from the spiky, small scale features and leaving the smooth global spiral pattern. This process is graphically displayed in Figure 4.4. The amount of light that is removed from the K-band image depends on the number of star forming regions in the particular galaxy, but usually ranges from 1 % to 4 %. This correction does not depend significantly on the number of Fourier terms included in the fit or the choice of the threshold.

4.1.5. Calculating the stellar potential

The final image was then used to calculate a maximal disk stellar potential. This was achieved by numerical summation over the whole mass distribution of the galaxy, which is defined by multiplying the surface luminosity density L by some constant mass-to-light

ratio $\Upsilon_\star$: $\Sigma(\mathbf{r}) = \Upsilon_\star L(\mathbf{r})$. $L(\mathbf{r})$ comes from the processed K'-band images.

$$\Phi_\star(\mathbf{r}_i) = -G \sum_{j \neq i} \frac{\Upsilon_\star L(\mathbf{r}_j)}{|\mathbf{r}_i - \mathbf{r}_j|} \tag{4.4}$$

with:

$$|\mathbf{r}_i - \mathbf{r}_j| = \sqrt{\Delta \mathrm{x}^2 + \Delta \mathrm{y}^2 + \epsilon^2}. \tag{4.5}$$

The indices i and j denote different radius vectors, specifying here the pixels of the image array. Outside the detector array, the surface mass density is assumed to be zero. The factor ϵ in Equation (4.5) accounts for the finite thickness of galactic disks following Gnedin, Goodman & Frei (1995). This softening factor was chosen to be compatible with a vertical exponential density scale height of $h_z = 400\,\mathrm{pc}$, independent of radius. This assumption most probably holds for late type spirals, whose central spheroids, extend only to about a disk scale length into the disk. Additionally, small bulges may not be spherical and thus might be well described by the constant scale height of 400 pc assumed for most of the simulations. Moreover, the derived potential does not depend significantly on the choice of h_z. Varying h_z by 10 % leads to relative changes of the resulting forces by $\sim 5.1 \times 10^{-3}$ on average. An explicit disk-bulge decomposition was performed only for the most massive stellar disk models and the softening factor for the bulge was increased substantially to about 800 pc. This was necessary to achieve a better fit at the very inner part of the observed rotation curves.

Additionally a potential $\Phi_{\star,\mathrm{ax}}$ from an equivalent *axisymmetric* density distribution fitted to the galaxy's (corrected) K-band luminosity profile was calculated. This axisymmetric model potential will be used later for initializing the hydrodynamic simulations, which are set up in an axisymmetric potential. Furthermore, the modelled rotation curves that were used to scale the potentials by comparison with the observed rotation curves were calculated from the axisymmetric disk model. The model rotation curves got evaluated numerically from the stellar potentials by

$$v^2_{\star,\mathrm{ax}}(R) = R \left. \frac{d\Phi_{\star,\mathrm{ax}}(r)}{dr} \right|_R . \tag{4.6}$$

When inserting the physical dimensions for L, $\mathbf{r}$ and $\Phi_\star$ into equation (4.4) the value for $\Upsilon_\star$ can be derived for any light distribution $L(\mathbf{r})$, e.g., K' or the color corrected density, by scaling the potential such that the derived rotation curve matches the observed one. Later, when combining stellar and dark halo potentials, fractions $\mathrm{f_d}$ of this stellar 'maximum disk' fit were taken, to explore various luminous-to-dark matter ratios.

4.1.6. Determining the halo parameters

For the present analysis the radial density profile of a pseudo-isothermal sphere is used as the dark matter component in the model. Its radial density profile, characterized by a core of radius R_c and a central density ρ_c, is given by:

$$\rho(R) = \rho_c \left[1 + \left(\frac{R}{R_c} \right)^2 \right]^{-1} . \tag{4.7}$$

The corresponding rotation curve is

$$v^2_{\mathrm{halo}}(R) = v^2_\infty \left[1 - \frac{R_c}{R} \arctan\left(\frac{R}{R_c} \right) \right] \tag{4.8}$$

(Kent 1986) and the potential is

$$\Phi_{\rm halo}(R) = \int_0^R \frac{v^2_{\rm halo}(r)}{r} dr, \tag{4.9}$$

which is realized by numerical integration over the velocity profile. The asymptotic circular velocity in this (infinite mass) halo v_∞ is related to the two other free parameters R_c and ρ_c by

$$v_\infty = \sqrt{4\pi G \rho_c R_c^2}. \tag{4.10}$$

Thus, v_∞ and R_c uniquely specify all properties of the halo. For any potential with an underlying mass fraction $\mathrm{f_d}$ of the maximal stellar mass contribution it is possible to obtain the halo parameters from the best fit of the *combined* stellar and halo rotation curve to the observed kinematics. The quality of the fit was determined from a least squares analysis in the reasonable parameter range of v_∞ and R_c.

4.1.7. Assembling the final potential

In the final potential the disk and halo components were combined in the following way:

$$\Phi_{\rm tot}(\boldsymbol{R}|\mathrm{f_d}) = \mathrm{f_d}\ \Phi_\star(\boldsymbol{R}) + \Phi_{\rm halo}(\boldsymbol{R}|\mathrm{f_d}) \tag{4.11}$$

with $\mathrm{f_d}$ ranging from 0 to 1, and $\Phi_\star$ denoting the stellar potential with maximal stellar mass-to-light ratio. The contributions to the circular velocity add quadratically:

$$v^2_{\rm tot}(\boldsymbol{R}, \mathrm{f_d}) = \mathrm{f_d}\ v^2_\star(\boldsymbol{R}) + v^2_{\rm halo}(\boldsymbol{R}, \mathrm{f_d}). \tag{4.12}$$

For every $\mathrm{f_d}$ it was possible to find a dark matter profile, which complements the luminous matter rotation curve to match the measured rotation curve with closely comparable quality. Figure 4.5 shows this for the example of NGC 4254.

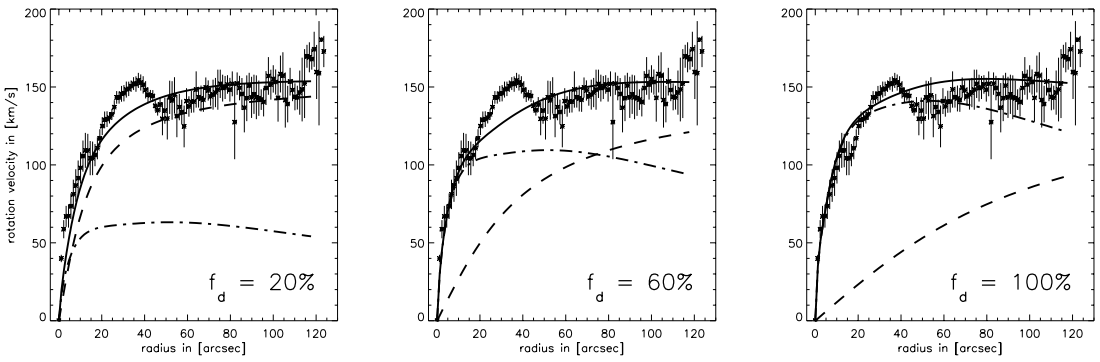

Figure 4.5 Different decompositions of the total gravitational potential into stellar and dark halo components, illustrated for the example of NGC 4254. The measured rotation curve (*data points with error bars*) – an average of six single rotation curves closest to the major axis – is well fit by all decompositions (*solid line*). Displayed are three cases for the contribution of the stellar disk $\mathrm{f_d} = 20\,\%$, 60 % and 100 % (*dash-dotted line*). The halo contribution (*dashed line*) was adjusted to yield a good fit to the measurements in combination with the pre-selected stellar contribution.

4.2. Hydrodynamic gas simulations

Hydrodynamic modelling of a gas flow could be based on either a macroscopic or microscopic description of the gas processes. In the macroscopic case the formalism is based on the Euler and Navier-Stokes equations, while the microscopic description relies on the (collisional) Boltzmann equation. A large fraction of hydrodynamic codes in the literature are based on solving the Euler equations, which do not include viscosity and heat conductivity in the gas description. To simulate realistic processes, additional terms, adapted to the Navier-Stokes problem must be included. These schemes work with varying success in realistic applications and often fail in extreme situations like strong shocks and rarefied gas dynamics. Alternatively, schemes may be based on the gas kinetic theory, evolving the particle distribution function with the Boltzmann equation. While schemes based on the collisionless Boltzmann equation are robust, the inclusion of the highly complex collision term into the hydrodynamic simulation scheme promises more accurate results. The hydrodynamic code, employed to model the gas flow in the sample of galaxies for this thesis is based on gas kinetic theory. It makes use of an approximation to the collisional Boltzmann equation, namely the Bhatnagar-Gross-Krook (BGK) scheme. The following sections provide a quick overview of the principles behind this approximation and the application of the numerical code to the astrophysical problem of galactic gas flows.

4.2.1. The BGK scheme

All macroscopically observed quantities characterizing a gas flow, such as mass, momentum and energy densities, rely on the microscopic behavior of the gas which can be described by the gas kinetic theory. For a numerical description of gas processes, it is possible to employ a scheme that is likewise based on the gas kinetic theory and its fundamental quantity, the particle distribution function $f(x_i, p_i, t)$. f gives the number density of particles in a six-dimensional phase space at a time t. The time evolution of the gas distribution function f is given by the collisional Boltzmann equation:

$$\frac{\partial f}{\partial t} + p_i \frac{\partial f}{\partial x_i} + a_i \frac{\partial f}{\partial p_i} = Q(f, f) \tag{4.13}$$

where a_i is the external force term acting on the particle in the i-th direction, and $Q(f, f)$ is the collision operator. For realistic gas processes, the highly non-linear and non-local collision operator is very complicated. However, for small deviations from thermodynamic equilibrium the collision operator can be substituted by a much simpler collision term, introduced by Bhatnagar, Gross & Krook (1954): $g - f/\tau$. The BGK term describes the relaxation of a non-equilibrium velocity distribution function f towards the local equilibrium state g, described by the Maxwell-Boltzmann distribution function. τ is defined as the collision time. It is the timescale on which f evolves to g. Assuming τ is the same for all particles regardless of their velocities, the collision term in the Boltzmann equation (without external forcing) becomes:

$$\frac{\partial f}{\partial t} + p_i \frac{\partial f}{\partial x_i} = \frac{g - f}{\tau}. \tag{4.14}$$

The underlying assumption in the BGK scheme is that there exists a collision process that transforms the particles from f to g, while conserving the total mass, momentum and

energy. Since the relaxation towards the equilibrium state is an irreversible, dissipative process it is accompanied with an increase in entropy. By evolving f through an equation which accounts for particle collisions, the fundamental mechanism for generating dissipation in the gas, the BGK scheme naturally renders the dissipative and viscous character of the gas and, at the same time, BGK satisfies the entropy condition. Moreover, due to its gas kinetic derivation, the BGK method satisfies the macroscopic Navier-Stokes and (inviscid) Euler solutions directly in smooth regions. A good review on the BGK approximation and its implications has been provided by Xu (1998).

4.2.2. The code

The code that is used for running the hydrodynamic simulations for this thesis is based on the BGK scheme. Details of its design, technical realization and capabilities can be found in Prendergast & Xu 1993; Slyz 1998; Slyz & Prendergast 1999). It is an Eulerian, grid-based hydrodynamics code that solves for the gas particle distribution function f and computes the physical quantities, like gas density, pressure and gas fluxes from the velocity moments of f. According to equation 4.14 a solution for f is a solution to the ordinary differential equation $\frac{\delta f}{\delta t} + \frac{f}{\tau} = \frac{g}{\tau}$, where $\frac{\delta}{\delta t}$ is the total time derivative along a particle trajectory in phase space. The differential equation is solved, obeying a set of boundary conditions, requiring that during particle collisions, mass, momentum and energy are conserved, i.e. the equivalence of the moments of f and g. The mean time between collisions, τ, is calculated locally for each cell from thermodynamic quantities at the cell interfaces. The code makes use of the fact, that local fluxes, and therefore a solution of f, is only required at cell interfaces of the underlying grid and for discrete time steps, therefore a solution for f can be numerically approximated. Clumpy structure of the gas on scales less than the grid size remains unresolved.

4.2.2.1. The collision time τ and its approximations

One of the basic parameters for the gas simulations is the collision time τ that needs to be locally computed during the runs according to the actual conditions. For the flux computation, the BGK scheme solves the BGK equation for f in the neighborhood of the boundary of each computational cell and for a short time, given by the usual Courant-Friedrichs-Lewy (CFL) condition, using a locally computed value for the collision time τ.

In practice the collision time, τ is composed of two terms: the first term corresponds to a real viscosity that is active everywhere including in smooth flow regions, whereas the second term is there for numerical purposes, namely to resolve discontinuities in the flow. For Euler calculations, which are used in the present case, the first term can be taken as $\mathcal{C}_1 \Delta \mathrm{t}_{\mathrm{CFL}}$, where a reasonable value for $\mathcal{C}_1$ is 0.01, i.e. assume 100 collisions per CFL timestep. Alternatively, for Navier-Stokes calculations, this term can be derived from gas kinetic theory which links the collision time to the gas density ρ and temperature T.

For problems in which the gas flow has discontinuities, the collision time τ serves an additional purpose. If the grid is not fine enough to resolve a discontinuity, then artificial dissipation must be added to broaden the discontinuity so that it is at least one grid cell thick. Because viscosity and heat conductivity are proportional to τ, the BGK scheme broadens shocks by enlarging τ at the location of the discontinuities. The expression for the collision time in the BGK scheme therefore contains a second term which is chosen in

such a way that shocks in the flow span at least one grid cell. This second term tunes the amount of artificial dissipation in the scheme. The notable difference between how the BGK scheme inputs artificial dissipation and how other schemes input artificial dissipation is that the BGK scheme puts it in exactly as if it were real dissipation corresponding to the numerically necessary value for τ. It should be emphasized that neither the artificial dissipation nor the physical dissipation enter the scheme as a predefined source term. When the second term in the collision time dominates, the order of the scheme is reduced and the true distribution function f is determined more by the initial distribution function f_0 than by the integral over g.

As far as approximations go when solving for f at a cell wall in the BGK scheme, it is assumed that all particles in that local region have the same particle collision time τ regardless of their velocity. As a result of this, the BGK scheme only gives Navier Stokes solutions with a fixed Prandtl number of 1. For this project that is acceptable because one is interested in getting accurate Euler solutions as opposed to Navier-Stokes ones. Another important point regarding τ is that it is a way to add dissipation into the flow homogeneously in all directions.

In summary, in the BGK scheme, the collision time τ ranges from a physically reasonable value, either computed locally on the basis of gas kinetic theory for Navier-Stokes problems, or assumed to be about 100th of the updating timestep for Euler problems, to a numerically necessary value (where $\tau \approx \Delta t_{\mathrm{CFL}}$, the CFL timestep). By this variation of the collision time throughout a hydrodynamical computation, the BGK scheme can describe a numerical fluid in both smooth and discontinuous regions.

4.2.2.2. Application to galactic gas simulations

The simulations of gas flows in galactic disks are challenging because cold gas in galactic disks rotates with such high Mach numbers that if the flow is diverted from a circular orbit by non-axisymmetric forces, the consequence is etched in the gas in patterns of shocks and rarefied regions. The BGK-code is well suited for these simulations because as verified by extensive tests on standard 1D and 2D test cases of discontinuous non-equilibrium flow (for a review, see Xu 1998), at shocks and contact discontinuities BGK behaves as well as the best high resolution codes and it gives better results at rarefaction waves because it naturally satisfies the entropy condition. However, treating rarefied gas dynamics with a hydrodynamics code will always be dissatisfactory because by definition, hydro assumes that there are an infinite number of collisions between the gas particles in a timestep or that the collision time is on the order of the updating timestep. In the regime where $\rho \to 0$ the collisional Boltzmann equation is inappropriate. The governing dynamical equation should be the collisionless Boltzmann equation in which case one is required to save much more information than the lower order moments of f. In BGK, when $\rho \to 0$, and hence $\tau \to \infty$, the distribution function f from which fluxes are computed goes to the initial distribution function f_0. The fact that BGK is not wired to exclusively solve the Euler or Navier-Stokes equations but that it can be applied to a broader range of τ's means that it is generally more robust for rarefaction waves than hydrodynamical codes based directly on the Euler or Navier-Stokes equations.

BGK has been used to solve Navier-Stokes problems in smooth flow regions both with (Slyz et al. 2002) and without (Xu & Prendergast 1994) gravity, and it has been tested

for its long-term stability and convergence to the equilibrium solution in a fixed external gravitational field (Slyz & Prendergast 1999). One additional reason for carrying out the disk simulations with this code, is its low diffusivity, a property that is critical not only to capture the shocks that form when the gas circulates in the non-axisymmetric potential, but also to properly model the loss of angular momentum and hence the resulting radial inflow of the gas due to the strong shear in the underlying differentially rotating disk. Slyz et al. (2002) showed that if an isothermal gas is initialized to be in centrifugal equilibrium within a purely axisymmetric galactic potential, simulation with the BGK scheme produces the steady-state Navier-Stokes solution to a high degree of accuracy. The success of BGK in giving viscous radial flows on the order of 1 $\mathrm{km\,s^{-1}}$ in a disk rotating differentially at 220 $\mathrm{km\,s^{-1}}$ is remarkable. It is a technical success which insures that when studying the kinematics of the gas in a galactic disk with BGK, with a decent grid resolution, one can worry less about artificial dissipation.

At its present state, the code does not allow the consideration of additional forces arising from the gas self-gravity. However, given that the gas surface mass density of the modelled galaxies is much lower than the density of the stellar disk and halo, it seems safe to assume that neglecting the gas self-gravity leads only to second order effects.

4.2.3. Boundary conditions

Since the computations were done on a Cartesian grid, the center of the disk (r = 0) is not a singular point, and therefore does not require special treatment via an inner boundary condition. Instead gas flow is computed through this point as it is computed through any other point on the grid.

An outer boundary condition is, on the other hand, unavoidable. Outside of a radius of R_{disk} two "rings" of ghost cells were kept, each "ring" being one cell thick. Beyond these ghost cells the evolution of the gas is not followed. Hence, effectively a circular grid is carved out of the square Cartesian grid. At the end of each updating timestep the values of the hydrodynamic quantities (mass, momentum and energy) were updated in the ghost cells by performing a bilinear interpolation to the cells in the vicinity of that ghost cell. To be more specific, for each ghost cell in the inner ring, for example, the coordinates of the intersection of the line extending radially from the center of the disk to the ghost cell with the circle bounding the true flow region of the grid get computed. After fitting a surface to the hydrodynamic quantities in the four cells surrounding this intersection (some of them might be other ghost cells) the ghost cell gets assigned the value that the fitted surface has at the intersection. Filling up the ghost cells via constant radial extrapolation that varies azimuthally around the disk, enables a better handling of situations in which there is a significant non-axisymmetry near the outer boundaries. The potential of NGC 4254 for example is quite non-axisymmetric near the upper boundaries thereby requiring an outer boundary condition which can take into account the possibility that the flow in the outer regions of the disk may also be non-axisymmetric.

As a further detail, it must be pointed out that this procedure for computing the outer boundary conditions is applied directly to the mass densities, however, for the velocities, additional steps were taken. The Cartesian velocity components were converted back to the non-rotating frame, then the radial and tangential components of the velocity were

constructed from the Cartesian components, and the bilinear interpolation and radial extrapolation procedure was finally performed on these components. By performing the interpolation and extrapolation on the radial and tangential components in the non-rotating frame, the boundary conditions were first set for quantities that are easier to interpolate and extrapolate: namely the tangential velocity which is nearly flat (constant in x and y) and the radial velocity which is nearly zero in the disk's outer regions in the non-rotating frame.

The outer boundaries allow gas flow across them. For different runs, mass loss/gain due to gas flow across them ranges after about 1 $t_{\rm dyn}$ from $\approx 2\%$ for runs performed in the non-corotating frame or slowly corotating frames, to at most $\approx 15\,\%$ for the fastest corotating frames that were simulated.

4.2.4. Performing the simulations

The gas density profiles were initialized to be exponential with a scale length which is a third of the radius of the observed disk. Upon estimating the total mass of the galaxy from the observed rotation curves, the mass of the gaseous disk was set to be 5% of this total mass so that the gas is moving in a potential produced by a mass much greater than the gaseous component, thereby justifying the neglect of the gas's self-gravity.

Given that the difficult question of how the spiral formed is beyond reach in these simulations, the focus is not to look for time-dependent solutions, but instead for steady or quasi-steady flow in NGC 4254's fixed external gravitational potential. The gas must therefore satisfy:

$$\boldsymbol{u} \cdot \nabla \boldsymbol{u} + 2\Omega_{\rm p} \times \boldsymbol{u} = -\nabla p/\rho \pm \nabla\Phi \tag{4.15}$$

$$\nabla \cdot (\rho \boldsymbol{u}) = 0 \tag{4.16}$$

where Φ is the potential of the *combined* centrifugal and gravitational forces. This system of equations must be completed by an equation of state and this introduces another parameter in the modelling, the gas sound speed. Since an effective equation of state is unknown for the interstellar medium (ISM), the simplest thing to do is to assume an isothermal equation of state so that $p = K\rho$. Here K is a constant. It is equal to ${c_s}^2/\gamma$ where γ is the ratio of specific heats of the gas, and $c_s = \sqrt{\gamma \mathsf{R}T/\mathsf{M}}$ is its sound speed. $\mathsf{R} = 8.314\ \mathrm{J\,mol^{-1}\,K^{-1}}$ is the gas constant; T is the ideal gas temperature in K; M is the molecular weight of the gas in $\mathrm{kg\,mol^{-1}}$. The isothermal equation of state implies a one-component model of the ISM. To compensate for a multiphase ISM, the behavior of the gas flow was studied with changing sound speed for the example of NGC 4254. The validity of the conclusions with a one-component ISM, depend mainly on the similarity between the large-scale dynamics of a one-phase model and a multi-phase model.

The simulations were performed on an evenly spaced Cartesian grid. The resolution per grid element was chosen to measure about 100 pc in real units for each galaxy. For NGC 4254 the additional cases for grid cell sizes of ≈ 50 and ≈ 200 pc were explored.

The simulations were started with the gas flowing on circular orbits in inviscid centrifugal equilibrium with respect to the axisymmetric gravitational potential which best fits the observed rotation curves. The non-axisymmetric perturbations (whose strength is determined by the disk fraction, $\mathrm{f_d}$, of the model), are then turned on gradually. As Sorensen

& Matsuda (1982) describe, if the potential is turned on too rapidly, material arms are produced in the gas simulations. These will be wound up by the differential rotation of the disk, and will eventually disappear by winding. A slow turn-on of the potential avoids or at least minimizes this transient. The criteria for the time in which the full potential was turned on, ($t_{\rm FP}$), was adjusted according to the sound crossing time ($t_{\rm s}$) across the diagonal of a grid cell. For the standard simulations $t_{\rm FP} = 40\ t_{\rm s}$ was chosen. Since the sound crossing time depends on the length of the grid cell, and for comparison's sake the total running time of each simulation should be similar, $t_{\rm FP}$ was scaled with $t_{\rm s}$ for the additional high- and low-resolution runs. After the full potential was turned on, the runs were set up to continue for another one to two dynamical times.

The computations were performed in the non-inertial coordinate system rotating with the pattern speed $\Omega_{\rm p}$. This is another parameter of the simulation which turns out to play a powerful role in shaping the morphology of the gas distribution. The direction of the coordinate system rotation depends on the sense in which the arms of a galaxy wind. It is chosen such that, inside corotation, the gas enters the spiral arms from the concave side.

The bulk part of the simulations were done using the SGI Origin 2000 located at the Rechenzentrum Garching and which is dedicated to the Theory group of MPI für Astronomie in Heidelberg. The Origin 2000 hardware consists of 16 processors MIPS R10000 operating at 195 MHz with 8 GB main memory available. The code has capabilities to run in parallelized mode and simulation scripts were set up to run on 4 processors each. One single simulation requires about 2 hours of CPU time, depending on the number of simulated timesteps. The code is also able to run on SUN workstations.

4.3. Comparing observations and simulations

To draw conclusions from the modelling of the analyzed galaxies, the results from the simulations, namely the gas density distribution and the gas velocity field, must be compared to the observations. This Section describes the procedures that were applied to estimate or quantify how well one simulation reproduces the real conditions in a particular galaxy.

4.3.1. The gas density

The gas density output of the simulations can be used to find the pattern speed of the galaxies. For this purpose, the modelled gas density was overlaid in contours onto a real image of the galaxy. The real image, which was usually the K'-image, was displayed such that the arm structure appeared enhanced on the image. This was achieved by either subtracting an azimuthally averaged disk model from the galaxy and plotting the residual non-axisymmetric structure, or by the unsharp masking technique. The unsharp mask was created by convolving the image with a two dimensional Gaussian with a FWHM of 28 image pixels. Plotting the difference of the mask and the original yields an image emphasizing the non-axisymmetric spiral structure.

The actual comparison and determination of the best fitting model was done by eye. This might appear to be a very qualitative or biased approach. However, it is one of the eye's most powerful attributes to recognize patterns and similar structures. And since the agreement of spiral features is of a two dimensional, global nature, the eye can distinguish with

high precision between a good fit and a less good one. Eventually, since the density profiles of a gaseous shock and that of a stellar spiral arm are considerably different, any kind of quantitative least squares comparison would be very difficult to interpret. Furthermore, in most cases the winding of the spiral pattern in the simulations evolves monotonically from tight to more open structures with increasing corotation radius, which allows the unambiguous identification of the range for the best matching pattern.

Even when determining the match by eye, there are some criteria according to which to pick one particular model. In general, gas shocks appear where the streaming gas encounters the spiral pattern. Inside corotation this is at the inward facing side of the spirals, if trailing arms are assumed, because there the gas circular velocity is larger than the pattern speed. Another criterion is the location of star forming H II regions along the arms. This is a characteristic of the density wave. The shocked gas triggers star formation along the spiral arms directly downstream from where the gas is compressed the most (Schweizer 1976, Beckman & Cepa 1990). Thus, a good matching morphology would place the gas density shocks at locations, where the most star forming regions come to lie in the spiral arms.

4.3.2. The gas velocity

The observations cover the gas velocity field only along the slit positions where the spectrograph was placed across the disk. Thus, the comparison was done along these slits. To correctly compare the simulated gas velocities to the observed data, the modelled velocity field needs to be projected according to the real orientation of the galaxy. From the projected velocity field, the line-of-sight component of the velocities must be obtained along the slit positions taken with the spectrograph. For this procedure the Cartesian velocity components were transformed into velocity components parallel and orthogonal to the galaxy's major axis. The simulations yield truly two dimensional velocity fields and the component parallel to the major axis does not contribute to the line-of-sight velocity as it reflects only tangential motion. The orthogonal velocity component is multiplied by the sine of the inclination of the galactic disk, to account for the line-of-sight fraction of the velocities.

The velocities are read along slits which correspond to the slit positions taken with the spectrograph. The angular width of the grid cells of the simulation ($1\farcs19$) is comparable to the slit width of the spectrograph that was used ($1\farcs5$), which was also the average seeing conditions. The angles between the spectrograph slit orientations that were taken from the projected galaxy on the sky, must be translated to angles in the plane of the galaxy to actually compare the same parts of the velocity fields. This translation makes use of the following relationship:

$$\tan(\varphi_{\rm int} - {\rm PA}) \cdot \cos(i) = \tan(\varphi_{\rm app} - {\rm PA}) \tag{4.17}$$

where $\varphi_{\rm app}$ is the apparent angle of the spectrograph slit across the galaxy on the sky and $\varphi_{\rm int}$ is the corresponding intrinsic angle within the plane of the galaxy. PA is the position angle of the galaxy's major axis on the sky. All angles are in degrees measured eastward from north. See Figure 4.6 for a graphic representation of the relevant angles and orientations. Solving for $\varphi_{\rm int}$ gives:

$$\varphi_{\rm int} = \varphi_{\rm diff} + {\rm PA} \tag{4.18}$$

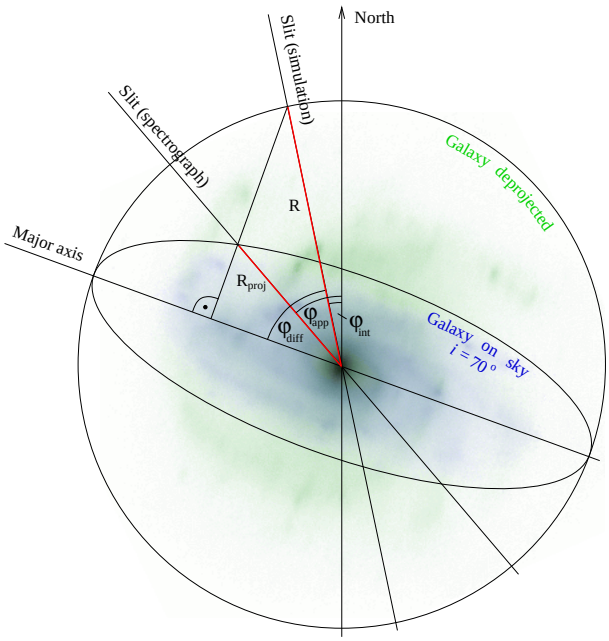

Figure 4.6 Schematic representation of the important elements of the deprojection process.

with φ_{diff} being the angle between φ_{int} and the major axis:

$$\varphi_{\mathrm{diff}} = \arctan\left(\frac{\tan(\varphi_{\mathrm{app}} - \mathrm{PA})}{\cos(i)}\right). \tag{4.19}$$

The foreshortening of the radial proportions due to projection in the direction of the minor axis is determined by

$$R_{\mathrm{proj}} = R \cdot \sqrt{\cos^2(\varphi_{\mathrm{diff}}) + (\sin(\varphi_{\mathrm{diff}}) \cdot \cos(i))^2}. \tag{4.20}$$

Finally the detector pixel sizes of the TWIN, where the observed velocities come from, and Omega Prime camera, whose pixel scale is the reference grid for the simulations, must be adjusted to perfectly align with each other.

4.3.2.1. Evaluation of the comparison

In order to quantify the degree of agreement between the observed and simulated velocity fields a least squares comparison along the spectrograph slit position was performed:

$$\chi^2 = \sum_{\text{all slits}} \sum_{\text{all r}_\mathrm{i}} \left[\frac{v(\mathrm{slit_i}, \mathrm{r_i})_{\mathrm{sim}} - v(\mathrm{slit_i}, \mathrm{r_i})_{\mathrm{obs}}}{\sigma(\mathrm{slit_i}, \mathrm{r_i})_{\mathrm{obs}} + \sigma_{\mathrm{sys}}}\right]^2 \tag{4.21}$$

where $v(\mathrm{slit_i}, \mathrm{r_i})_{\mathrm{sim}}$ and $v(\mathrm{slit_i}, \mathrm{r_i})_{\mathrm{obs}}$ are the simulated and the observed velocities respectively. $\sigma(\mathrm{slit_i}, \mathrm{r_i})_{\mathrm{obs}}$ is the error that was attributed to the measured velocities (see Section 3.3.2). Additionally, a systematic error σ_{sys} was added to all measured data points, in order to consider uncertainties that are not accounted for, like asymmetries in the Hα-line

profiles, errors in the zero-point determination of the rotation curves or eventual mismatch between the positions of the observed slit and the artificial slit across the simulated velocity field. For all galaxies a systematic error of $9.5\,\mathrm{km\,s^{-1}}$ was added to each measured data point for the χ^2-analysis. Furthermore, since the χ^2/N is very sensitive to single outliers (they add in quadratically), in ambiguous cases the median of the sum in equation (4.21) was considered too.

However, as it became evident during the process of the analysis, on small scales the simulations fail to reproduce all structures in the observed rotation curves. This effect comes from the systematic approach of the study and originates from the fact that in the modelling only the gravitationally induced gas kinematics can be reproduced. All other local gas dynamic processes, like stellar winds in the vicinity of star forming regions or supernova remnants, are left unaccounted for. Also the two dimensional nature of the simulations introduces systematic errors. These effects will be discussed in more details in the following chapters. In light of this, a global least squares comparison, including all observed data points might not be the right approach to evaluate the best match. If the amount of kinematic wiggles induced by gravity and the amount caused by other processes roughly commensurate, the global least squares comparison will systematically favor the models that exhibit the least non-axisymmetric structures to which the axisymmetric gravitational potential of the galaxy was tuned to fit, i.e. light disks.

All attempts to constrain non-gravitational wiggles from the observations turned out to yield unsatisfying results. Hα line profiles or intensities emerged as a rather inconclusive basis to separate gravitational from non-gravitational gas kinematic features. High resolution Hα maps were not available to identify gas shells or supernova bubbles. On the other hand, the hydrodynamic simulations can be used in a rather robust statistical approach to find the locations along the spectrograph slits, where the velocity fields exhibit an essentially undisturbed gravitational response to the underlying potential.

By using the simulations for the best matching pattern speed the gravitation dominated regions can be determined by selecting those parts of the rotation where the individual terms of the least squares analysis (equation 4.21) do not exceed a predefined treshold. To do this coherently, the selection process involves the models for all disk mass fractions f_d. As a criterion for an observed data point to enter the final subset for comparison, it must have been flagged at least by two f_d models as "gravity wiggle". The treshold was chosen to exclude roughly half of the total data points.

This method provides a rather unbiased approach to exclude non-gravitationally induced gas shocks because it utilizes the information from the simulations and does not preselect for a certain mass model. The final evaluation of the fit quality between the observations and simulation results for the different galaxy mass models is then performed by restricting the least squares analysis to the data points from the observations that most likely render gravitationally induced gas kinematic features.

The above described selection method was not applied to NGC 4254 because it was developed only after the results for this galaxy were published. However, applying this method to NGC 4254 does not change the conclusions derived in the paper.

CHAPTER V
NGC 4254 – a case study

Based on: "Probing for dark matter in spiral galaxy disks"
Kranz, Slyz & Rix 2001, ApJ, 562, 164

We[1] selected NGC 4254 (Messier 99) as the first galaxy from our sample to be analyzed, because it shows a clear spiral structure with high arm-inter-arm contrast. NGC 4254 is a bright Sc I galaxy located in the Virgo galaxy cluster with a recession velocity of $2453\,\mathrm{km\,s^{-1}}$ adopted from the SIMBAD database. We assume a distance of 20 Mpc towards NGC 4254, taken from the literature (Sandage & Tammann 1976; Pierce & Tully 1988; Federspiel, Tammann & Sandage 1998). It has a total blue magnitude of $B_T = 10.2$ and a diameter of 5.4×4.7 arcmin on the sky. At 20 Mpc one arc second is 97 parsecs in the galaxy which translates to 38.4 pc per detector pixel. Our Hα rotation curve for NGC 4254 (see Figure 4.5) rises steeply out to $\sim 35''$ (3.4 kpc) and then flattens at a rotation velocity of $\sim 155\,\mathrm{km\,s^{-1}}$. This agrees well with earlier estimates (Phookun, Vogel & Mundy 1993). From the kinematics we know that the south-western part of the galaxy is approaching. If we assume trailing spiral arms then the galaxy rotates clockwise when viewed from our perspective.

In the K-band NGC 4254 shows very prominent two-arm spiral features at most radii. The northern arm bifurcates at R $\approx$ 4.5 kpc, causing a three arm pattern in the outer disk. Furthermore, the galaxy exhibits considerable lopsidedness. NGC 4254 shows a strong arm-interarm brightness contrast, noted by Schweizer (1976) to be even stronger than the one for NGC 5194 (M 51). Even in the K-band the brightness contrast is rather high, more than one magnitude over a wide radial range. González & Graham (1996) argued that, combined with a usual density wave, some external mechanism is needed to invoke such high contrasts. However, NGC 4254 is well separated from any other galaxy in the cluster. Phookun, Vogel & Mundy (1993) reported in their paper the detection of high velocity H I clouds outside the disk's H I emission. The authors argue that in-falling H I gas may be responsible for the unusual "one armed" outer structure of the spiral. In that case the spiral structure of NGC 4254 may have been recently reorganized, enhancing the southern arm or the arm-interarm mass density distribution. Recent interactions could in principle corrupt the project's assumption of a steady state spiral pattern. But as we will find from our full analysis, the steady state assumption is seemingly not far off on time scales of a few dynamical periods.

NGC 4254 harbors a small bar-like structure at its center with a major axis position angle of $\approx 40°$ (see Figure 5.1a). From both ends of the bar two major arms emerge with a third

[1] The use of plural emerges from the fact, that the content of this Chapter was partially copied from a multi-author paper.

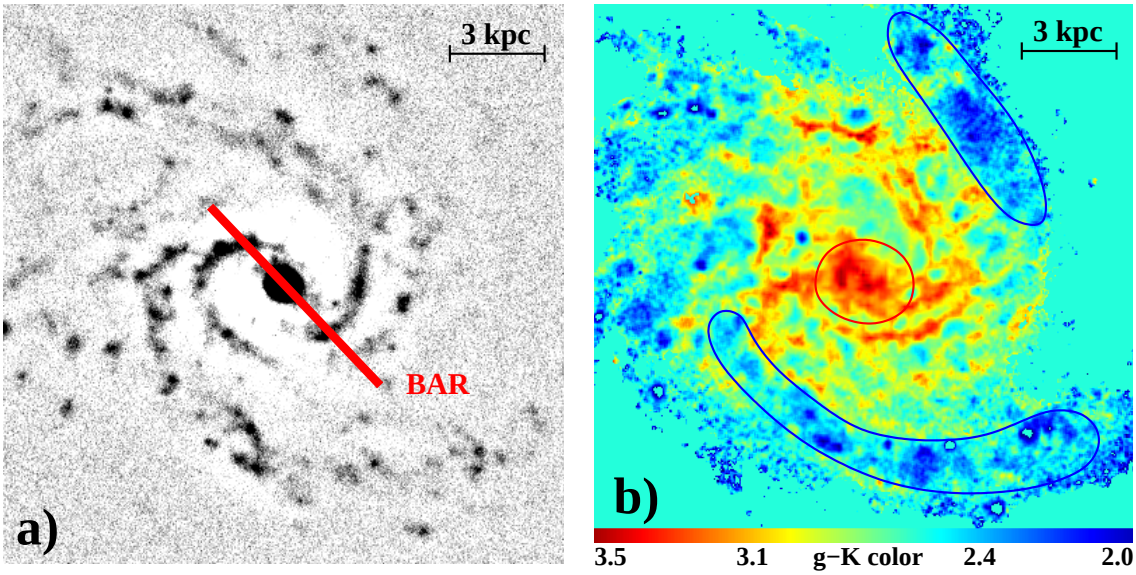

Figure 5.1 Properties of NGC 4254. Panel **a)** shows the morphology and the position of the small bar. The image has been treated with the unsharp mask subtraction technique to enhance the spiral features. **b)** shows the $g - K$ color map of NGC 4254. The bulge exhibits a redder color while the spiral arms appear bluer (circled areas).

arm splitting off the northern arm. By analyzing a $g - K$ color map of NGC 4254 one learns that this third arm, together with the southern strong arm, is significantly bluer than the other regions of the galaxy and thus consists of a younger stellar population. The inner small bulge appears red in the color map (see Figure 5.1b).

In the K-band the disk of NGC 4254 is well approximated by an exponential with a scale length of $R_{exp} \approx 36''$, corresponding to ≈ 3.5 kpc if a brightness average of the arm and interarm regions is considered and bright H II regions are removed from the image. Except for the very center, the whole surface brightness profile is well fitted by a double exponential model with an inner 'bulge' scale length of ≈ 0.6 kpc.

5.1. Hydrodynamic simulations for NGC 4254

To model the two-dimensional gas surface densities and velocity fields for NGC 4254 we carried out a set of simulations on a 201 by 201 evenly spaced Cartesian grid. Our data for NGC 4254 extend out to a radius of about 11.6 kpc, hence on a 201 by 201 grid this gives a resolution of about 116 pc per side of a grid cell, which is considerably higher than the effective force smoothing of 400 pc.

The gas temperature profile is taken to be uniform and by imposing an isothermal equation of state throughout the simulation we assume that the gas instantaneously cools to its initial temperature during each updating timestep. The initial density profile of the gas is exponential with a scale length equal to a third of the disk radius, namely 3.86 kpc. We begin each simulation with the gas initially in inviscid centrifugal equilibrium in the axisymmetric potential given by $\Phi_{\star,ax}$ and Φ_{halo} (see Section 4.1.5). Following the initial-

Table 5.1 Dark halo parameters.

f_d (M_D/M_{Dmax})	R_c (kpc)	v_∞ ($km\,s^{-1}$)	χ^2/N
0.2	1.08	155	2.45
0.4444	2.00	150	3.42
0.6	3.03	150	3.30
0.85	5.68	155	2.00
1.0	7.30	155	1.84

Note: Dark halo parameters used to generate the potentials used for simulations. The χ^2/N-values refer to an axisymmetric model.

ization of the gas in centrifugal balance, we slowly turn on the non-axisymmetric potential at a linear rate computed by interpolating between the final non-axisymmetric potential and the initial axisymmetric potential so that the potential is fully turned on by the time 40 sound crossing times of the code have passed. Here the sound crossing time is defined as the time it takes to traverse the length of the diagonal of a grid cell at sound speed. For an isothermal simulation with a sound speed of $10\,km\,s^{-1}$ the sound crossing time of a cell in our simulation is about 16 Myr, so that by 40 sound crossing times, the gas has evolved for 640 Myr which is about 1.4 times the dynamical time of the galaxy measured at a radius of 11.6 kpc. After the non-axisymmetric part of the gravitational potential has been fully turned on, we continue to run the simulation for about another dynamical time.

We ran a large set of simulations both to understand the power and limitation of our modelling in general and to match the observations. Simulations were performed for a total of five different fractions f_d of the stellar disk: disk only, i.e. $f_d = 1$, and $f_d = 0.85$, 0.6, 0.4444 and 0.2, or accordingly f_d is given in percent from 20 % to 100 %. In all the cases the core radius and the asymptotic velocity of the pseudo-isothermal halo were adjusted to best match the averaged rotation curve, as summarized in Table 5.1. The variations in χ^2/N between the low mass disks and the massive ones are mainly caused by the attempt to keep R_c and v_∞ at physically reasonable values. The bump at $20''$ to $40''$ (Figure 4.5) is fitted better for the high mass disks, which reduces the overall χ^2 compared to the low mass disks.

We have no secure prior knowledge of the spiral pattern speed Ω_p. We determine it by assuming different values for Ω_p and then comparing a simulation to the data. For every simulation with a different stellar/dark halo combination, we get slightly different values for the best matching Ω_p or equivalently for the corotation radius R_{CR}. We covered the complete range of reasonable R_{CR}, i.e. from about a disk scale length to well outside the disk. We even made simulations for the case of no spiral pattern rotation, $R_{CR} \to \infty$.

To test how the amplitude of the velocity perturbations depends on the responsiveness of the gas, we ran simulations at a variety of temperatures corresponding to sound speeds c_s, of 10, 15, 20 and $30\,km\,s^{-1}$. In the following Sections we discuss some of the results from the simulations.

5.2. Results for NGC 4254

5.2.1. Simulated Gas Density

Figure 5.2 shows eight views of the simulated gas density for different pattern speeds overplotted as contours over the deprojected, color corrected K-band image of NGC 4254. The simulated gas density follows an overall exponential profile with a scale length of ≈ 4.2 kpc, comparable to the one of the disk itself. The contours in the Figure are chosen to highlight the density enhancements and locations of the gas shocks caused by the spiral arms. For almost all simulated cases the strong part of the galaxy's spiral structure lies well inside corotation, where the circular velocity is larger than the spiral pattern speed. The gas will thus enter the spiral arms from their inward facing side, producing the strongest shocks there. For a well matching simulation, we expect the shocks to be near the OB associations that trace the spiral arms.

It is remarkable how well the overall morphology of NGC 4254 can be matched by the gas density simulations. Not only are the two major spiral arms clearly identifiable in most simulations but the less prominent northern arm and the locations where the arms bifurcate are reproduced in some cases well. For fast pattern speeds ($R_{\rm CR} = 5.4 - 7.58$ kpc in Figure 5.2) we find a strong shock in the northern part of the galaxy that cannot be correlated with any mass feature. We believe it develops because the potential close to the upper boundaries of the computational grid is quite non-axisymmetric, and this leads to a spurious enhancement of a shock. The shock does not propagate into regions inside the corotation radius, and therefore we refrain from smoothing the potential.

It is important to note that the simulations lead to a very stable gas density distribution that does not change much after the non-axisymmetric potential is fully turned on. When the contribution of the disk is increased in the combined potential, all spiral features get enhanced in the gas density but the galaxy morphology is essentially unchanged. With increasing pattern rotation (smaller corotation radii in Figure 5.2) we find that the predicted spiral arms become more and more tightly wound. For a comparison to the stellar spiral morphology we need to define some criteria to pick the right model. If the situation in NGC 4254 is similar to NGC 4321, whose gas and dust distributions and their connection to star forming regions have been discussed in detail by Knapen & Beckman (1996), then a good matching gas morphology is one where for radii smaller than the corotation radius, the shocks in the gas density lie on the inside of the stellar spirals. Shortly downstream from there, many star forming H II regions, triggered by gas compressions, should show up as patches in the arms. According to these criteria, the best matching morphology can be unambiguously identified to be produced by a simulation with $R_{\rm CR} \approx 7.6$ kpc (Figure 5.2 upper right panel), corresponding to a pattern speed of $\Omega_{\rm p} \approx 20\,{\rm km\,s^{-1}kpc^{-1}}$. $R_{\rm CR} = 6.4$ kpc and $R_{\rm CR} = 8.3$ kpc enclose the range of possible values. This corresponds to an uncertainty of $\sim 15\%$ in the value of $R_{\rm CR}$.

Our results were compared to values of $R_{\rm CR}$ for NGC 4254 from the literature, which were determined by different means. The results $R_{\rm CR} \sim 8.45$ kpc (Elmegreen et al. 1992) and $R_{\rm CR} = 10.2 \pm 0.8$ kpc (González & Graham 1996), scaled to our distance assumptions, provide larger estimates than ours. However, given the picture of non-linear orbital models, where the strong part of the stellar spiral is expected to end inside the inner 4/1 resonance

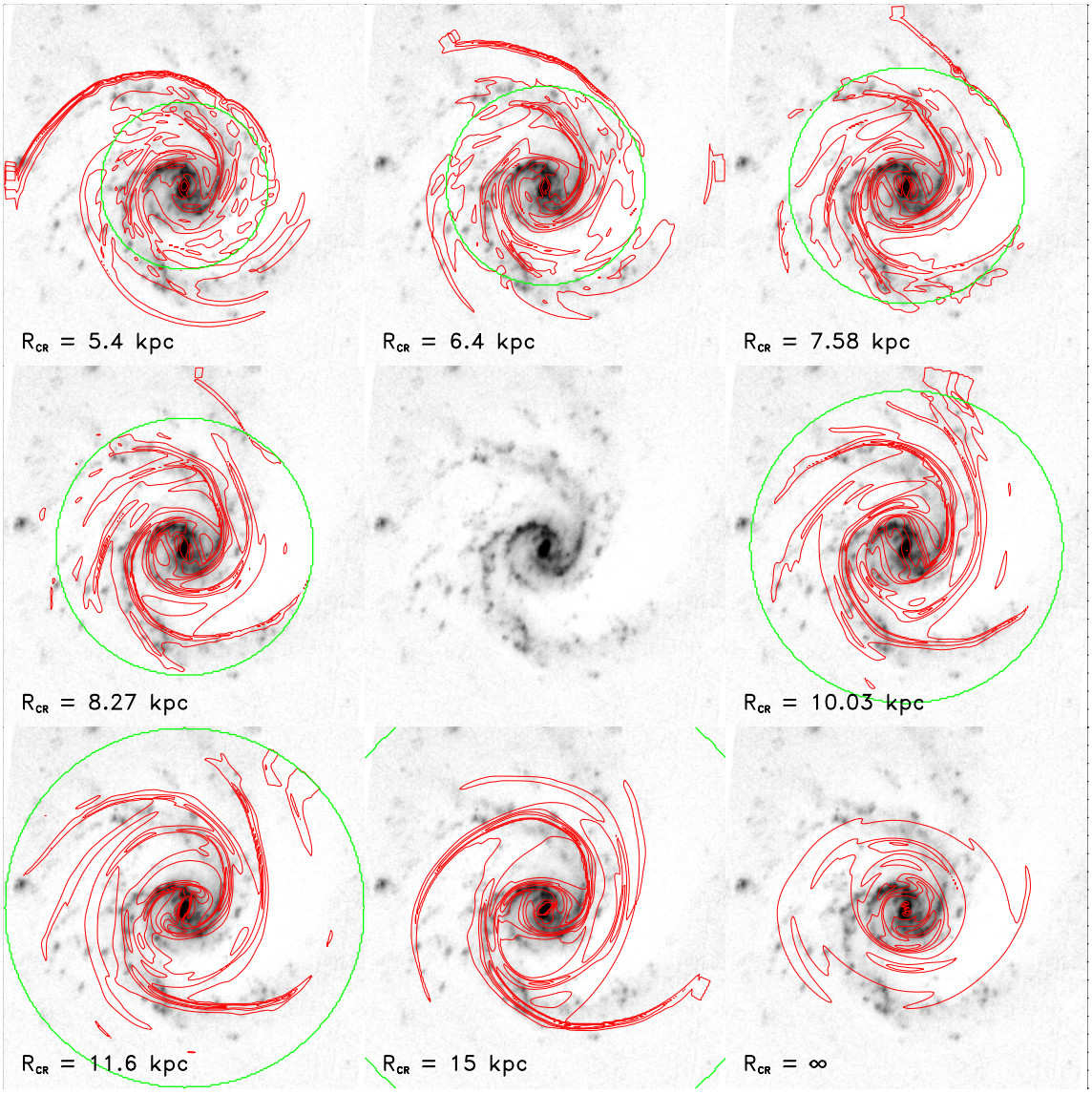

Figure 5.2 Simulation results of the gas density distribution over-plotted in red contours on the deprojected K'-band image of NGC 4254 (center). From the image an axisymmetric radial brightness profile has been subtracted to enhance the contrast of the spiral arms. The results are displayed for eight different assumptions for the pattern speed, respectively the corotation radius $R_{\rm CR}$. The green circle marks corotation. The range goes from fast rotation $R_{\rm CR} = 5.4\,$kpc to slow pattern rotation $R_{\rm CR} = 15\,$kpc, lying mostly outside the image frame and finally for no pattern rotation. Displayed are the results from the $\mathrm{f_d} = 60\,\%$ case.

(Patsis et al. 1991) we find that $R_{\rm CR} \approx 7.6\,$kpc is consistent with the galaxy's morphology. In short, these simulated gas densities provide us with an excellent tool to determine the pattern rotation speed of the galaxy. Apart from requiring a constant global pattern rotation our approach is independent of an underlying spiral density wave model. The overall very good representation of the whole spiral structure by the simulated gas density makes us rather confident that the simulations render realistic processes affecting the gas.

5.2.2. Simulated Gas Velocity Fields

As another output of our simulations we get the two-dimensional velocity field of the gas. As is evident from a comparison to the gas density distribution, the velocity jumps are – as expected – at the locations where the density map shows the shocks. They show up as areas of lower local circular velocity compared to the elsewhere rather smoothly varying gas velocity field. The velocity wiggles, as well as the density shocks themselves, have very tight profiles and thus are even more narrow than the physical extent of the stellar arms. They have to be compared to the observed kinematics.

5.2.2.1. The observed kinematics

The rotation curves at the 16 slit positions from the observations are shown in Figure 5.3 as data points. It is apparent that the longslit spectra allow a good velocity coverage along the slits. Almost all rotation curves show contiguous data points out to a radius of $\gtrsim 1\farcm5$. The spectra exhibit a lot of wiggles on a small spatial scale. Jumps of $\lesssim 30\,\mathrm{km\,s^{-1}}$ on a scale of $\sim 5''$ are common. The very prominent jumps that we observed in slit positions $22\fdg5$ and $225°$ clearly exceed the average wiggle sizes. Inside of about $0\farcm3$ the small bar influences the velocity field. The most prominent trace of the bar occurs at its minor axis at the slit positions of $135°/157\fdg5$ and $315°/337\fdg5$.

The trace of kinematic features in the outer disk is not conspicuous in subsequent slits. The eastern part of the disk (slit positions $45°$ – $135°$) displays a quite smooth velocity field, while the western part shows some large scale variations. Aside from the inter-arm region between the inner disk and the southern arm where a $\approx 0\farcm5$ wide depression is moving outward in subsequent slits (positions $\geq 247\fdg5$) no significant features are apparent in the outer disk. Unfortunately in this inter-arm region the S/N is not so good. Does that mean we do not see the trace of the arms in the velocity field, or is the single slit representation of the 2D velocity field misleading and does not allow us to identify coherent features in adjacent slits? Clearly, the wiggles associated with spiral arms in NGC 4254 are not nearly as strong as in M 81 (Visser 1980), thus their identification is harder. A CO map of NGC 4254's center (Sakamoto et al. 1999) shows also no coherent wiggles across spiral arms and we doubt that it would be much different on a Fabry-Perot image. Rather than being confused by the one dimensional nature of our rotation curve slices we believe that the spiral features in the velocity field are intrinsically weak.

5.2.2.2. Overall Fit Quality

Figure 5.3 shows the 16 separate rotation curves with a corresponding simulated velocity field over-plotted. The simulation used here for comparison is the one for which the gas density distribution best-fit the K-band image (displayed in Figure 5.2). It has a corotation radius of $R_{\mathrm{CR}} = 7.58\,\mathrm{kpc}$ – corresponding to a pattern speed of $\Omega_{\mathrm{p}} = 20\,\mathrm{km\,s^{-1}kpc^{-1}}$ – and a stellar disk mass fraction $\mathrm{f_d}$ of 60 %. A gas sound speed of $c_s = 10\,\mathrm{km\,s^{-1}}$ was assumed here.

The general fit quality is governed by the effect that the projection of the simulated velocity field introduces. The good overall match indicates that we quite reliably found the right position angle and inclination for the galaxy. The simulated velocities align very well with the measured data points. In addition to the good overall match, the general

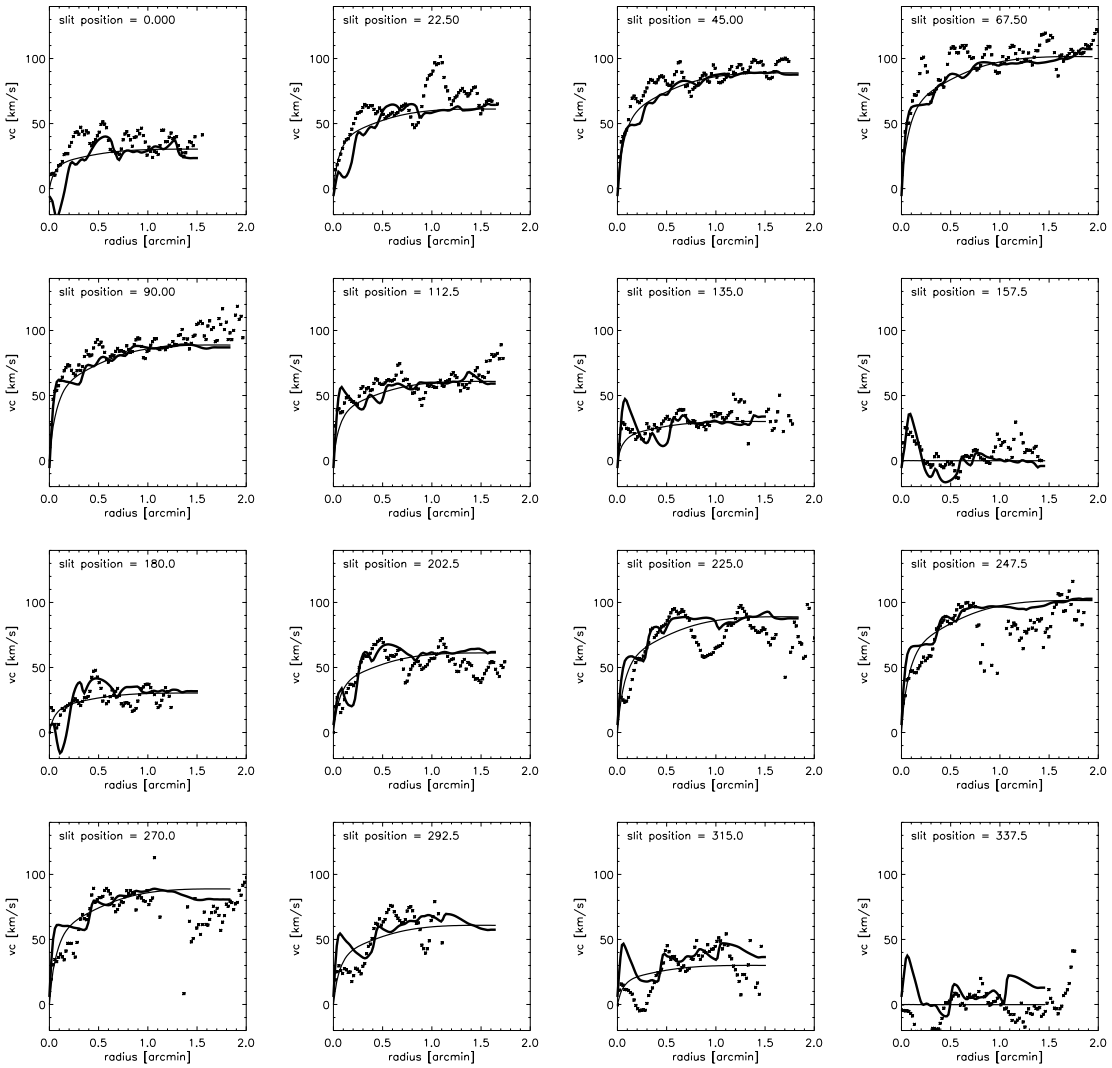

Figure 5.3 Simulation results of the gas velocity field in comparison to the observed rotation curves. Displayed are the measured rotation curves (data points), the axisymmetric model (thin line) and the rotation curves from the hydrodynamical simulations (thick line) for all 16 slit position angles. The parameters for the simulation were: f_d of 60 % and $R_{CR} = 7.58$ kpc. There are no error bars plotted for the data, but the errors can be estimated from the point-to-point scatter of the data.

rising or falling shape of the separate curves is also excellently reproduced by the simulations. The lopsidedness of the galaxy is reflected in the shape of the rotation curves on the receding and approaching side of the disk. At the receding side (67°.5) the rotation curve rises steeply and continues to rise out to 2′, while the approaching side (247°.5) rises less steeply but flattens out or even drops beyond 0′.7. These characteristics are closely reproduced by the models.

A close inspection of the two profiles shows however that the overlap in the match of the simulated velocities with the measurements is not always satisfactory. The agreement of local features in the simulations and the measured data is sometimes very good and

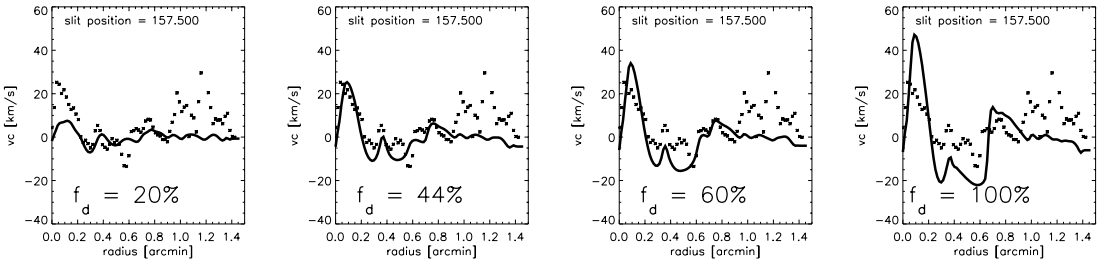

Figure 5.4 Comparison of four simulations for different fractions f_d of the stellar mass component. The simulation was done with a corotation radius of 7.58 kpc and a gas sound speed of $10\,\mathrm{km\,s^{-1}}$. Displayed is one of the 16 slit positions. Clearly the predicted "wiggles" in the rotation curve grow much stronger for higher disk mass fractions.

even occurs in subsequent slit positions. However, there are also many locations, where the match is poor. This is particularly the case in the inner region of the galaxy, where the small bar dominates the kinematics. Both profiles show strong wiggles where the slit crosses the bar, especially close to the minor axis of NGC 4254's velocity field, which is also close to the minor axis of the bar itself. While the simulations show a rather symmetric imprint, the measurements exhibit a signature different from that, leading to a significant mismatch at several slit positions, e.g., 292.°5 and 337.°5. This might be caused by the bar, having a slightly different pattern speed. In the outer parts of the rotation curve we also find several wiggles in the observed data that have no correspondence to the wiggles in the simulations and vice versa. It is important to note that we do not expect to reproduce all the wiggles in the galaxy's rotation curves, since we are only modelling those created by the non-axisymmetric gravitational potential. The wiggles originating for another reason – like expanding SN gas shells – are not considered by the simulations and thus do not show up in the resulting velocity field.

An overall fit quality gets determined by a global χ^2-comparison of the simulated velocity field to the actual observed velocity field along the 16 measured slit positions. The χ^2-fitting excludes the very central region hosting the small bar because the modelling is not intended to fit the central bar, which might have a different pattern speed. The total number of data points included in the χ^2-fitting is 1077.

5.2.2.3. Varying the Stellar to Dark Matter Ratio

As already mentioned in Section 5.1, we performed simulations for five stellar disk and dark halo combinations, as listed in Table 5.1. Since the non-axisymmetric perturbations are induced in the potential by the stellar contribution, we expect the amplitude of the wiggles in the modelled rotation curves to depend significantly on the non-axisymmetric contribution of the stellar potential whereas we expect the radial distribution of the wiggles to be rather independent of the stellar mass fraction. As expected, in the simulations with the lightest disk, the wiggles look like modulations on the axisymmetric rotation curve. In the case of the maximum disk, the rotation curves are strongly non-axisymmetric (see Figure 5.4). This is also very evident from Figure 5.5, which shows the log of the gas density for the sequence of simulations. The density contrast between high and low density regions increases dramatically as the disk fraction increases. To describe this characteristic

more quantitatively, we learn from Figure 5.6 that the amplitude of the deviations from axisymmetry increases linearly with the mass fraction of the stellar disk, which proves the general validity of the concept with which we try to approach this problem.

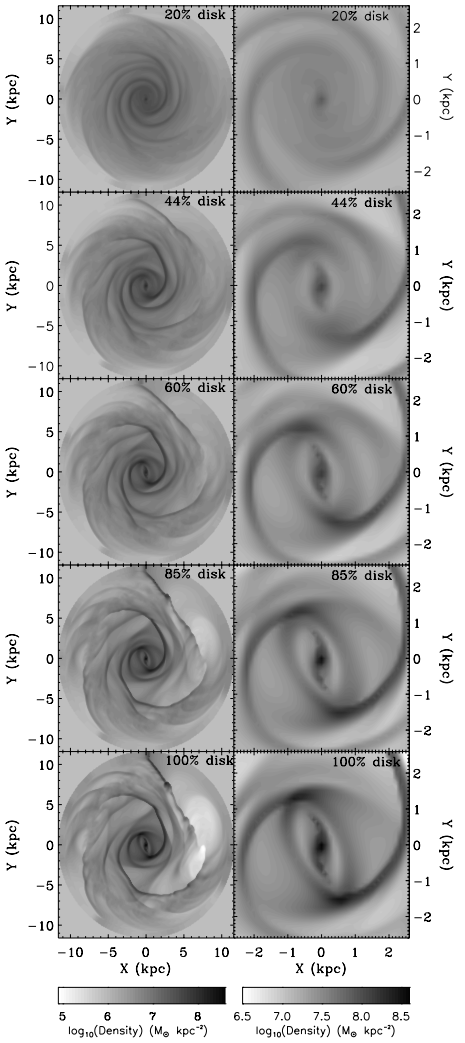

Figure 5.5 Grey scaled maps of the log of the density from simulations on a 201×201 grid, with $c_s = 10\,\mathrm{km\,s^{-1}}$, and $R_{\mathrm{CR}} = 7.58\,\mathrm{kpc}$, and with increasing disk contribution to the total galactic potential. The left column shows the entire simulated region, and the right column shows only the inner $2.6\,\mathrm{kpc}^2$ region.

For the lowest disk fraction case (20 % disk), we find that the spiral arms are most tightly wound and most smooth in their curvature. Increasing the disk fraction to 44 %, also increases the pitch angle of the spiral arms. The overall morphology of the structure appearing over the full disk (11.6^2 kpc) is mostly unchanged once the disk fraction is 44 % and higher. There are slight differences in the details. As seen further from the right column of Figure 5.5, the barred structure in the central region also grows stronger. In fact, the strongest velocity wiggles arising in the modelled velocity fields are the ones connected to the central bar-like feature. However, since here we are not interested in modelling the dynamics of the bar, we exclude this inner part from the analysis. If we do a formal χ^2 comparison of the models with the observed data we find that for most of the sub-maximal disks the fit is considerably better than for heavy stellar disks. By formal, we mean that we use all data points for the χ^2-fit, regardless of whether a certain part matches well or not with two exceptions: we exclude the very central part with the bar and we correct for the outer strong shock appearing in the fast rotating models (see Figure 5.2).

The result from this χ^2-fit is presented in Figure 5.7. In all cases, $\mathrm{f_d} = 100\,\%$ gives the worst fit to the observed rotation curves. For the lower mass disks it is very hard to decide, whether a particular disk mass is preferred. For $R_{\mathrm{CR}} = 6.4\,\mathrm{kpc}$ we find about the same χ^2 for all non-maximal disk models. Since we can not reject data on a physical basis, we can state only a trend at this point. Thus, our conclusion from this part of the analysis is that the disk is most likely less than 85 % maximal.

One very interesting thing to mention is the fact that the formally preferred axisymmetric maximum-disk decomposition (see Table 5.1) turns out to be the most unfavored model, once the simulations were performed. This implies that even if an axisymmetric model

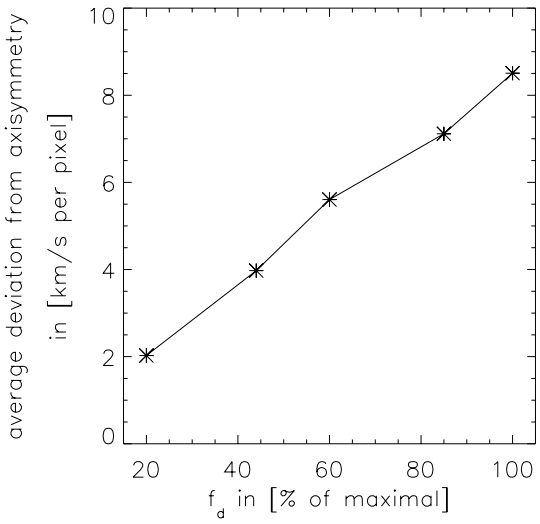

Figure 5.6 Deviation of the simulation from axisymmetry. Displayed is the average deviation of each radial simulation bin from the axisymmetric rotation curve. It rises linearly with the stellar disk mass contribution f_d.

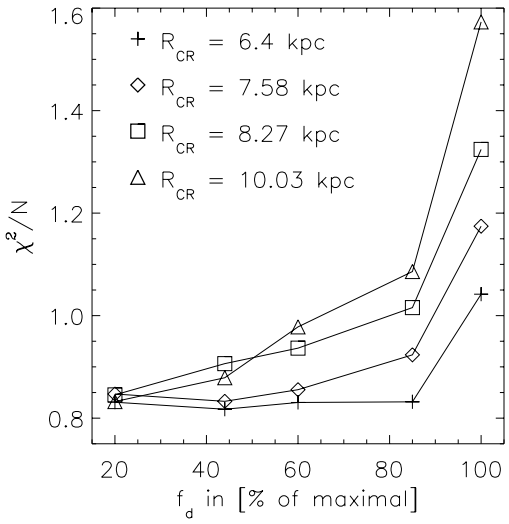

Figure 5.7 Formal χ^2-fit of the gas velocity simulations for different stellar mass contributions f_d, normalized by the χ^2-fit for the axisymmetric model rotation curve. Displayed are cases for four different values of R_{CR}. From the simulations we can rule out the cases with the highest disk mass.

profile provides a better fit to a measured rotation curve, it does not necessarily mean, that this combination provides the best fit when one considers the 2D non-axisymmetric gas evolution.

5.2.2.4. Varying the Gas Temperature

This kind of analysis may be very sensitive to the temperature of the gas which is assumed for the modelling. Higher gas temperature corresponds to a higher cloud velocity dispersion c_s and thus to a reduction in the response of the gas to any feature in the gravitational potential.

Within the Milky Way Galaxy c_s varies from $\approx 6\,\mathrm{km\,s^{-1}}$ in the solar neighborhood to $\approx 25\,\mathrm{km\,s^{-1}}$ in the Galactic center (Englmaier & Gerhard 1999). For simulations of a galactic disk with an isothermal equation of state, the most commonly used values for c_s are $8 - 10\,\mathrm{km\,s^{-1}}$, corresponding to $< 10^4\,\mathrm{K}$ in gas temperature (Englmaier & Gerhard 1999; Weiner et al. 2001a). In these simulations the authors make the statement that within the reasonable limits of $c_s = 5 - 30\,\mathrm{km\,s^{-1}}$ the modelled gas flows across the primary shocks is not considerably affected.

Only when modelling strong bars in galaxies the simulations might be dependent on the choice of the gas sound speed (Englmaier & Gerhard 1997). For the main set of simulations we chose $c_s = 10\,\mathrm{km\,s^{-1}}$, corresponding to a gas temperature of 7250 K. To probe the effect of the gas temperature, we performed simulations for four different gas sound speeds, c_s, of 10, 15, 20 and $30\,\mathrm{km\,s^{-1}}$. The resulting gas density distributions for the high resolution

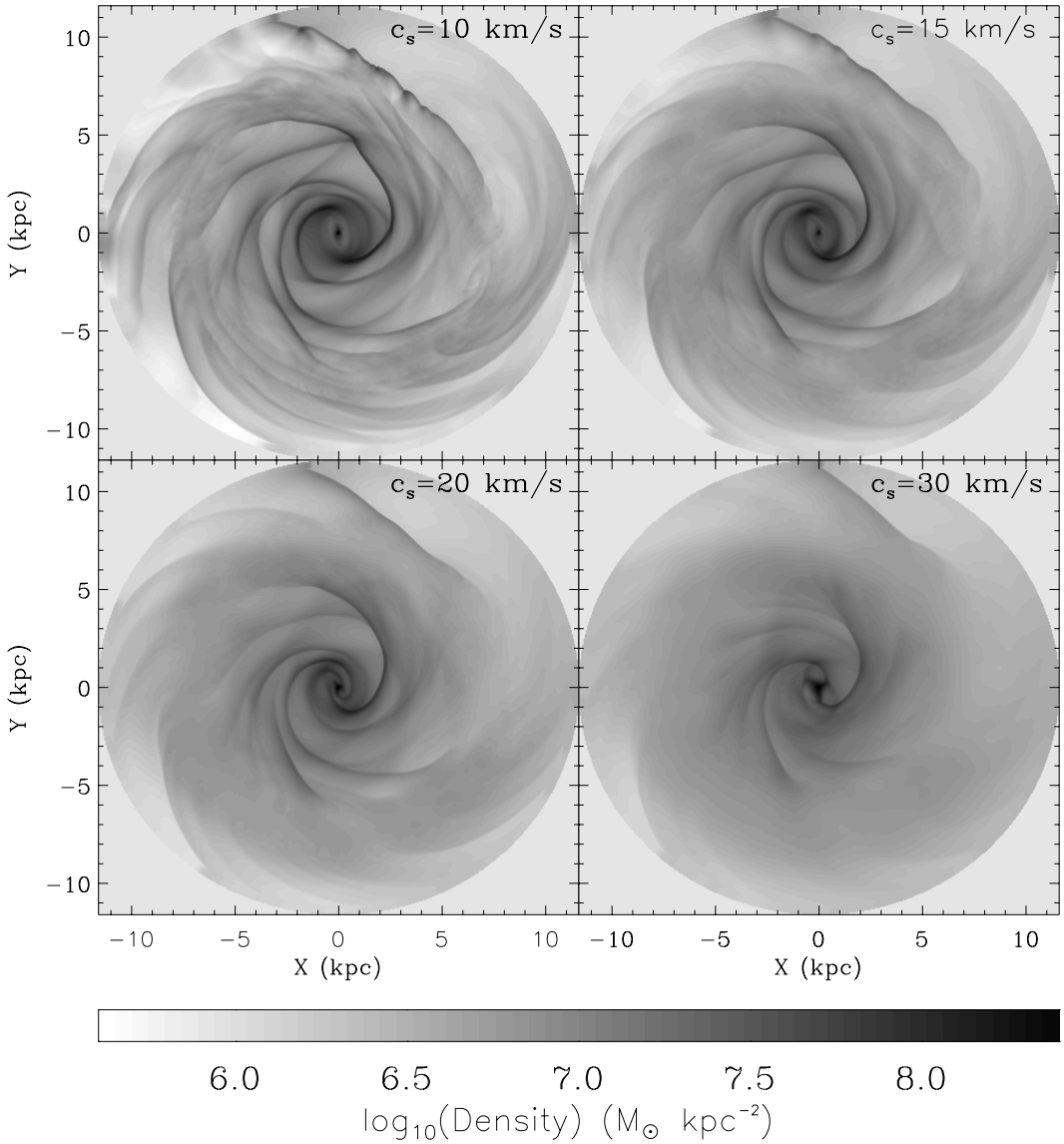

Figure 5.8 Grey scaled maps of the log of the gas density from simulations on a 401 × 401 grid, with 60 % disk fraction, $R_c = 7.58\,\mathrm{kpc}$. Four cases are displayed with increasing sound speed c_s, of 10, 15, 20 and 30 $\mathrm{km\,s^{-1}}$. The entire simulated region is shown.

simulation are displayed in Figure 5.8. Since at higher sound speeds the pressure of the gas becomes more important, the gas responds less strongly to the stellar density wave forcing. This is obvious when one looks at figure 5.8 where in a sequence of simulations differing only in their sound speed we see the non-axisymmetric features in the gas gradually fade with increasing sound speed. By $c_s = 30\,\mathrm{km\,s^{-1}}$ the spiral structure does not extend as far as it does in the colder gas cases even though there are still traces of some of the major spiral features. However, a sound speed of $c_s = 30\,\mathrm{km\,s^{-1}}$ implies a gas temperature of $\approx 65.000\,\mathrm{K}$ for a monatomic ideal gas. This is an extreme test case that does not apply to real galaxies. Furthermore, the strength of the wiggles in the velocity field vary only

very little between $c_s = 10 - 20\,\mathrm{km\,s^{-1}}$. We conclude that varying the value for c_s within reasonable limits, the morphology and velocity fields of the simulations are affected not enough to change the conclusions for this galaxy.

5.2.2.5. Varying the Grid Resolution

The choice of the grid size was mainly motivated by the desire to achieve reasonable computing times, and not to exceed the seeing resolution. To check the grid cell size's effect on the results, for selected cases we also ran simulations on grids with two times higher resolution, 401×401 cells, as well as on grids with two times lower resolution on a 101×101 grid.

Decreasing the grid resolution increases the numerical diffusivity of the code. One reason for this is that on a coarser grid one stores hydrodynamical information in larger cells, meaning that information is averaged over larger areas, thus causing loss of information on finer scales. Figure 5.9 shows how the shock transitions are increasingly blurred on coarser grids. Many features in the density map that appear for the 201×201 and the 401×401 grids are not present at all on the 101×101 map. The morphology of the 201×201 map on the other hand, is very similar to the 401×401 grid.

The final χ^2-fit deviation between simulations with different grid cells ranges at about 6 % and does not change the conclusions of this paper. Accordingly we consider it safe to perform the simulations on the medium resolution grid we used.

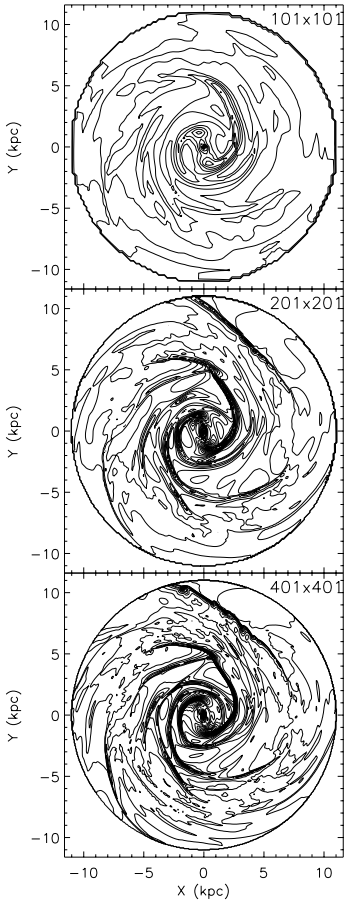

Figure 5.9 Contour maps of the density from simulations with $c_s = 10\,\mathrm{km\,s^{-1}}$, 60 % disk fraction, $R_{\mathrm{CR}} = 7.58\,\mathrm{kpc}$, and with increasing grid resolution. The full potential is turned on in 20 cell sound crossing times for the 101×101 grid, 40 t_s for the 201×201 grid, and 80 t_s for the 401×401 grid. The result is shown after 1590 Myr (t_{dyn}) have elapsed.

5.3. Discussion of possible caveats

A comparison of the observed and simulated kinematics has turned out to be challenging. Although the overall shapes of the different rotation curves were very well reproduced by the simulations, some small scale structure remains unmatched. The formal comparison of the gas velocity field to the observed Hα kinematics favors simulations with small disk mass fractions $\mathrm{f_d}$ (see Figure 5.7) and correspondingly small values for the stellar mass-to-light ratio. With the K-band mass-to-light ratio discussed in Section 4.1.5 our results yield an overall stellar M/L of $\Upsilon_\star \lesssim 0.5$. We can estimate the relative mass fractions from their contributions to the total rotation velocity. At a radius of 2.2 uncorrected K'-band exponential disk scale lengths

($2.2\,R_{\rm exp} \approx 79''$ or 7.7 kpc), the individual rotational support of the stellar and dark halo components for $f_d = 85\,\%$ are $v_\star = 125\,{\rm km\,s^{-1}}$ and $v_{\rm halo} = 86\,{\rm km\,s^{-1}}$. If a total mass is estimated via

$$\mathrm{M}(2.2R_{\rm exp}) = \frac{v^2(2.2R_{\rm exp}) \times 2.2R_{\rm exp}}{G} \tag{5.1}$$

we find that $M_{\rm halo} \approx 0.47\,M_\star$ at $R = 2.2\,R_{\rm exp}$, or accordingly $\gtrsim 1/3$ of the total mass inside $R_{\rm exp}$ is dark. Since our confidence limits are not very tight, we cannot use them to test other authors' findings in detail. Projects yielding results in favor of a sub-maximal stellar disk usually find a disk mass fraction less than our upper limit estimate. Bottema (1997) as well as Courteau & Rix (1999) conclude that the contribution of the stellar disk to the total rotation is $v_\star \sim 0.6\,v_{\rm tot}$ which translates to $M_{\rm halo} \sim 0.6\,M_{\rm tot}$. At the current state of the project we cannot exclude or confirm these findings. This issue is going to be discussed more thoroughly as soon as we have a few more examples analyzed.

In the following Sections we will discuss the details that could cause deviations from a perfect match between the simulations and the measurements.

5.3.1. Is the Concept Reasonable?

If the self-gravity of the stellar mass in the disks of spiral galaxies plays an important role then undoubtedly the potential becomes non-axisymmetric. The trajectory of any kinematic tracer in the galaxy, such as the gas, should be affected by these potential modulations. But is the H II component of the gas the best choice for tracing the galaxy's potential? Analytic calculations of gas shocks in the gravitational potential of a spiral galaxy (Roberts 1969) tell us that we should expect velocity wiggles with an amplitude of 10 to $30\,{\rm km\,s^{-1}}$ while crossing massive spiral arms. However, kinematic feedback to the gas from regions of massive star formation, from expanding gas shells produced by supernova explosions and from other sources of turbulence, introduces small-scale random noise in the velocity fields. These fluctuations typically lie in the range of 10 to $15\,{\rm km\,s^{-1}}$ (Beauvais & Bothun 1999) and seem even higher in the case of NGC 4254. The kinematic small-scale noise could be increased if the dynamics of the brightest H II regions is kinematically decoupled from the global ionized gas distribution. To check this we over-plotted the Hα-intensity on the rotation curves to see if the star formation regions coincide with the strongest wiggles in the rotation curves. There is, however, no discernible relation between the amplitude of a wiggle and the intensity of the H II region, indicating that the deviations are not confined to compact H II regions (see Figure 5.10).

As an alternative to observing the ionized phase of the hydrogen gas, one could consider using H I radio observations. However, available H I data are limited by the larger size of the radio beam that smears out kinematic small-scale structures in the gas. In principle, stellar absorption spectra could also provide relevant kinematic information, but this approach has two disadvantages compared to an approach using gas kinematics. First, the acquisition of stellar absorption spectra with sufficient S/N would take a prohibitively large amount of telescope time. Second, stellar kinematics cannot be uniquely mapped to a given potential; there are different sets of orbits resulting in the same observed surface mass distribution and kinematics. Thus, despite its apparent shortcomings H II measurements seem to be the most promising method with which to approach the problem.

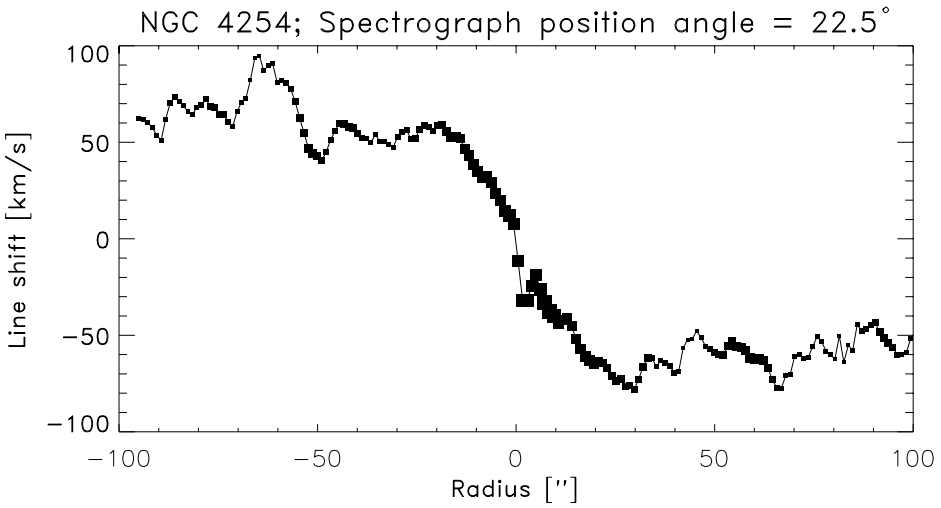

Figure 5.10 NGC 4254 rotation curve for the slit position angle of 22°.5. The plot symbol sizes reflect the intensity of the Hα-line at each radius. It is apparent that stong wiggles are not directly related to single H II regions.

Could the discrepancies between modelled and observed kinematics be related to taking the NIR K-band image of a galaxy as the basis to calculate its stellar potential? As already discussed in Section 4.1.2 there are several factors which throw into question whether the K-band image is a good constant mass-to-light ratio map of the stellar mass distribution despite the color correction we applied. However, the two major factors – population effects and dust extinction – tend to affect the arm-interarm contrast, rather than the location of the K-light spiral arms. Dust lanes lie preferentially inside the $m = 2$ component of a galaxy's spiral (Grosbøl, Block & Patsis 2000) absorbing interarm light, while the red super giants may actually have their highest density in the spiral arms directly, where they emerged from the fastest evolving OB stars. This effect should become apparent in the simulations as slightly wrong amplitudes of the gas wiggles, leaving their radial position mostly unchanged. So even if the K-band images might actually include unaccounted mass-to-light ratio variations, they most probably introduce only small errors, which should not result in an overall mismatch of the models with the data. The color-corrected K-band images should therefore reflect the stellar mass accurately enough for our analysis. Certainly, there appears to be no better practical mass estimate that we could use for our analysis.

5.3.2. Are there Systematic Errors in the Modelling?

The most critical part of this study are the several modelling steps required to predict the gas velocity field for the comparison with the data. We apply a spatial filter to the K-band image before calculating the disk potential to reduce the significance of the clumpy H II regions (as described in Section 4.1.4). The residual map of the discarded component shows all the bright H II regions in the disk, giving us confidence that we have excluded much of the structures that reflect small-scale M/L variations. This correction removes

roughly 3.5 % of the total K-band light and does not depend strongly on the number of Fourier components used for the fit. For two extreme decompositions employing 6 and 16 Fourier components, the mean resulting relative discrepancy in the derived potentials is only $\approx 10^{-6}$. One remaining concern in calculating the potential might be that the mass density map cuts at the border of the image. However, the galaxy completely fits in the frame, fading into noise before the image border. Moreover, we do not perform the simulations for the complete galaxy, but only for the inner 11.6 kpc in radius. So the edge cutoff effect is very small and affects the part of the potential we are looking at even less.

For the dark matter component we chose an isothermal halo with a core because of its flexibility in fitting rotation curves. The functional form of the dark halo profile has only a second order effect on the results of the simulations compared to the variations due to its two basic parameters R_c and v_∞. We decided not to distinguish between different dark halo profiles for the present analysis.

The most complex step surely is the hydrodynamical simulation of the gas flow in the galaxy's potential. Beyond the tests of the code discussed in Section 4.2.2, it is the excellent morphological agreement between the simulated gas density profiles and the observed spiral arms that gives credence to the results of the code. However, for NGC 4254 and other galaxies whose inclination with respect to the line-of-sight is relatively low, shortcomings in the kinematics comparison may arise from the two dimensional nature of the simulations. While in such cases the observations are rather sensitve to gas motions perpendicular to the plane of the disk, those velocity components cannot be modelled. This is certainly a systematic error that must be kept in mind.

In a real galaxy the assumption of a global constant pattern rotation speed may not be fulfilled. In particular, we should expect the central bar to have a different pattern speed. Also, the pattern might be winding slowly, rather than being fixed in a corotating frame. Furthermore, the gas may not have a uniform temperature. If these simplifications were relaxed, the location of the spiral arms in the hydro-simulations would change, and eventually lead to a different overall fit quality. Lacking any solid basis to constrain these parameters, we are unable to implement these effects into the modelling procedure. Finally, the code does not include gas self-gravity. The effect of gas self-gravity is difficult to quantify without actually performing simulations, but from the literature we know that it tends to amplify the gas response. Gas self-gravity also suppresses the tendency of the gas to shock (Lubow, Balbus & Cowie 1986). Since we are interested in the strength of the gas response to the gravitational potential and we already find that for high disk M/L the response is too strong, we assume that our upper limit holds also if gas self-gravity was included. Given the good morphological match, we may confidently assume that all our approximations are not far off.

This leaves non-gravitationally induced gas motions and the fact that any gas motion perpendicular to the plane of the disk cannot be reproduced by two dimensional gas simulations as the main complications in the comparison of the models to the observed kinematics. Eliminating mismatching wiggles from the rotation curve is not possible since we have no means to reliably identify the ones that are non-gravitationally induced. Any method we apply to excluding parts of the data will be affected by some kind of bias[2].

[2]The method that was described in Section 4.3.2.1 was developed after this paper have been published.

5.3.3. Is the Galaxy Suited for this Analysis?

Finally we must consider the possibility that the galaxy we picked for our analysis might not be as suited as it appeared to be. NGC 4254 is not the prototype of a classical grand design spiral galaxy in optical wavelengths. However, as it can be seen in the central frame of Figure 5.2, the galaxy exhibits in the M/L corrected K'-band image mainly an $m = 2$ spiral pattern with a strong symmetric part, that ends at ≈ 5.5 kpc and fainter outer extensions. With its large angular size and moderate inclination, NGC 4254 seems to be one of the most promising candidates for this kind of study in our sample. However, as discussed in the first paragraph of this Chapter, there are indications that this galaxy might not be as isolated and undisturbed as one might expect. In fact, the morphology itself implies some perturbative event in its recent evolution history: NGC 4254 shows a clear $m = 1$ mode and a lopsided disk. In this respect it was argued earlier that in-falling H I gas clumps, which are visible in radio data and do not emit in Hα, might be responsible for triggering deviations from pure grand design structure (Phookun et al. 1993). So have we reason to believe that NGC 4254 is far from equilibrium? This is hard to tell, because on the other hand we find plenty of arguments that a stable propagating density wave in NGC 4254 is responsible for its morphology. This galaxy shows many similarities to the spiral galaxy NGC 5247 whose morphological and dynamical properties were discussed by Patsis, Grosbøl & Hiotelis (1997), based on SPH simulations. We note that in our best model, the strong bisymmetric part of the K' spiral, ends well inside the corotation radius, although fainter extensions reach out to it. This picture is in agreement with the 4/1 SPH models of Patsis et al. (1997). Assuming corotation close to the characteristic bifurcation of the arms at ≈ 5 kpc on the other hand, we do not obtain satisfactory results (upper left frame in Figure 5.2). Based on this is seems appropriate to conclude that NGC 4254 is at least close to an equilibrium state and it should be suited for a case study.

5.4. Conclusions

We performed hydrodynamical simulations to predict the gas velocity field in a variety of potentials for the spiral galaxy NGC 4254 and compared them to observations. These potentials consisted of different combinations of luminous (non-axisymmetric spiral) and dark matter (axisymmetric) components. The resulting gas spiral morphology reflects very accurately the morphology of the galaxy and allows us to specify the corotation radius or the pattern speed of the spiral structure quite precisely. It is noteworthy that within the error range given, the best matching pattern speed does not depend on the mass fraction of the stellar disk relative to the dark halo. For NGC 4254 we find that the corotation lies at 7.5 ± 1.1 kpc, or at about 2.1 exponential K'-band disk scale lengths. From the kinematics of the gas simulations we could rule out a maximal disk solution for NGC 4254. Within the half-light radius the dark matter halo still has a non-negligible influence on the dynamics of NGC 4254: specifically, our fraction $f_d \lesssim 0.85$ implies that $\gtrsim 1/3$ of the total mass within 2.2 K-band disk scale lengths is dark. However, the comparison of the simulated gas velocity field to the observed rotation curves turned out to be a delicate matter. The observed rotation curves show a significant number of bumps and wiggles, presumably resulting from non-gravitational gas effects, that complicate the identification of wiggles induced by the massive spiral arms. Therefore, beyond concluding that the disk

is less than 85 % of maximal, we were unable to specify a particular value for the disk mass or to test the results from Bottema (1997) or Courteau & Rix (1999). But already with this statement we differ from the conclusions of Debattista & Sellwood (2000) and Weiner et al. (2001b), who argue that their conclusions for maximal disks of barred galaxies also hold for non-barred spirals. Since we only analyzed one galaxy so far it is inappropriate to state here that the centers of unbarred spirals, what we still consider NGC 4254 to be despite its small bar-like structure in the very center, are generally governed by dark matter.

In the next Chapter the results from more galaxies are presented. This will create a broader basis to decide, whether single galaxies differ very much in their dark matter content, or if the bulk of the spirals show similar characteristics.

CHAPTER VI
Analysis of more galaxies

The detailed analysis of NGC 4254 has proven the overall feasibility of the approach. It showed that the gas contribution in galaxies can be modelled to a high enough precision to enable the comparison to real measured data and to draw valuable conclusions. However, the agreement between the simulated and the measured gas velocity field was only partly satisfactory on a wiggle-to-wiggle basis. Further, the analysis of a single galaxy could not provide any insight, whether the result is characteristic for luminous, non-barred spirals as a whole. The extension of the analysis on a sample of galaxies might promise a better comprehension of the relevant gas processes in spiral galaxies, leading to a more reliable and representative estimate of the dark matter content and distribution.

The analysis was applied to the rest of the galaxies from the sample, for which sufficient kinematic data could be taken and optical photometry was available, hence the color correction could be performed. This applied to four more galaxies: NGC 3810, NGC 3893, NGC 5676 and NGC 6643 as listed in Tables 4.1 and 4.2. NGC 5364 was not included, since only 5 slit positions could be taken, providing only a relatively poor guess of the two-dimensional velocity field.

The modelling of the gravitational potentials followed the procedure that was outlined in Chapter 4. Only where a differing, individual treatment was needed for single galaxies modelling issues will be described further in this Chapter. For all galaxies a large set of simulations was performed for a wide range of the spiral pattern speeds. Furthermore, following the example of NGC 4254, simulations were carried out for five different mass fractions of the stellar disk, namely $f_d = 20\,\%$, $45\,\%$, $60\,\%$, $85\,\%$ and a maximal disk. Since it became evident from the analysis of NGC 4254 that the choice of the gas sound speed affects the conclusions only at unphysically high values for c_s, all further simulations were performed assuming a sound speed $c_s = 10\,\mathrm{km\,s^{-1}}$. To account for the uniqueness of each galaxy, this Chapter is divided into Sections describing the simulations and results for each galaxy separately.

6.1. NGC 3810

NGC 3810 is a relatively bright Sc galaxy located in the Leo group of galaxies. It exhibits a fairly strong two-arm morphology with an arm to inter-arm contrast of $0.45 - 0.75$ mag in K'. At radii larger than $\approx 45''$ the two arm structure gradually fades into a more fragmented or flocculent structure (see Figure 6.1). The flocculence of NGC 3810 is even

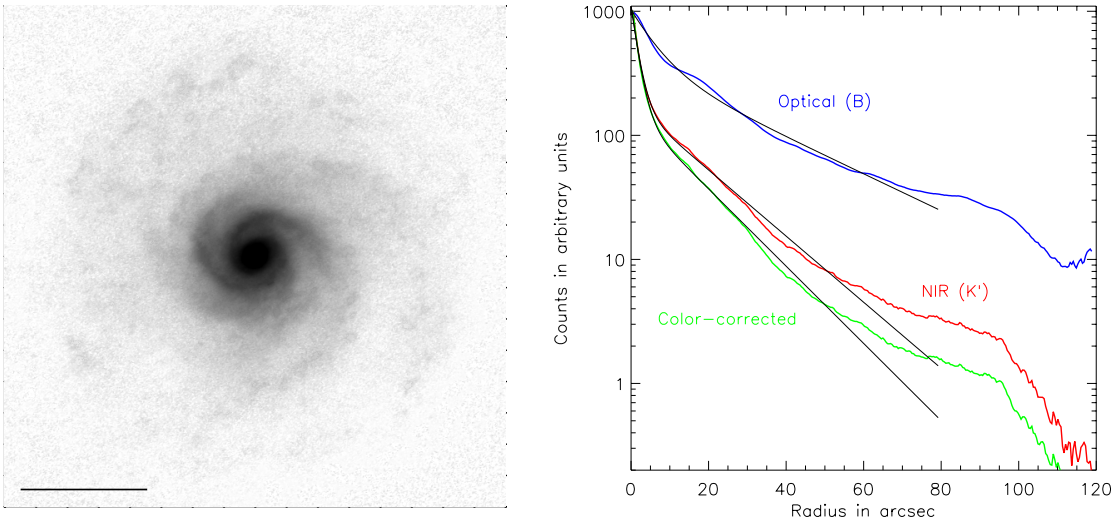

Figure 6.1 NGC 3810. At left the deprojected, color-corrected, H II-region cleaned image of NGC 3810 is shown. It was used as an input to calculate the gravitational potential of the stellar disk contribution to the total gravitational potential. The scaling bar is 1′. At right, the effect of the color correction on the disk scale length of NGC 3810 is shown. Note the deviation of the azimuthally averaged radial light profiles from a simple exponential. The fitted part (black lines) of the color corrected profile steepens by 14.7 %, as compared to the K-band.

more apparent in the visible, and is seen best in the 'Color Atlas of Galaxies' (Wray 1988). In a study of the NIR appearance of flocculent galaxies Elmegreen et al. (1999) argue that the flocculent optical appearance might be caused by higher than usual dust extinction between the arm pieces. Indeed, dust might play a role, but most probably not the most important, since 10 out of their sample of 14 galaxies kept their flocculent appearance also in the NIR. Elmegreen et al. (1999) further note that the arms of NGC 3810 are reasonably well matched by logarithmic spirals, however, they find a break in mid-disk, where emerging arms have a higher pitch angle than the main arms, perhaps evidence for a spur (Elmegreen 1980). This flocculent part of the disk has a rather constant surface brightness of ≈ 21 mag per square arcsecond. Beyond about $100''$ the surface brightness drops steeply until reaching the exponential decline of the inner disk at about a radius of $115''$ (see Figure 6.1). A distance of 13.5 Mpc was assumed towards NGC 3810, taken as an average literature value. At this distance the galaxy's a K-band exponential scale length of $16\farcs3$ corresponds to 1.07 kpc; although the profile is not entirely exponential. This is the shortest scale length of all 5 galaxies in the sample. NGC 3810 has a total blue magnitude of $B_T = 11.3$ mag and the bright part of the disk measures 3.4×2.4 arcminutes on the sky. The major axis position angle, PA $= 22\fdg0$, and the inclination of the disk, $i = 46\fdg0$, were determined from the measured kinematics. The inclination corrected rotation curve rises gently and flattens at a radius of about $40''$ to a constant value of 150 km s^{-1}. There is no evidence for a bar at the center.

The color correction leaves the overall morphology of NGC 3810 basically unchanged. There seem no large arm-to-arm population differences that cause the spiral structure to change drastically. However, the color correction causes the radial profile to become

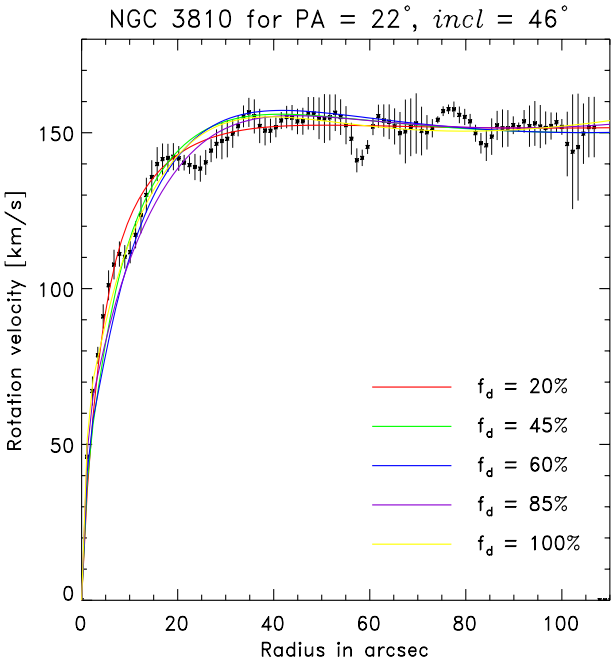

Halo parameters

f_d [%]	R_{core} [kpc]	v_∞ [km s^{-1}]
20	0.23	168
45	0.39	150
60	0.62	139
85	1.74	141
100	3.06	149

Figure 6.2 Rotation curve comparison for NGC 3810. The five axisymmetric model potentials for different fractions of the stellar disk potential yield rotation curves that are very similar and match well with the observed kinematics.

steeper by 14.7 %, the largest change from a color correction in any of the sample galaxies (see Figure 6.1 and Table 4.2).

Five models of the total gravitational potential were prepared for NGC 3810, varying the stellar disk mass fraction f_d. Figure 6.2 shows the rotation curves from the five axisymmetric model potentials, as compared to the observed kinematics. All model rotation curves can explain the galaxy's observed rotation curve similarly well. The Table accompanying Figure 6.2 lists the core radii and asymptotic rotation velocities of the five pseudo-isothermal halo models used to assemble the final galaxy potentials.

6.1.1. Performing the hydrodynamical gas simulations

To model the two-dimensional gas surface densities and velocity fields for NGC 3810 a set of simulations was carried out on a 201×201 Cartesian grid. The grid cells were chosen to give a resolution of 77.76 pc per cell for the assumed distance towards the galaxy of 13.5 Mpc. As for NGC 4254 the gas is taken to be isothermal throughout the simulation, implying that the gas cools instantaneously to its initial temperature during each updating timestep. Following the initialization of the gas in centrifugal balance in an axisymmetric potential, the final non-axisymmetric potential is gradually turned on and the simulation is completing the initialization phase by the time 40 sound crossing times of the code have passed. For NGC 3810, assuming a gas sound speed $c_s = 10\,\mathrm{km\,s^{-1}}$, that occurs after about 436 Myrs.

To find the spiral pattern speed Ω_p, or equivalently the corotation radius R_{CR}, the following cases were modelled: $R_{CR} = 3.15$, 3.43, 5.04, 6.14, 6.45, 7.00, 7.79, 10.0 kpc and no pattern rotation. For the different stellar disk mass fractions f_d not all of the above listed corotation radii were simulated. Table 6.1 provides an overview of the runs which were performed for NGC 3810.

Table 6.1 Hydrodynamic simulations for NGC 3810. Given is the duration of the individual simulation in units of 10^6 years.

f_d	corotation radius R_{CR} [kpc]								
[%]	3.15	3.43	5.04	6.14	6.45	7.00	7.79	10.0	∞
20	1302	1302	1302	1302	1302	1302	1302	1302	—
45	1302	1302	882	1222	1282	1042	—	—	—
60	602	862	642	722	802	942	1002	1302	1302
85	702	421*	562	702	782	582	—	—	—
100	441	441	522	742	762	502	—	—	—

* Note: This run terminated before ending the initialization phase of the simulation, which occurs at 436 Myrs.

6.1.2. Premature termination of simulations

As apparent from Table 6.1 some of the simulations, especially the ones for a fast pattern rotation (small R_{CR}) and high disk mass fractions, terminated before the simulation reached the anticipated run time of 1302 Myrs. For one run, the simulation terminated even before the full non-axisymmetric galaxy potential was turned on. In such a case, problems occur at certain grid cells during the simulation. Usually the gas density in the particular grid cell becomes very low, implying conditions that are at the limit of the code's range of application. For treating the gas flows in disk galaxies on a Cartesian grid, high order interpolations have to be applied. In extreme situations, they cause the code to produce unphysical negative gas density values for the next updating time step. Repeated occurrence of this problem eventually causes the simulation to stop. The occurrence of these negative densities is aggravated by various processes. First, in the central regions the gas density contrast can get very high, triggered by the non-axisymmetric nature of the potential. Second, these conditions become more severe, if the potential has a higher degree of non-axisymmetry, i.e. for the $f_d = 85$ and 100 % cases. Third, if the pattern rotation is high, shocks tend to become stronger since the gas is exposed to faster potential changes. Finally, for massive galaxies with high rotation velocities in the disk the velocity gradient in the inner parts of the disk is very large. Eventually, one of these processes, or a combination of them, might produce such extremely rarefied gas conditions in a grid cell, terminating the simulation prematurely.

If the parameters for a simulation are close to the ones yielding the best representation of the galaxy properties the χ^2/N comparison between the simulated gas kinematics and the observations retains a very constant value, once the simulation proceeded past its initialization phase. This is demonstrated in Figure 6.3. The χ^2/N value fluctuates at maximum on a few-percent level. Thus, the evaluation of any simulation timestep past the initialization phase can be regarded as being equivalent. For the data analysis, a mean is calculated. The median of the χ^2 exhibits a very similar behavior. However, if the parameters for a simulation are far from representing a good description of the modelled galaxy, the simulation might not reach a stationary solution and the χ^2/N value increases without limits. Often in these cases the simulation terminates prematurely. An example is displayed in Figure 6.4.

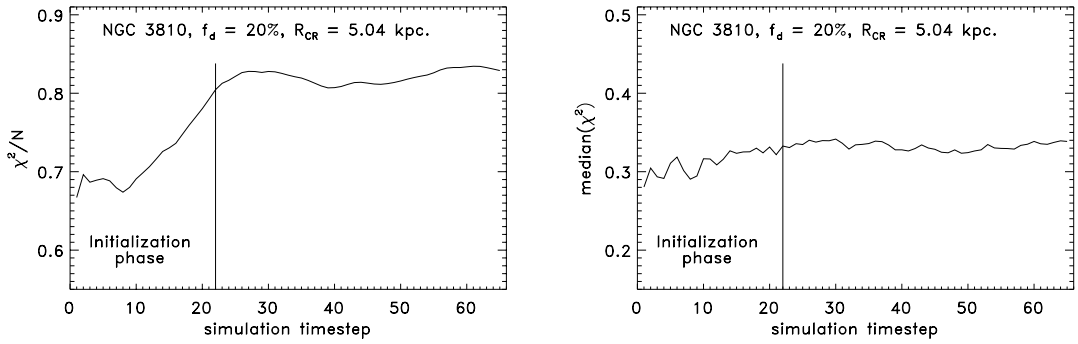

Figure 6.3 The overall χ^2/N-value and the median(χ^2) of the model-to-observed kinematics comparison, plotted for a successful simulation of NGC 3810. The full non-axisymmetric potential is turned on at timestep 22. χ^2/N is quite stable after the initialization phase as well as the median(χ^2).

Any simulation that terminated before the full non-axisymmetric potential was fully turned on will give χ^2-values that are slightly off. In general these simulations tend to give lower χ^2s than what would be expected if the simulation had continued to the end. In the further analysis, some results of prematurely terminated simulations are included into the discussion, but they are always marked as being less reliable.

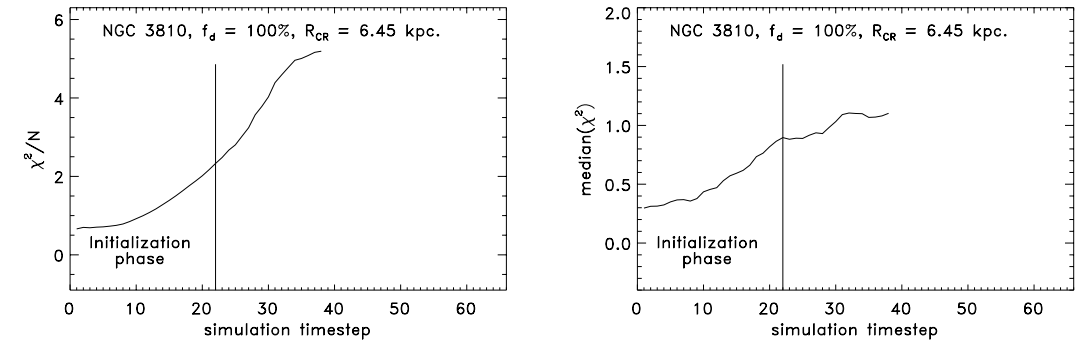

Figure 6.4 The overall χ^2/N-value and the median(χ^2) of the model-to-observed kinematics comparison, plotted for a terminated simulation of NGC 3810. The full non-axisymmetric potential is turned on at timestep 22. χ^2/N does not reach a stationary value after the simulation proceeded past its initialization phase. The median(χ^2) follows the same trend, although less vigorous. Note the different scales on the χ^2-axis.

6.1.3. Results from the hydrodynamical gas simulations

6.1.3.1. The gas density

NGC 3810 has a disk with a two-fold morphology. In fact, only the inner disk reveals a fairly strong spiral structure. In the outer disk no well defined high contrast arms can be found. In the simulation for the best matching corotation radius (Figure 6.5), primarily the inner spiral determines the degree of how well observations and simulations agree. The simulated gas density exhibits a fairly regular 3-arm morphology, that splits into several pieces before it almost dissolves at the corotation radius. The simulations trace quite well

the underlying spiral structure, putting the strongest gas shocks to where the spiral arms are best defined and most of the star forming H II-regions are located. Beyond corotation the simulation develops long and continuous shocks that form in response of the weak outer spiral pattern. These shocks come to lie close to where the arms are. Thus, the overall agreement between the simulated gas density morphology and the galaxy's spiral pattern is good.

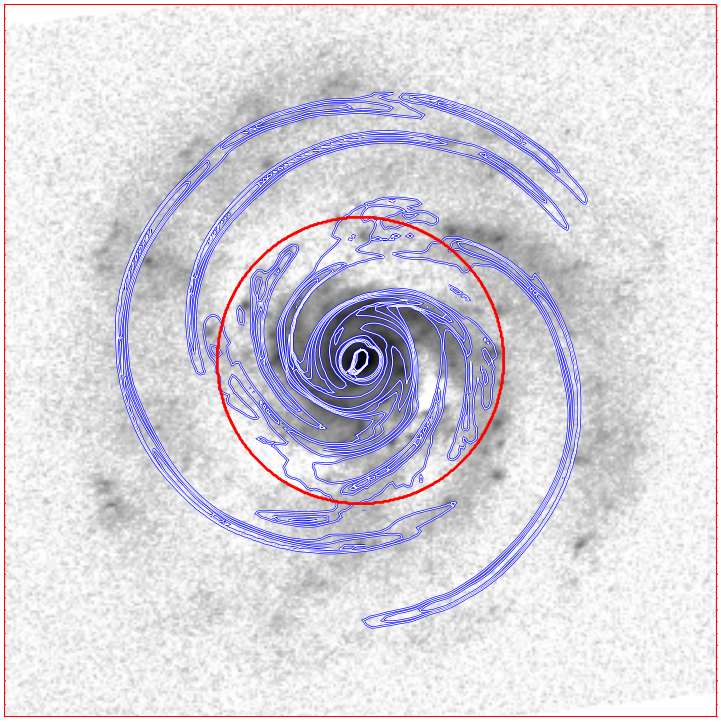

Figure 6.5 Simulation results of the gas density distribution overlaid in contours onto the deprojected K'-band image of NGC 3810. From the image an axisymmetric radial brightness profile has been subtracted to enhance the contrast of the spiral arms. The Figure shows the contours for the simulation with $f_d = 60\,\%$ and a corotation radius (red circle) of 3.15 kpc. The full set of simulation results is shown in Appendix A.

NGC 3810 appears to be a galaxy with a fast pattern rotation. The simulations resulting in a gas density pattern that resembles the observed spiral morphology the most were the ones with the smallest corotation radius that could be performed for this galaxy. This corotation radius $R_{CR} = 3.15$ kpc, measuring about 3 exponential disk scale lengths in K', corresponds to a spiral pattern rotation of $\Omega_p \approx 48\,\mathrm{km\,s^{-1}kpc^{-1}}$. This puts the corotation radius in the radial range that separates the inner disk with the stronger spiral and the outer disk with the flocculent morphology (see Figure 6.5). According to the discussion from Section 2.3, it is indeed found that at the corotation the number of star forming regions is reduced. Solely in the the inner arm emerging to the west shows few H II-regions at the corotation radius. This fact might be regarded as some evidence that even though, due to numerical limitations, no faster pattern speeds could be probed the location of the corotation resonance is probably well determined.

Certainly something is happening to the spiral pattern between the inner and the outer disk that makes it lose strength. However, since the model-to-observations comparison cannot be very detailed in the outer disk, there is no solution to the question if a single pattern rotation speed is a good approximation for NGC 3810.

6.1.3.2. The gas velocity field

The observed gas velocity field from NGC 3810 is governed by a large amount of small scale fluctuations and jumps. There are almost no measurements that exhibit a longer radial range of smooth, unshocked gas kinematics. Certainly, most of these small scale wiggles are not induced by gravity.

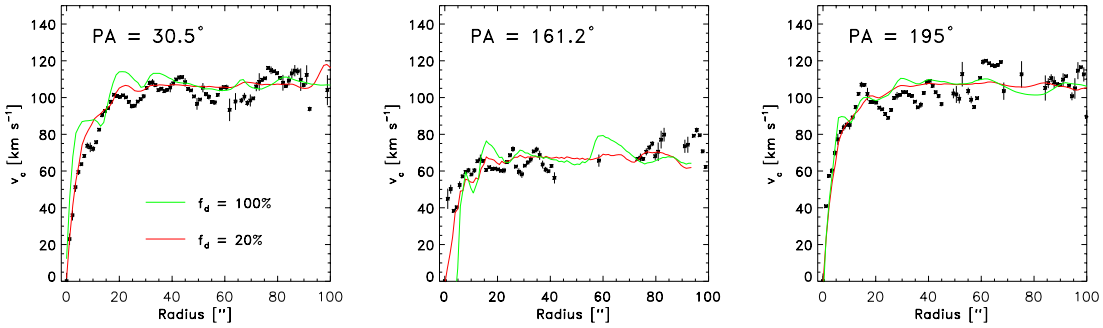

Figure 6.6 Example of the comparison of the simulation results to the observed kinematics of NGC 3810. The "maximal disk" and "minimal disk" velocity field are shown for three position angles. Presented are results from simulations assuming a fast pattern rotation $\Omega_{\rm p} \approx 48\,{\rm km\,s^{-1}\,kpc^{-1}}$ ($R_{\rm CR} = 3.15\,{\rm kpc}$). The full comparison is shown in Appendix A.

In Figure 6.6 the comparison of the simulations with the observed data is presented for a sample of three position angles of NGC 3810, illustrating the overall fit quality. Shown are the simulated curves for the maximal disk case ($f_d = 100\,\%$ in green) and the one for the setup using the most massive halo ($f_d = 20\,\%$ in red). An overview on all position angles is provided in the Appendix A. Like for NGC 4254, the global shape of the rotation curve gets very well approximated by the models. This applies to all five simulated disk-halo combinations, including the two shown extreme cases. On small scales the situation is clearly less satisfying. Although a few wiggles overlap fairly well, most of the structures cannot be reproduced by the simulated gas velocity fields. Especially in the outer parts of the disk, the agreement between simulated and observed wiggles is poor.

As for NGC 4254, the global least squares analysis loses much of its significance in such a case. By using the χ^2-analysis the least deviant model velocity field can be identified. This could in principle allow two conclusions: either the best matching case or the least disagreeing simulation result. If the majority of the kinematic structures do not match or coincide with the observations, the latter of the above will most likely be the preferred scenario from the χ^2-analysis. The left partition of Figure 6.7 gives an overview on the results from the global χ^2-analysis. Larger boxes indicate a smaller χ^2/N-value and thus a smaller deviation from the observed data. It must be noted, that – like for NGC 4254 –

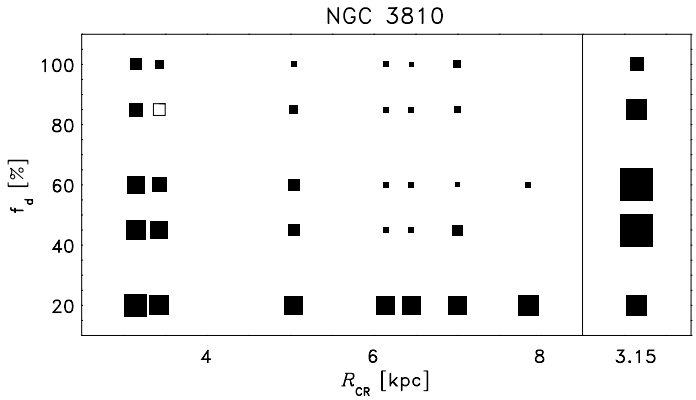

Figure 6.7 Graphical presentation of the global χ^2-analysis of all the velocity simulations for NGC 3810 (left partition). At right, the χ^2-analysis of the reduced data set is shown for a corotation radius $R_{\rm CR} = 3.15\,$kpc. Large boxes indicate better agreement between the simulated velocity field and the observed kinematics. The open box represents the simulation that terminated before passing the initialization phase. The actual χ^2-values can be found in Appendix A.

an additional systematic error of $9.5\,\mathrm{km\,s^{-1}}$ has been added to each observed data point (see Section 4.3.2).

The global χ^2-distribution across the parameter space for NGC 3810 appears very smooth. While for large disk mass fractions and large corotation radii the agreement between the simulations and the data is worst, it almost continuously turns better for lighter disks and smaller corotation radii. The trend in corotation reflects a real effect, since for the fast pattern rotation the morphology match of the gas density turned out best. However, the trend for the lighter disks to provide a better fit to the observed rotation curves is likely to be a systematic effect from the global χ^2-analysis. As discussed above, on small scales the simulations fail to reproduce the structure of the observed rotation curves in a sufficient way. In light of this, the models that exhibit the least non-axisymmetric structures from the two-dimensional simulations will be the ones that deviate the least from the observed rotation curves, to which the axisymmetric gravitational potential of the galaxy was tuned to fit.

However, following the method explained in Section 4.3.2.1, it can be seen that if considering only the parts of the observed velocity field where the gas dynamics appear to be dominated by gravitational forces, a medium disk solution is preferred (see the right partition of Figure 6.7). In this case the model with the lightest stellar disk turns out to give a less good agreement to the data as compared to the $\mathrm{f_d} = 45$ and 60 % models. During the rejection process of non-gravitationally induced wiggles, 51 % of the data points were discarded from the comparison (see Appendix A for details). This implies that about half of the gas dynamic small scale structures could not be related to gravitational influence of the stellar spiral. Thus, NGC 3810 does certainly not qualify as an excellent laboratory for this study. Nevertheless, the results are in favor of a dynamically fairly important stellar disk, indicating that the mass comprised in stars roughly balances the mass of the dark halo inside the optical radius of the disk.

6.2. NGC 3893

NGC 3893 is a grand design Sc galaxy located in the Ursa Major Cluster of galaxies. The galaxy is interacting with the Magellanic dwarf type galaxy NGC 3896, located at a projected distance of 3.′9 to the south-east. Radio data reveal a H I-bridge between NGC 3893 and NGC 3896 (Verheijen & Sancisi 2001). The most striking optical evidence for the interaction is a very clear two-arm morphology at all radii and the slightly disturbed symmetry, seen in the north-eastern arm of NGC 3893. The strong $m = 2$ spiral has an arm to inter-arm contrast of $0.4 - 0.5$ mag in K'. The interacting arm shows a kink and a change in the pitch angle at a position angle of 150° and another one at a position angle of 95°. Furthermore the interacting arm exhibits a over-abundance of H II-regions relative to the rest of the galaxy, indicating enhanced star formation. Despite of its disturbed morphology, the radial brightness profile is fairly well described by a double exponential model profile. Only beyond a radius of $\approx 100''$ the disk appears slightly brighter. The galaxy's K-band exponential disk scale length of 21.″9 corresponds to 1.8 kpc, if a distance of 17 Mpc is assumed towards NGC 3893, taken as an average literature value. See also Figure 6.8 for an illustration of the radial K' profile.

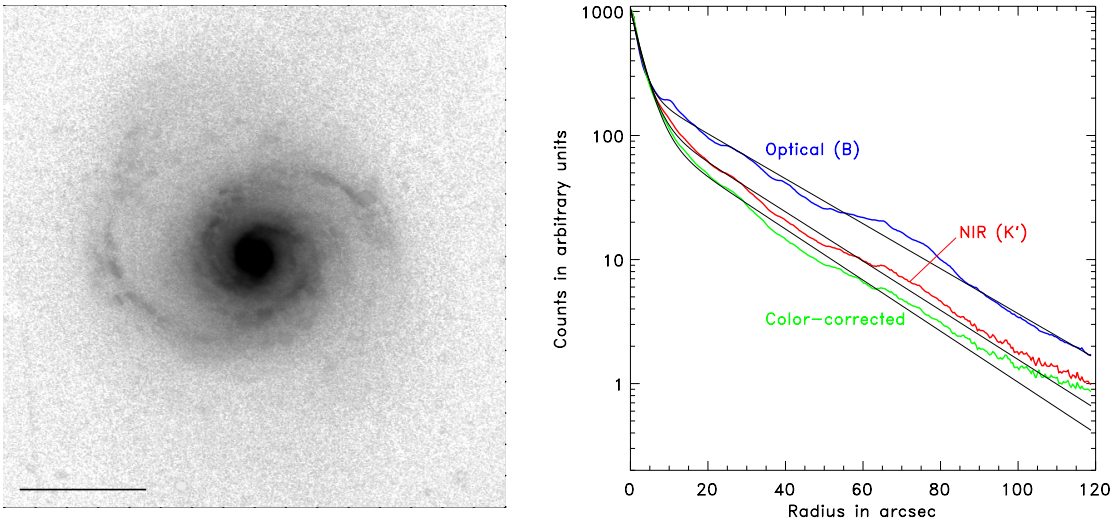

Figure 6.8 NGC 3893. At left the deprojected, color-corrected, H II-region cleaned image of NGC 3893 is shown. It was used as an input to calculate the gravitational potential of the stellar disk contribution to the total gravitational potential. The scaling bar is 1′. At right, the effect of the color correction on the disk scale length of NGC 3893 is shown. The azimuthally averaged radial light profile is fairly well approximated by a double exponential disk model (black lines). The color correction causes the profile to steepen by only 3.5 %, as compared to the K-band.

NGC 3893 has a total blue magnitude of $B_T = 11.2$ mag and the disk measures about 4.3×2.5 arcminutes on the sky, although further out very faint arms can still be traced in long exposures. The major axis position angle, PA = 166.°0, and the inclination of the disk, $i = 42.°0$, were determined from the measured kinematics. The inclination corrected rotation curve rises gently and does not reach the flat part of the rotation curve inside

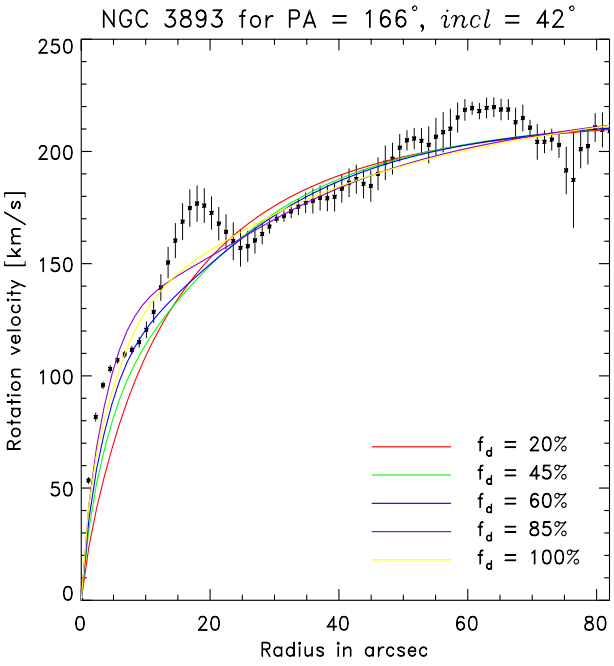

Halo parameters

f_d [%]	R_{core} [kpc]	v_∞ [km s^{-1}]
20	1.04	228
45	1.55	230
60	1.96	233
85	3.43	262
100	4.62	287

Figure 6.9 Rotation curve comparison for NGC 3893. The five axisymmetric model potentials for different fractions of the stellar disk potential yield rotation curves that are very similar, but differ slightly in steepness of the inner rising part.

a radius of 85″. At this radius the rotation velocity reaches about 220 km s^{-1}. From H I-observations it is known that further out the rotation curve drops to ≈ 150 km s^{-1} (Verheijen & Sancisi 2001), most likely influenced by the interaction. From the K-band images, there is no evidence for a bar at the center. However, other authors find evidence for a weak bar in optical images (Eskridge et al. 2000).

The color correction has no drastic effect on the overall morphology of NGC 3893. While the clear $m = 2$ spiral structure remains very prominent, the largest effect of the of the correction is seen in the interacting arm. There the arm inter-arm contrast gets reduced to ≈ 80 % of its K-band value. This is certainly the result from a younger stellar population occupying the north-eastern arm, where the interaction acted as a trigger to induce recent star formation. For NGC 3893, the steepening of the radial profile due to the color correction amounts to only 3.5 % (see also Figure 6.8 and Table 4.2). This leads to the conclusion that the induced star formation yielding younger, and therefore bluer, stellar populations found in the interacting arm is a very local effect, i.e. local within the disk and in time. If the interaction had taken place on large timescales the younger stellar population would have spread across the disk, leading to a overall blue outer disk.

Five models of the total gravitational potential were also prepared for NGC 3893, varying the stellar disk mass fraction f_d. Figure 6.9 shows the rotation curves from the five model potentials, as compared to the observed kinematics. The Table accompanying Figure 6.9 lists the core radii and asymptotic rotation velocities of the five pseudo-isothermal halo models used to assemble the total galaxy potentials. All of the axisymmetric model rotation curves can approximate the galaxy's observed rotation curve fairly well. However, in the inner parts the models with a higher stellar disk contribution provide a better match to the observations. The 'bump' at 17″, which is caused by the strong spiral arms, cannot be reproduced by axisymmetric models. To achieve this, 2D hydro-simulations are needed.

Table 6.2 Hydrodynamic simulations for NGC 3893. Given is the duration of the individual simulation in units of 10^6 years.

f_d	corotation radius R_{CR} [kpc]							
[%]	3.18	5.47	6.46	7.06	7.55	8.56	9.84	∞
20	281*	1064	1064	1064	1064	1064	1064	1064
45	—	1064	1064	1064	1064	1064	1064	1064
60	281*	1064	1064	1064	1064	1064	983	1064
85	281*	1064	441*	1064	1064	963	1064	1064
100	281*	1064	1064	1064	1064	1064	1064	1064

* Note: This run terminated before ending the initialization phase of the simulation, which occurs at 550 Myrs.

6.2.1. Performing the hydrodynamical gas simulations

For modelling the two-dimensional gas surface densities and velocity fields for NGC 3893 again a Cartesian grid of 201×201 grid cells was chosen. The adopted distance towards NGC 3893 of 17 Mpc puts the grid cell size to 97.9 kpc. According to this cell size and a gas sound speed $c_s = 10\,\mathrm{km\,s^{-1}}$, the sound crossing time for one cell is about 13.8 Myrs, which puts the empirical time of 40 sound crossing times to initialize the final potential for the simulation to 550 Myrs.

To find the spiral pattern speed Ω_p, the following corotation radii R_{CR} were modelled: R_{CR} = 3.18, 5.47, 6.46, 7.06, 7.55, 8.56, 9.84 kpc and no pattern rotation. Table 6.2 provides an overview of the runs that were performed for NGC 3893.

6.2.2. Results from the hydrodynamical gas simulations

6.2.2.1. The gas density

The pure two-arm morphology of NGC 3893 turns out to provide a more elementary basis for the simulations as compared to flocculent, multi-arm galaxies. In the simulation for the best matching corotation radius (Figure 6.10), the gas density renders very accurately the shape of the underlying spiral morphology. The strongest gas shocks come to lie where the spiral arms are best defined and most of the star forming H II-regions are located. Even beyond the corotation, which is indicated by the red circle, the shocks are well in place. Like for NGC 3810, outside corotation the simulation develops a long and continuous shock in response of the outskirts of the interacting arm. In the galaxy's inter-arm regions there are also some weaker shocks.

Given the good agreement of the gas density distribution with the galaxy's morphology, the pattern rotation of NGC 3893 can get determined very well. The best matching model places the corotation at the vicinity of about 3 exponential K' disk scale lengths, $R_{CR} = 5.5 \pm 0.5$ kpc, corresponding to a pattern speed $\Omega_p \approx 38\,\mathrm{km\,s^{-1}kpc^{-1}}$. On the other hand, a global pattern rotation speed might not hold for the interacting part of the spiral. As seen from Figure 6.10, beyond the corotation radius, the interacting spiral arm broadenes considerably. this indicates the disintegration of the density wave. Still, in the inner part, where the spiral exhibits a very symmetric pattern, the approximation with a single pattern rotation speed appears to work very well. The analysis of the kinematic data will eventually confirm this notion.

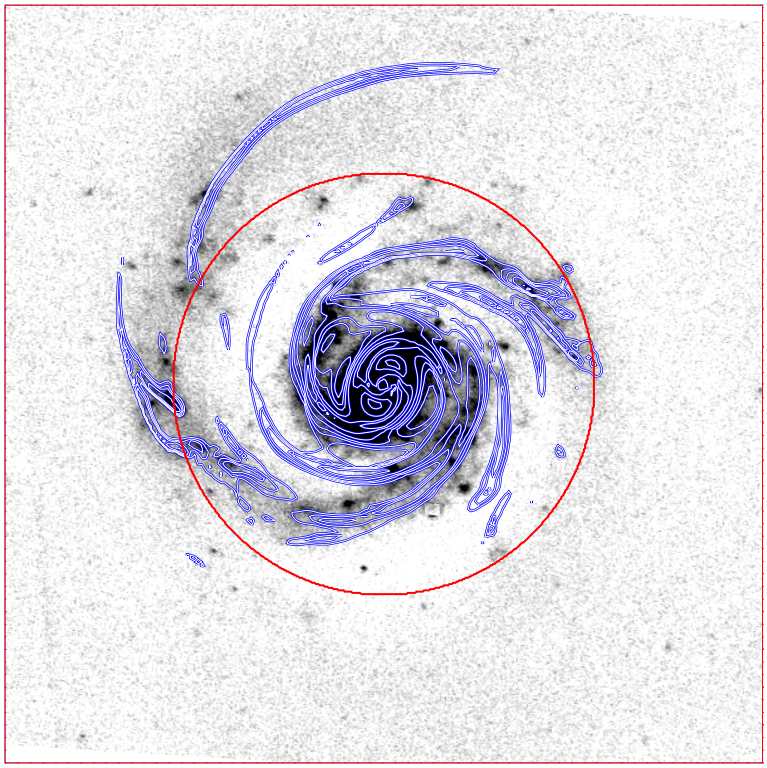

Figure 6.10 Simulation results of the gas density distribution overlaid in contours onto the deprojected K'-band image of NGC 3893. From the image an axisymmetric radial brightness profile has been subtracted to enhance the contrast of the spiral arms. The Figure shows the contours for the simulation with $f_d = 100\,\%$ and a corotation radius (red circle) of 5.47 kpc. The full set of simulation results is shown in Appendix B.

6.2.2.2. The gas velocity field

Differing from NGC 3810 and NGC 4254, in the observed gas velocity field from NGC 3893 small scale wiggles and jumps are less prominent. As seen in Figure 3.2, the rotation curves along many slit positions are smooth and steady, revealing broad wiggles where the slit was crossing a spiral arm. The interpretation of this finding would be that the gas velocity field of NGC 3893 seems indeed to be governed by large scale gravitational effects rather than local gas bubbles and turbulences. These are favorable conditions for carrying out the hydrodynamic simulations.

In Figure 6.11 the comparison of the simulations with the observed data is presented for a sample of three position angles of NGC 3893, illustrating the overall fit quality. Shown are the simulated curves for the maximal disk case ($f_d = 100\,\%$ in green) and the one for the setup using the most massive halo ($f_d = 20\,\%$ in red). An overview on all position angles is provided in the Appendix B. The match of the $f_d = 100\,\%$ simulation is striking! In the inner parts the wiggles found in the simulated velocity fields coincide almost perfectly with the observations. This applies also to most of the slit position angles that are not shown here, although in some cases the amplitude of the wiggles deviates slightly. This finding complements very well the good match of the gas density morphology with the underlying galaxy structure. At the outer parts of the rotation curves the agreement be-

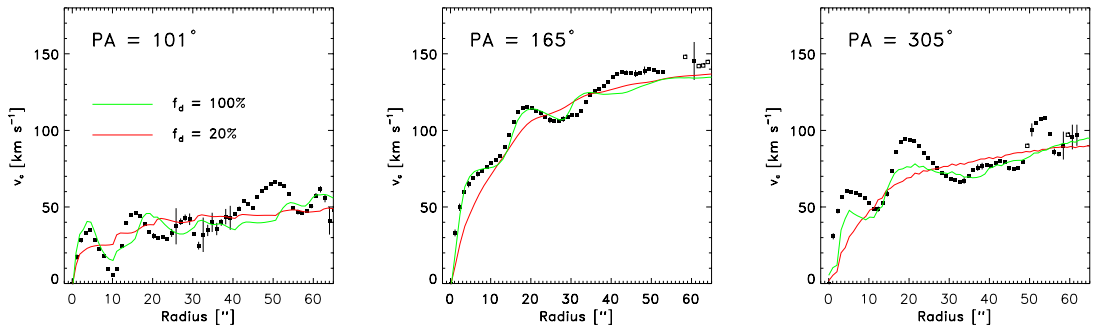

Figure 6.11 Example of the comparison of the simulation results to the observed kinematics of NGC 3893. The "maximal disk" and "minimal disk" velocity field are shown for three position angles. Presented are results from simulations assuming a pattern rotation $\Omega_{\rm p} \approx 38\,{\rm km\,s^{-1}\,kpc^{-1}}$ ($R_{\rm CR} = 5.47\,{\rm kpc}$). Clearly the maximum disk simulation provides an excellent fit to the observations. The full comparison is shown in Appendix B.

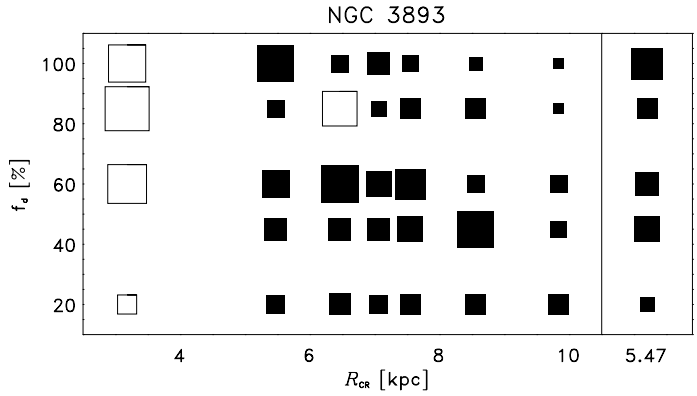

Figure 6.12 Graphical presentation of the global χ^2-analysis of all the velocity simulations for NGC 3893 (left partition). At right, the χ^2-analysis of the reduced data set is shown for a corotation radius $R_{\rm CR} = 5.47\,{\rm kpc}$. Large boxes indicate better agreement between the simulated velocity field and the observed kinematics. The open boxes represent simulations that terminated before passing the initialization phase. The actual χ^2-values can be found in Appendix B.

tween simulations and observations turns into a good global fit. Beyond $\approx 45''$ the wiggles in the observed velocity fields tend to exhibit a larger amplitude than what can be found in the simulations. Corotation is at $65''$.

Given the excellent overlap of features, the conditions are such that the global χ^2-analysis may yield conclusions about the mass composition within the galaxy. The left partition of Figure 6.12 provides an overview on the results from the global χ^2-analysis. Larger boxes indicate a smaller χ^2/N-value and thus a smaller deviation from the observed data. The best matching simulation results lie in the fast pattern rotation and high disk mass range. The open boxes denote simulations that terminated before passing the initialization phase. As discussed in Section 6.1.2, these runs tend to render a better fit than what the equilibrium state would yield. Still these simulations demonstrate that in the vicinity of the

best fitting run ($R_{\mathrm{CR}} = 5.5\,\mathrm{kpc}; \mathrm{f_d} = 100\,\%$) the overall fit quality is generally high. The region of good agreement for the medium disk models is lacking the detailed fit quality on a wiggle-by-wiggle basis, that is found for the maximal disk simulation which is displayed in Figure 6.11.

The analysis of only the fraction of the velocity field, for which most likely gravity is the dominant driving force of the gas (see Section 4.3.2.1 for a description of the method) provides even stronger support to this trend. See the right partition of Figure 6.12. Eventually, the least squares comparison is not very sensitive to non-gravitationally induced gas dynamic features. The selection process rejected about 40 % of the data points from the observations (see Appendix B for a Figure), with almost no effect on the conclusions. Thus, the analysis of NGC 3893 yields a very robust result and it can be concluded that a maximum disk is needed to explain the observations well.

Eventually, a detailed look at the data reveals that the good agreement between observations and simulations mainly relies on the inner part of the disk. In the outer parts the simulations fail to predict the disk kinematics as detailed, pointing to dynamic processes, most likely correlated with the interaction, that cannot get treated with a single spiral pattern speed.

6.3. NGC 5676

NGC 5676 is a Sc starburst galaxy located in a small group of galaxies with 11 reported members (Garcia 1993). It reveals a fairly strong two arm grand design morphology. However, as it can be seen in the left panel of Figure 6.13, the deprojected spiral pattern shows frequent kinks making the inner spirals appear hexagonal. At a radius of about $30''$ the spirals become smoother. While the eastern (left) arm continues for another $180°$ after the last kink, the western arm (right) breaks up and fragments into a more flocculent morphology. From the K-band images, there is evidence for a weak bar at the center. It is displayed in the right panel of Figure 6.13. Its position angle is at about $38°$ and its radius is about $12''$, or 1.9 kpc.

Although situated in a group, no evidence for ongoing interaction has been reported. On the other hand, past interactions certainly occured and might have triggered the spiral density wave and the starburst. The radial brightness profile is very well described by a double exponential model profile (see Figure 4.1a). The galaxy's K-band exponential disk scale length of $22\farcs4$ corresponds to 3.6 kpc, if a distance of 33 Mpc is assumed towards NGC 5676, taken as an average literature value. NGC 5676 has a total blue magnitude of $B_T = 11.9$ mag and the disk measures about 3.9×1.9 arcminutes on the sky at the 22 K-mag per square arcsecond isophote. The major axis position angle, $\mathrm{PA} = 45\fdg8$, and the disk inclination, $i = 64\fdg0$, were determined from the measured kinematics.

The inclination corrected rotation curve rises very steeply at the center and reaches the flat part of the rotation curve at a radius of $25''$ (see Figure 6.14). The rotation velocity levels at about $240\,\mathrm{km\,s^{-1}}$, which is the highest rotation velocity of all galaxies from the sample with measured kinematics.

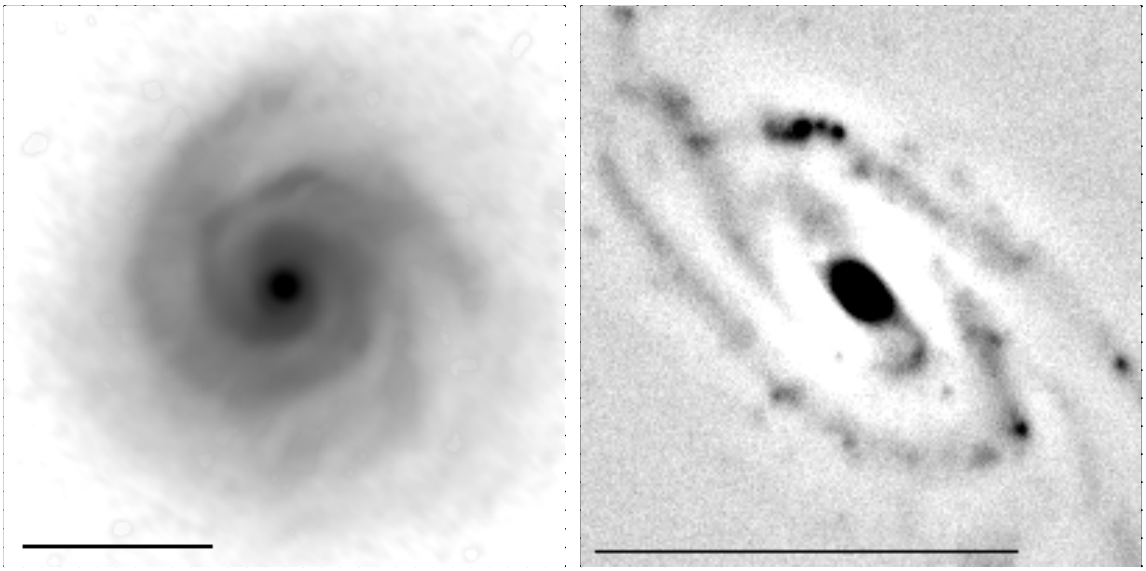

Figure 6.13 NGC 5676. At left the deprojected, color-corrected, H II-region cleaned image of NGC 5676 is shown. It was used as an input to calculate the gravitational potential of the stellar disk contribution to the total gravitational potential. At right, the central region of NGC 5676 (K-band) is shown. Using the unsharp masking technique, a weak central bar can be identified. The horizontal bar at the bottom of both images measures $1'$.

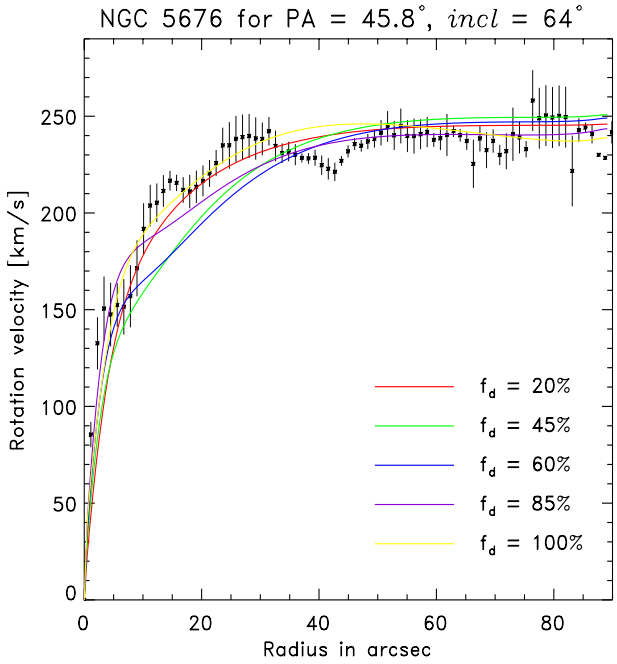

Halo parameters

f_d [%]	R_{core} [kpc]	v_∞ [km s^{-1}]
20	0.82	240
45	2.09	240
60	3.30	240
85	8.87	280
100	12.0	280

Figure 6.14 Rotation curve comparison for NGC 5676. The five axisymmetric model potentials for different fractions of the stellar disk potential yield rotation curves that fit fairly well with the observed rotation curve. However, the steep central rise from 10″ to 30″ is approximated best by either the maximal or minimal disk model.

The color correction clearly enhances the $m = 2$ spiral structure of NGC 5676. Some of the features in the disk appear very blue and hence get largely reduced in the color corrected image (for example the inter-arm feature seen in the upper left corner of the K-band image, displayed in the right panel of Figure 6.13). However, NGC 5676 might have a considerable amount of dust in the disk, that obscures especially at optical wavelengths. Since the optical image has only a moderate resolution of 2.″3 (FWHM) it is very hard to tell from the image, if a region is less bright because of dust or because less star formation activity. High amounts of dust can in principle cause the color correction to fail at places where the dust is optically thick. On the other hand, the color correction works well in the presence of dust as long as not all the light gets absorbed. Moreover, in galaxies with violent star formation going on – like NGC 5676 – the population differences are large and the color correction is expected to have a stronger effect on the two dimensional mass distribution. However, the IMF of starburst galaxies is distincly different from the universal IMF that was used to derive the M/L to color relation. This fact leads to the conclusion that even the color corrected K-band image still does not provide a highly accurate mass map of the galaxy. In light of this, even if the mass map will not be perfect, applying the color correction still yields a better mass map than just the K-band image and that it is worthwhile doing it. The color correction causes the arms to appear more continuous and better defined. The radial K-band light profile steepens by 12.9 % as a result from the color correction, still remaining exponential.

NGC 5676's inclination on the sky (64°) is rather high and the deprojected image has been convolved with a transposed distortion function, as shown in Figure 4.3. Additionally, even though the center reveals the weak bar, the very center was replaced by a truly axisymmetric model of the inner part. This was done to avoid problems at the very center, when running the hydrosimulations. Due to the high rotation velocity and the steep cen-

Table 6.3 Hydrodynamic simulations for NGC 5676. Given is the duration of the individual simulation in units of 10^6 years. The dynamical time scale for NGC 5676 is 383 Myrs.

f_d	corotation radius R_{CR} [kpc]										
[%]	5.6	6.6	7.65	8.6	9.6	10.6	11.6	12.6	13.6	14.16	∞
20	—	—	902	902	902	902	902	902	902	—	—
45	571	1052	1292	1292	1292	1292	1292	691	781	812	1292
60	—	—	602*†	452*†	572*†	—	873	993	873	843	1714
85	—	—	511*	571	541	511*	511*	511*	541	—	—
100	—	—	541	511*	511*	511*	541	451*	451*	511*	—

Notes: * This run terminated before ending the initialization phase of the simulation, which occurs at 529 Myrs.
† The $f_d = 60\,\%$ simulations were performed on a grid with a larger cell size, leading to longer initialization phases (704 Myrs).

tral velocity gradient, NGC 5676 is very susceptible to creating these extremely rarefied gas conditions in the simulations that were described in Section 6.1.2.

Also for NGC 5676 five models of the total gravitational potential were prepared, varying the stellar disk mass fraction f_d. Figure 6.14 shows the rotation curves from the five model potentials, as compared to the observed kinematics. The Table accompanying Figure 6.14 lists the core radii and asymptotic rotation velocities of the five pseudo-isothermal halo models used to assemble the total galaxy potentials. The model rotation curves match fairly well with the observed rotation curve, however not as well as it can be achieved for other galaxies in the sample. A reason for this is the steep rise in the center and the righ rotation velocity. For the "medium-disk" models the isothermal sphere with a core is not flexible enough to account for the steep rise, lacking massive contribution from the small bulge and the inner disk. As it will be seen later, the two dimensional gas simulations yield velocity fields that reproduce the observed rotation curves better than the axisymmetric model rotation curves.

6.3.1. Performing the hydrodynamical gas simulations

The two-dimensional gas modelling for NGC 5676 was performed on a 301×301 Cartesian grid. The larger grid size was motivated by the fact the NGC 5676 is located at a distance of 33 Mpc, thus relatively far away. The grid was scaled to yield a similar cell size in real dimensions within the galaxy. In this setup the length of one grid cell measures 95.1 pc. According to this cell size and a gas sound speed $c_s = 10\,\mathrm{km\,s^{-1}}$, the sound crossing time for one cell is about 13.2 Myrs, which puts the empirical time of 40 sound crossing times to initialize the final potential for the simulation to 530 Myrs. Only for the earliest runs ($f_d = 60\,\%$), the grid cell size was larger (127 pc), putting the initialization time for the code to 704 Myrs. The later increase in grid resolution was motivated by the gain of higher accuracy as well as reducing the simulation time fur the runs.

To find the spiral pattern speed Ω_p models with the following corotation radii R_{CR} were simulated: $R_{CR} = 5.6$, 6.6, 7.65, 8.6, 9.6, 10.6, 11.6, 12.6, 13.6, 14.16 kpc and no pattern rotation. Table 6.3 provides an overview of the runs that were performed for NGC 5676.

As seen from Table 6.3, the premature termination of simulations is a serious issue for NGC 5676. For heavy disk simulations, all the runs terminated close to the end of the initialization phase. The main reason for this to happen, is the very steep velocity gradient of $\approx 400\,\mathrm{km\,s^{-1}}$ within a radial scale of $\approx 40''$ at the center. Furthermore the small bar introduces additional non-axisymmetric structures, that cause strong shocks in the simulated gas flow. As a preventive strategy, the center of the mass map, which was used as the input to calculate the stellar disk contribution of the gravitational potential, was replaced by a truly axisymmetric model in order to minimize the non-axisymmetric central structures in the final potential. Even though, for heavy disks, the runs encounter extreme shocks at the center that eventually produce negative gas densities at certain grid cells. In a second attempt, simulations were done using a higher gas sound speed of $c_s = 15\,\mathrm{km\,s^{-1}}$, intending the gas to respond less to non-axisymmetric features in the potential. Also this modification could not extend the run time of the simulation considerably. These results are not discussed.

Yet, the simulation situation for NGC 5676 is very unsatisfactory. As seen in the following section, preliminary conclusions can be drawn, but a thoroughly successful modelling of the galaxy still needs to be achieved. At the present status of the simulation process there is still a variety of hitherto unexplored options that offer good chances for success. So far it seems that the very bright emission of the many strong star forming regions in the arms of this starburst galaxy has not been corrected well enough by the standard treatment that was described in Chapter 4.

6.3.2. Preliminary results from the hydrodynamic gas simulations

6.3.2.1. The gas density

The spiral structure of NGC 5676 is fairly regular, but still the arms deviate from smooth logarithmic radial profiles. Apparently this behavior is challenging for the simulations to match. Figure 6.15 shows the gas density distributions resulting from two simulations which yield the best matching morphology. The gas density contours are overlaid onto the deprojected K-band image, treated by the unsharp masking technique to enhance the contrast of the underlying spiral structure. While the simulation with the slower pattern speed ($\Omega_\mathrm{p} \approx 21\,\mathrm{km\,s^{-1}kpc^{-1}}$ or $R_\mathrm{CR} = 11.6\,\mathrm{kpc}$, right panel of Figure 6.15) reproduces very well the inner spiral structure, the one with the faster pattern speed ($\Omega_\mathrm{p} \approx 25\,\mathrm{km\,s^{-1}kpc^{-1}}$ or $R_\mathrm{CR} = 9.6\,\mathrm{kpc}$, left panel of Figure 6.15) yields a better fit to the outer spiral. In both simulations the modelled gas shocks follow rather closely the spiral structure of the arm emerging from the north top of the bar for about 270°. Further out, other shocks, coming from the inner or outer inter-arm region then take the place of the primary shock. The replaced shock quickly loses its strength and fades away. Thus, the simulated gas shocks come to lie in the vicinity of nearly all arm parts and fragments.

The fact that simulations for different pattern speeds tend to reproduce the spiral structure better at different radii can be regarded as evidence that the pattern speed is not constant for the entire disk. Additionally, if the velocity field is considered, it can be found that there is a severe mismatch at the central arcseconds too, which indicates that also the dynamic processes at the bar cannot be modelled successfully along with the rest of the disk. In light of this, describing the disk dynamics of NGC 5676 by a single pattern speed

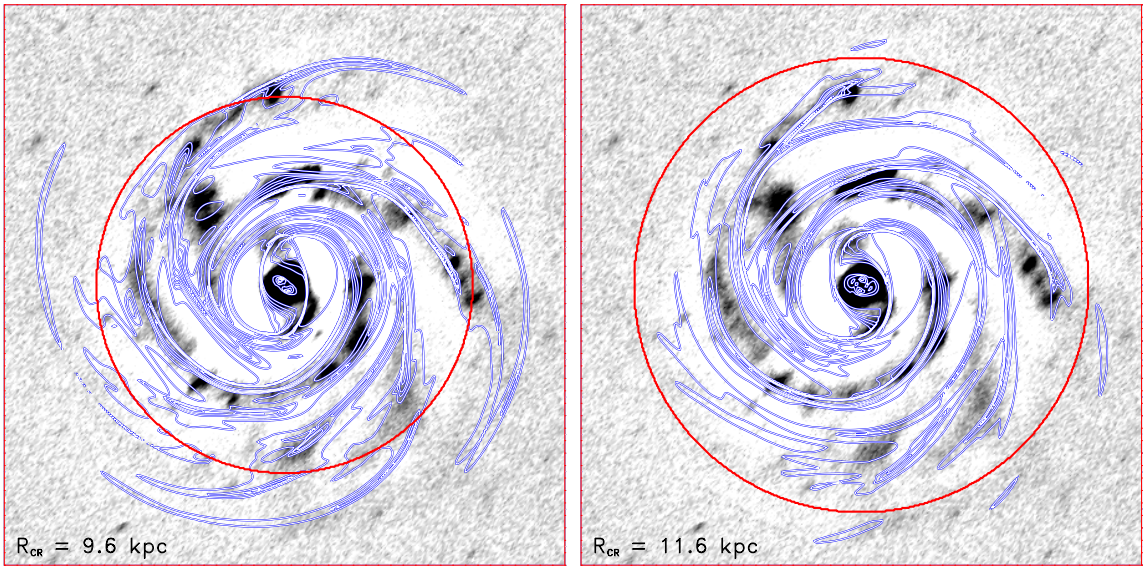

Figure 6.15 Simulation results of the gas density distribution overlaid in contours onto the deprojected K'-band image of NGC 5676. From the galaxy image a unsharp mask was subtracted to enhance the contrast of the spiral arms. The Figures show the contours for the simulation with $f_d = 85\,\%$ and corotation radii (red circles) of 9.6 and 11.6 kpc. The full set of simulation results is shown in Appendix D.

might not be appropriate. However, the range of best fitting pattern speeds is still rather narrow ($R_{CR} \approx 9 - 12$ kpc). Furthermore, as it will be seen from the velocity comparison, the simulations with $R_{CR} = 11.6$ kpc render very well the observed gas dynamics across most of the disk.

Thus, a good matching corotation model places the resonance at the vicinity of about 3 exponential K' disk scale lengths, $R_{CR} = 11^{+1}_{-2}$ kpc, corresponding to a pattern speed $\Omega_p \approx 22\,\mathrm{km\,s^{-1}kpc^{-1}}$. In this case the corotation resonance is located in the direct vicinity to where the stellar spiral ends. Beyond corotation there is no regular spiral structure.

6.3.2.2. The gas velocity field

The observed gas velocity field of NGC 5676 is governed by a very steep rise at the center, levelling at $\approx 240\,\mathrm{km\,s^{-1}}$ along the major axis position angle at about 45° (see Figure 6.16). In general, the gas velocity field reveals a considerable amount of small scale structure. Scaling with the overall high rotation velocity there are many observed abrupt velocity jumps in the range of 30 – 50 $\mathrm{km\,s^{-1}}$. The observed data comprise only 7 slit positions, missing one measurement at the 0° position angle.

In Figure 6.16 the comparison of the simulations with the observed data is presented for a sample of three position angles of NGC 5676, illustrating the overall fit quality. Shown are the simulated curves for the near maximal disk case ($f_d = 85\,\%$ in green) and the one for the setup using the most massive halo ($f_d = 20\,\%$ in red). The match of the $f_d = 85\,\%$ simulation is very good along the displayed postion angles. Even some of the small scale wiggles are reproduced very accurately. As it is appearent from the overview on all position angles in Appendix D, for most position angles the comparison turns out

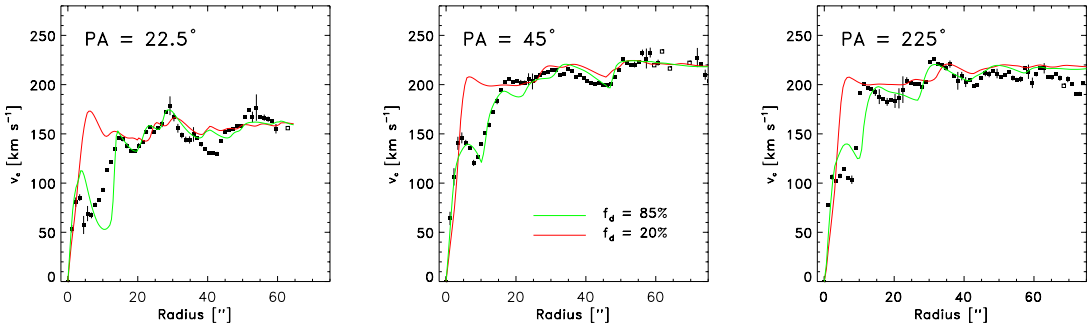

Figure 6.16 Example of the comparison of the simulation results to the observed kinematics of NGC 5676. Velocity field are shown for three position angles. Presented are results from simulations with $f_d = 20$ and 85 %, assuming a pattern rotation $\Omega_p \approx 21\,\mathrm{km\,s^{-1}\,kpc^{-1}}$ ($R_{CR} = 11.6\,\mathrm{kpc}$). There are severe discrepancies in the central parts. The full comparison is shown in Appendix D.

very good. Only in the inner $\approx 20''$ the simulated velocity fields exhibit exceedingly high velocity jumps, that eventually grow to such magnitudes that the simulation terminates prematurely. These extreme shocks are associated with the steep velocity gradient in the central velocity field of NGC 5676 and the presence of a small bar in the same region. This central bar could further possess a pattern speed, differing from that of the disk, introducing even more dynamic challenges for the simulations. In light of this, it must be pointed out that the $f_d = 85\,\%$ results, which are displayed in Figure 6.16, are indeed from a run that did not reach the final, stationary simulation phase. The run crashed at the timestep where the final realistic, non-axisymmetric gravitational potential was being turned on. The $f_d = 20\,\%$ simulation proceeded for more than a galactic dynamical time scale beyond this point. In fact, as seen from the results from the full χ^2-analysis that is presented in Figure 6.17, none of the heavy disk simulations proceeded significantly past the initialization phase.

Nonetheless, there is reason to argue that the $f_d = 85\,\%$ scenario is characteristic to the galaxy, and not just a numerical effect. First, the wiggle-to-wiggle agreement between the simulations and observations is undoubtedly better for the heavy disk model. Second, as seen from Figure 6.18, the evolution of the fit quality during the initialization phase of the simulation proceeds towards even better agreement (smaller χ^2) until the run terminated. It seems safe to extrapolate that median(χ^2) lies in the close vicinity of the last fit even beyond simulation timestep 18, after which the stationary simulation conditions are accomplished. The better fit quality of the $f_d = 20\,\%$ models as compared to the 45 and 60 % models is a result from the smoother and more axisymmetric model rotation curve. The basic axisymmetric disk model was tuned to match the overall rotation curve. This effect has been discussed for NGC 3810.

As a conclusion of this discussion, it seems fair to state that the simulations provide evidence for a heavy disk scenario in NGC 5676, even though the simulations did not yet provide an entirely satisfactory degree of completeness. A disk mass fraction $f_d \approx 85\,\%$ indicates that about 2/3 of the total mass inside 2.2 K-band disk scale lengths is contributed from the stellar disk. The core radius of the pseudo-isothermal halo is in that case in the range of several disk scale lengths. In this scenario, the halo begins only beyond the extent of the bright stellar disk to dominate the dynamics of the galaxy.

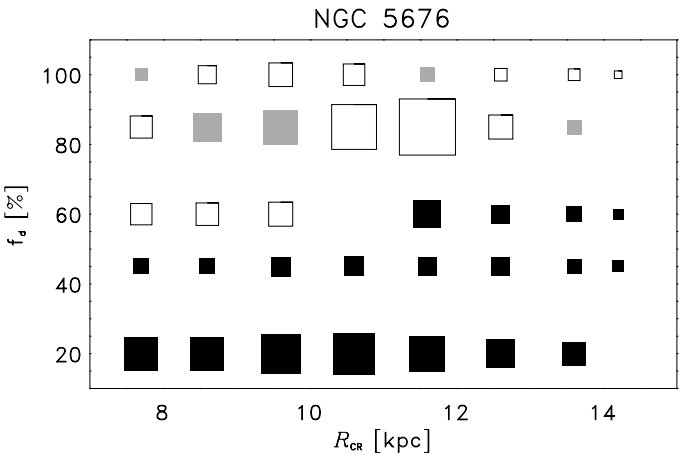

Figure 6.17 Graphical presentation of the preliminary, global χ^2-analysis of all the velocity simulations for NGC 5676. Large boxes indicate better agreement between the simulated velocity field and the observed kinematics. The open boxes represent simulations that terminated before passing the initialization phase. Grey boxes represent simulations that terminated immediately after reaching the stationary simulation phase. Premature terminations are a serious issue for NGC 5676.

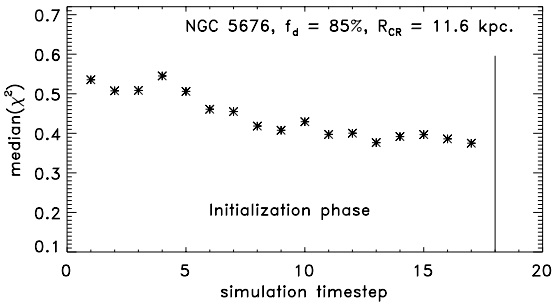

Figure 6.18 Evolution of the fit quality of the $\mathrm{f_d} = 85\,\%$, $R_{\mathrm{CR}} = 11.6\,\mathrm{kpc}$ simulation during its initialization phase as measured from the median(χ^2) from the comparison. The simulation terminated during the calculation of timestep 18. The simulation evolves towards a better fit quality and might be safely extrapolated into the stationary simulation phase.

6.4. NGC 6643

NGC 6643 is probably the least suited galaxy for this experiment that is in the sample. Although it is classified as Sc, the galaxy reveals a very flocculent morphology with many star forming regions and knotty arms. In the NIR, the spiral structure is more pronounced, however, the arms appear still knotty and the arm to inter-arm contrast is very variable: $0.2 - 0.6\,K'$-mag. The regular two-arm spiral that direcly emerges from the tiny bulge breaks up into several arm pieces at a radius of about $20''$. These arms continue to wind outward for $\approx 180^\circ$ with changing pitch angles. At the radius where the spiral breaks its symmetry, there is a massive over-abundance of star forming H II-regions. This over-abundance is also distincly notable in the radial brightness profiles, shown in the right panel of Figure 6.19. At the radial range from about 15 to $25''$ the brightness in B increases while in K' it stays constant. The color corrected radial profile almost entirely corrects this discontinuity and produces a very smooth exponential profile. This can be considered as a strong argument in favor of the color correction method. Especially, since for NGC 6643 it is not obvious that the color correction should work accurately. Like NGC 3810, also NGC 6643 was studied by Elmegreen et al. (1999) looking for underlying NIR symmetric structures in optically flocculent galaxies. These authors argued that dust might play a major role in explaining the flocculent optical appearance. Also Evans (1993) finds high dust extinction in the central region of NGC 6643. As discussed already for the case of NGC 5676, strong dust extinction might corrupt the outcome of the color correction. However, considering the above, the color correction seems to yield a much better mass map than the K-band image would be.

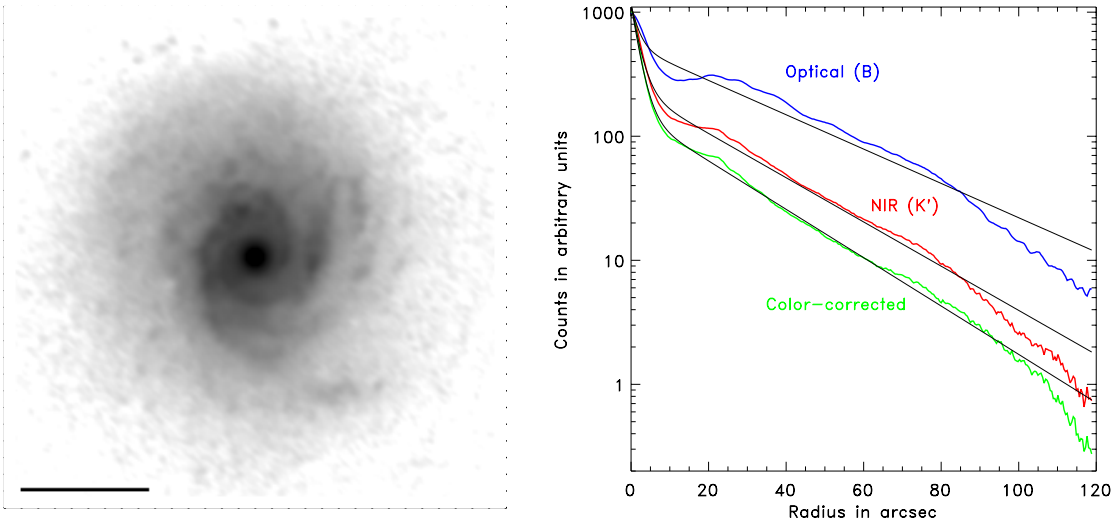

Figure 6.19 NGC 6643. At left the deprojected, color-corrected, H II-region cleaned image of NGC 6643 is shown. It was used as an input to calculate the gravitational potential of the stellar disk contribution to the total gravitational potential. The bar is $1'$. At right, the effect of the color correction on the disk scale length of NGC 6643 is shown. Note the deviation of the optical and K-band azimuthally averaged light profiles from a simple exponential. The model fit (black lines) of the color corrected profile steepens by 8.6 %, as compared to the K-band.

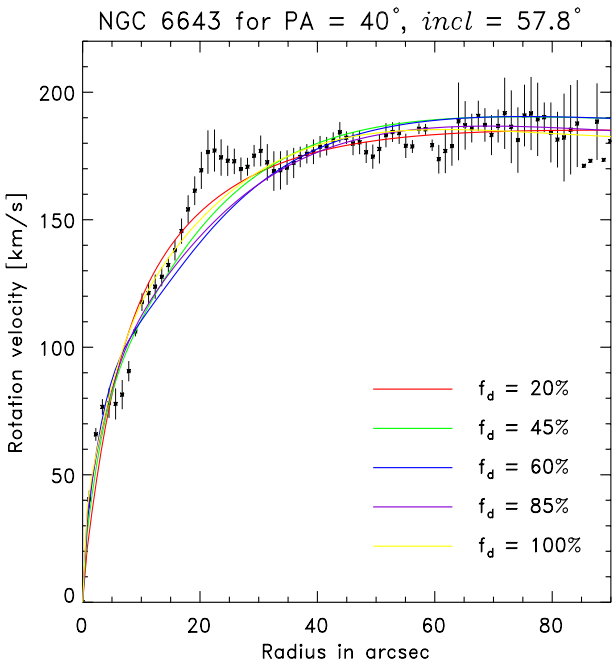

Halo parameters

f_d [%]	R_{core} [kpc]	v_∞ [km s^{-1}]
20	0.80	183.5
45	1.46	180
60	2.34	180
85	4.90	180
100	11.5	242

Figure 6.20 Rotation curve comparison for NGC 6643. The five axisymmetric model potentials for different fractions of the stellar disk potential yield rotation curves that are very similar and match well with the observed kinematics.

A distance of 23 Mpc was assumed towards NGC 6643, taken as an average literature value. At this distance the galaxy's K-band exponential scale length of $24\farcs4$ corresponds to 2.72 kpc. NGC 6643 has a total blue magnitude of $B_T = 11.8$ mag and the disk measures about 3.6×2.1 arcminutes on the sky at the 22 K-mag per square arcsecond isophote. The major axis position angle, PA $= 40\fdg0$, and the inclination of the disk, $i = 57\fdg8$, were determined from the measured kinematics. The inclination corrected rotation curve rises about linearly out to a radius of about $20''$, where there is a sharp break and the rotation curve levels to a constant value of $\approx 185\,\mathrm{km\,s^{-1}}$.

Five models of the total gravitational potential were prepared for NGC 6643, varying the stellar disk mass fraction f_d. Figure 6.20 shows the rotation curves from the five model potentials, as compared to the observed kinematics. All model rotation curves can explain the galaxy's observed rotation curve similarly well. Again, small scale features in the rotation curve like the "bump" at $\approx 20''$ cannot be matched by a simple axisymmetric model. The Table accompanying Figure 6.20 lists the core radii and asymptotic rotation velocities of the five pseudo-isothermal halo models used to assemble the total galaxy potentials.

6.4.1. Performing the hydrodynamical gas simulations

The two-dimensional gas modelling for NGC 6643 was performed on a 257×257 Cartesian grid. The grid size was chosen to yield a cell size in real dimensions within the galaxy that is similar to the others from the sample. In this setup the length of one grid cell measures 88.3 pc. According to this cell size and a gas sound speed $c_s = 10\,\mathrm{km\,s^{-1}}$, the sound crossing time for one cell is about 12.2 Myrs, which puts the empirical time of 40 sound crossing times to initialize the final potential for the simulation to 488 Myrs.

Table 6.4 Hydrodynamic simulations for NGC 6643. Given is the duration of the individual simulation in units of 10^6 years. The full potential is turned on at 488 Myrs.

f_d	corotation radius R_{CR} [kpc]							
[%]	4.18	5.1	6.0	6.5	7.00	8.0	9.0	10.0
20	782	842	842	842	842	842	842	842
45	842	842	842	842	842	842	842	842
60	692	842	842	—	842	842	842	842
85	842	842	842	842	782	511	842	842
100	661	782	601	812	—	842	842	842

To find the spiral pattern speed Ω_p, or equivalently the corotation radius R_{CR}, the following cases were modelled: $R_{CR} = 4.18$, 5.1, 6.0, 6.5, 7.0, 8.0, 9.0 and 10.0 kpc. Table 6.4 provides an overview of the runs, performed for NGC 6643. All runs carried on well beyond the initialization phase, so that premature simulation terminations are no issue for NGC 6643.

6.4.2. Results from the hydrodynamical gas simulations

6.4.2.1. The gas density

As mentioned before, the morphologic appearance of NGC 6643 does not qualify it as the perfect laboratory for the anticipated analysis. It does not exhibit a clear grand design spiral structure that helped to yield the good results for NGC 3893, but rather a patchy and flocculent morphology. Figure 6.21 shows the gas density distribution that resulted from two simulations with different corotation radii, which reproduce the galaxy's spiral structure comparably well. The gas density contours are overlaid onto the deprojected, unsharp masked K-band image, representing the underlying spiral structure. Since NGC 6643's arms do not wind with a constant pitch angle, the simulations encounter difficulties to reproduce all spiral features. While for the model with the faster pattern speed ($R_{CR} = 6.5$ kpc) the most prominent eastern (left) arm cannot be traced by one single gas shock, it still exhibits gas shocks in the vicinity of all major star forming regions. The scenario with the slower pattern speed ($R_{CR} = 8.0$ kpc) results in a fairly well overall matching morphology, only the arms in the gas simulation seem to wind too long, ultimately deviating from the observed morphology. Eventually, the spiral structure that develops in both gas simulations matches well with the galaxy's true spiral pattern. However, the results from the kinematic comparison favor the faster pattern speed model.

From the modelling, the location of the corotation resonance can be placed close to the end of the stronger spiral pattern. This is in the vicinity of about 2.4 exponential K' disk scale lengths, $R_{CR} = 6.5^{+1.5}_{-0.5}$ kpc, corresponding to a pattern speed $\Omega_p \approx 28.5\,\mathrm{km\,s^{-1}kpc^{-1}}$. Due to the moderate morphological match, the precision, with which the corotation can be determined is comparably low. However, the results from simulations outside the corotation range of $R_{CR} = 6 - 8$ kpc yield to even less satisfying comparisons (see Appendix E).

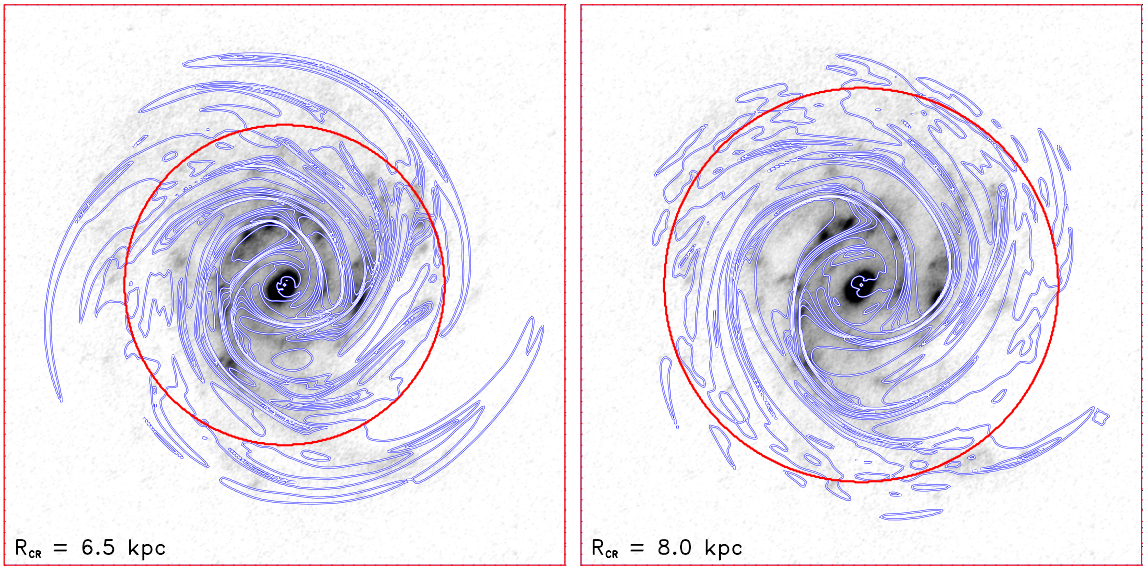

Figure 6.21 Simulation results of the gas density distribution overlaid in contours onto the deprojected K'-band image of NGC 6643. From the galaxy image a unsharp mask was subtracted to enhance the contrast of the spiral arms. The Figures show the contours for the simulation with $f_d = 45\,\%$ and corotation radii (red circles) of 6.5 and 8.0 kpc. These two simulations reproduce the galaxy's morphology comparably well. The full set of simulation results is shown in Appendix E.

6.4.2.2. The gas velocity field

The observed gas velocity field of NGC 6643 does not reveal an exceedingly high amount of small scale noise (see Figure 6.22 for three position angles). In the central region the rise of the rotation curve is not particularly steep. As for NGC 5676, the observed data comprise only 7 slit positions, missing one measurement at the 0° position angle.

In Figure 6.22 the comparison of the simulations with the observed data is presented for a sample of three position angles of NGC 6643, illustrating the overall fit quality. Shown are the simulated curves for a near maximal disk case ($f_d = 85\,\%$ in green) and the one for the setup using the most massive halo ($f_d = 20\,\%$ in red). Considering the rather moderate match of the gas density field with the spiral structure, the correspondance of the simulated velocity field of the light disk model with the data is respectably good. Particularly, the global overlap of the curves is striking. From all observed 14 slit positions, given in Appendix E, it can be seen that the comparison turns out very good for the complete velocity field. The simulations fail however, to reproduce a substantial number of the single wiggles pointing towards non-gravitationally induced gas dynamics. This will complicate the conclusion process, which disk mass fraction setup eventually explains the observed gas dynamics best.

The left partition of Figure 6.23 shows the results from the full χ^2-analysis of the runs. As for NGC 3810, the result from the global χ^2-analysis yields a very smooth distribution across the studied parameter space. Accordingly it must be concluded that the amount of non-gravitationally induced gas dynamic wiggles is rather high and probably as abundant as the gravitationally induced ones.

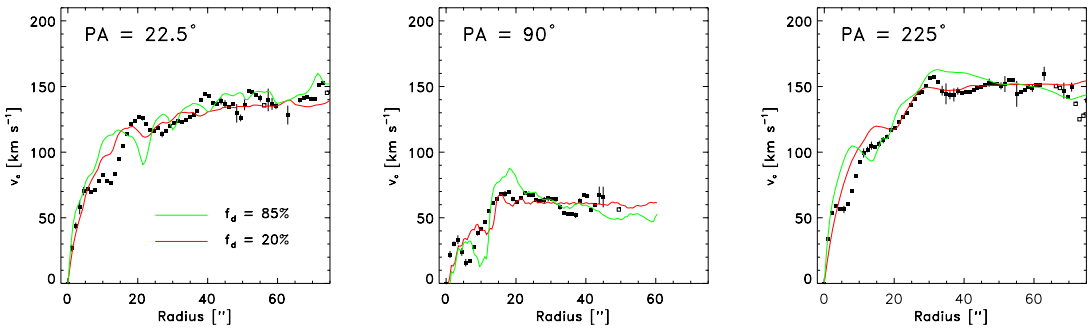

Figure 6.22 Example of the comparison of the simulation results to the observed kinematics of NGC 6643. Velocity field are shown for three position angles. Presented are results from simulations with $f_d = 20$ and 85 %, assuming a pattern rotation $\Omega_p \approx 28.5\,\mathrm{km\,s^{-1}\,kpc^{-1}}$ ($R_{CR} = 6.5$ kpc). Both simulations yield a comparably good match. The full comparison is shown in Appendix E.

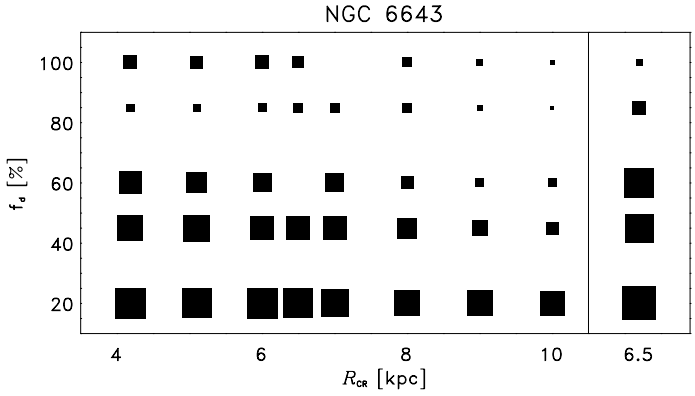

Figure 6.23 Graphical presentation of the global χ^2-analysis of all the velocity simulations for NGC 5676 (left partition). At right, the χ^2-analysis of the reduced data set is shown for a corotation radius $R_{CR} = 6.5$ kpc. Large boxes indicate better χ^2/N agreement between the simulated velocity field and the observed kinematics.

The analysis of only the fraction of the velocity field, for which most likely gravity is the dominant driving force of the gas (see Section 4.3.2.1 for a description of the method) allows slightly more reliable conclusions. As for NGC 3810, slightly more than 50 % of the observed data points have been rejected from the comparison. From the results of the χ^2/N comparison on the reduced data set, displayed in the right partition of Figure 6.23, it can be seen that low and medium disk models provide a comparably good agreement between observations and simulations. This rather vague result comes not unexpected, considering the weak spiral density wave in NGC 6643. If the stellar mass is only poorly concentrated within the spiral arms, the gravitational influence of the arms excerts also weak forcing on the gas. Reproducing these subtle effects with the simulations is difficult. In light of this, the conclusion that a heavy disk scenario is unlikely for NGC 6643 can already be regarded as a respectable success.

CHAPTER VII
Synthesis of the Results and Conclusions

For this thesis detailed maps of the stellar structure and the H II kinematics were obtained for the five galaxies NGC 3810, NGC 3893, NGC 4254, NGC 5676 and NGC 6643. The observations were compared to the results from a set of hydrodynamic gas simulations. The simulations were performed for realistic two dimensional gravitational potentials, combined from stellar disk and dark halo contributions. The gravitational potential of the stellar disk was derived directly from the observations of the galaxies, using color-corrected NIR photometry to represent the stellar mass fraction. For the dark halo, the mass density distribution was chosen to be an axisymmetric isothermal sphere with a core. The potential of the halo was calculated in the two-dimensional plane of each galaxy's disk. The sequence of potentials was assembled by preselecting certain disk mass fractions and adjusting the halo parameters so that the rotation curve emerging from the total potential matches the mean observed H II rotation curve. The hydrodynamic simulations were performed by using the BGK hydro-code, contributed by Adrianne Slyz. This is a Eulerian, grid based hydrodynamics code which is derived from gas kinetic theory. The gas density distributions and gas velocity fields resulting from these simulations were then compared to the observed galaxy morphologies and to the measured H II kinematics. The comparison enables the study of the disk dynamics as well as relative luminous-to-dark matter fractions for the sample galaxies. The inferences from this analysis, presented in detail in Chapters 4 to 6, will be now discussed in context in this final Chapter.

7.1. Results from the analysis

7.1.1. The color correction

First, a short conclusion about Bell & de Jong's color correction is given, since this correction plays a fairly important role for the project. Bell & de Jong (2001) showed, based on population synthesis models and a universal IMF, that a galaxy's color can be related to its mass-to-light ratio. This applies to a galaxy's global color as well as to local colors. Consequently, this relation can be employed to improve the estimate of the stellar surface mass density distribution, $\Sigma_\star$, of galaxies taken from the measured NIR surface brightness,

μ_K, by using color maps of the galaxy:

$$2.5 \log \Sigma_\star = -\mu_K + a_V(V-K) + c_V \qquad \text{for the example of } (V-K) \text{ color maps.} \quad (7.1)$$

Although this correction is physically motivated, its performance must be examined carefully since much of the correction relies on empirical constants a and c[1] determined from numerical studies. Bell & de Jong themselves used the relations in their paper to explore the stellar mass Tully-Fisher relation of the Ursa Major Cluster. Their results were in support of a universal stellar IMF for normal spiral galaxies.

Since this is a very recent approach that has not yet been applied in the present context, there is no reported experience with two dimensional color corrections available from the literature. Thus, it is interesting to look at the experimental evidence from this study, regarding the performance of this approach as applied to late type spiral galaxies.

At first, applying the correction maintains the radial exponential profile of spiral galaxy disks. This very basic characteristic of spiral galaxy disks can be found in optical and NIR wavelengths and reflects the overall stellar mass distribution. The color correction retains this characteristic and, moreover, it can sometimes even scale down local deviations from the pure exponential profile (e.g., for NGC 6643). Secondly, the color corrected morphology appears dynamically realistic. The correction procedure does not create features in a galaxy's disk, whose existence would require complicated dynamic processes that disagree with density wave theories or that cannot be observed in numerical experiments.

Further, the correction not only applies to population differences, but also works for moderate dust absorption ($\tau_{\rm opt} < 1$). Dust extinguishes preferentially the optical stellar light, making it dimmer. On the other hand it also reddens the stellar populations, implying a larger stellar M/L. To first order, these effects cancel out. A good example for the color correction success is again the moderately dusty NGC 6643. As expected for such a procedure, the corrected K-band radial profile appears less dust-affected than the uncorrected one (see Figure 6.19).

Despite the above cited success of the color correction for NGC 6643, the derived mass map still bears systematic uncertainties from the fact that NGC 6643 is classified as a starburst galaxy. The same applies to NGC 5676. The high luminosity end of a starburst galaxy IMF is distinctly different from the universal IMF that was adopted to derive the M/L to color relation. Bursts of star formation bias the stellar M/L to lower values at a given color. However, even for starburst galaxies the color correction provides an improved mass map as compared to the K-band. Its application is still favorable, but the bias from the starburst should be kept in mind.

Another beneficial consequence of the color correction is the fact that it accounts for the outward blueing of the disk. Color gradients are very common in disk galaxies, since the bulge is generally populated by older stars than the disk. In all the examined cases, the color correction yields a shortening of the disk scale length, which can be attributed to this effect. Interestingly, even in the K-band, which is usually considered as a quite good estimate of the stellar mass distribution, the color correction changes the radial scale length

[1] The constant c combines both empirical parameters and ones that are specific to the particular galaxy that is studied: $c = c\prime + \mu_\odot$, where $c\prime$ is the empirical constant and $\mu_\odot$ is the surface brightness of $1\,{\rm M}_\odot$ at the galaxy's physical distance.

of a galaxy by about 10 %. Consequently, this causes the inferred radial force components in the disk to change their magnitude, affecting the shape of the rotation curve. However, using K-band photometry this is not a major concern when fitting rotation curves to medium resolution data because it simply implies a small change in the halo parameters (see Figure 4.2). More attention should be paid to the correction effects if the two dimensional force field within a galactic disk is studied. The non-axisymmetric forces that appear due to inhomogeneities in the stellar mass density distribution, amount to only 2 – 5 % of the total forces, however, the color correction can considerably affect them. For the galaxies in the sample, the non-axisymmetric force components changed by $\sim 30\,\%$ (median). These effects are not negligible for accurate studies.

Based on the experience gained from this project, the use of the color-correction to account for local stellar population differences is strongly encouraged when properties of galactic disks are studied which rely on their stellar mass distributions. The use of more than only two colors for the correction, could further improve the quality of the mass density distribution that can be derived.

7.1.2. Disk dynamics

The secular evolution of spiral structures in disk galaxies is an issue that has not yet been satisfyingly understood. The debate is about whether spirals arise from quasi-stationary, self-sustained density waves, or if they are transient features, triggered by internal or external processes, that fade away if not continuously replenished. However, this study is not very dependent on the long-term evolution of the spiral. The gravitational potentials used for the modelling are calculated from the morphological "snapshot" that the measurements provide and were not allowed to evolve during the simulation process. Nevertheless, one crucial assumption about the disk dynamics had to be made to link the snapshot character of the simulation to the long term evolution of the spiral pattern: It was necessary to adopt a constant pattern speed for the dominant spiral structure in time as well as in the radial extent. This is more a technical assumption that is necessary for the simulations, rather than an established result from the literature. However, in the end this approximation might not be far off. The fact that most of the simulations yield gas distributions and velocity fields that reproduce very well the observed gas properties leads to the conclusion that a quasi-stationary spiral pattern is probably a good first order approximation for all spiral galaxies from the sample. Furthermore, it must be noted that the modelling only requires that the spiral morphology is stable over about one dynamical period, the time required for the gas to adjust to moderate changes in the pattern speed. Aside from some subtle evidence that weak central bars reveal pattern rotations that are decoupled from the rest of the disk, the rigid spiral pattern assumption seems to be consistent for most of the studied disks.

7.1.2.1. Location of the corotation resonance

In light of the above, the determination of resonance locations within galactic disks actually has some meaning. With the simulation techniques described in this thesis, it is possible to measure the dynamic state of the disk from its gas kinematics. This determination is essentially independent of the density wave theory applied to explain the disk dynamics. It has been proven already that such kind of approach yields valuable information on disk

dynamics of several galaxies, like M 51 (Garcia-Burillo et al. 1993), M 100 (Garcia-Burillo et al. 1994), NGC 7479 (Sempere et al. 1995) and M 94 and NGC 3310 (Mulder & Combes 1996). However, since these studies were mostly dealing with single systems, the results were not put into a more general context.

The present study consists of a sample of five galaxies, for which it was possible to individually identify the location of the corotation resonances with a comparably high precision. Table 7.1 compiles the results for the five analyzed galaxies. Already from this rather small sample it is possible to outline general trends for spiral galaxies.

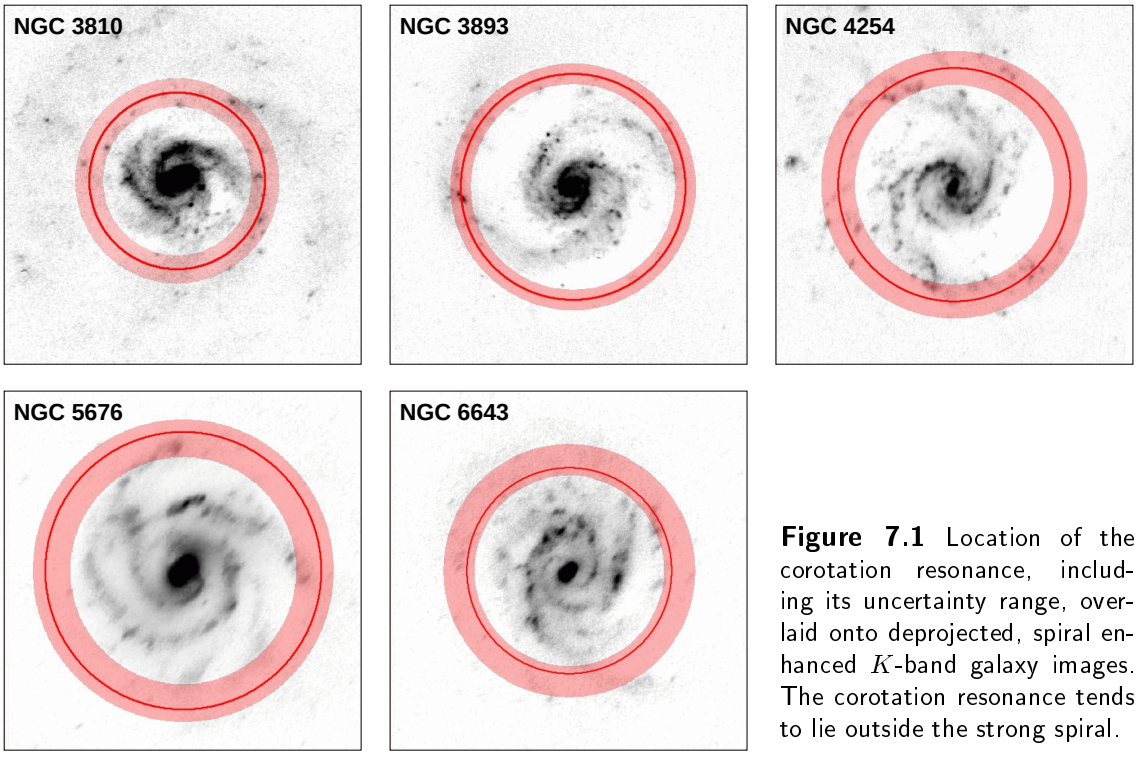

Figure 7.1 Location of the corotation resonance, including its uncertainty range, overlaid onto deprojected, spiral enhanced K-band galaxy images. The corotation resonance tends to lie outside the strong spiral.

First, one can examine the spiral morphologies and how they reflect the dynamical state of the disk. In the modal theory of spiral structure (Bertin et al. 1989a,b) the corotation resonance is typically located in the outer parts of the optical disk, where the gas-to-star density ratio is larger. The stellar spiral should exhibit a basic continuity across the corotation resonance and a reversal of the properties of the spiral tracers, such as the locations of H II-regions (Bertin 1993). As it is apparent from Figure 7.1, these predictions are only partly satisfied for the galaxies from the sample. On the other hand, some of the galaxies reveal multi-arm or flocculent spiral properties that cannot be explained by linear, quasi-stationary modal theories. Non-linear mechanisms or transient amplification processes might play important roles and affect the location of the corotation resonance too. The results from non-linear orbital modelling of spiral structures (Patsis et al. 1991) indicate that the strong, symmetric, logarithmic stellar spirals end already at the inner 4:1 resonance, located well inside the corotation resonance. In this picture, the end of the strong spiral pattern is found at a radial range of 2 – 3 exponential disk scale lengths. As seen from Figure 7.2, the corotation radii from this project's galaxy sample tend to fall in that range.

Table 7.1 Corotation radii and exponential scale lengths for the galaxies from the simulation sample, calculated for the respective distance estimation. $R_{\rm exp}(K'_{\rm corr})$ specifies the color corrected exponential scale lengths. All values are given in kpc.

Galaxy	NGC 3810	NGC 3893	NGC 4254	NGC 5676	NGC 6643
$R_{\rm CR}$	3.15 ± 0.5	5.5 ± 0.5	7.5 ± 1.1	$11.0\ ^{+1.0}_{-2.0}$	$6.5\ ^{+1.5}_{-0.5}$
$R_{\rm exp}(K')$	1.07	1.80	3.54	3.59	2.72
$R_{\rm exp}(K'_{\rm corr})$	0.913	1.74	3.06	3.12	2.48

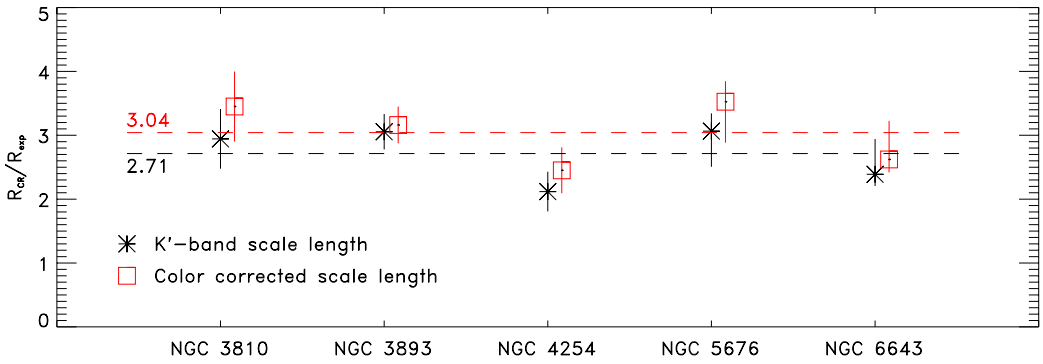

Figure 7.2 Location of the corotation radius in terms of the exponential disk scale length for the sample galaxies. The asterisks mark the values for the K-band disk, while the red boxes refer to the color corrected scale lengths. The error bars come from uncertainties in the corotation radius estimations. The horizontal lines represent the mean values.

Taking the K-band exponential disk scale length, the mean ratio of the corotation radius and the disk scale length is 2.71 ± 0.43, increasing to 3.04 ± 0.49 for the color corrected exponential disk scale lengths. Figure 7.1 compares these corotation radii to the image morphologies. Clearly, the dominant two-arm pattern in these galaxies lies mostly within the corotation resonance. This finding agrees fairly well with the conclusions of Patsis et al. (1991) and Patsis & Kaufmann (1999), derived from non-linear orbital modelling. However, also the linear modal theory of spiral structure predicts that the corotation radius falls into the radial range, which was found for the sample galaxies discussed here (Bertin 1993 states $R_{\rm CR} \approx 3-4\,R_{\rm exp}$). Thus, the locations of the corotation resonances in the sample galaxies are mostly in agreement with the predictions from linear as well as non-linear theories. The good agreement between the measured disk properties and the theoretical expectations from spiral density wave theories can be regarded in support of these theories.

Determining the location of the corotation resonance from hydrodynamic modelling is a rather elaborate and time consuming process. However, looking at Figure 7.1 it becomes clear that there is no obvious common feature in the galactic disks that would enable an easy identification of the corotation resonance otherwise. It is not always the case that at corotation the star forming rate is largely reduced. Furthermore, there is no characteristic

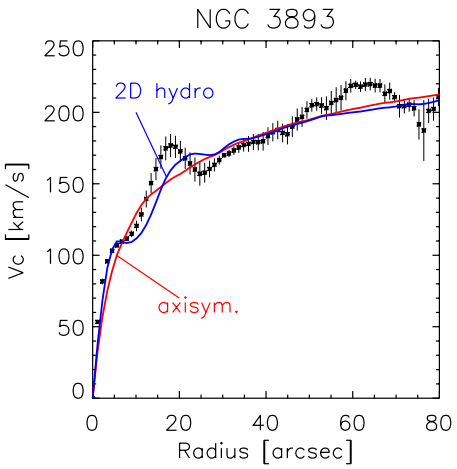

Figure 7.3 Effect of the two dimensional simulation on the average rotation curve, displayed for NGC 3893. The two dimensional fit (blue curve) provides a better general representation of the rotation curve features than the axisymmetric fit (red curve) does. However, the large wiggle is slightly misplaced.

feature in the amplitudes of the low Fourier components at the radius of the corotation resonance. This lack of any reliable corotation tracer complicates the connection between density wave theories and their application to real galaxies. Eventually, the appearance of any real galaxy in the universe is the product of a combination of many processes. In some cases, the linear modal density wave theory can be applied to describe the relevant issues, but in many galaxies non-linear effects in the density wave dynamics and other processes seem to play a role. Nevertheless, assuming a fixed spiral pattern rotation speed seems, to first order, to be a viable assumption for the simulations of gas flows in fixed galaxy potentials. In light of this, it is a very promising conclusion that the hydrodynamic gas simulations provide a powerful tool to learn about disk dynamics and to determine the location of resonances in spiral galaxies.

7.1.2.2. The disk kinematics

In addition to the good agreement of the simulated gas density distribution with the observations, the modelled gas velocity fields provide a good overall match to the measured kinematics too. In all cases, the global structure of the velocity field could be reproduced with satisfying accuracy by the model velocity field. This is a very non-trivial result which speaks highly for the fine quality of the hydrodynamics code.

Furthermore, the simulated two dimensional velocity fields also tend to render rotation curve features that can never be fitted by an axisymmetric model. This is shown for the averaged rotation curve of NGC 3893 in Figure 7.3. Although the match of the large wiggle at about $18''$ radius is not perfect, the simulated velocity field provides a better general representation of the rotation curve features.

In order to achieve the goals of this project, the above mentioned good performance of the hydrodynamic code was actually a mandatory prerequisite. The focus of the analysis was mainly on comparing the amplitude of individual wiggles and rotation curve features to the observations. To yield good results the code was required to not only reproduce global gas dynamics but also to properly model the small scale features. However, within the galactic disks, there are also other processes than local gravity fluctuations which create additional gas-dynamic effects. The gas dynamic traces of expanding supernova gas shells

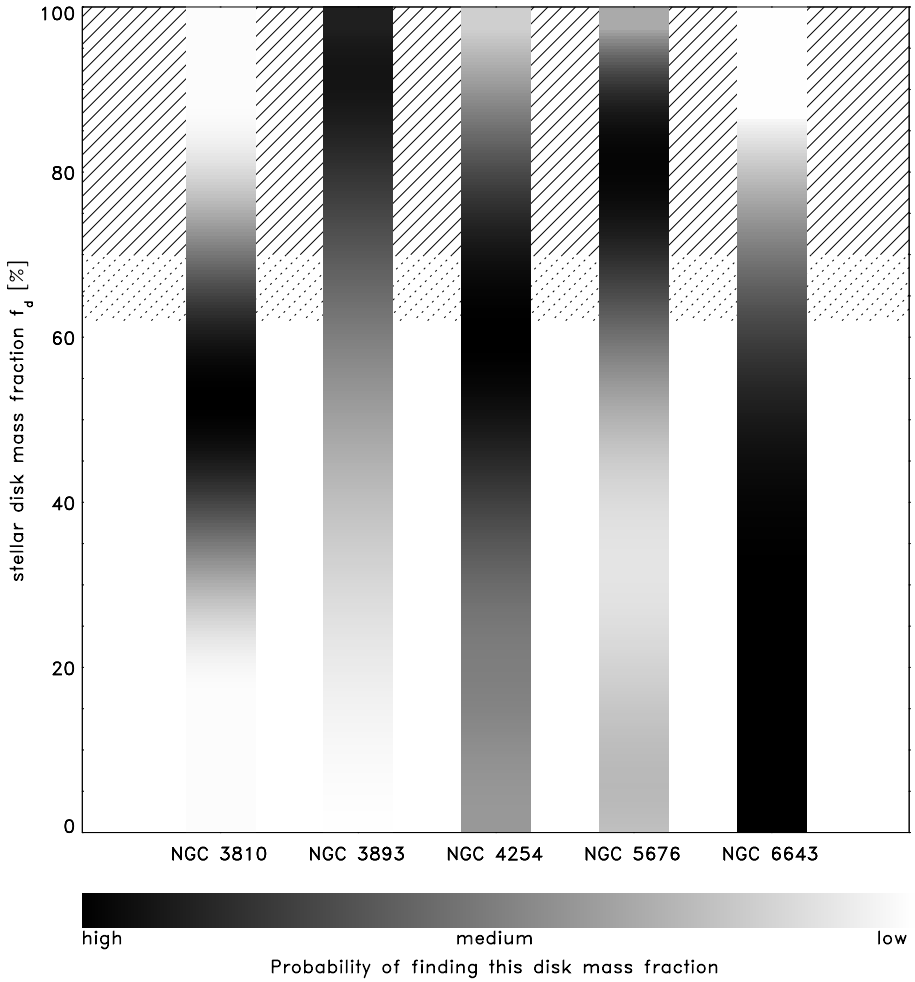

Figure 7.4 Graphical presentation of the simulation results regarding the dark matter content in the galaxies from the sample. The hashed area marks the region of maximal disks, according to the definition of Sackett (1997).

or outflows from young star forming regions are superimposed on the larger scale response to the gravitational potential wells and can eventually cover up the features that are relevant for this project. Indeed, for NGC 3810 and NGC 4254, which are galaxies with a high abundance of such "polluting" small scale velocity features in the velocity field, the model-to-data comparison allowed only less far reaching conclusions.

7.1.3. The dark matter content in the analyzed galaxies

The main objective of this study was to find the relative stellar disk to dark halo mass fractions. All conclusions were drawn from the comparison of modelled gas flows within realistic galaxy gravitational potentials of known dark and luminous matter composition. The potentials were assembled by preselecting the stellar mass contribution in terms of the maximum possible stellar mass fraction $f_d\Phi_\star$, and adding in the halo contribution to reproduce the averaged rotation curve of the galaxy. Five models were analyzed for each

galaxy with discrete values for f_d

$$\Phi_{tot}(\boldsymbol{R}|f_d) = f_d\,\Phi_\star(\boldsymbol{R}) + \Phi_{halo}(\boldsymbol{R}|f_d) \qquad \text{with } f_d = 0.2, 0.45, 0.6, 0.85 \text{ and } 1. \tag{7.2}$$

The results from the model-to-data comparison is presented in Figure 7.4 for the five galaxies NGC 3810, NGC 3893, NGC 4254, NGC 5676 and NGC 6643. The vertical axis on the five bars represent the probability that a certain mass model applies to the specific galaxy. These probabilities were determined by performing a least squares comparison between the simulated gas velocity fields and the observed kinematics of the system. As can be seen from Figure 7.4, the precision with which a certain scenario can be attributed to a particular galaxy is not equally good for all sample galaxies. For NGC 3893 the disk mass fraction could be identified very well, placing this galaxy into the realm of maximum disks. Both for NGC 3810 and NGC 6643 the least squares comparison mostly argued for a light to medium disk scenario. Especially for NGC 6643 the analysis was difficult since this galaxy exhibits only a weak stellar spiral density wave, leading to a larger uncertainty range for the disk mass fraction. The analysis of NGC 4254 suffered from the high abundance of strong non-gravitationally induced gas kinematic features in the observed velocity field. The main conclusion for NGC 4254 was to exclude the strictly maximal disk solution. For NGC 5676 the χ^2-analysis mostly argues for a heavy disk scenario, although the simulations were only partly successful, so far allowing only preliminary conclusions.

As defined by Sackett (1997), the designation "maximal disk" applies to a galactic disk when $85 \pm 10\,\%$ of the total rotational support of a galaxy at a radius $R = 2.2\ R_{exp}$ is contributed by the stellar disk mass component. In the extreme case of $v_{disk} = 0.75\,v_{tot}$, this definition allows a relatively massive halo to almost comprise the same amount of mass as the disk within that radius.

The above definition translates into the notation used here in the following way: Reading from Equation (4.12), the rotational support from the stellar disk is $v_{disk}(R_{2.2}) = \sqrt{f_d}\,v_\star(R_{2.2})$, where $v_\star(R_{2.2})$ is the rotational support from the maximal stellar disk at a radius of 2.2 disk scale lengths. Since also a maximal disk model includes a halo contribution $v_\star(R_{2.2}) = f_{max}\,v_{tot}(R_{2.2})$, with f_{max} typically 0.9. Accordingly, the rotational support from the disk is about 0.9 ($f_d = 100\,\%$), 0.83 ($f_d = 85\,\%$), 0.7 ($f_d = 60\,\%$), 0.6 ($f_d = 45\,\%$), and 0.4 ($f_d = 20\,\%$). All of the $f_d = 85\,\%$ models clearly represent maximal disk scenarios. The $f_d = 60\,\%$ models are at the lower border of the maximal disk realm, representing compositions with about an equal amount of dark and luminous mass within 2 – 3 exponential disk scale lengths.

In light of this, Figure 7.4 shows that a maximal disk scenario applies to NGC 3893 and NGC 5676. For the other galaxies the results from the modelling favor less massive stellar disks. NGC 3810, NGC 4254 and NGC 6643 possess stellar disks that appear to balance the mass of the dark halo inside the optical disk ($f_d \approx 60\,\%$), although for NGC 6643 an even lighter stellar mass component could not be excluded.

Table 7.2 gives an overview of the stellar mass-to-light ratios that could be derived from the calculations of the potentials (see Section 4.1.5). The values are given for a maximum disk and mostly fall in the range between $M/L_K = 0.6 - 0.7$. A smaller value for M/L_K was only found for NGC 4254. These stellar mass-to-light ratios agree very well with those emerging from the color correction procedure of Bell & de Jong (2001), which are

Table 7.2 Maximum disk stellar K-band mass-to-light ratios and the associated mass of the stellar disk. Given are the M/Ls, which were used to calculate the galaxy potentials and the ones that the Bell & de Jong (2001) color correction yields for the respective overall galaxy colors. The disk mass has been scaled for the galaxies' most probable disk mass fraction f_d. All values are given in solar units.

Galaxy	NGC 3810	NGC 3893	NGC 4254	NGC 5676	NGC 6643
M/L_K	0.63	0.56	0.23	0.67	0.71
M/L_{BdJ}	0.55	0.54	0.74	0.83	0.65
M_{disk}	0.89×10^{10}	2.32×10^{10}	2.12×10^{10}	8.12×10^{10}	2.54×10^{10}
f_d	60 %	100 %	60 %	85 %	60 %

based on population synthesis models[2]. Using these mass-to-light ratios, the total mass of the stellar disk can be inferred. The values given in Table 7.2 apply to a disk mass fraction which, as taken from Figure 7.4, is a reasonable assumption for the particular galaxy. These disk masses appear realistic and scale well with the maximal velocities in the rotation curves, i.e. attributing a high disk mass to NGC 5676 and a light disk to NGC 3810. The mismatch for NGC 4254 appears to be a modelling inconsistency rather than a characteristic of the galaxy. It might be related to the possibility that, after all, the disk inclination might not have been determined correctly, and that the rotation velocity and disk mass scale differently.

7.1.3.1. Discussion

Much evidence has accumulated in recent years that the disks of high surface brightness spiral galaxies dominate the dynamics of the inner regions. Most of the studies arguing for a maximal disk scenario, are based on the detailed analysis of high resolution rotation curve measurements (Blais-Ouellette et al. 1999; Palunas & Williams 2000; Ratnam & Salucci 2000; Salucci 2001). These studies, however, generally derive the rotational support of the stellar disk from an axisymmetric disk mass model and allow no consideration of non-circular rotation components. More sophisticated modelling strategies have been applied to spiral galaxies with variable significance (Erickson et al. 1999; Pignatelli et al. 2001). Mostly those studies also support heavy disks for high surface brightness galaxies but find also candidates for which lower disk mass fractions are more likely. The most convincing arguments for the maximal disk scenario come from the studies of strong bars in spiral galaxies. These features induce a strong dynamic trace in the velocity field and provide a good laboratory for estimating the stellar mass component. Based on fluid dynamic modelling, Englmaier & Gerhard (1999) find a maximal disk solution for the Milky Way and Weiner et al. (2001a) for the disk of NGC 4123. Furthermore, theoretical considerations argue for the requirement of a non-massive halo contribution in the central regions of strongly barred galaxies, because otherwise dynamical friction would slow down the bar very quickly, leading to its destruction (Debattista & Sellwood 1998, 2000).

[2]Bell & de Jong (2001) used an initial mass function that was scaled to a maximal disk scenario, which was established from measured disk kinematics. In light of this, also the population synthesis M/Ls eventually rely on disk dynamics.

However, there is also evidence that even high surface brightness spiral galaxies might be dominated by the dark matter mass component in their central disk regions. Bottema (1997) inferred from stellar velocity dispersions in spiral galaxy disks that a more massive halo component is needed to explain the findings. There are two recent studies that argue for lighter disk models by making use of previously hardly exploited, relations. Courteau & Rix (1999) applied a statistical Tully-Fisher relation analysis to a large sample of galaxies trying to relate the maximal rotation velocity of a galaxy to its disk size. Maller et al. (2000) used the geometry of a gravitational lensed system to disentangle the effects of the stellar disk and the halo mass. Both groups found that the dark halo also dynamically dominates the galaxies' inner regions.

The results from this study fit well into the overall picture that has emerged lately. Even the population of high surface brightness spiral galaxies seems to comprise not an entirely homogeneous class of objects. As it can be inferred from the maximum rotation velocity, presented in Figure 3.7, the most massive of the analyzed galaxies, NGC 3893 and NGC 5676, tend also to possess the most massive stellar disks which dominate the dynamics of the central regions. The other galaxies from the sample are less massive systems that exhibit a maximum rotation velocity $v_c < 200\,\mathrm{km\,s^{-1}}$. For those objects the total mass of the dark halo within the optical radius is higher and was found to, at least, equal the stellar mass. This trend is graphically presented in Figure 7.5. In light of this, the results from Courteau & Rix (1999) might be explained that in a statistical sample of spiral galaxies the heavy and clearly maximum disk galaxies account for only a relatively small fraction and most of the "lighter" high surface brightness galaxies exhibit already a considerable dark mass fraction.

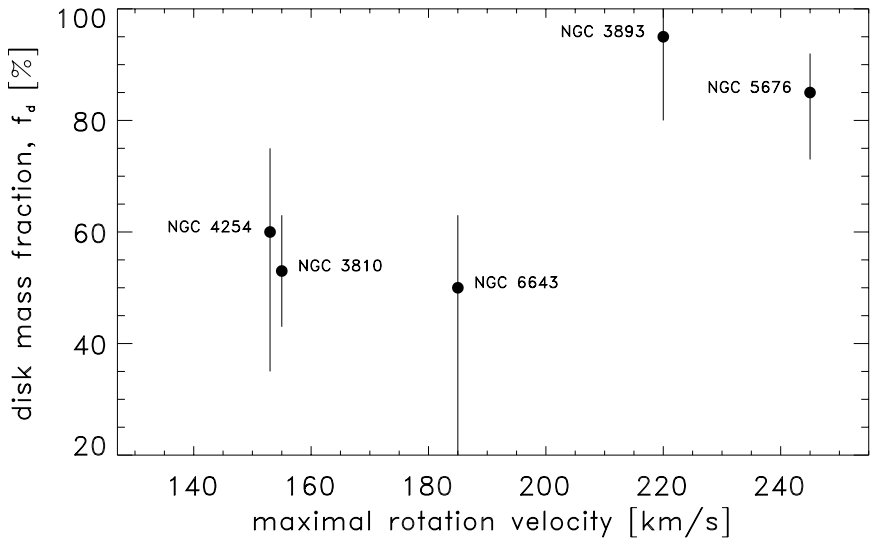

Figure 7.5 The galaxies from the analyzed sample can be separated into two classes. The most massive galaxies – as inferred from their maximum rotation velocity – tend to possess also disks with high mass fractions, f_d. Less massive systems exhibit already a considerable dark mass fraction.

However, beyond the discussion of the disk mass fraction in spiral galaxies, at present there is growing evidence that galaxy size dark halos are not cuspy in their centers, as claimed by standard cold dark matter (CDM) models. (Moore 1994, Flores & Primack 1994, Moore et al. 1999b, Salucci & Burkert 2000; Boriello & Salucci 2001; de Blok et al. 2001, van den Bosch & Swaters 2001). This circumstance was first found for low surface brightness and dwarf galaxies, that supposedly are comprised of a massive dark halo. Most of the authors argued that this also applies to high surface brightness galaxies. For the present analysis, the functional form of the dark halo profile has only a second order effect on the results as long as the models describe well the overall shape of the observed rotation curves. Thus, it was decided not to distinguish between different dark halo profiles. However, the results from this study, which mostly confirm the strong dynamic influence of the stellar disk in massive high surface brightness spiral galaxies within the optical radius, provide evidence that the halo is not particularly cuspy at its center.

After all, the dark matter research is far from presenting a conclusive and self consistent picture. The new observational evidence against standard CDM models challenge the future for the CDM cosmology and the nature of the dark matter that is involved in building our present day galaxies.

7.2. Lessons learned and outlook

It has been demonstrated with this project that an analysis similar to the one applied to barred galaxies (Englmaier & Gerhard 1999; Weiner et al. 2001) can also be applied to non-barred spiral galaxies. This fact should not be taken for granted, since the spiral arms provide a much less prominent dynamical feature in the velocity field than a strong bar does. In the end, however, the precision of the conclusion that can be drawn depends extremely on the strength of the spiral structure. If the spiral arms appear strong and well defined, significant conclusions could be drawn. A good example confirming this trend was the analysis of NGC 3893. This galaxy exhibits a clear grand design structure with strong spiral arms. The comparison of the simulations to the observations yielded a good agreement.

The reason for the strong spiral structure in NGC 3893 is the interaction with its companion NGC 3896 that triggered the density wave during a recent flyby. Due to the initial suspicion towards interacting systems for not being in a stationary state and therefore possibly presenting gas dynamics that are difficult to model, most of these systems were rejected during the sample selection. In the end, however, the contrary has turned up. As long as the galaxy is not undergoing a major merger, the interaction does not seem to spoil the analysis, but allows even wider conclusions. Apparently the gas responds rather quickly to the gravitational pull of an enhanced density wave and an equilibrium is reached rapidly. A strong gas response to a triggered density wave has also been found for other interacting systems, e.g., M81 (Visser 1980; Adler & Westpfahl 1996) and M51 (Aalto et al. 1999). Eventually, this class of objects might comprise the best suited galaxies for this kind of analysis.

Still, strong spiral arms are not the only criterion that determines the success of the analysis. NGC 4254, for example, has a very strong arm to inter-arm density contrast, but the conclusions which could be drawn were only vague. Its velocity field contains a high

abundance of small scale "noise" induced by non-gravitational gas dynamic effects (SN-bubbles, etc.). These small scale wiggles corrupt the model-to-observation comparison and complicate the identification of the best mass model. Smooth galaxy velocity fields hint for better candidates.

Considering these criteria it must be stated that the final galaxy sample, which has been made available for this study via the initial sample selection and various observing constraints, was only moderately suited. The spiral structures of NGC 3810 and NGC 6643 were very weak and posed a difficult case to enable robust conclusions from the hydrodynamic modelling. According to the experience gained from this project through the techniques described in this thesis, an ideal candidate for which one has a good chance of finding its relative dark to luminous mass fractions, exhibits strong spiral arms in NIR photometry data and a clear trace in the velocity field that is elsewhere smooth. Interactions do not necessarily spoil the success of this approach.

7.2.1. Outlook

Although this project is in principle completed, a few interesting developments are coming up in the near future that might improve the significance of results gained by such an approach. First of all, any future improvements of the code, like including gas self gravity or three dimensional capabilities, might allow an even better modelling of the gas flow. A. Slyz is continuously using the BGK hydrodynamics code for a variety of applications and its development will continue for several years.

In the same line, faster computers will allow higher grid cell numbers and therefore a better resolution of the modelled samples. Although the BGK code can also cope with low resolution grids, a better sampling of the gravitational potential will lead to a better approximation of the gas flow.

However, even if the resolution of the imaging data could not be fully applied to the modelling, high resolution data is still vitally important to create good mass maps for deriving the potentials. For nearby objects, high resolution imaging by powerful instruments (HST: WFPC2 and NICMOS, VLT: CONICA, ...) might help to get a better hold on the dust extinction effects that corrupt the quality of the observed mass maps of galaxies. On the side of the observed kinematics, sensitive high resolution integral field spectrographs (e.g., SAURON) will provide better and truly two dimensional observed gas velocity fields, that would allow a more complete comparison of the simulated gas properties to reality.

One final and very bold perspective might be to apply this strategy to probe the masses of galaxies at higher redshifts. In this way it might be possible to follow the buildup of the stellar mass in galaxies over time. However, even if this would be a very interesting project, it will not become feasible before the advent of NGST or comparable instruments.

APPENDIX
Appendix

This appendix consists of a compilation of Figures with simulation results from the galaxy sample discussed in Chapter 5 and Chapter 6. For the five galaxies NGC 3810, NGC 3893, NGC 4254, NGC 5676 and NGC 6643 tables are provided, listing the results from the least squares comparison between the measured and simulated kinematics. Furthermore it includes figures presenting the gas density match for the range of modelled pattern speeds and figures, comparing the measured and simulated velocity fields for the best fitting pattern speed along all of the observed position angles of the spectrograph.

A NGC 3810

Table A.1 χ^2/N of the comparison between observed and simulated kinematics for NGC 3810. $N = 971$ data points. The errors refer to $1\,\sigma$ χ^2/N-variations after simulation has passed the initialization phase.

f_d	corotation radius R_{CR} [kpc]							
[%]	3.15	3.43	5.04	6.14	6.45	7.00	7.79	
20	0.678	0.807	0.821	0.817	0.820	0.819	0.747	χ^2/N
	0.010	0.049	0.009	0.006	0.008	0.014	0.008	$\pm\,(1\,\sigma)$
45	0.771	0.909	1.534	3.357	3.212	1.595	—	χ^2/N
	0.005	0.011	0.125	0.857	1.267	0.159	—	$\pm\,(1\,\sigma)$
60	0.872	1.093	1.493	3.161	3.780	4.882	3.270	χ^2/N
	0.019	0.039	0.060	0.179	0.554	1.494	1.120	$\pm\,(1\,\sigma)$
85	1.165	(1.420)	2.217	3.248	3.404	2.857	—	χ^2/N
	0.035	(0.235)	0.139	0.634	0.644	0.396	—	$\pm\,(1\,\sigma)$
100	1.411	2.128	3.286	3.867	4.047	2.476	—	χ^2/N
	0.264	0.450	0.362	0.873	0.973	0.115	—	$\pm\,(1\,\sigma)$

Note: Values in brackets refer to runs that terminated before ending the initialization phase of the simulation.

Table A.2 median(χ^2) of the comparison between observed and simulated kinematics for NGC 3810. The errors refer to $1\,\sigma$ median(χ^2)-variations after simulation has passed the initialization phase.

f_d	corotation radius R_{CR} [kpc]							
[%]	3.15	3.43	5.04	6.14	6.45	7.00	7.79	
20	0.295	0.310	0.333	0.349	0.368	0.395	0.343	median(χ^2)
	0.005	0.010	0.005	0.004	0.005	0.008	0.004	$\pm\,(1\,\sigma)$
45	0.361	0.380	0.482	0.692	0.711	0.664	—	median(χ^2)
	0.009	0.007	0.018	0.099	0.106	0.029	—	$\pm\,(1\,\sigma)$
60	0.414	0.416	0.492	0.786	0.919	1.027	0.697	median(χ^2)
	0.009	0.007	0.008	0.054	0.059	0.169	0.016	$\pm\,(1\,\sigma)$
85	0.423	(0.415)	0.502	0.679	0.810	0.854	—	median(χ^2)
	0.011	(0.036)	0.008	0.028	0.030	0.056	—	$\pm\,(1\,\sigma)$
100	0.456	0.443	0.587	0.850	1.011	0.863	—	median(χ^2)
	0.053	0.046	0.037	0.056	0.089	0.011	—	$\pm\,(1\,\sigma)$

Note: Values in brackets refer to runs that terminated before ending the initialization phase of the simulation.

NGC 3810, $f_d = 60\,\%$

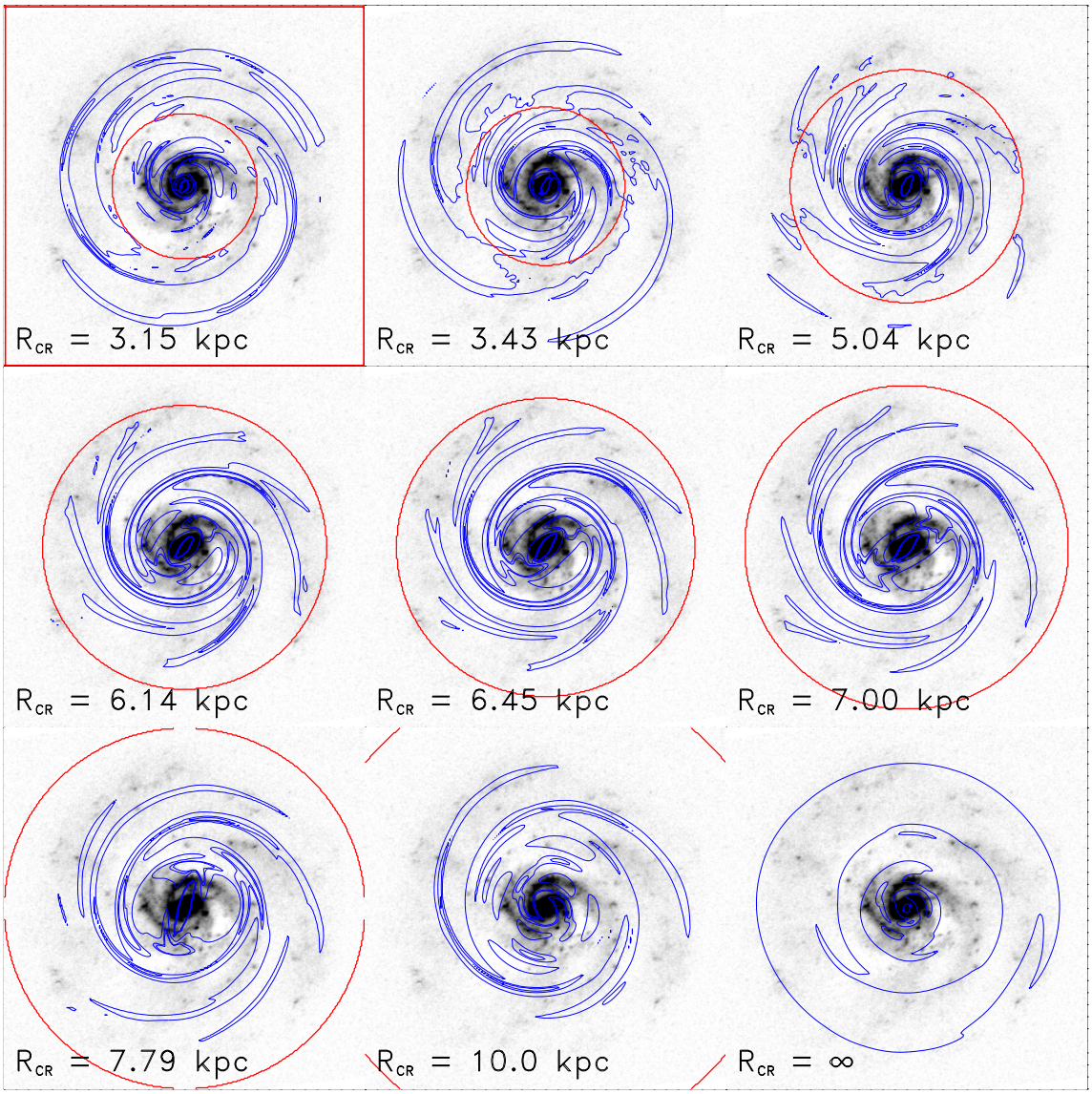

Figure A.1 Morphology comparison between the simulated gas density field (in contours) and the the observed structure of NGC 3810 (underlying, contrast enhanced image). Shown are the results for the $f_d = 60\,\%$ runs. Displayed is always the last time step during a simulation run (see Table 6.1). The red circle gives the location of the corotation resonance, that applies to the particular simulation. The red bordered panel displays the simulation with the best matching parameter set.

NGC 3810, $f_d = 20\,\%$, $R_{CR} = 3.15\,\mathrm{kpc}$

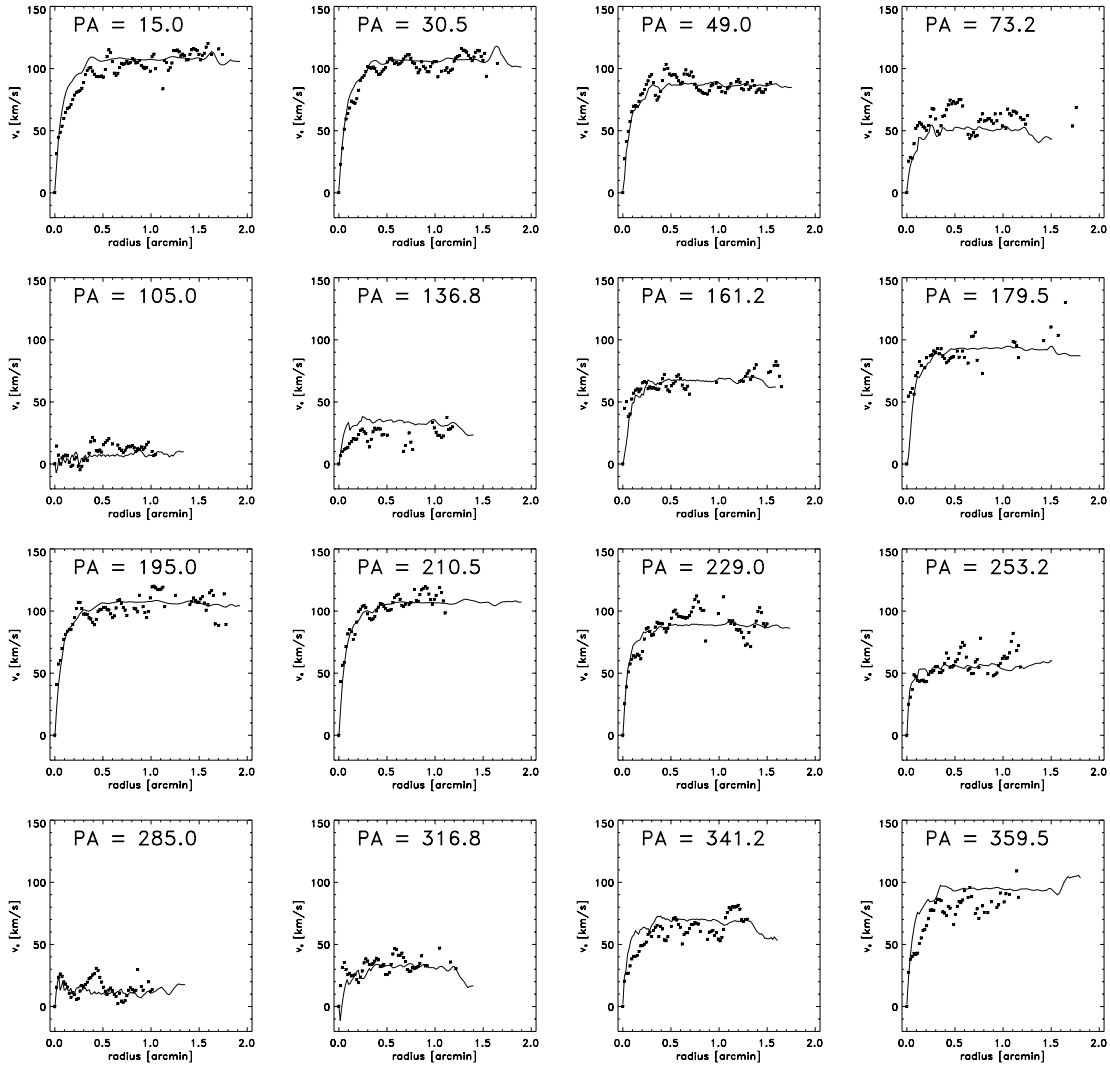

Figure A.2 Comparison of the measured (data points) and simulated (continuous line) kinematics. The results are displayed for NGC 3810 with a light disk ($f_d = 20\,\%$) and $R_{CR} = 3.15\,\mathrm{kpc}$.

NGC 3810, $f_d = 85\,\%$, $R_{CR} = 3.15\,\mathrm{kpc}$

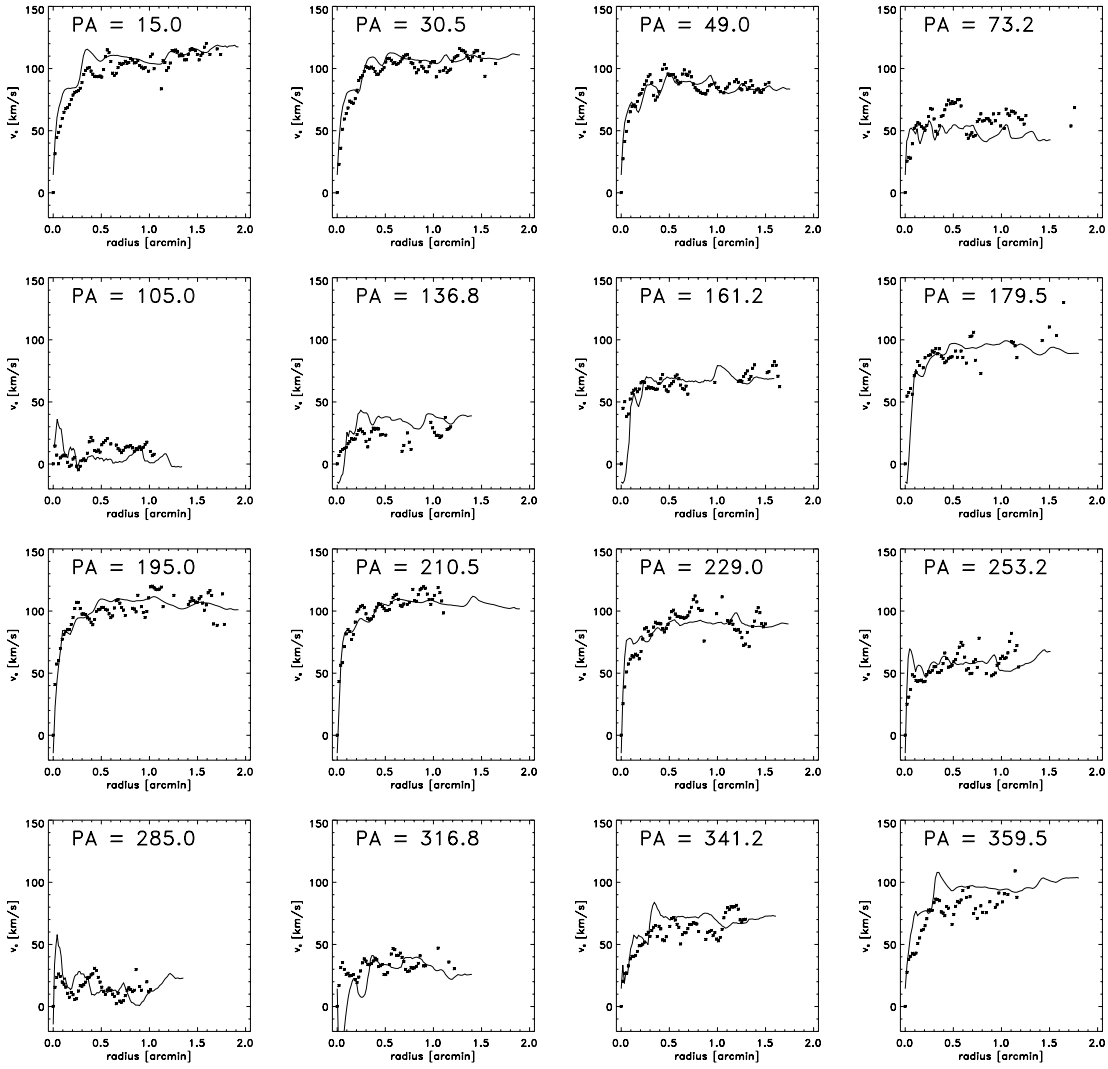

Figure A.3 Comparison of the measured (data points) and simulated (continuous line) kinematics. The results are displayed for NGC 3810 with a heavy disk ($f_d = 85\,\%$) and $R_{CR} = 3.15\,\mathrm{kpc}$.

NGC 3810, $f_d = 60\,\%$, $R_{CR} = 3.15\,kpc$, selected data

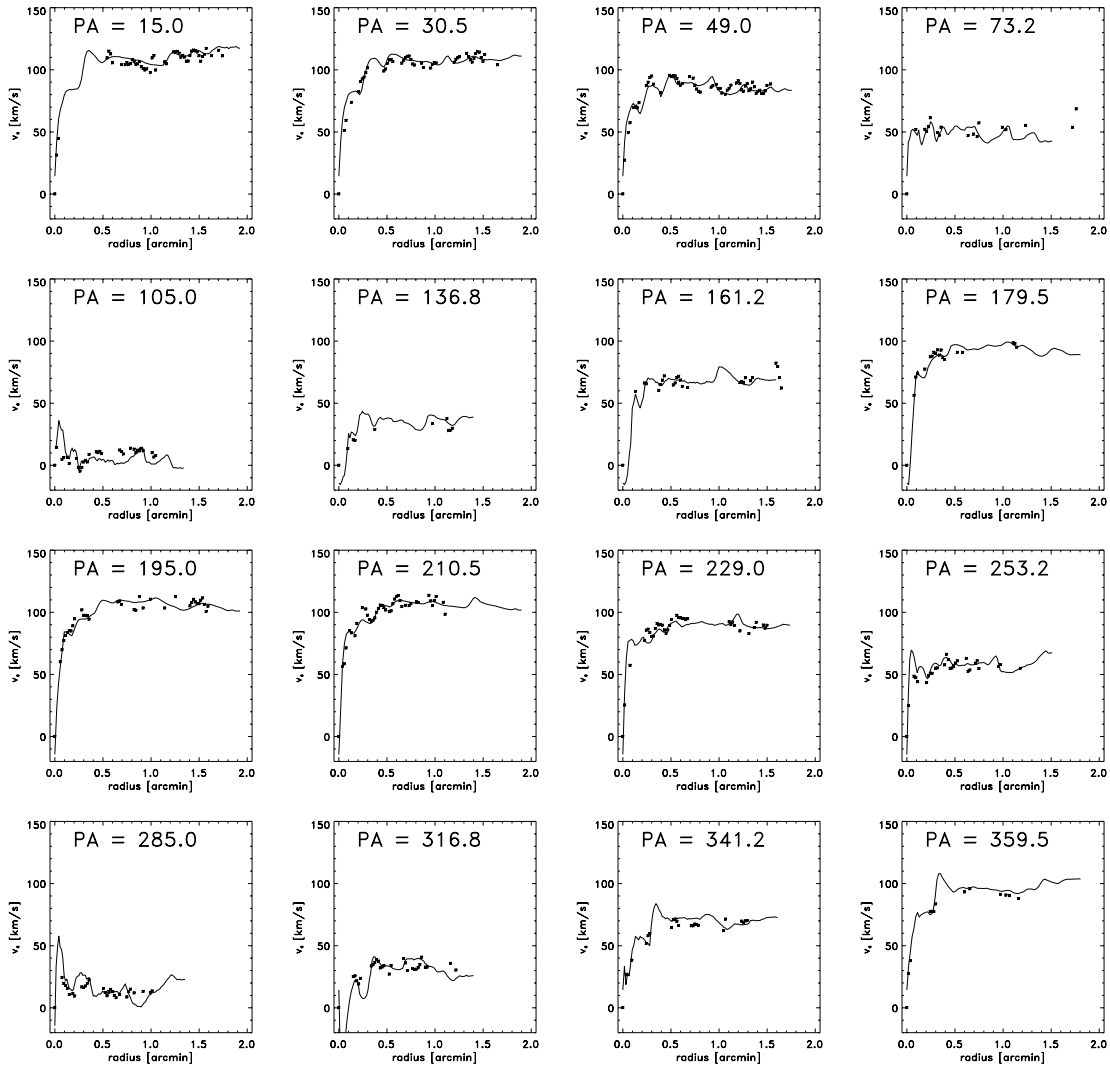

Figure A.4 Comparison of a selection of the measured kinematics (data points) and simulated (continuous line) kinematics. A selection criterion was introduced to only look at parts of the observed velocity field where the gas dynamics is mainly induced by gravity. About 49 % of the initial data points are used for comparison. See Section 4.3.2.1 for a description of the method. The results are displayed for NGC 3810 with a medium disk ($f_d = 60\,\%$) and $R_{CR} = 3.15\,kpc$.

Table A.3 χ^2/N and median(χ^2) of the comparison between observed and simulated kinematics for NGC 3810. Considered were only $N = 474$ selected data points.

Disk fraction f_d [%]	20	45	60	85	100
χ^2/N	0.319	0.220	0.221	0.314	0.427
median(χ^2)	0.107	0.122	0.115	0.134	0.125

B NGC 3893

Table B.1 χ^2/N of the comparison between observed and simulated kinematics for NGC 3893. $N = 911$ data points. The errors refer to $1\,\sigma$ χ^2/N-variations after simulation has passed the initialization phase.

f_d	corotation radius R_{CR} [kpc]								
[%]	3.18	5.47	6.46	7.06	7.55	8.56	9.84	∞	
20	(1.382)	1.355	1.355	1.343	1.343	1.327	1.307	1.455	χ^2/N
	(0.018)	0.003	0.005	0.002	0.004	0.005	0.009	0.005	$\pm\,(1\,\sigma)$
45	—	1.217	1.213	1.173	1.148	1.127	1.383	1.423	χ^2/N
	—	0.005	0.010	0.005	0.008	0.018	0.025	0.009	$\pm\,(1\,\sigma)$
60	(1.145)	1.095	1.118	1.147	1.205	1.455	1.744	1.393	χ^2/N
	(0.031)	0.004	0.012	0.018	0.009	0.048	0.131	0.013	$\pm\,(1\,\sigma)$
85	(1.046)	1.144	(1.114)	1.461	1.566	1.540	1.570	1.426	χ^2/N
	(0.040)	0.018	(0.032)	0.067	0.046	0.049	0.050	0.022	$\pm\,(1\,\sigma)$
100	(1.053)	1.046	1.251	1.240	1.365	1.694	1.868	1.526	χ^2/N
	(0.033)	0.005	0.015	0.037	0.050	0.113	0.056	0.027	$\pm\,(1\,\sigma)$

Note: Values in brackets refer to runs that terminated before ending the initialization phase of the simulation.

Table B.2 median(χ^2) of the comparison between observed and simulated kinematics for NGC 3893. The errors refer to $1\,\sigma$ median(χ^2)-variations after simulation has passed the initialization phase.

f_d	corotation radius R_{CR} [kpc]								
[%]	3.18	5.47	6.46	7.06	7.55	8.56	9.84	∞	
20	(0.457)	0.463	0.440	0.464	0.448	0.448	0.446	0.472	median(χ^2)
	(0.017)	0.005	0.005	0.006	0.005	0.003	0.007	0.007	$\pm\,(1\,\sigma)$
45	—	0.431	0.430	0.431	0.414	0.368	0.478	0.467	median(χ^2)
	—	0.005	0.008	0.013	0.006	0.008	0.009	0.008	$\pm\,(1\,\sigma)$
60	(0.361)	0.405	0.365	0.414	0.390	0.467	0.467	0.470	median(χ^2)
	(0.013)	0.008	0.010	0.010	0.006	0.012	0.024	0.008	$\pm\,(1\,\sigma)$
85	(0.346)	0.472	(0.374)	0.485	0.444	0.446	0.552	0.528	median(χ^2)
	(0.015)	0.008	(0.015)	0.025	0.019	0.014	0.018	0.016	$\pm\,(1\,\sigma)$
100	(0.366)	0.368	0.469	0.431	0.481	0.512	0.556	0.609	median(χ^2)
	(0.014)	0.007	0.011	0.013	0.025	0.024	0.028	0.019	$\pm\,(1\,\sigma)$

Note: Values in brackets refer to runs that terminated before ending the initialization phase of the simulation.

NGC 3893, $f_d = 100\,\%$

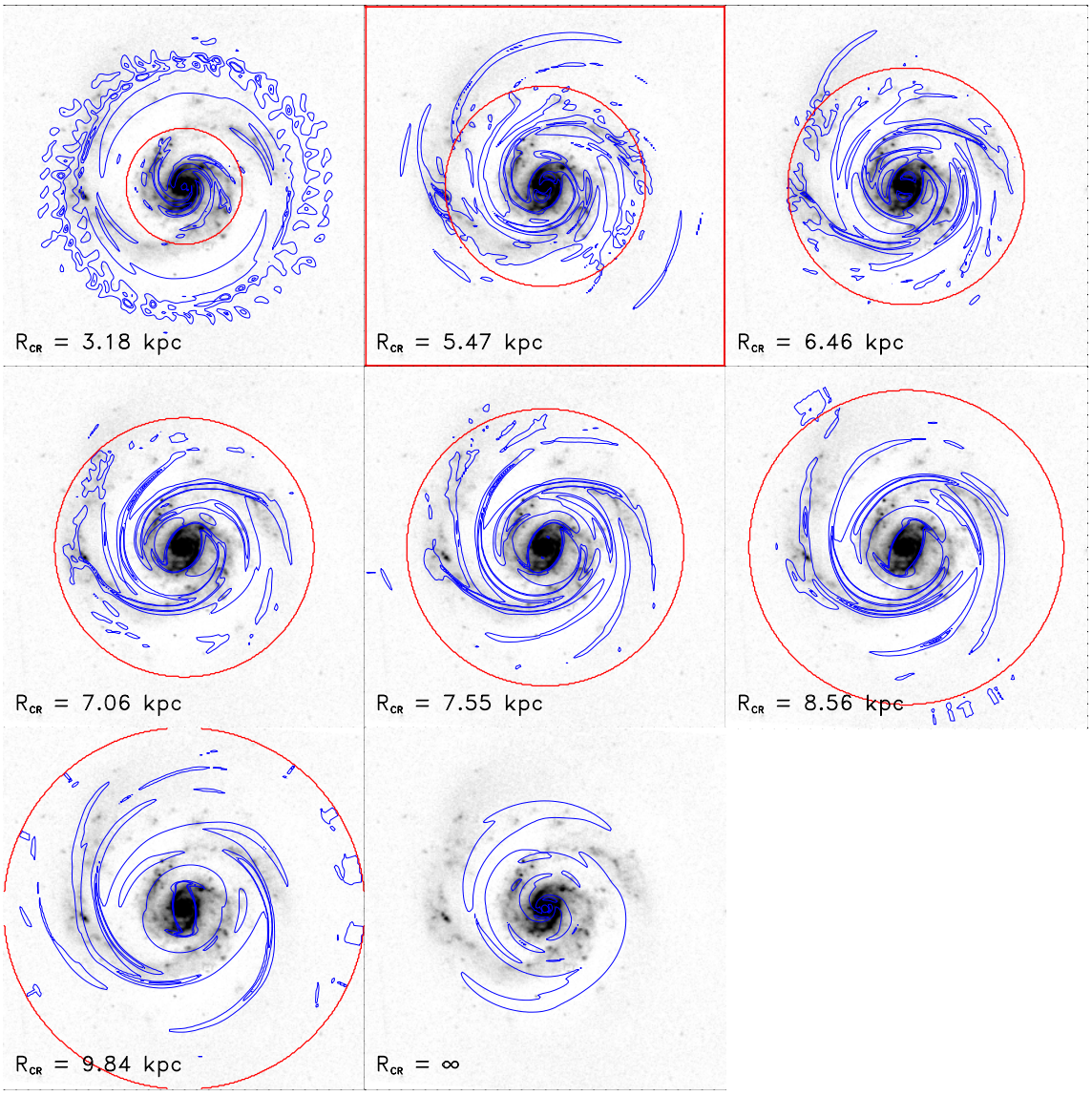

Figure B.1 Morphology comparison between the simulated gas density field (in contours) and the the observed structure of NGC 3893 (underlying, contrast enhanced image). Shown are the results for the maximal disk scenario $f_d = 100\,\%$. Displayed is always the last time step during a simulation run (see Table 6.2). The red circle gives the location of the corotation resonance, that applies to the particular simulation. The red bordered panel displays the simulation with the best matching parameter set.

NGC 3893, $f_d = 20\,\%$, $R_{CR} = 5.47\,\mathrm{kpc}$

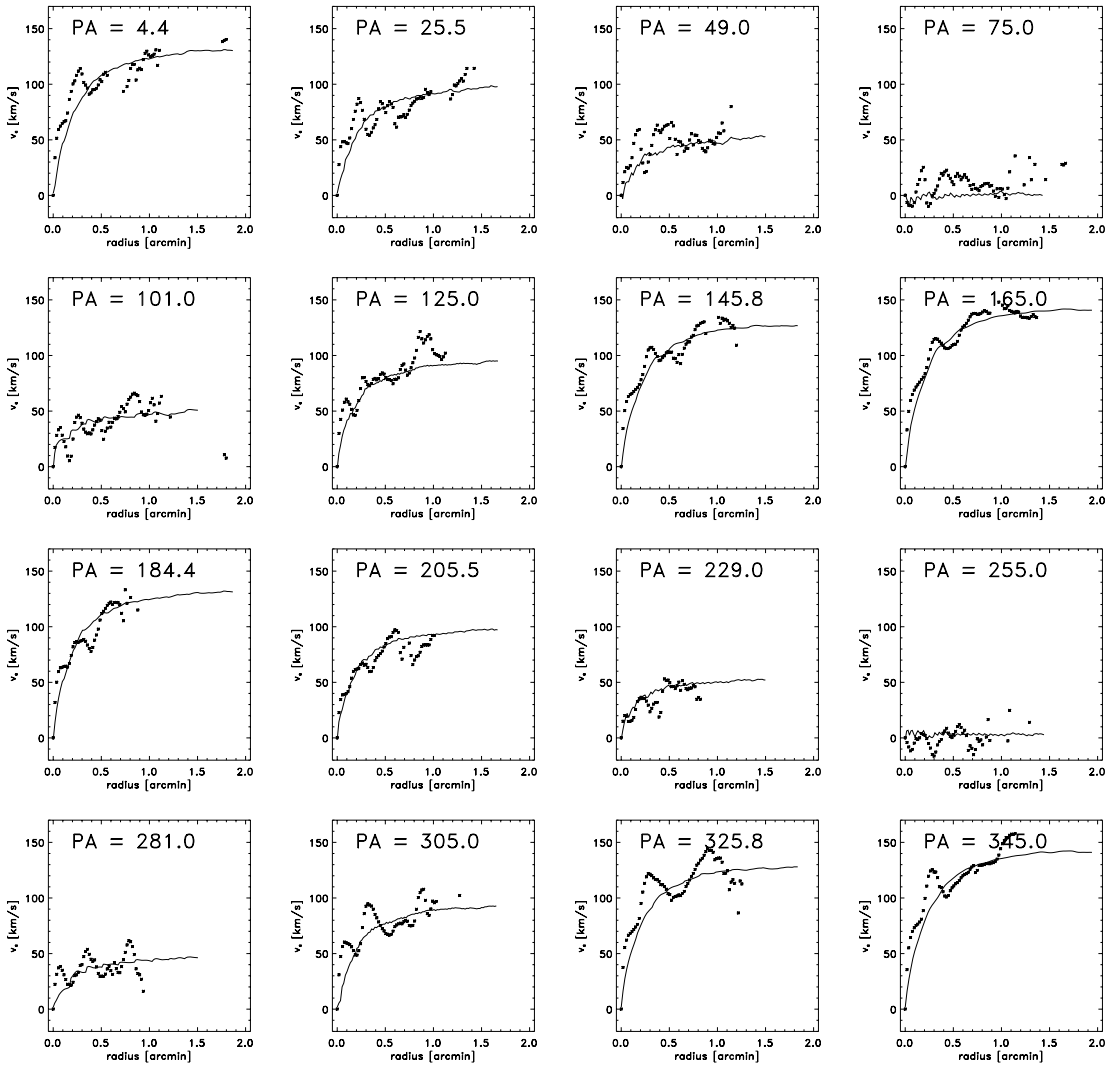

Figure B.2 Comparison of the measured (data points) and simulated (continuous line) kinematics. The results are displayed for NGC 3893 with a light disk ($f_d = 20\,\%$) and $R_{CR} = 5.47\,\mathrm{kpc}$.

NGC 3893, $f_d = 60\,\%$, $R_{CR} = 5.47\,\mathrm{kpc}$

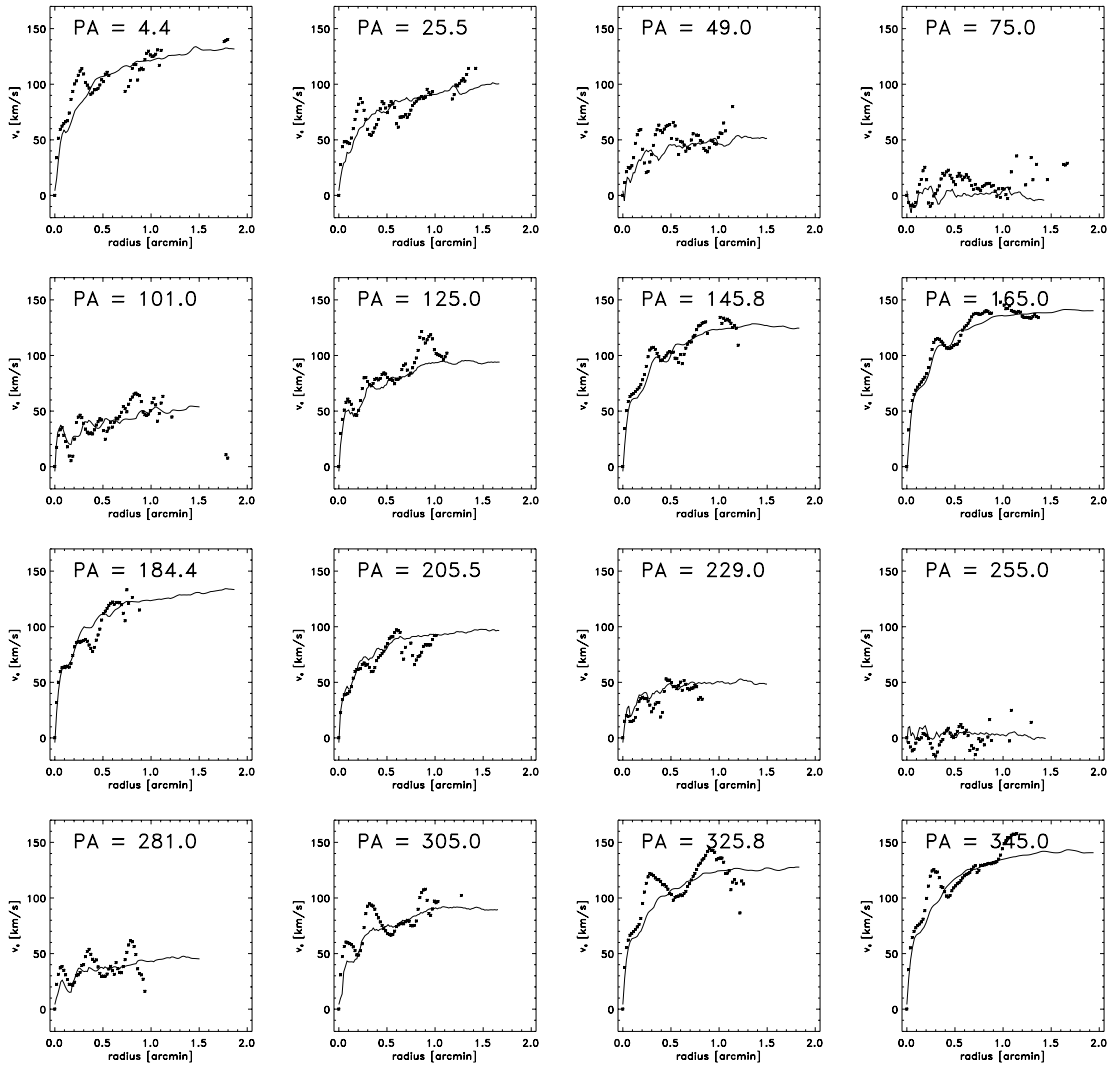

Figure B.3 Comparison of the measured (data points) and simulated (continuous line) kinematics. The results are displayed for NGC 3893 with a medium disk ($f_d = 60\,\%$) and $R_{CR} = 5.47\,\mathrm{kpc}$.

NGC 3893, $f_d = 100\,\%$, $R_{CR} = 5.47\,\mathrm{kpc}$

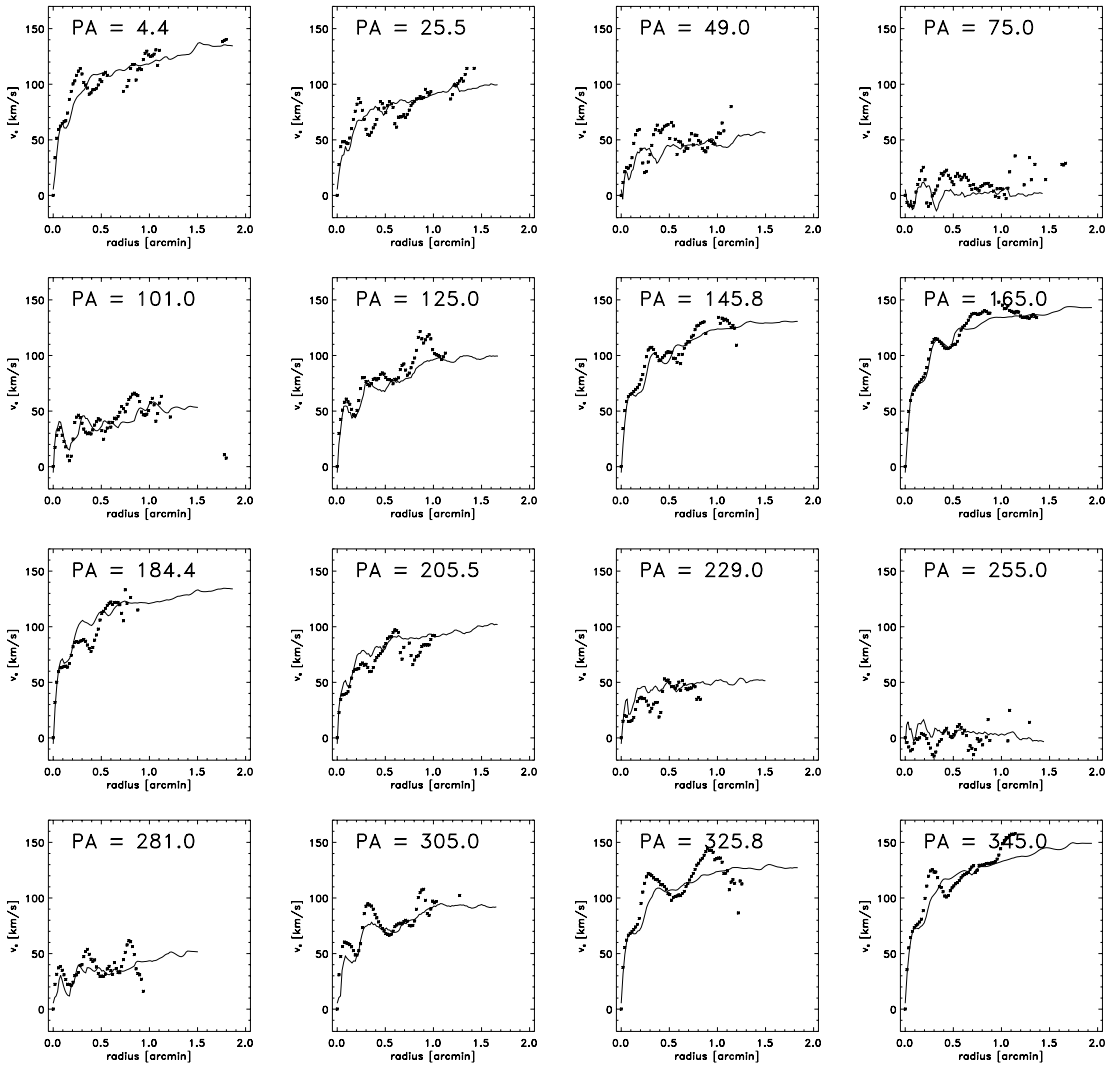

Figure B.4 Comparison of the measured (data points) and simulated (continuous line) kinematics. The results are displayed for NGC 3893 with a maximal disk ($f_d = 100\,\%$) and $R_{CR} = 5.47\,\mathrm{kpc}$.

NGC 3893, $f_d = 100\,\%$, $R_{CR} = 5.47\,\mathrm{kpc}$, selected data

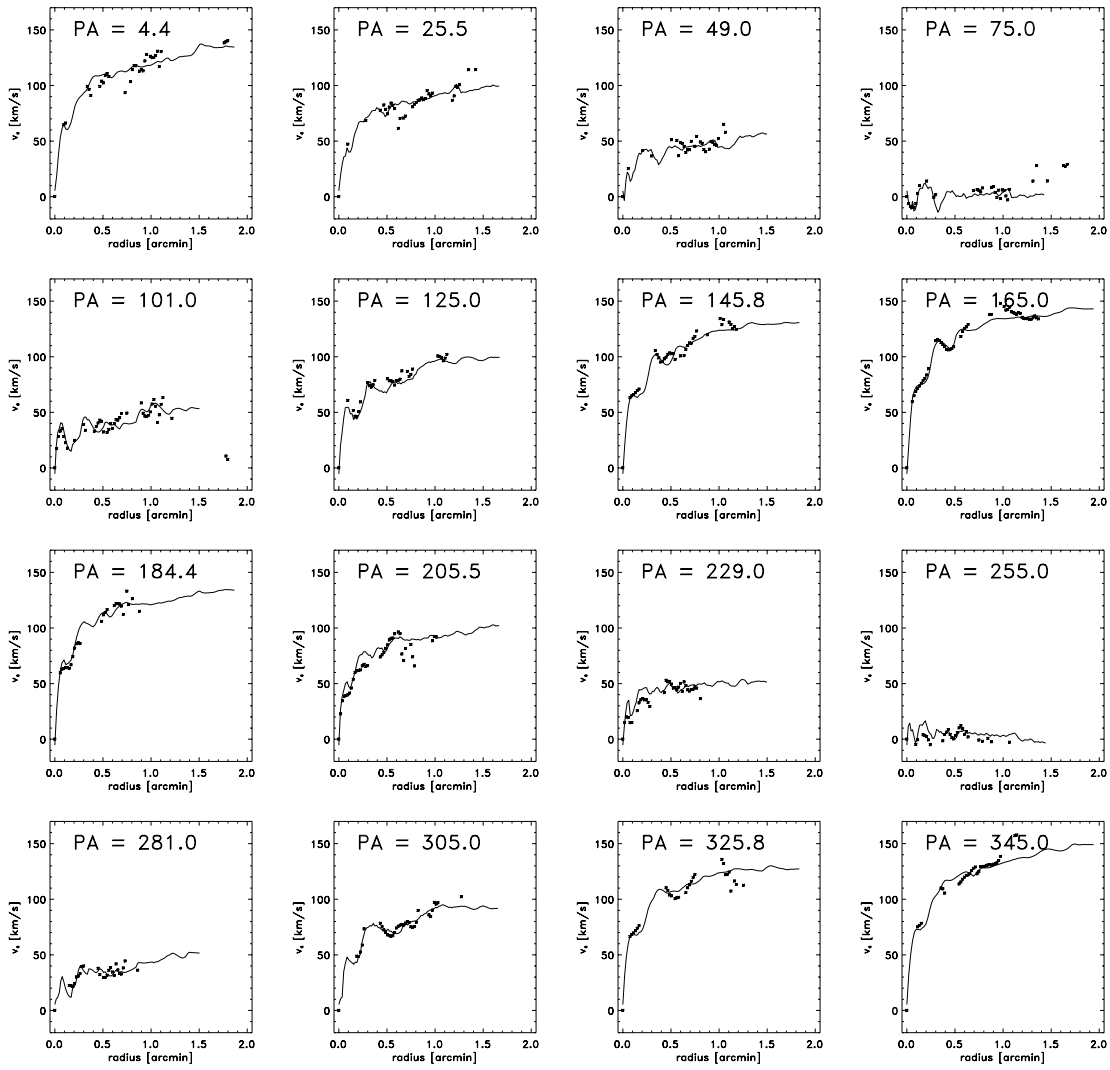

Figure B.5 Comparison of a selection of the measured kinematics (data points) and simulated (continuous line) kinematics. A selection criterion was introduced to only look at parts of the observed velocity field where the gas dynamics is mainly induced by gravity. About 60 % of the initial data points are used for comparison. See Section 4.3.2.1 for a description of the method. The results are displayed for NGC 3893 with a maximal disk ($f_d = 100\,\%$) and $R_{CR} = 5.47\,\mathrm{kpc}$.

Table B.3 χ^2/N and median(χ^2) of the comparison between observed and simulated kinematics for NGC 3893. Considered were only $N = 512$ selected data points.

Disk fraction f_d [%]	20	45	60	85	100
χ^2/N	0.774	0.650	0.602	0.794	0.601
median(χ^2)	0.236	0.197	0.202	0.213	0.182

C NGC 4254

For NGC 4254 the procedure was slightly different than for the other galaxies. The simulations were evaluated at the last timestep of the run without calculating a confidence limit of the χ^2-value. It was, however, made sure that the timestep that was analyzed was representative. All runs went past the initialization phase.

Table C.1 χ^2/N of the comparison between observed and simulated kinematics for NGC 4254. $N = 1077$ data points.

f_d	corotation radius R_{CR} [kpc]					timestep
[%]	6.4	7.58	8.27	10.03	11.6	[Myrs]
20	0.831	0.847	0.845	0.832	1.078	1125.9
44.4	0.817	0.833	0.906	0.879	1.354	965.1
60	0.831	0.856	0.937	0.978	1.492	1125.9
85	0.832	0.923	1.016	1.086	—	804.4
100	1.042	1.174	1.324	1.573	—	772.3

Figures showing the gas density distributions and the gas velocity field comparison have been presented in Chapter 5, i.e. Figure 5.2 and Figure 5.3 respectively.

D NGC 5676

Table D.1 χ^2/N of the comparison between observed and simulated kinematics for NGC 5676. $N = 546$ data points. The errors refer to $1\,\sigma$ χ^2/N-variations after simulation has passed the initialization phase.

f_d	corotation radius R_{CR} [kpc]								
[%]	7.65	8.6	9.6	10.6	11.6	12.6	13.6	14.16	
20	1.362	1.324	1.330	1.408	1.492	1.632	1.967	—	χ^2/N
	0.022	0.012	0.027	0.048	0.159	0.125	0.140	—	$\pm\,(1\,\sigma)$
45	1.857	1.839	1.744	1.843	1.825	1.690	1.958	2.107	χ^2/N
	0.122	0.142	0.113	0.160	0.208	0.045	0.137	0.187	$\pm\,(1\,\sigma)$
60	(1.568)	(1.521)	(1.501)	—	1.872	2.276	2.821	3.170	χ^2/N
	(0.040)	(0.037)	(0.049)	—	0.067	0.191	0.184	0.181	$\pm\,(1\,\sigma)$
85	(1.865)	1.860	1.816	(2.006)	(2.171)	(2.516)	3.186	—	χ^2/N
	(0.179)	0.172	0.154	(0.209)	(0.246)	(0.351)	0.577	—	$\pm\,(1\,\sigma)$
100	2.465	(2.067)	(2.313)	(2.539)	3.067	(2.990)	(3.473)	(4.382)	χ^2/N
	0.396	(0.255)	(0.337)	(0.408)	0.585	(0.553)	(0.716)	(1.021)	$\pm\,(1\,\sigma)$

Note: Values in brackets refer to runs that terminated before ending the initialization phase of the simulation.

Table D.2 median(χ^2) of the comparison between observed and simulated kinematics for NGC 5676. The errors refer to $1\,\sigma$ median(χ^2)-variations after simulation has passed the initialization phase.

f_d	corotation radius R_{CR} [kpc]								
[%]	7.65	8.6	9.6	10.6	11.6	12.6	13.6	14.16	
20	0.486	0.486	0.448	0.436	0.468	0.531	0.580	—	median(χ^2)
	0.015	0.012	0.012	0.013	0.010	0.025	0.039	—	$\pm\,(1\,\sigma)$
45	0.721	0.706	0.633	0.633	0.650	0.650	0.728	0.817	median(χ^2)
	0.048	0.041	0.038	0.045	0.065	0.022	0.016	0.027	$\pm\,(1\,\sigma)$
60	(0.608)	(0.592)	(0.572)	—	0.534	0.656	0.726	0.866	median(χ^2)
	(0.021)	(0.018)	(0.023)	—	0.029	0.042	0.042	0.033	$\pm\,(1\,\sigma)$
85	(0.597)	0.524	0.480	(0.419)	(0.375)	(0.572)	0.740	—	median(χ^2)
	(0.029)	0.029	0.032	(0.052)	(0.059)	(0.043)	0.067	—	$\pm\,(1\,\sigma)$
100	0.787	(0.661)	(0.578)	(0.606)	0.740	(0.792)	(0.822)	(1.017)	median(χ^2)
	0.104	(0.065)	(0.040)	(0.060)	0.096	(0.096)	(0.133)	(0.189)	$\pm\,(1\,\sigma)$

Note: Values in brackets refer to runs that terminated before ending the initialization phase of the simulation.

NGC 5676, $f_d = 45\,\%$

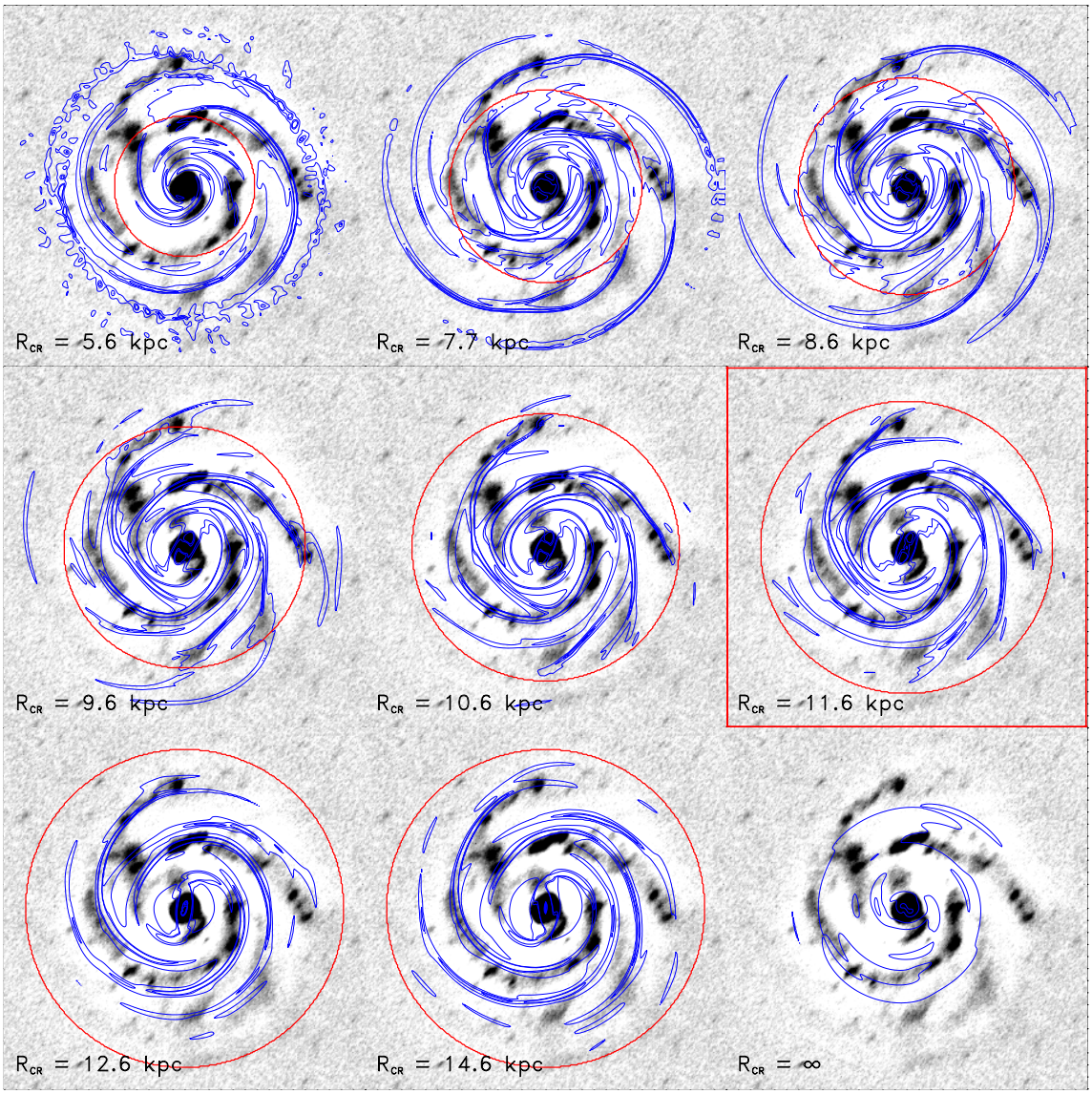

Figure D.1 Morphology comparison between the simulated gas density field (in contours) and the the observed structure of NGC 5676 (underlying, contrast enhanced image). Shown are the results for the $f_d = 45\,\%$ runs. Displayed is always the last time step during a simulation run (see Table 6.3). The red circle gives the location of the corotation resonance, that applies to the particular simulation. The red bordered panel displays the simulation with the best matching parameter set.

NGC 5676, $f_d = 20\,\%$, $R_{CR} = 9.6\,\mathrm{kpc}$

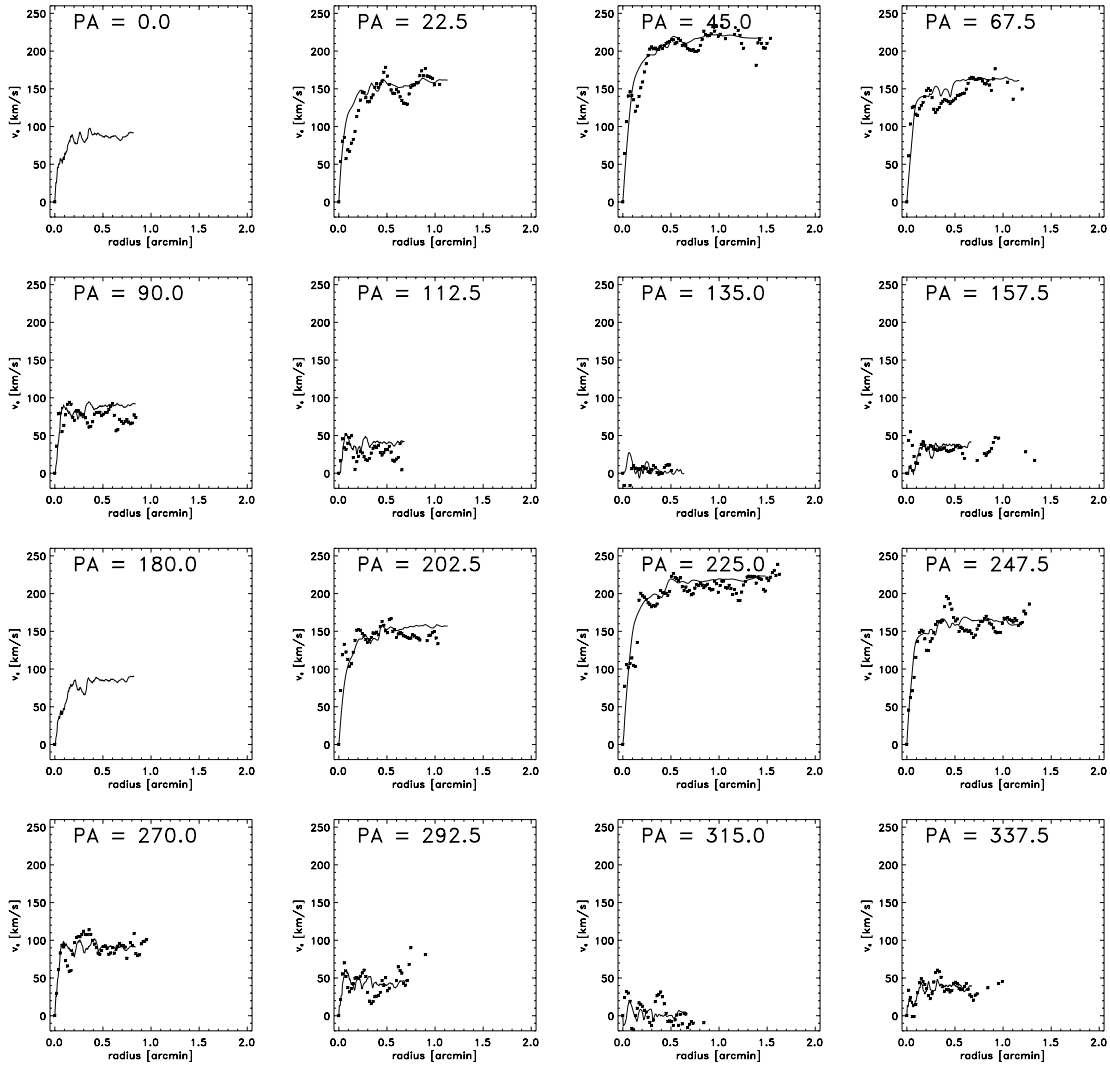

Figure D.2 Comparison of the measured (data points) and simulated (continuous line) kinematics. The results are displayed for NGC 5676 with a light disk ($f_d = 20\,\%$) and $R_{CR} = 9.6\,\mathrm{kpc}$.

NGC 5676, $f_d = 85\,\%$, $R_{CR} = 9.6\,\mathrm{kpc}$

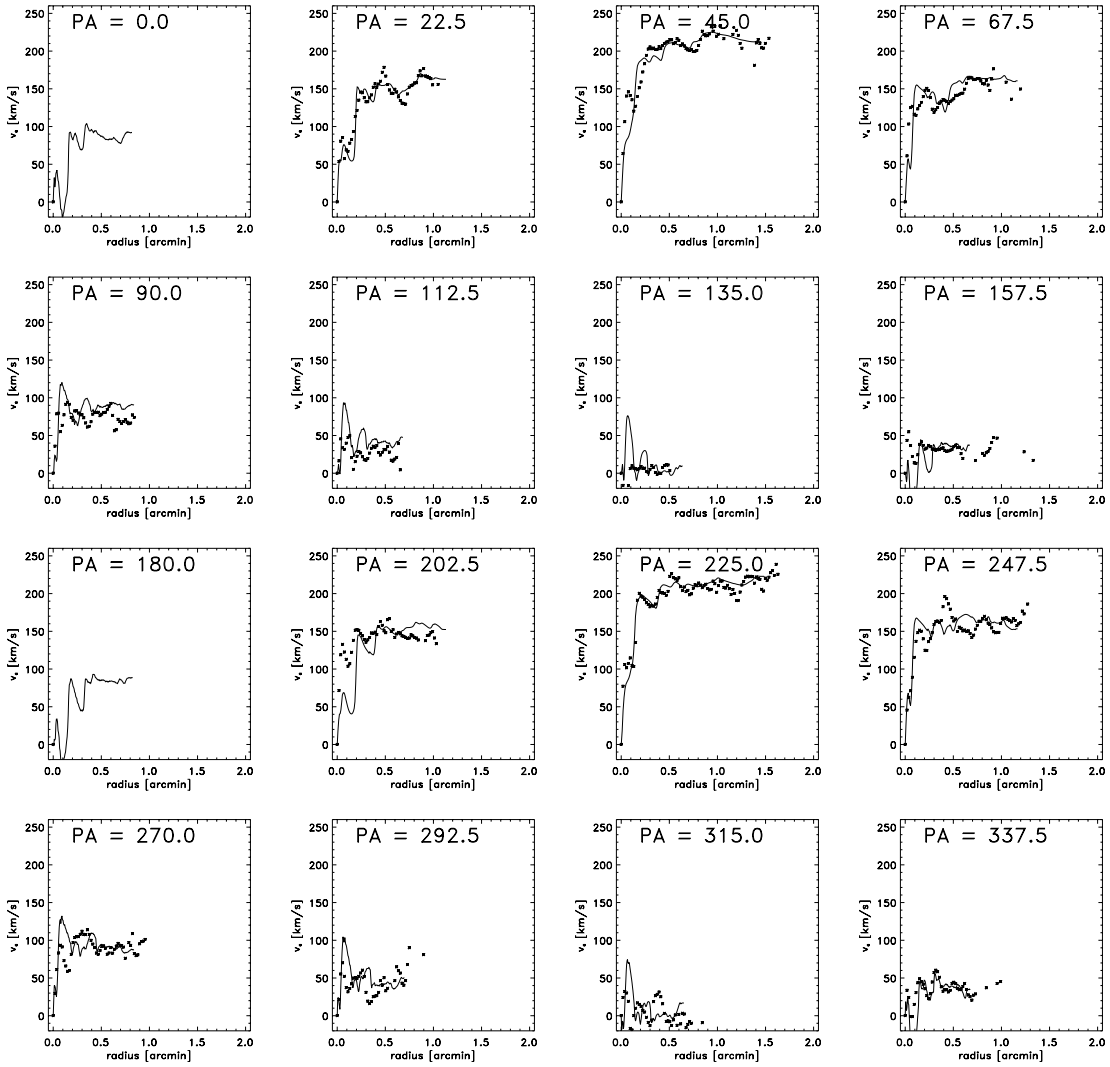

Figure D.3 Comparison of the measured (data points) and simulated (continuous line) kinematics. The results are displayed for NGC 5676 with a heavy disk ($f_d = 85\,\%$) and $R_{CR} = 9.6\,\mathrm{kpc}$.

NGC 5676, $f_d = 20\,\%$, $R_{CR} = 11.6\,\mathrm{kpc}$

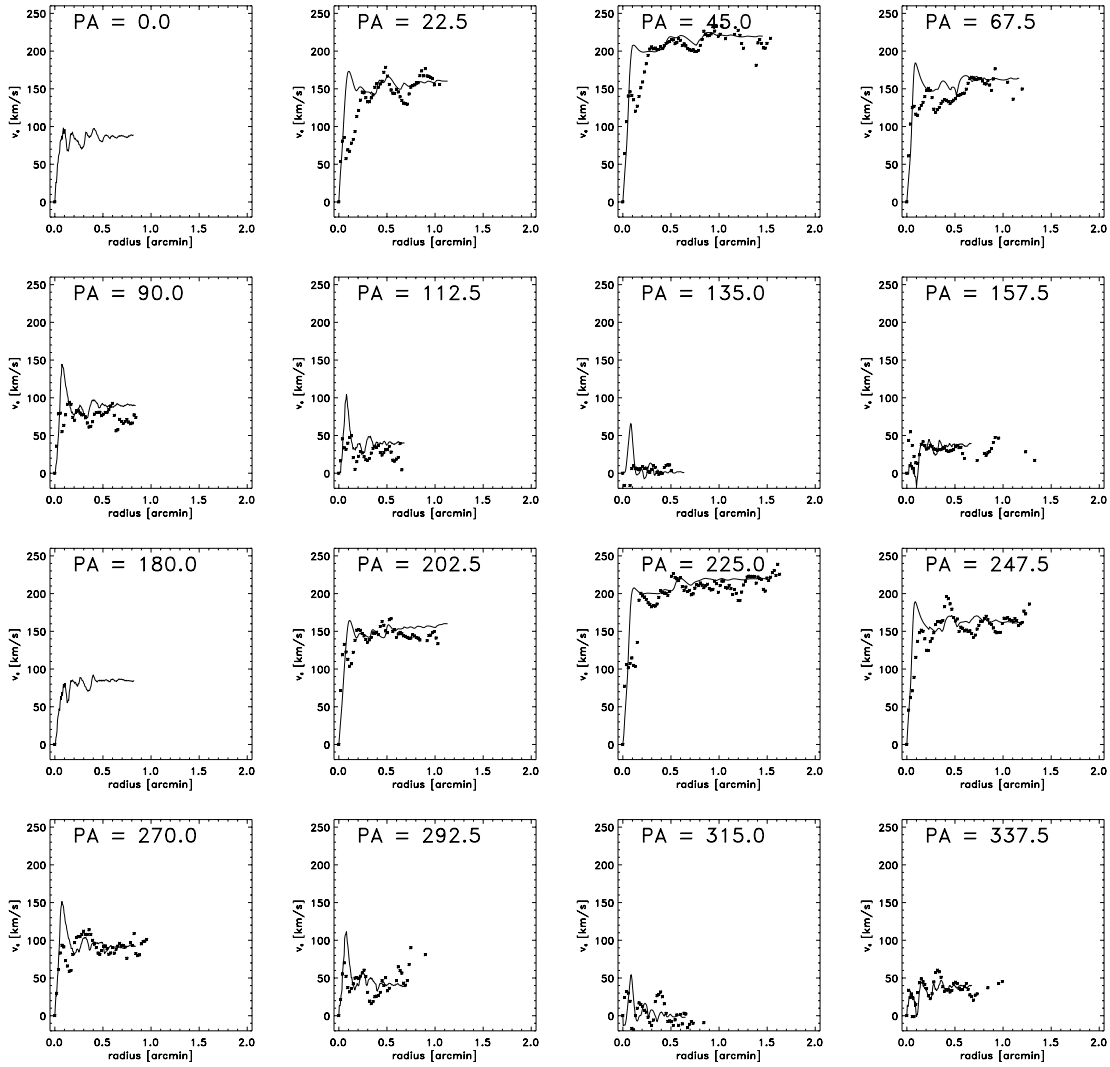

Figure D.4 Comparison of the measured (data points) and simulated (continuous line) kinematics. The results are displayed for NGC 5676 with a light disk ($f_d = 20\,\%$) and $R_{CR} = 11.6\,\mathrm{kpc}$.

NGC 5676, $f_d = 85\,\%$, $R_{CR} = 11.6\,kpc$

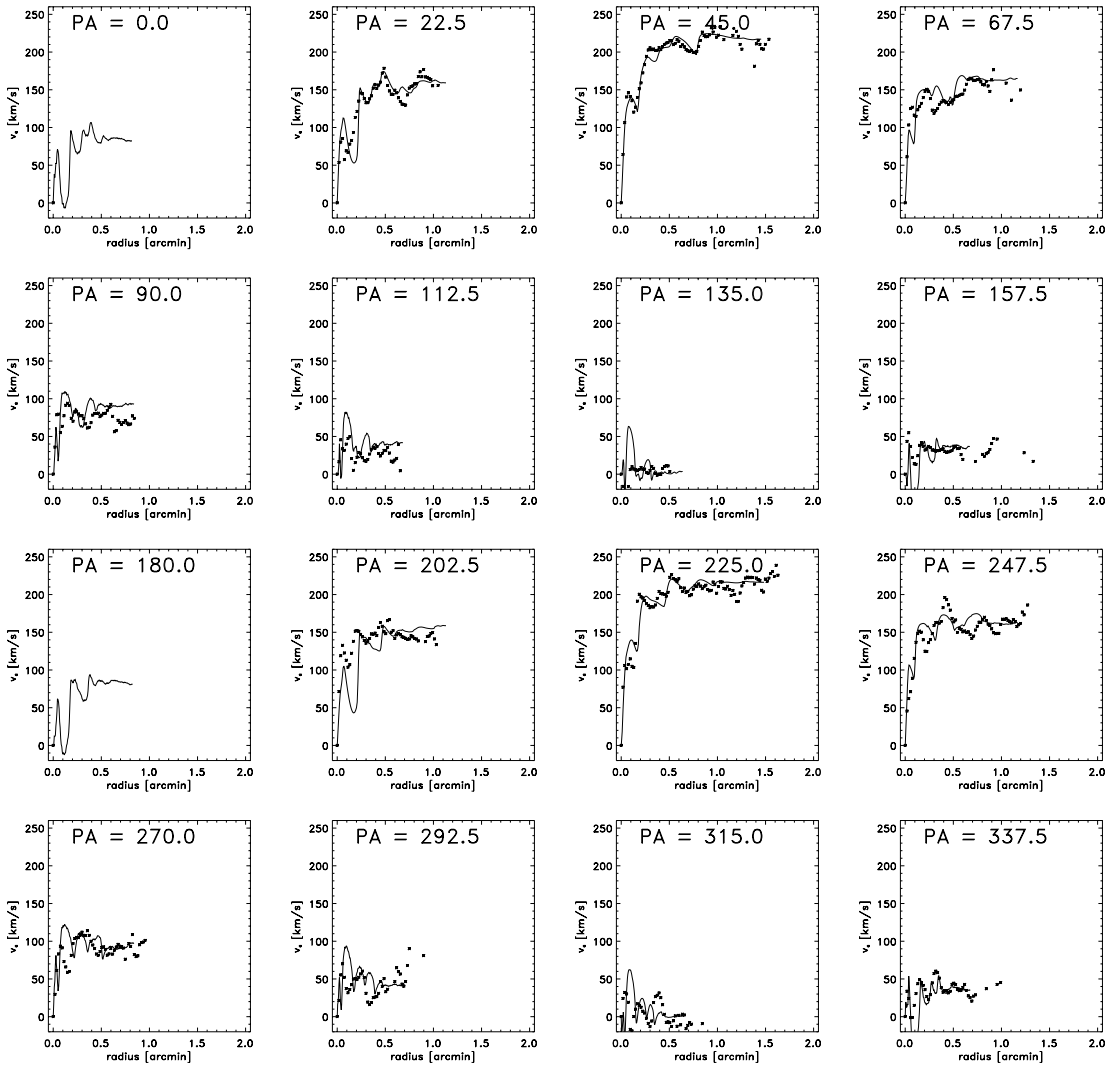

Figure D.5 Comparison of the measured (data points) and simulated (continuous line) kinematics. The results are displayed for NGC 5676 with a heavy disk ($f_d = 85\,\%$) and $R_{CR} = 11.6\,kpc$. Note that this simulation did not run past the initialization phase.

E NGC 6643

Table E.1 χ^2/N of the comparison between observed and simulated kinematics for NGC 6643. $N = 715$ data points. The errors refer to $1\,\sigma$ χ^2/N-variations after simulation has passed the initialization phase.

f_d	corotation radius R_{CR} [kpc]								
[%]	4.18	5.1	6.0	6.5	7.00	8.0	9.0	10.0	
20	1.025	1.048	1.023	1.050	1.128	1.170	1.171	1.237	χ^2/N
	0.021	0.023	0.018	0.017	0.027	0.036	0.050	0.059	$\pm\,(1\,\sigma)$
45	1.176	1.162	1.256	1.259	1.269	1.427	1.765	2.061	χ^2/N
	0.075	0.061	0.096	0.082	0.080	0.086	0.183	0.412	$\pm\,(1\,\sigma)$
60	1.292	1.395	1.510	—	1.509	2.005	2.767	2.858	χ^2/N
	0.064	0.118	0.164	—	0.115	0.249	0.649	0.759	$\pm\,(1\,\sigma)$
85	1.005	1.003	0.992	0.988	1.014	1.088	1.146	1.106	χ^2/N
	0.015	0.008	0.014	0.012	0.012	0.026	0.054	0.078	$\pm\,(1\,\sigma)$
100	1.924	2.095	1.966	2.167	—	2.582	3.380	4.564	χ^2/N
	0.147	0.284	0.070	0.319	—	0.390	0.337	0.452	$\pm\,(1\,\sigma)$

Table E.2 median(χ^2) of the comparison between observed and simulated kinematics for NGC 6643. The errors refer to $1\,\sigma$ median(χ^2)-variations after simulation has passed the initialization phase.

f_d	corotation radius R_{CR} [kpc]								
[%]	4.18	5.1	6.0	6.5	7.00	8.0	9.0	10.0	
20	0.404	0.405	0.389	0.407	0.403	0.415	0.429	0.513	median(χ^2)
	0.021	0.009	0.012	0.007	0.010	0.010	0.016	0.041	$\pm\,(1\,\sigma)$
45	0.421	0.472	0.520	0.482	0.464	0.507	0.553	0.802	median(χ^2)
	0.025	0.031	0.039	0.039	0.040	0.035	0.069	0.120	$\pm\,(1\,\sigma)$
60	0.404	0.486	0.592	—	0.511	0.661	0.752	0.953	median(χ^2)
	0.028	0.010	0.065	—	0.030	0.098	0.118	0.179	$\pm\,(1\,\sigma)$
85	0.390	0.349	0.342	0.372	0.377	0.371	0.356	0.380	median(χ^2)
	0.009	0.008	0.007	0.014	0.008	0.010	0.016	0.034	$\pm\,(1\,\sigma)$
100	0.499	0.655	0.652	0.652	—	0.852	1.145	1.586	median(χ^2)
	0.032	0.061	0.029	0.093	—	0.094	0.136	0.256	$\pm\,(1\,\sigma)$

NGC 6643, $f_d = 45\,\%$

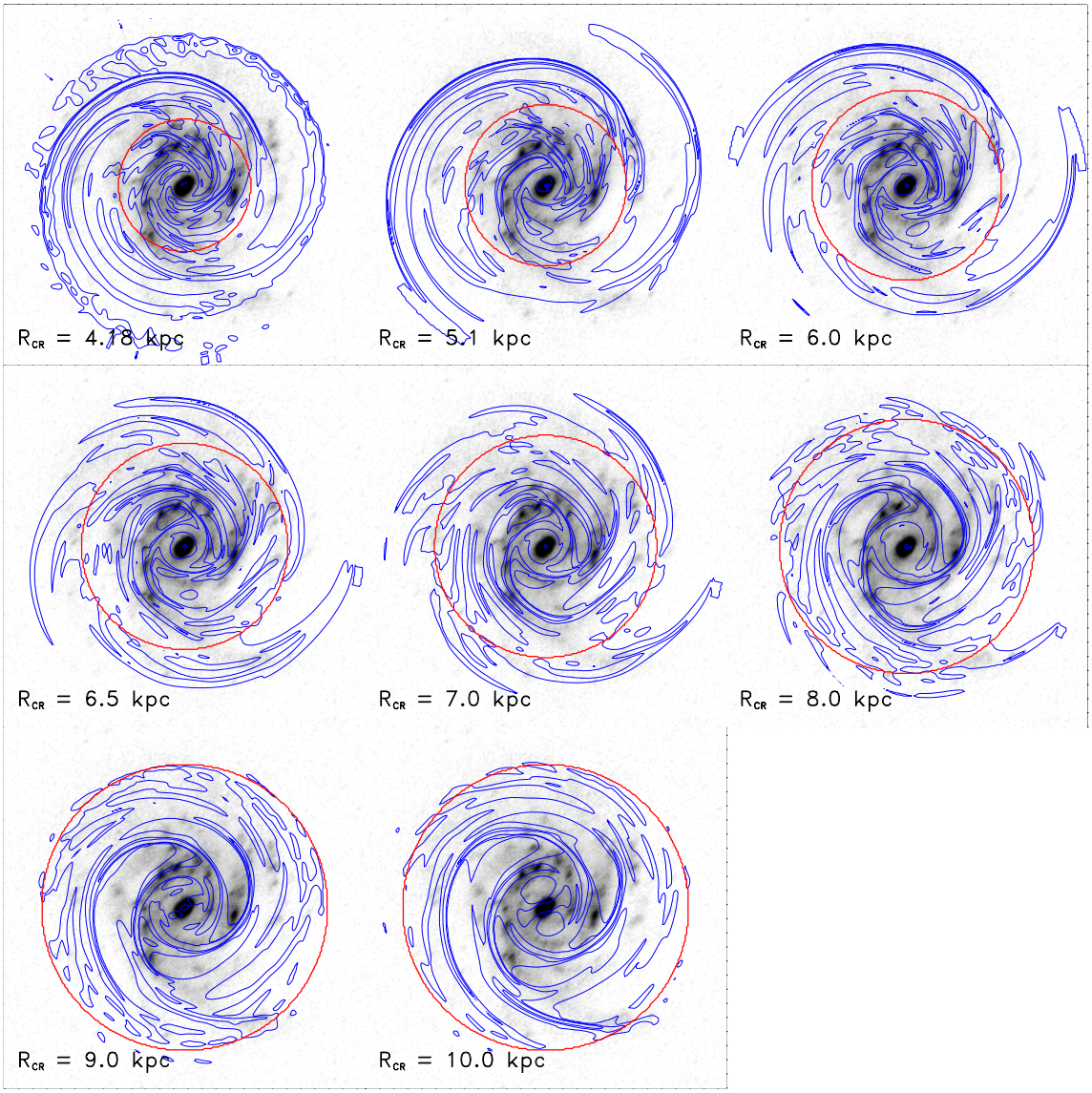

Figure E.1 Morphology comparison between the simulated gas density field (in contours) and the the observed structure of NGC 6643 (underlying, contrast enhanced image). Shown are the results for the $f_d = 45\,\%$ runs. Displayed is always the last time step during a simulation run (see Table 6.4). The red circle gives the location of the corotation resonance, that applies to the particular simulation.

NGC 6643, $f_d = 20\,\%$, $R_{CR} = 6.5\,\mathrm{kpc}$

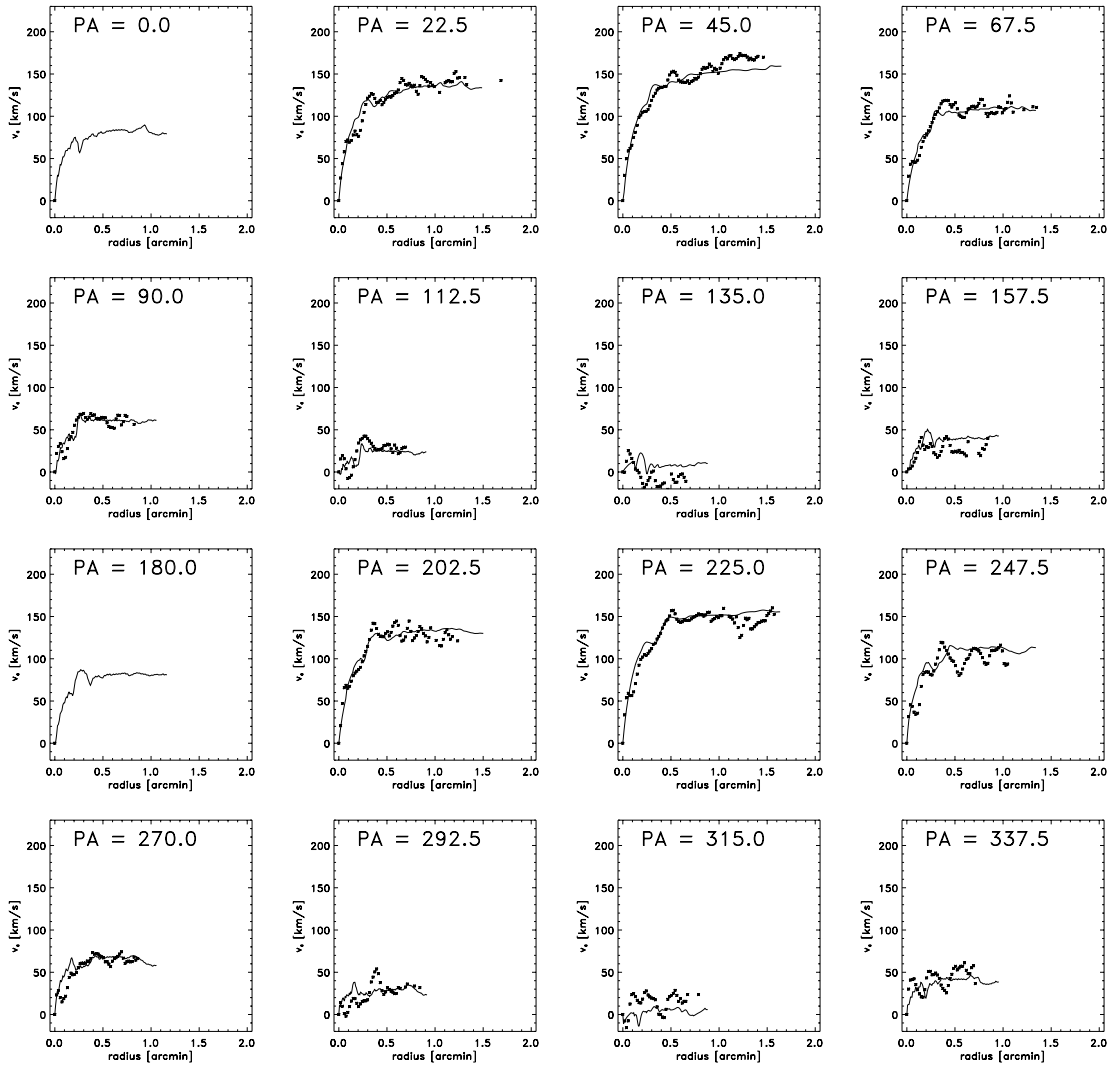

Figure E.2 Comparison of the measured (data points) and simulated (continuous line) kinematics. The results are displayed for NGC 6643 with a light disk ($f_d = 20\,\%$) and $R_{CR} = 6.5\,\mathrm{kpc}$.

NGC 6643, $f_d = 85\,\%$, $R_{CR} = 6.5\,\mathrm{kpc}$

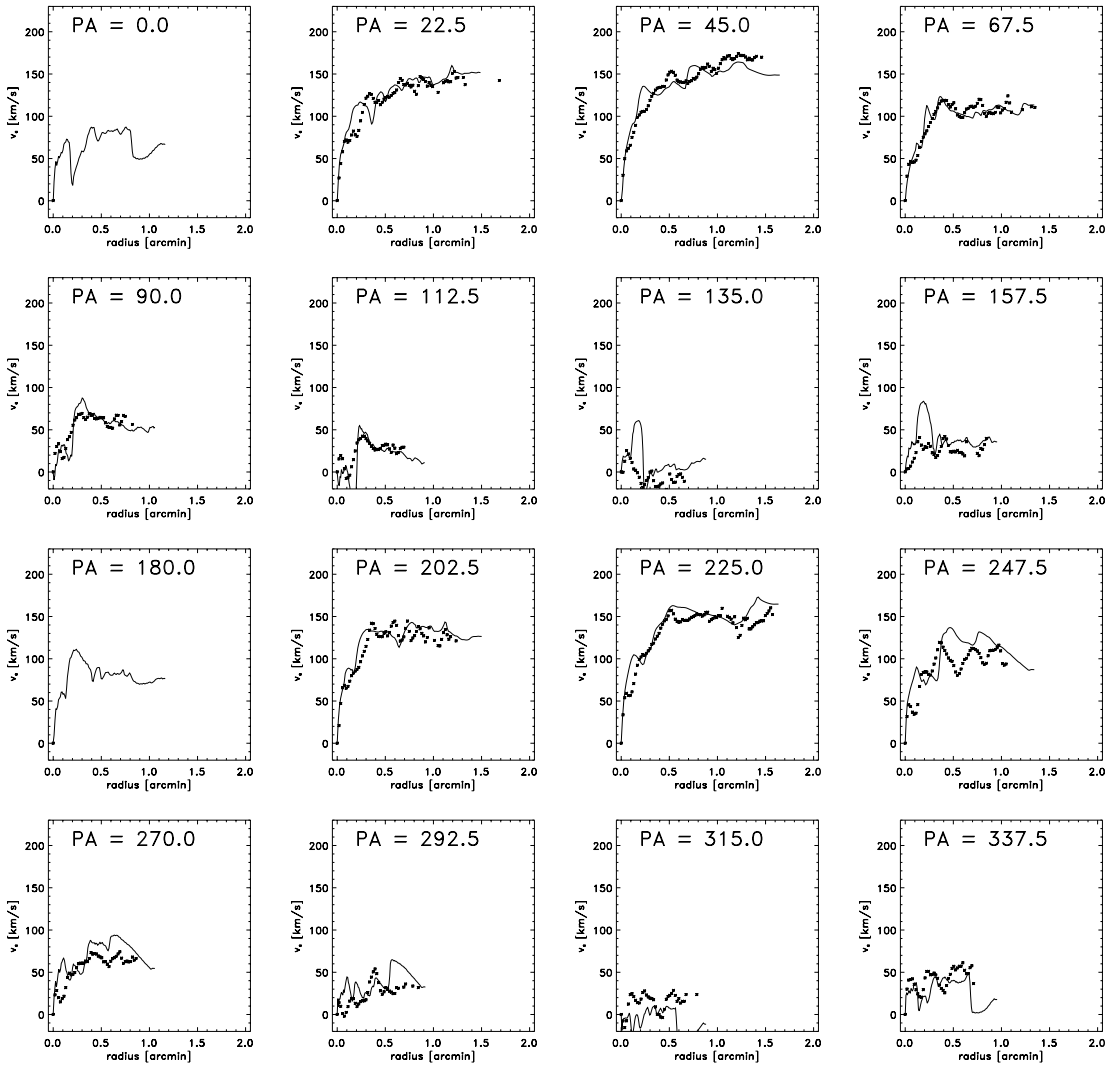

Figure E.3 Comparison of the measured (data points) and simulated (continuous line) kinematics. The results are displayed for NGC 6643 with a heavy disk ($f_d = 85\,\%$) and $R_{CR} = 6.5\,\mathrm{kpc}$.

NGC 6643, $f_d = 45\,\%$, $R_{CR} = 6.5\,\mathrm{kpc}$, selected data

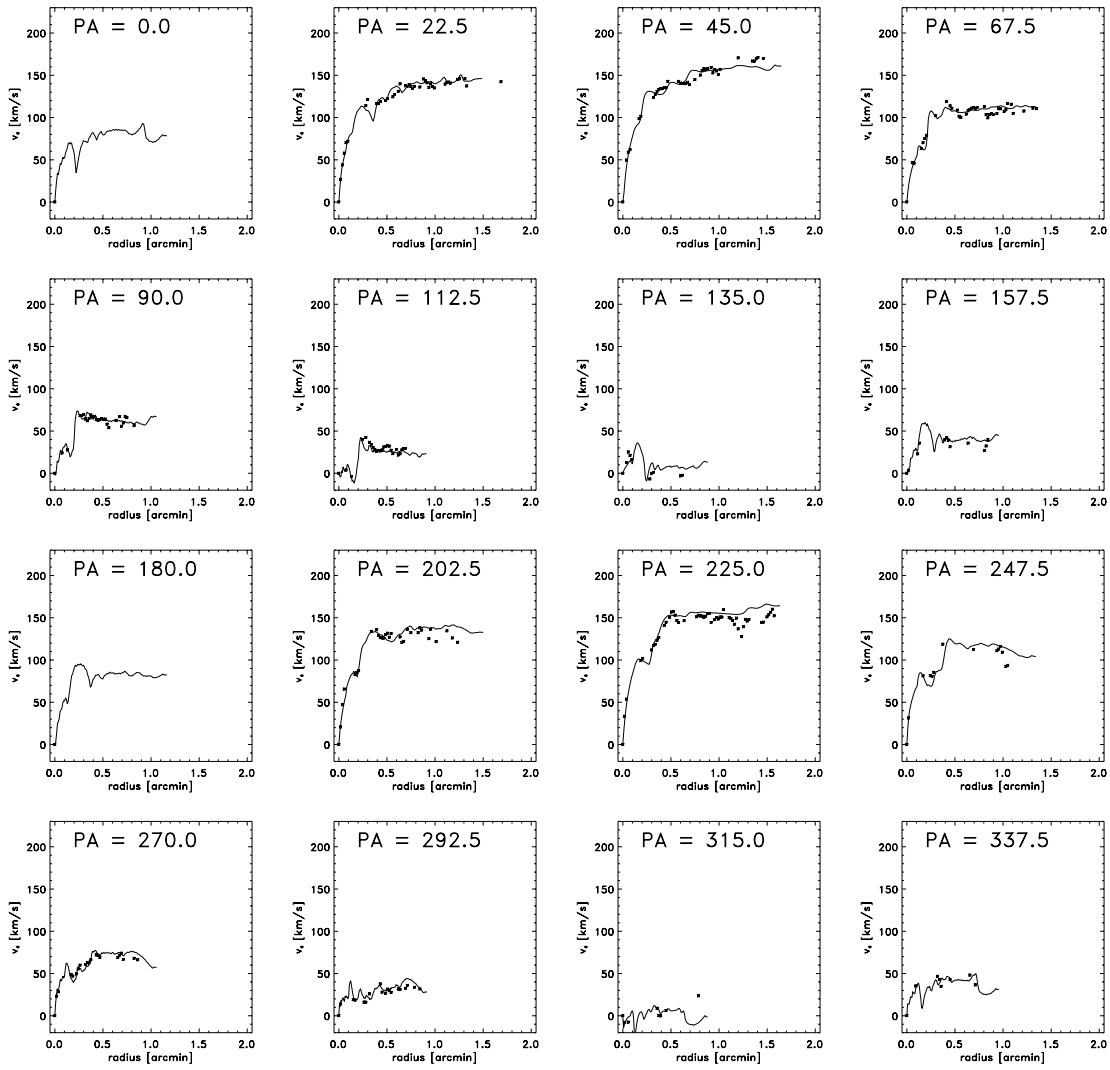

Figure E.4 Comparison of a selection of the measured kinematics (data points) and simulated (continuous line) kinematics. A selection criterion was introduced to only look at parts of the observed velocity field where the gas dynamics is mainly induced by gravity. About 47 % of the initial data points are used for comparison. See Section 4.3.2.1 for a description of the method. The results are displayed for NGC 6643 with a medium disk ($f_d = 45\,\%$) and $R_{CR} = 6.5\,\mathrm{kpc}$.

Table E.3 χ^2/N and median(χ^2) of the comparison between observed and simulated kinematics for NGC 6643. Considered were only $N = 331$ selected data points.

Disk fraction f_d [%]	20	45	60	85	100
χ^2/N	0.653	0.745	0.737	1.600	3.272
median(χ^2)	0.236	0.222	0.222	0.276	0.255

REFERENCES
Bibliography

Aalto, S., Hüttemeister, S., Scoville, N. Z., & Thaddeus, P. 1999, ApJ, 522, 165

Adler, D. S., & Westpfahl, D. J. 1996, AJ, 111, 735

Alcock, C., & The MACHO collaboration 2000, ApJ, 542, 281

Athanassoula, E. 1978, A&A, 69, 395

Athanassoula, E. 1984, in Physics Reports (Review Section of Physics Letters) 114, Nos. 5 & 6, (Amsterdam: North-Holland Phys. Publ.), 319

Athanassoula, E., Bosma, A., & Papaioannou, S. 1987, A&A, 179, 23

Avila-Reese, V., Colín, P., Valenzuela, O., D'Onghia, E., & Firmani, C. 2001, ApJ, 559, 516

Bacon, D. J., Refregier, A. R., & Ellis, R. S. 2000, MNRAS, 318, 625

Beauvais, C., & Bothun, G. 1999, ApJS, 125, 99

Beckman, J. E., & Cepa, J. 1990, A&A, 229, 37

Bell, E. F., & de Jong, R. S. 2001, ApJ, 550, 212

Bernabei, R., & The DAMA Collaboration 1999, Phys. Lett., B450, 448

Bertin, G. 1993, PASP, 105, 640

Bertin, G., Lin, C., Lowe, S., & Thurstans, R. 1989a, ApJ, 338, 78

Bertin, G., Lin, C., Lowe, S., & Thurstans, R. 1989b, ApJ, 338, 104

Bizenberger, P., McCaughrean, M., Birk, C., Thompson, D., & Storz, C. 1998, SPIE, 3354, 825

Bhatnagar, P. L., Gross, E. P., & Krook, M. 1954, Phys. Rev., 94, 511

Blais-Ouellette, S., Carignan, C., Amram, Ph., & Côté, S. 1999, AJ, 118, 2123

Blumenthal, G. R., Faber, S. M., Flores, R., & Primack, J. R. 1986, ApJ, 301, 27

Borriello, A., & Salucci, P. 2001, MNRAS, 323, 285

Bottema, R. 1997, A&A, 328, 517

Braine, J., Combes, F., Casoli, F., Dupraz, C., Gerin, M., Klein, U., Wielebinski, R., & Brouillet, N. 1993, A&AS, 97, 887

Broeils, A. H., & Courteau, S. 1997, in 'Dark and Visible Matter in Galaxies and Cosmological Implications', ASP Conf. Ser. 117, ed. M. Persic, & P. Salucci, (San Francisco: ASP), 74

Bruzual, A. G., & Charlot, S. 2002, in preparation

Caldwell, D. 1999, in 'The Identification of Dark Matter, Proceedings of the Second International Workshop', Eds. N. J. Spooner & V. Kudryavtsev (Singapore: World Scientific), 527

Cannon, D. B., Ponman, T. J., & Hobbs, I. S. 1999, MNRAS, 302, 9

Canzian, B., Allen, R. J., & Tilanus, R. P. J. 1993, ApJ, 406, 457

Canzian, B., & Allen, R. J. 1997, ApJ, 479, 723

Carlberg, R., Yee, H., Ellingson, E., Abraham, R., Gravel, P., Morris, S., & Pritchet, C. 1996, ApJ, 462, 32

Carroll, B. W., & Ostlie, D. A. 1996, An Introduction to Modern Astrophysics (Reading: Addison-Wesley)

Cen, R., & Ostriker, J. P. 1999, ApJ, 514, 1

Cirimele, G., Nesci, R., & Trevese, D. 1997, ApJ, 475, 11

Cole, S., Lacey, C. G., Baugh, C. M., & Frenk, C. S. 2000, MNRAS, 319, 168

Contopoulos, G., & Grosbøl, P. 1986, A&A, 155, 11

Contopoulos, G., & Grosbøl, P. 1988, A&A, 197, 83

Courteau S., & Rix H.-W. 1999, ApJ, 513, 561

David, L. P., Jones, C., & Forman, W. 1995, ApJ, 445, 578

Debattista V. P., & Sellwood J. A. 1998, ApJ, 493, L5

Debattista V. P., & Sellwood J. A. 2000, ApJ, 543, 704

de Bernardis, P. et al. 2000, Nature, 404, 955

de Blok, W., McGaugh, S., Bosma, A., & Rubin, V. 2001, ApJ, 552, L23

Dehnen, W., & Binney, J. 1998, MNRAS, 294, 429

Donner, K. J., & Thomasson, M. 1994, A&A, 290, 785

Elmegreen, B. G., Elmegreen, D. M., & Montenegro, L. 1992, ApJS, 79, 37

Elmegreen, D. M. 1980, ApJ, 242, 528

Elmegreen, D. M., Chromey, F. C., Bissell, B. A., & Corrado, K. 1999, ApJ, 118, 2618

Englmaier, P., & Gerhard, O. 1997, MNRAS, 287, 57

Englmaier, P., & Gerhard, O. 1999, MNRAS, 304, 512

Erickson, L. K., Gottesman, S. T., & Hunter, J. H. Jr. 1999, ApJ, 515, 153

Eskridge, Paul B., Frogel, Jay A., Pogge, Richard W., et al. 2000, AJ, 119, 536

Evans, Rh. 1993, AAS, 182, 3120

Federspiel, M., Tammann, G. A., & Sandage, A. 1998, ApJ, 495, 115

Fields, B. D., Freese, K., & Graff, D. S. 2000, ApJ, 534, 265

Flores, R. A., & Primack, J. R. 1994, ApJ, 427, L1

Frei, Z., Guhathakurta, P., Gunn, J. E. , & Tyson, J. A. 1996, AJ, 111, 174

Frogel, J., Quillen, A., & Pogge, R. 1996, in 'Cold Dust and Galaxy Morphology, Proceedings of the international conference', held in Johannesburg, South Africa, Eds. D. L. Block and J. M. Greenberg (Dordrecht: Kluwer) 1996, 65

Fukugita, M., Hogan, C. J., & Peebles, P. J. E. 1998, ApJ, 503, 518

Fukushige, T., & Makino, J. 1997, ApJ, 477, L9

Gadotti, D. A., & dos Anjos, S. 2001, AJ, 122, 1298

Garcia, A. M. 1993, A&AS, 100, 47

Garcia-Burillo, S., Combes, F., & Gerin, M. 1993, A&A, 274, 148

Garcia-Burillo, S., Sempere, M. J., & Combes, F. 1994, A&A, 287, 419

Gavazzi, G., Pierini, D., & Boselli, A. 1996, A&A, 312, 397

Gerola, H., & Seiden, P. E. 1978 ApJ, 223, 129

Giraud, E. 1998, AJ, 116, 1125

Gnedin, O. Y., Goodman, J., & Frei Z. 1995, AJ, 110, 1105

González, R. A., & Graham, J. R. 1996, ApJ, 460, 651

Graff, D. S., & Freese, K. 1996, ApJ, 456, L49

Gray, M., Taylor, A., Meisenheimer, K., Dye, S., Wolf, C., & Thommes E. 2002 ApJ, in press (astro-ph/0111288)

Griffiths, R. E., Casertano, S., Im, M., & Ratnatunga, K. U. 1996, MNRAS, 282, 1159

Grosbøl, P. J., Block, D. L., & Patsis, P. A. 2000, in 'Dynamics of Galaxies', ASP Conf. Ser. 197, eds. F. Combes, G. A. Mamon, & V. Charmandaris, (San Francisco: ASP), 191

Helfer, T., Regan, M., Thornley, M., Wong, T., Sheth, K., Vogel, S., Bock, D., Blitz, L., & Harris, A. 2001, Ap&SS, 276, 1131

Héraudeau, P., & Simien, F. 1996, A&AS, 118, 111

Howard, S., Keel, W. C., Byrd, G., & Burkey J. 1993, ApJ, 417, 502

Ibata, R., Irwin, M., Bienaymé, O., Scholz, R., & Guibert, J. 2000, ApJ, 532, L41

Ibata, R., Richer, H., Gilliland, R. I., & Scott, D. 1999, ApJ, 524, L95

Jedamzik, K., 2001, in 'Dark Matter in Astro- and Particle Physics, Proceedings of the International Conference, Dark 2000', ed. H. V. Klapdor-Kleingrothaus (Berlin: Springer), 289

Jones, C., Stern, C., Forman, W., Breen, J., David, L., Tucker, W., & Franx, M. 1997, ApJ, 482, 143

Jungman, G., Kamionkowski, M., & Griest, K., 1996, Phys. Rep. 267, 195

Kamionkowski, M. 1998, in 'High Energy Physics and Cosmology, Proceedings of 1997 ITCP Summer School', eds. E. Gava, A. Masiero, K. Narain, S. Randjbar-Daemi, G. Senjanovic, A. Smirnov, Q. Shafi (Singapore: World Scientific), 394

Kauffmann G., Colberg J., Diaferio A., & White S. D. M. 1999, MNRAS, 303, 188

Kent, S. M. 1986, AJ, 91, 1301

Knapen, J. H., & Beckman, J. E. 1996, MNRAS, 283, 251

Kneib, J. P., Mellier, Y., Pello, R., Miralda-Escude, J., Le Borgne, J.-F., Böhringer, H., & Picat, J.-P. 1995, A&A, 303, 27

Kranz, T., Slyz, A., & Rix, H.-W. 2001, ApJ, 562, 164

Kuijken, K. 1995, in 'Stellar Populations', IAU Symp. Proc. 164, eds. P. C. van der Kruit, & G. Gilmore, (Dordrecht: Kluwer), 195

Lasserre, T., & The EROS collaboration 2000, A&A, 355, L39

Lin, C. C., & Shu, F. H. 1964, ApJ, 140, 646

Lin, C. C., & Shu, F. H. 1966, Proc. Nat. Acad. Sci., 55, 229

Lin, C. C., Yuan, C., & Shu, F. H. 1969, ApJ, 155, 721

Loewenstein, M., & White, R. E., 1999, ApJ, 518, 50

Lubow, S. H., Balbus, S. A., & Cowie, L. L. 1986, ApJ, 309, 496

Maller, A., Simard, L., Guhathakurta, P., et al. 2000, ApJ, 533, 194

Massey, P. 1997, 'A User's Guide to CCD Reductions with IRAF', available from http://iraf.noao.edu/docs/recommend.html

Massey, P., Valdes, F., & Barnes, J. 1992, 'A User's Guide to Reducing Slit Spectra with IRAF', available from http://iraf.noao.edu/docs/recommend.html

McGaugh, S. S. 2000, ApJ, 541, L33

McGaugh, S. S., & de Blok, W. J. G. 1998, ApJ, 499, 66

Mellier, Y. 1999, ARA&A, 37, 127

Meneghetti, M., Yoshida, N., Bartelmann, M., Moscardini, L., Springel, V., Tormen, G., & White, S. D. M. 2001, MNRAS, 325, 435

Milgrom, M. 1983, ApJ, 270, 365

Milgrom, M. 1998, ApJ, 496, L89

Miralda-Escude, J. 2002, ApJ, 564, 60

Moore, B. 1994, Nature, 370, 629

Moore, B., Ghigna, S., Governato, F., et al. 1999a, ApJ, 524, L19

Moore, B., Quinn, T., Governato, F., Stadel, J., & Lake, G. 1999b, MNRAS, 310, 1147

Mulder, P. S., & Combes, F. 1996, A&A, 313, 723

Navarro J., Frenk C., & White S. D. 1996, ApJ, 462, 563

Navarro J., Frenk C., & White S. D. 1997, ApJ, 490, 493

Ostriker, J. P. 2000, Phys. Rev. Lett., 84, 5258

Palunas, P., & Williams, T. B. 2000, AJ, 120, 2884

Patsis, P. A., Contopoulos, G., & Grosbøl, P. J. 1991, A&A, 243, 373

Patsis, P. A., Grosbøl, P. J., & Hiotelis, N. 1997, A&A, 323, 762

Patsis, P. A., & Kaufmann, D. E. 1999, A&A, 352, 469

Pearce, F. R., Jenkins, A., Frenk, C. S., White, S. D. M., Thomas, P. A., Couchman, H. M., Peacock, J. A., & Efstathiou, G. 2001, MNRAS, 326, 649

Peccei, R. D. & Quinn, H. R. 1977, Phys. Rev. D, 16, 1791

Peebles, P. J. E. 2000, ApJ, 534, L127

Perlmutter, S. et al. 1999, ApJ, 517, 565

Persson, S., Murphy, D., Krzeminski, W., Roth, M., & Rieke, M. 1998, AJ, 116, 2475

Phookun, B., Vogel, S. N., & Mundy, L. G. 1993, ApJ, 418. 113

Pierce, M. J., & Tully, R. B. 1988, ApJ, 330, 579

Pignatelli, E., Corsini, E. M., Vega Beltrán, J. C., Scarlata, C., Pizzella, A., Funes, J. G., Zeilinger, W. W., Beckman, J. E., & Bertola, F. 2001, MNRAS, 323, 188

Prendergast, K. H., & Xu, K. 1993, J. Comput. Phys., 109, 53

Primack, J., & Gross, M. 2001, in 'Current aspects of neutrino physics', ed. David O. Caldwell (Berlin: Springer), 287

Quillen, A. C., & Pickering, T. E. 1997, AJ, 113, 2075

Quillen, A. C. 1999, in ASP Conf. Ser. 182, Galaxy Dynamics, ed. by D. Merritt, M. Valluri, & J. Sellwood, (San Francisco: ASP), 251

Ratnam, C., & Salucci, P. 2000, New Astronomy, 5, 427

Regan, M. W., Teuben, P. J., Vogel, S. N., & van der Hulst, T. 1996, AJ, 112, 2549

Rix, H.-W., de Zeeuw, P. T., Cretton, N., van der Marel, R. P., & Carollo, C. M. 1997, ApJ, 488, 702

Rix, H.-W., & Rieke, M. 1993, ApJ, 418, 123

Rix, H.-W., & Zaritsky, D. 1995, ApJ, 447

Roberts, W. W. 1969, ApJ 158, 123

Sackett P. 1997, ApJ, 483, 103

Sakamoto, K., Okumura, S. K., Ishizuki, S., & Scoville, N. Z. 1999, ApJS, 124, 403

Salpeter, E. E. 1955, ApJ, 121, 61

Salucci, P. 2001, MNRAS, 320, L1

Salucci, P., & Burkert, A. 2000, ApJ, 537, L9

Salucci, P., & Persic, M. 1999, A&A, 351, 442

Sandage A., & Tammann, G. A. 1976, ApJ, 210, 7

Sanders, R. H. 2000, MNRAS, 313, 767

Sanders, R. H., & Huntley, J. M. 1976, ApJ, 209, 53

Sarazin, C. L. 1988, 'X-Ray Emissions from Clusters of Galaxies', (Cambridge: Cambridge University Press)

Schindler, S., Binggeli, B., & Böhringer, H. 1999, A&A, 343, 420

Schweizer, F. 1976, ApJS, 31, 313

Scott, D., White, M., Cohn, J. D., & Pierpaoli, E. 2001, MNRAS submitted (astro-ph/0104435)

Sellwood, J. A. 2000, ApJ, 540, L1

Sempere, M. J., Combes, F., & Casoli, F. 1995, A&A, 299, 371

Shapiro, P. R., & Iliev, I. T. 2000, ApJ, 542, L1

Silva, L., Granato, G. L., Bressan, A., & Danese, L. 1998, ApJ, 509, 103

Slyz, A., 1998, PhD thesis, Columbia University, New York

Slyz, A., Devriendt, J., Silk, J., & Burkert, A. 2002, MNRAS, in press

Slyz, A., & Prendergast, K. H. 1999, A&AS, 139, 199

Sorensen, S.-A., & Matsuda, T. 1982, MNRAS, 198, 865

Spergel, D. N., & Steinhardt, P. J. 2000, Phys. Rev. Lett., 84, 3760

Squires, G., Kaiser, N., Babul, A., Fahlman, G., Woods, D., Neumann, D., & Böhringer, H. 1996, ApJ, 461, 572

Steinmetz, M., & Müller, E. 1995, MNRAS, 276, 549

Stompor, R. et al. 2001, ApJ, 561, L7

Thuan, T. X., & Gunn, J. E. 1976, PASP, 88, 543

Toomre, A. 1974, in 'The Formation and Dynamics of Galaxies', ed. J. Shakeshaft (Dordrecht: Reidel Pub.), 347

Toomre, A. 1981, in 'The Structure and Evolution of Normal Galaxies', eds. S. M. Fall, & D. Lynden-Bell (Cambridge: Cambridge University Press), 111

Tully, R. B., Verheijen, M. A. W., Pierce, M. J., Huang, J.-S., & Wainscoat, R. J. 1996, AJ, 112, 2471

Tytler, D., O'Meara, J. M., Suzuki, N., & Lubin, D. 2000, Physics Reports, 333-334 (1-6), 409

Udalski, A., Szymański, M., Kałużny, J., Kubiak, M., & Mateo, M. 1992, Acta Astronomica, 42, 253

Valageas, P., Silk, J., & Schaeffer, R. 2001, A&A, 366, 363

van Albada, T. S., Bahcall, J. N., Begeman, K., & Sancisi, R. 1985, ApJ, 295, 305

van Albada, T. S., & Sancisi, R. 1986, Phil. Trans. of the Roy. Soc. (London), Ser. A 320, no. 1556, 447

van den Bosch, F. C., & Swaters, R. A. 2001, MNRAS, 325, 1017

Verheijen, M. A. W. 1997, PhD thesis, University of Groningen

Verheijen, M. A. W., & Sancisi, R. 2001, A&A, 370, 765

Visser, H. C. D. 1980, A&A, 88, 159

Weiner, B. J., Sellwood, J. A., & Williams, T. B. 2001a, ApJ, 546, 931

Weiner, B. J., Williams, T. B., van Gorkom, J. H., & Sellwood, J. A. 2001b, ApJ, 546, 916

Wilson, G., Kaiser, N., & Luppino, G. A. 2001, ApJ, 556, 601

Wray, J. D. 1988, 'The Color Atlas of Galaxies', (Cambridge: Cambridge University Press)

Xu, K. 1998, Gas-Kinetic Schemes for Unsteady Compressible Flow Simulations, VKI report 1998-03 von Karmann Institute Lecture Series

Xu, K., & Prendergast K. H. 1994, J. Comput. Phys., 114, 9

Yoshida, N., Springel, V., White, S. D. M., & Tormen, G. 2000, ApJ, 544, L87

Yuan, C., & Kuo, C.-L. 1997, ApJ, 486, 750

Zwicky, F. 1937, ApJ, 86, 217

Acknowledgements

It is a pleasure to express my gratitude to the many people who contributed with different kinds of support to the success of this thesis. My thanks to all!

Especially, I'd like to thank my advisor Hans-Walter Rix for sharing his experience and enthusiasm with me! His ability to inspire and encourage is outstanding and had a considerable part in making this project thoroughly enjoyable. Thanks for coming to Heidelberg at the right time and making it all possible!

In particular, I'd like to thank my collaborator Adrianne Slyz. I'm forever indebted to her for having been extremely generous with her time, expertise and patience. It took countless hours of coding, discussing and fighting stupid computers to achieve these excellent results – especially for certain, uncooperative galaxies! Moreover, she invested immense amounts of time to improve my writing style in several manuscripts! Thanks for all this, I enjoyed it a lot!

Furthermore, I'm grateful to all numerous people with whom I had enlightening scientific discussions! Particular thanks go to Panos Patsis for his continuous interest and feedback on the project. I dedicate him Figure 7.1! Special thanks also go to Philippe Héraudeau for providing observational data from his personal archive. It helped a lot during various stages of this work!

I'm grateful also to Rainer Spurzem for co-refereeing this thesis. I appreciated his feedback and his unbureaucratic style in dealing with time and location constraints!

Moreover, I'm indebted to the Calar Alto team, for letting me return after my inglorious debut at the 3.5 m telescope. (I'm sorry, Luzma!) Nevertheless, I enjoyed every single stay!

Also I appreciated the splendid working atmosphere at the MPIA! Thanks go to all my fellow students and postdocs for fruitful discussions as well as pointless slacking! Extra thanks go to Henry Lee for proofreading parts of the manuscript.

Besonderen Dank schulde ich dem Direktorium des MPIA und der Max-Planck Gesellschft für die Möglichkeit einer Promotion und die Bereitstellung finanzieller Mittel. Mein weiterer Dank gilt der EDV Abteilung für die stets effiziente Unterstützung im Kampf gegen Hard- und Softwarebugs, dem Technischen Dienst für unermüdliche Hilfsbereitschaft sogar nach Dienstschluss, dem Küchenpersonal für das tägliche Brötchen und Frau Schleich für die hervorragende Organisation meiner Reisen in sonnige Gefilde!

This research has made use of NASA's Astrophysics Data System Abstract Service (ADS) and the NASA/IPAC Extragalactic Database (NED), which is operated by the Jet Propulsion Laboratory, California Institute of Technology, under contract with the National Aeronautics and Space Administration. I acknowledge the use of the astro-ph preprint archive, the SIMBAD database, operated at CDS, Strasbourg, France and LEDA, the Lyon-Meudon extragalactic database, through the CISM of the Lyon Claude-Bernard University. Furthermore, I acknowledge the use of data reduction software packages ESO-`MIDAS`, which is developed and maintained by the European Southern Observatory and `IRAF`, which is written and supported by the IRAF programming group at the National Optical Astronomy Observatories (NOAO) in Tucson, Arizona.

Der Thilo.